UAB
Universitat Autònoma de Barcelona

Engineering Chiral Interactions and Current-induced Switching in Magnetic Heterostructures for Efficient Spintronics

Stefano Fedel

UNIVERSITAT AUTÒNOMA DE BARCELONA

DOCTORAL THESIS

Engineering Chiral Interactions and Current-induced Switching in Magnetic Heterostructures for Efficient Spintronics

---

A thesis submitted in the fulfillment of the requirements

for the degree of Doctor of Philosophy in Physics

in the

Laboratory of Multifunctional Thin Films and Complex Structures (MULFOX)

ICMAB-CSIC

by

Stefano Fedel

Barcelona, November 2025

Thesis Supervisor

Dr. Can Onur Avci

Thesis Tutor

Prof. Dr. Jordi Sort Viñas

Examination Committee

President:	Prof. Dr. Sergio O. Valenzuela
Secretary:	Prof. Dr. Saül Vélez
Vocal:	Dr. Stefania Pizzini

Barcelona, November 2025

Abstract

This thesis investigates chiral magnetic interactions and current-induced control of magnetization in magnetic heterostructures comprising ferrimagnetic insulators and metallic multilayers, aiming to address outstanding challenges in the field of spintronics. Spintronics, which exploits the electron's spin in addition to its charge, offers a promising alternative to conventional electronics by enabling non-volatile, high-speed, and low-power devices. Particular focus is placed on terbium iron garnet (TbIG), a representative ferrimagnetic insulator that combines low damping, tunable anisotropy, and compatibility with spin–orbit torque (SOT) switching.

Before beginning the experimental work, significant effort was devoted to the design and implementation of a custom wide-field magneto-optical Kerr effect (MOKE) microscope. Developed from scratch, this system enables imaging of magnetic domains and domain wall (DW) dynamics under applied magnetic fields and electrical currents. It integrates automated control, high-sensitivity imaging, and cryogenic compatibility, providing a versatile platform for studying field- and current-driven magnetization processes in both insulating and metallic heterostructures.

Using this MOKE setup, we first quantified the interfacial Dzyaloshinskii–Moriya interaction (DMI) in GGG/TbIG/heavy-metal (HM) bilayers through DW depinning experiments combined with harmonic Hall analysis, addressing an open question regarding the origin of DMI in these systems. DMI stabilizes chiral magnetic textures such as Néel DWs and skyrmions, which efficiently couple to SOTs for next-generation devices like racetrack memories. DMI was measured as a function of HM thickness and composition. By correlating these measurements with atomically-resolved electron microscopy, revealing a sharp TbIG/Pt interface and a highly intermixed GGG/TbIG interface, the TbIG/HM interface was identified as the dominant source of DMI. Interfacial spin transport measurements further highlighted the key role of the top interface in generating DMI.

We also demonstrated DMI tunability via nonmagnetic spacers. Inserting Cu as a spacer significantly modified the interfacial DMI due to long-range interactions between TbIG and the secondary Cu/HM interface. Density functional theory (DFT) calculations on similar structures support these experimental findings. Cu insertion reduced DMI by approximately 70% in TbIG/Pt systems but enhanced it by around 40% in TbIG/W stacks. These results suggest evidence of additional long-range contributions to DMI beyond the immediate interface.

Next, we investigated current-induced switching in TbIG mediated by SOTs originating from ultrathin Pt and light-metal overlayers such as Ti and Mn. Beyond conventional spin currents, we explored orbital contributions to SOTs, revealing signatures of the orbital Hall effect (OHE). These structures exhibited an approximate 90% increase in switching efficiency and a significant reduction in power dissipation, highlighting the active role of the light-metal overlayer, an element often overlooked in spintronics due to its low spin–orbit coupling (SOC) and inability to generate

spin currents.

This study also addressed the effectiveness of SOT mechanisms at ultrathin Pt thicknesses. Remarkably, we demonstrated that Pt layers as thin as 0.6 nm can achieve switching efficiencies comparable to those of thicker films. This enhancement arises from the granular morphology of sputtered Pt, which enables two complementary mechanisms, enhanced spin–orbit scattering at grain boundaries, increasing the effective spin Hall angle, and localized current density amplification due to non-uniform conduction paths. Three distinct regimes of SOT–morphology interplay were identified: (i) efficient bulk Pt (>1.2 nm), where the conventional spin Hall effect (SHE) dominates; (ii) inefficient intermediate Pt (0.7–1.2 nm), where the conventional SHE weakens and morphology effects are not yet active; (iii) efficient ultrathin Pt (∼0.6 nm), where morphology-induced mechanisms restore efficient spin–charge conversion. In this ultrathin regime, the current density and power consumption during switching events are comparable (or even lower) to those observed in traditional bulk Pt systems.

Finally, we extended the study of chiral magnetism to metallic multilayers, demonstrating the observation and control of spiral magnetic domains in Co/Pt/Co trilayers ortogonally magnetized, driven by interlayer DMI (IL-DMI). We identified unconventional spiral magnetic domains arising around magnetic imperfections or patterned magnetic structures. These domains and their evolution under applied magnetic fields were systematically analyzed, revealing strong dependence on layer thicknesses, external fields, and interfacial asymmetry. Furthermore, we demonstrated control of these chiral structures through patterning and engineered magnetic geometries, opening pathways for device concepts based on reconfigurable spin textures. The working hypothesis on the origin of these structures relies on the interplay between the ground-state spin configuration of the in-plane bottom Co layer around magnetic imperfections during deposition and IL-DMI, which stabilizes chiral structures, specifically spirals, coupled to the out-of-plane Co layer. These spirals are readily observable via MOKE imaging.

Overall, this work advances the understanding of chiral interactions and spin–orbit phenomena in both insulating and metallic systems. The results provide fundamental insights and practical strategies for engineering energy-efficient spintronic devices, such as racetrack memories and logic devices, and future architectures exploiting spin and orbital degrees of freedom.

Acknowledgements

A PhD is a long and often difficult journey, and if there is one part of this thesis that truly matters, the one people actually read, it is this: the acknowledgments, where I get to express my deepest gratitude to those who made it possible.

First and foremost, I want to thank my supervisor, Can. I wouldn't be here if it weren't for you approaching a nervous guy during his master's thesis in the ETH corridors and asking if I'd consider a PhD in Barcelona. Thank you for believing in me even before I believed in myself, and for the support you've shown throughout these years. As the first PhD to graduate from your group, I truly appreciate the extra effort you put into guiding me through every "first time."

The first year was particularly complicated, but thankfully, the group expanded very quickly with amazing researchers and even better people, who are now part of our SPINMAD team. I would like to thank each of you individually: Martin, Matteo, Silvia, Weronika, Teodor, Alejandro, Taka, and Mustafa. Silvia, thank you especially for your guidance and support through both scientific challenges and real-life struggles. And thank you, Matteo, for bringing with you exactly what I needed to make the most of this journey. I deeply admire your passion and creativity in taking on new challenges, and I'm truly grateful for the friendship that grew between us. Sharing this path with you has been one of the most valuable parts of my PhD.

I'm deeply grateful to Otani-sensei for welcoming me into his lab and giving me one of the most unforgettable and meaningful experiences of my life, halfway across the world.

Thanks also to everyone at ICMAB with whom I shared endless lunches, coffees, and so much more. The list could be longer than the thesis itself. Thank you Emma, Ema, Giulia, Gio, Mario, Aish, Neil, Aleix, Thomas, Tom, Vittorio, Mila, Marco, Luca, Ona, Darla, and everyone else. Special thanks to the Barbell girls, for believing in a Barbell world. Training after work has long been my comfort zone. Thank you, Gio, for introducing me to it.

I cannot forget to thank the Montflorit family, who gave me stories to tell for years to come. Living in a big house is a blessing when it's filled with people like you. I especially want to thank Anna, who made me feel at home in a place that wasn't. Without you, I probably wouldn't have made it to the end of this journey. You've played a bigger role in this and in my life than you can imagine, and I deeply admire your perseverance and empathy in everything you do.

Thanks to all the friends who came to the barbecue parties, which became an institution and remain among the best memories of my life. Thank you Matteo, Pedro, Tomek, Davide, and all my friends in Barcelona for making those moments so special.

Després, voldria agraïr a en Pol, a l'Adru i a tots els amics de La Flama per haver acollit un grup d'italians als seus concerts i a les seves tradicions, i per haver-me fet sentir part d'alguna cosa, fins i tot lluny de casa.

Thanks to my friends back home for showing me that real friendship can withstand years of distance. Even if we only see each other twice a year, it always feels like I never left. Thank you Mich, Piso, Fau, Pippo, Manuel, Ale, Angi, and everyone else.

Thanks also to all my friends around the world, whom I met at conferences or during my stays abroad. One of the best parts of doing a PhD is meeting incredible people everywhere, and I feel truly lucky for each and every one of you.

Finally, I left the most important part for the end: my family.

Non potrò mai ringraziare abbastanza mia mamma Roberta per tutto quello che ha fatto per me in questi anni. A parole non posso esprimere quanto sia stato importante il suo costante supporto, senza il quale questo traguardo sarebbe stato per me irraggiungibile.

Grazie a papà Andrea, per essere sempre un punto di riferimento, per l'esempio che mi dai ogni giorno e per avermi insegnato cosa conta davvero nella vita.

Grazie a mio fratello Daniele, perché anche se la vita ci ha portati su strade diverse, le nostre differenze e la distanza non cambiano il legame che ci unisce.

Grazie alle nonne, sempre fiere di tutto quello che faccio; grazie a zii e cugini, perché i pranzi e le cene in famiglia sono ogni volta una ricarica di energia senza la quale non avrei portato a termine questo lavoro.

Contents

Chapter 1

Introduction

The ongoing digital transformation is reshaping modern society, driving an ever-increasing demand for faster, more energy-efficient computing technologies. As global energy consumption by electronic devices continues to rise, estimated between $14 and $18 billion annually [1], developing sustainable solutions has become a critical challenge. A promising strategy lies in advancing memory and logic technologies beyond conventional charge-based electronics.

Spintronics, or spin electronics, addresses this challenge by exploiting not only the electron's charge but also its intrinsic angular momentum, the spin [2]. This additional degree of freedom enables the design of devices that combine non-volatility, high speed, and low power consumption, making spintronics a key candidate for next-generation memory and logic architectures [3, 4]. Applications range from magnetic random-access memory (MRAM), already commercialized for embedded systems, to neuromorphic computing and energy-efficient logic devices, offering pathways to overcome the limitations of Complementary Metal-Oxide-Semiconductor (CMOS) scaling. At its core, spintronics relies on a fundamental interaction: magnetism in solid-state systems. Magnetism originates from the collective alignment of electron spins mediated by exchange interactions, and its manipulation underpins all spintronic functionalities. By controlling spin orientation through external fields, spin-polarized currents, or spin–orbit effects, it becomes possible to encode, process, and store information in a robust and energy-efficient manner. This interplay between fundamental physics and technological innovation positions spintronics as a transformative approach to sustainable computing.

The emergence of spintronics has been closely tied to advances in thin-film magnetism. In the 1960s, the development of deposition techniques such as molecular beam epitaxy and sputtering enabled the fabrication of ferromagnetic thin films with tailored properties, including magnetic anisotropy. The anisotropy determines the preferred orientation of magnetization, either in-plane (IP) or out-of-plane (OOP). In 1968, Gradmann and Müller observed that ultrathin NiFe films grown on Cu(111) could exhibit perpendicular magnetic anisotropy (PMA) due to interfacial effects [5]. While magnetic thin films were initially used in hard drives [6], it took decades before PMA-enabled structures became viable for advanced spintronic applications [7, 8].

A major breakthrough came with the discovery of giant magnetoresistance (GMR) by Grünberg [9]

and Fert [10]. GMR arises in trilayer structures composed of two ferromagnetic layers separated by a non-magnetic metal spacer. The resistance of the structure depends on the relative alignment of the magnetizations: it is higher for antiparallel and lower for parallel configurations, due to spin-dependent electron scattering (typical GMR ratios are about 10–20% at room temperature, reaching up to $\sim 40\%$ in optimized structures).

A related phenomenon, tunnel magnetoresistance (TMR), occurs when the metallic spacer in a GMR structure is replaced by a thin insulating barrier, allowing quantum tunneling of electrons. First observed by Julliére in 1975 [11], TMR depends on the relative spin-dependent density of states in the two ferromagnetic layers. The resistance is low when the spin states match across the barrier and high when they do not. Interest in TMR surged after Yuasa *et al.* [12] and Ikeda *et al.* [13] demonstrated giant TMR in epitaxial Fe/MgO/Fe and CoFeB/MgO/CoFeB structures, respectively (with TMR ratios of 150–250% at room temperature and exceeding 600% in state-of-the-art devices).

TMR underpins the operation of magnetic tunnel junctions (MTJs), which consist of a reference layer with fixed magnetization, a free layer with switchable magnetization, and a tunnel barrier in between. MTJs form the core of MRAMs, where data is stored based on the relative alignment of the reference and free layers: parallel alignment yields low resistance (bit '0'), and antiparallel alignment yields high resistance (bit '1'). Reading in MRAM involves measuring resistance, while writing can be achieved via spin-transfer torque (STT) [14] or spin-orbit torque (SOT) [15]. STT, predicted by Slonczewski and Berger in 1996 [16, 17], uses a spin-polarized current to exert torque on the free layer magnetization, enabling switching. STT-MRAM offers high speed, low power, and endurance [15], but suffers from shared read/write paths, which can degrade the tunnel barrier over time [18].

SOT provides an alternative by separating read and write paths. Originating from spin-orbit coupling (SOC) in heavy-metal (HM)/ferromagnet (FM) bilayers, SOTs arise due to spin accumulation at interfaces, driven by the spin Hall effect (SHE) or Rashba-Edelstein effect (REE) [19, 20]. The first demonstration of SOT-induced switching was achieved in Pt/Co structures [19, 21]. Materials like Pt and W are now benchmarks for efficient SOT switching [22, 23]. In SOT-MRAM, a current pulse through the HM generates torques that switch the free layer magnetization without passing through the tunnel barrier. This decoupling enhances device reliability and scalability, making SOT a promising candidate for next-generation memory technologies.

Among the most promising materials for next-generation spintronic devices are rare-earth iron garnets (REIGs). The electrical manipulation of magnetization in REIGs represents a recent and promising advancement in spintronics. These ferrimagnetic insulators offer low damping, tunable magnetic properties, and compatibility with SOT switching, making them ideal for energy-efficient memory applications [24]. Their role will be explored in depth throughout this thesis.

The first demonstration of robust SOT-induced switching in REIGs was reported by Avci *et al.* in 2017 using a TmIG/Pt bilayer [25]. Since then, efficient SOT switching has been observed in various REIG/HM systems, including TmIG/Pt, TbIG/Pt, YIG/Pt, and Bi:YIG/Pt [26, 27, 28, 29, 30]. Notably, TmIG/W structures exhibit reversed switching polarity compared to TmIG/Pt, reinforcing the SHE as the dominant torque mechanism [31]. Recent studies have extended SOT switching to less common REIGs such as GdIG/Pt [32], HoIG/Pt [33], and YTmIG/Pt [34], highlighting the versatility of REIGs in spintronic applications.

Deterministic, field-free switching has been achieved in REIGs by engineering magnetic anisotropy or introducing structural asymmetries, such as REIG/FM bilayers or tailored interfaces [35, 36, 37,

38, 39]. These advances eliminate the need for external magnetic fields, enhancing device scalability and integration.

Beyond spin currents, REIG-based systems have also enabled magnetization control via orbital currents, leveraging the orbital Hall effect (OHE) [40, 41, 42, 43, 44]. In this mechanism, an electric field in a normal metal (NM) with weak SOC generates a transverse orbital angular momentum flow. Several multilayer structures have demonstrated orbital-current-driven SOT in REIGs, including TmIG/Pt/CuOx [45], Ta/Pt/TmIG [46], YIG/Pt/CuOx [47, 48], YIG/Pt/TaOx [49], and BiYIG/CuOx [50]. Depending on the stack geometry, the torque originates from interfacial orbital Rashba–Edelstein effects (OREE) or bulk OHE in the metallic layers.

These findings open new avenues for REIG-based spintronic devices that exploit both spin and orbital degrees of freedom, offering a path toward highly efficient, scalable, and sustainable memory technologies.

Furthermore, domain walls (DWs) in REIGs can be efficiently driven by the interplay between SOTs and the Dzyaloshinskii–Moriya interaction (DMI). REIGs offer an ideal platform for ultrafast DW motion due to their high crystallinity, low saturation magnetization, ultralow damping, and ferrimagnetic ordering with tunable compensation temperatures. The presence of interfacial DMI further stabilizes chiral Néel walls.

In 2019, Avci *et al.* [51] demonstrated that TmIG and TbIG exhibit DMI-stabilized left-handed Néel walls, using SOT-induced DW motion measurements. Their study revealed that the DMI originates primarily from the interface with the GGG substrate, a conclusion supported by several subsequent works [28, 52, 27, 53, 54, 55]. However, other studies have identified the REIG/HM interface as the dominant DMI source [56, 57, 58, 59, 60, 36, 61], leading to ongoing debate.

It was also demonstrated that chiral DWs in TmIG can reach velocities up to 800 m/s under current densities of 1.2×10^8 A/cm^2, attributed to the ferrimagnetic nature of TmIG and the suppression of precessional dynamics. Unlike metallic FM, ferrimagnets (FI) exhibit strong antiferromagnetic coupling between sublattices, which minimizes net magnetization precession. As a result, DW velocity is limited by the exchange field rather than the DMI field [62]. A particularly striking result was reported by Caretta *et al.* [30], who achieved DW velocities approaching the relativistic limit ($\sim$ 4300 m/s) in Bi:YIG at room temperature (RT). This performance was attributed to strong DMI, ferrimagnetic ordering, and the ultralow damping associated with Bi ions.

Finally, DMI in REIGs has also been linked to the formation of magnetic skyrmions. While direct imaging remains challenging, evidence from topological Hall effect measurements suggests their presence in TmIG and YIG [56, 63]. More recently, Velez *et al.* [64] directly observed nanoscale skyrmions and their current-driven dynamics in YIG/TmIG/Pt trilayers, confirming the existence of these topologically protected textures.

The unique properties of REIGs and their compatibility with advanced spintronic mechanisms position them as key materials for next-generation memory technologies. These include racetrack memory, first proposed by Parkin in 2008 [65, 66], which stores data along nanowires via current-driven domain wall motion. REIGs offer strong potential for ultrafast, low-power racetrack devices due to their efficient SOT switching and high domain wall mobility. Beyond memory, REIG-based systems are being explored in several emerging areas. In magnonics, their low damping, high crystallinity, and efficient spin-wave transport make them ideal candidates for wave-based computing [67]. Moreover, their tunable properties and versatility enable applications in neuromorphic computing, magnetic sensors, and other innovative spintronic platforms.

Another recently discovered magnetic interaction is the long-range interlayer Dzyaloshinskii–Moriya interaction (IL-DMI), a chiral coupling between two ferromagnetic layers separated by a HM. This interaction introduces a novel degree of freedom for controlling magnetic chirality and domain configurations in multilayer systems.

In this thesis, we focus primarily on chiral magnetism, with the following objectives: (i) to investigate the origin of DMI in REIG/HM heterostructures; (ii) to study the role of IL-DMI in the formation of magnetic domains in fully metallic multilayers such as Co/Pt/Co; and (iii) to explore current-driven magnetization switching in unconventional systems, specifically ultrathin granular Pt interfaced with REIGs and non-magnetic overlayers, aiming to uncover new mechanisms and material platforms for efficient SOT control.

The thesis is organized as follows. *Chapter 2* provides a brief overview of the fundamental concepts of magnetism relevant to this work, along with an introduction to magnetoelectric transport phenomena in solids. *Chapter 3* focuses on the physics of spin accumulation, its origin and symmetry, and the resulting SOTs and their influence on magnetization dynamics. *Chapter 4* discusses chiral interactions, particularly the DMI, and their effects on the static and dynamic behavior of magnetic domains and DWs. *Chapter 5* outlines the experimental methods and materials used throughout the thesis, including sample preparation and measurement techniques. *Chapter 6* describes the custom-built MOKE (Magneto-Optical Kerr Effect) microscope developed for this work, covering both theoretical principles and practical implementation. *Chapter 7* presents results on DMI in REIG/HM heterostructures, revealing evidence of long-range interactions not previously discussed in the literature. *Chapter 8* investigates SOTs in REIG/Pt systems and explores the potential orbital contributions from light metals such as Ti and Mn, introduced as top layers. *Chapter 9* introduces an ongoing project focused on IL-DMI in Co/Pt/Co metallic heterostructures and the emergence of unconventional domain formation in these systems. Finally, in *Chapter 10*, conclusions and an outlook on future developments are presented.

Chapter 2

Basic Concepts of Magnetism and Magnetotransport

Contents

2.1 Magnetic Interactions in Crystals

This chapter introduces the fundamental mechanisms that govern magnetic behavior in crystalline solids. It begins with the quantum origins of magnetism, including orbital and spin angular momentum, and progresses through key interactions such as SOC, exchange interactions, and anisotropy. These concepts are essential for understanding how microscopic magnetic moments give rise to macroscopic magnetic order, which underpins technologies ranging from permanent magnets to spintronic devices.

2.1.1 Electron Angular Momentum and Spin-Orbit Interaction

The magnetic properties of materials originate fundamentally from two sources: the orbital and spin angular momentum of electrons.

An electron orbiting a nucleus can be viewed as a microscopic current loop, since its position changes with time, consistent with the definition of electric current [68, 69]. According to Ampère's law, the magnetic moment associated with this orbital motion is:

$$\mathbf{m} = IA, \tag{2.1}$$

where I is the current and $A = \pi r^2$ is the area enclosed by the orbit. The magnetic moment $\mathbf{m}$ is oriented perpendicular to the plane of the orbit, following the right-hand rule.

From quantum mechanics, the orbital angular momentum of an electron is quantized as $m_e v r = m_l \hbar$, where m_e is the electron mass, v its velocity, r the orbital radius, m_l the magnetic quantum number (an integer), and $\hbar$ the reduced Planck constant. This leads to an orbital magnetic moment:

$$\mathbf{m}_{\mathrm{L}} = -\frac{e\hbar}{2m_e} m_l = -\mu_B m_l, \tag{2.2}$$

where $\mu_B = \frac{e\hbar}{2m_e}$ is the Bohr magneton, which is the fundamental unit of magnetic moment, with a value of approximately $\mu_B \approx 9.274 \times 10^{-24}\,\mathrm{J/T}$.

In addition to orbital motion, electrons possess an intrinsic angular momentum known as spin. The magnetic moment associated with spin is:

$$\mathbf{m}_{\mathrm{S}} = -g_e \mu_B m_s, \tag{2.3}$$

where $g_e \approx 2.0023$ is the electron g-factor, and $m_s = \pm\frac{1}{2}$ is the spin quantum number. Although electron spin has no classical analogue as literal rotation, it gives rise to a real and measurable magnetic moment.

In many-electron atoms, the total orbital angular momentum and total spin angular momentum are given by $L = \sum m_l$ and $S = \sum m_s$, respectively. To determine the total angular momentum of the atom, Hund's rules are applied:

1. Maximize S,
2. Maximize L consistent with the first rule,
3. The total angular momentum J is given by $J = |L \pm S|$, where the sign depends on whether the electron shell is more or less than half-filled.

The total magnetic moment is then:

$$\mathbf{m} = -g\mu_B M_J, \tag{2.4}$$

where M_J is the projection of the total angular momentum on the quantization axis (usually the z-axis), and g is the Landé g-factor, given by:

$$g = 1 + \frac{J(J+1) + S(S+1) - L(L+1)}{2J(J+1)}. \tag{2.5}$$

Together, the spin and orbital contributions determine the total magnetic moment of electrons in atoms and form the foundation for understanding magnetic ordering, anisotropy, and spintronic phenomena.

Spin Orbit Coupling

SOC is a fundamental relativistic phenomenon in solid-state physics that gives rise to a wide range of magnetic and magnetotransport effects. It originates from the interaction between an electron's spin and its motion through an electric field, typically that of an atomic nucleus.

A classical way to understand SOC is to consider an electron (with charge $-e$) orbiting a nucleus (charge $+Ze$) with velocity $\mathbf{v}$. In the rest frame of the nucleus, the electron experiences a radial electric field $\mathbf{E}$. However, in the electron's rest frame, the nucleus appears to orbit the electron, generating a magnetic field $\mathbf{B}_{\mathrm{SO}}$ due to its motion, according to Ampère's law. This magnetic field acts on the spin magnetic moment $\mathbf{s}$ of the electron, with magnitude given by:

$$B_{\mathrm{SO}} = \frac{\mu_0 Zev}{4\pi r^2}, \tag{2.6}$$

where μ_0 is the vacuum permeability, Z is the atomic number, and $\mathbf{r}$ is the radial vector from the nucleus to the electron. The direction of $\mathbf{B}_{\mathrm{SO}}$ is perpendicular to both $\mathbf{v}$ and $\mathbf{E}$, and thus parallel to the electron's orbital angular momentum $\mathbf{l}$. As a result, the spin and orbital magnetic moments are coupled through this internal magnetic field [68].

This picture can be generalized to multi-electron atoms by replacing the single-particle angular momenta with the total orbital and spin angular momenta $\mathbf{L}$ and $\mathbf{S}$, respectively. The SOC interaction can then be described by the following Hamiltonian:

$$H_{\mathrm{SO}} = \frac{Ze^2}{8\pi\epsilon_0 m_e^2 c^2 r^3}\,\mathbf{L}\cdot\mathbf{S}, \tag{2.7}$$

where c is the speed of light and ϵ_0 the vacuum permittivity. This expression shows that SOC strength increases with atomic number Z, making it negligible in light elements but significant in heavy elements such as platinum (Pt), bismuth (Bi), or iridium (Ir). This equation is often expressed as:

$$H_{\mathrm{SO}} = \lambda\,\mathbf{L}\cdot\mathbf{S}, \tag{2.8}$$

where λ characterizes the strength of the spin-orbit interaction (Fig. 2.1).

SOC plays a central role in phenomena such as magnetocrystalline anisotropy, SHE, REE, SOTs, and DMI, all of which are key to modern spintronics.

2.1.2 Exchange Interaction and Magnetic Ordering

Although individual atomic magnetic moments originate from spin and orbital angular momentum, long-range magnetic order in solids arises only through interactions between these moments. In ferromagnets, for example, neighboring moments align parallel, producing a spontaneous magnetization even without an external field. In contrast, antiferromagnets exhibit antiparallel alignment, while in paramagnets, thermal fluctuations prevent long-range order.

The driving force behind these different types of order is the *exchange interaction*, a purely quantum mechanical effect with no classical analogue. It originates from the combined action of Coulomb repulsion and the Pauli exclusion principle, which requires the total electronic wavefunction to be antisymmetric under particle exchange. Depending on the spatial overlap of electronic orbitals, the exchange energy can favor either parallel (ferromagnetic) or antiparallel (antiferromagnetic) alignment of neighboring spins.

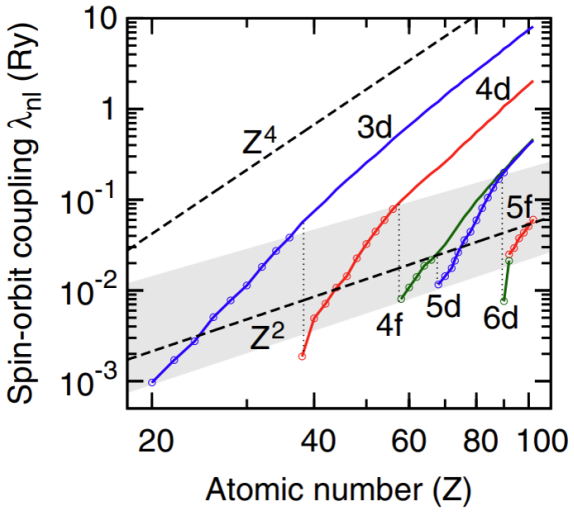

Figure 2.1: Strength of SOC as a function of the atomic number Z. Taken from [70].

Importantly, the exchange interaction should not be confused with classical magnetic dipole–dipole forces, which are typically much weaker and act over longer distances. Instead, exchange is a short-range interaction that sets the fundamental energy scale for magnetic ordering in solids, thereby determining whether a material becomes ferromagnetic, antiferromagnetic, or remains paramagnetic.

Consider two electrons with spatial coordinates $\mathbf{r}_1$ and $\mathbf{r}_2$, and spin states χ_1, χ_2. The total two-electron wavefunction must be antisymmetric under exchange of the two particles:

$$\Psi(\mathbf{r}_1, \mathbf{r}_2; \chi_1, \chi_2) = \psi(\mathbf{r}_1, \mathbf{r}_2)\, \chi(\chi_1, \chi_2), \tag{2.9}$$

where ψ is the spatial part and χ the spin part. If the spin wavefunction is symmetric (triplet state, parallel spins), then the spatial part must be antisymmetric, which reduces the probability of finding the two electrons at the same position. This reduced spatial overlap lowers the Coulomb repulsion. Conversely, for the antisymmetric spin state (singlet, antiparallel spins), the spatial part is symmetric, leading to higher spatial overlap and therefore larger Coulomb repulsion.

The energy difference between these two cases can be captured by an effective interaction term, described by the Heisenberg exchange Hamiltonian:

$$\mathcal{H}_{\text{ex}} = -2J \sum_{\langle i,j \rangle} \mathbf{S}_i \cdot \mathbf{S}_j, \tag{2.10}$$

where $\mathbf{S}_i$ and $\mathbf{S}_j$ are spin operators on neighboring sites i and j, and J is the exchange integral. The latter is defined as

$$J = \frac{E_{\text{S}} - E_{\text{T}}}{2}, \tag{2.11}$$

where E_{S} and E_{T} are the energies of the singlet and triplet states, respectively. The sign and magnitude of J determine the nature of the interaction:

- $J > 0$: the triplet state is energetically favored, spins align parallel, leading to **ferromagnetism**.

- $J < 0$: the singlet state is favored, spins align antiparallel, leading to **antiferromagnetism**.

The value of J is strongly influenced by how electronic orbitals overlap and by the balance between kinetic energy (which favors electron hopping) and Coulomb repulsion. In crystals, these microscopic exchange interactions give rise to the various types of magnetic order observed in materials. As a result, the exchange interaction is fundamental to magnetism, underlying phenomena such as spontaneous ferromagnetism, antiferromagnetic order, and other collective magnetic behaviors in condensed matter systems.

Other than the already cited cases of ferromagnetism, where neighboring spins align parallel due to positive exchange, producing a spontaneous macroscopic magnetization even without an external field, antiferromagnetism, where neighboring spins align antiparallel, leading to zero net magnetization [71, 72], and paramagnetism, where spins are randomly oriented by thermal fluctuations but weakly align with an applied magnetic field, several other types of magnetic order exist in nature.

All materials exhibit diamagnetism, a generally weak effect in which an applied field induces small opposing currents that generate a magnetic response opposite to the external field. More relevant for this thesis is ferrimagnetism, where opposing magnetic sublattices align antiparallel but with unequal magnetic moments, resulting in a net magnetization [71, 72]. In fact, most of this work relies on REIGs, which are insulating ferrimagnets with three distinct magnetic sublattices, as will be described in detail in subsequent chapters.

Non-collinear states of magnetism are also possible. In frustrated antiferromagnets, for example, competing interactions prevent simple antiparallel alignment, so the orientation of each spin depends on its local environment. Altermagnetism represents a recently identified class, in which spins on different sublattices are collinear, yet symmetry-breaking in momentum space produces spin-split bands despite zero net magnetization [73]. Finally, in some materials below a characteristic freezing temperature, spins enter a disordered state where they freeze into random orientations without long-range order but also without full randomness, a phenomenon known as the spin-glass state [74].

2.1.3 Superexchange Interaction

In insulating materials, where conduction electrons are absent, magnetic coupling between localized moments cannot occur via direct wavefunction overlap or through conduction electrons, as in metallic systems. Instead, an indirect exchange mechanism known as superexchange governs the interaction between magnetic ions.

Superexchange is defined as an indirect interaction between non-neighboring magnetic cations, mediated by a non-magnetic anion situated between them. The mechanism arises from virtual electron hopping between the cation and anion orbitals, treated within second-order perturbation theory. Due to the Pauli exclusion principle and Coulomb repulsion, the energy cost of these virtual processes depends on the relative spin orientation, resulting in an effective spin–spin coupling.

A classic example is the Mn^{2+}-O-Mn^{2+} chain found in manganese oxides, where the half-filled $3d$ orbitals of neighboring Mn ions are indirectly coupled via the $2p$ orbitals of the oxygen atom (see Fig. 2.2). Depending on orbital occupancy and symmetry, the resulting superexchange interaction can be either ferromagnetic or antiferromagnetic, though it is most often antiferromagnetic. The interaction was first described theoretically by P.W. Anderson in the 1950s [75] and later generalized

by the Goodenough–Kanamori–Anderson (GKA) rules [76], which predict the sign and strength of the interaction based on orbital geometry and electronic configuration.

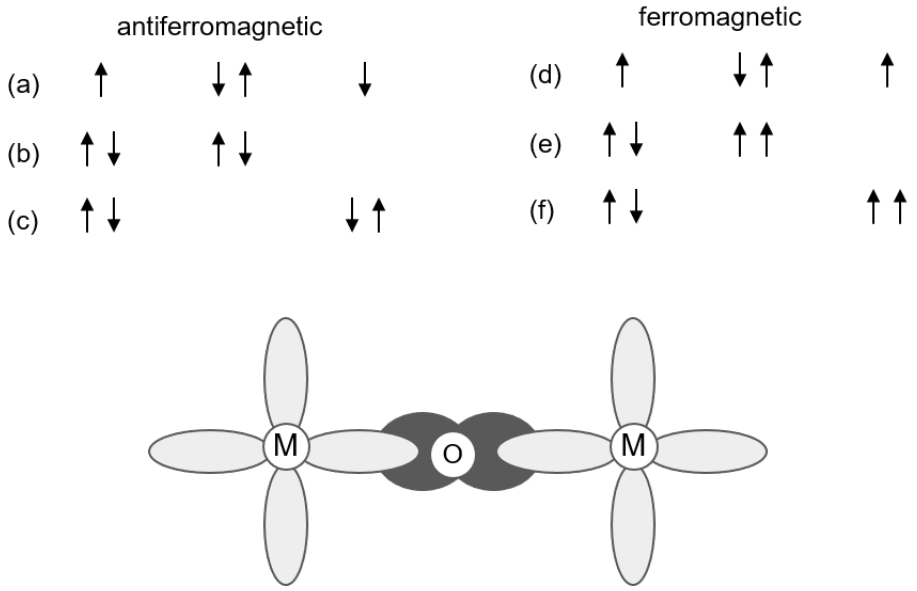

Figure 2.2: Schematic illustration of superexchange interaction in a magnetic oxide. The diagram shows spin configurations of four electrons distributed across a transition metal (M) and an oxygen (O) atom. In the antiferromagnetic case (a–c), the ground state (a) can hybridize with excited configurations (b) and (c), allowing magnetic electrons to delocalize over the M–O–M unit and lower the kinetic energy. In contrast, for ferromagnetic coupling (d–f), the ground state (d) cannot mix with excited states (e) and (f) due to the Pauli exclusion principle, resulting in a higher energy configuration. Adapted from [68].

This mechanism plays a central role in explaining antiferromagnetic ordering, Mott insulating behavior, and the magnetism of high-temperature superconductors. As such, superexchange remains a cornerstone of modern theories of strongly correlated electron systems.

Superexchange is particularly important in REIGs, where the magnetic coupling between Fe ions occurs via oxygen-mediated superexchange, giving rise to their characteristic ferrimagnetic behavior. Understanding this mechanism is essential for interpreting the magnetic properties and spin dynamics of REIGs thin films, which are discussed in detail in the following chapters.

2.1.4 RKKY Interaction

The strength and sign of the exchange interaction between localized magnetic moments in metals can be mediated indirectly by conduction electrons, a mechanism known as the Ruderman–Kittel–Kasuya–Yosida (RKKY) interaction [77, 78, 79]. This interaction is central to the magnetic behavior of diluted magnetic alloys, rare-earth intermetallics, and many spintronic systems.

The underlying process is as follows: a localized moment $\mathbf{S}_i$ induces a spin polarization in the surrounding conduction electrons. This polarization extends through the electron sea and influences the spin orientation at another site $\mathbf{S}_j$, effectively coupling the two moments. The resulting interaction is both long-ranged and oscillatory, with its period set by the Fermi wavevector.

The RKKY interaction energy between two localized moments separated by a distance $r = |\mathbf{r}_i - \mathbf{r}_j|$ can be expressed as [68]:

$$\mathcal{H}_{\mathrm{RKKY}} = -J_{\mathrm{RKKY}}(r)\,\mathbf{S}_i \cdot \mathbf{S}_j, \tag{2.12}$$

where the coupling constant has the form:

$$J_{\mathrm{RKKY}}(r) = \frac{A}{r^3}\cos(2k_F r), \tag{2.13}$$

with A being a material-dependent prefactor and k_F the Fermi wavevector of the conduction electrons. This form reveals two key features: it decays as $1/r^3$, making it significantly longer-ranged than direct Heisenberg exchange (only between nearest neighbors), and it oscillates in sign, so the coupling can be either ferromagnetic or antiferromagnetic depending on the distance r between moments.

The oscillatory nature of RKKY leads to frustration and complex magnetic ordering in systems with multiple interacting spins at varying distances, such as spin glasses and certain rare-earth alloys. This mechanism has been extensively studied both theoretically and experimentally [80, 81, 82]. The period and magnitude of the RKKY coupling have been shown to depend on the thickness and type of nonmagnetic spacer layer (e.g., Cu, Ag, Au) between ferromagnetic layers [83, 84].

Microscopically, the RKKY interaction can be derived using second-order perturbation theory applied to the s–d (or s–f) exchange Hamiltonian, which couples localized magnetic moments to the spin density of itinerant electrons:

$$\mathcal{H}_{sd} = -J_{sd}\sum_i \mathbf{S}_i \cdot \mathbf{s}(\mathbf{r}_i), \tag{2.14}$$

where $\mathbf{s}(\mathbf{r}_i)$ is the conduction electron spin density operator at site $\mathbf{r}_i$, and J_{sd} is the local exchange coupling constant.

The RKKY interaction is central to understanding magnetic coupling in multilayer systems. It forms the basis for the behavior of engineered magnetic multilayers and GMR devices, where the coupling between ferromagnetic layers separated by a nonmagnetic spacer oscillates between ferromagnetic and antiferromagnetic as the spacer thickness changes. Beyond this, the RKKY mechanism also underlies other long-range exchange effects, such as the IL-DMI, which will be discussed later and is particularly relevant to the work presented in this thesis.

2.1.5 Magnetic Anisotropy

In ferromagnetic materials, magnetic properties are generally not isotropic in space. The magnetization vector $\mathbf{M}$ often prefers one or more specific directions in space, referred to as easy axes. This directional dependence is called magnetic anisotropy, and it can arise from various physical origins.

The effect is typically described by an anisotropy energy density E_a, which quantifies the energy cost of deviating from the easy axis. For uniaxial anisotropy, the energy can be expressed as [69]:

$$E_a = K_u \sin^2\theta, \tag{2.15}$$

where θ is the angle between the magnetization direction and the easy axis, and K_u is the anisotropy constant, measured in $\mathrm{J/m^3}$. A positive K_u indicates a preferred alignment along the easy axis ($\theta = 0°$).

Shape Anisotropy

Shape anisotropy originates from the demagnetizing field, which depends on the geometry of the magnetic sample. Each magnetic moment in the material acts as a dipole and interacts with others through long-range dipolar (magnetostatic) interactions. The dipole–dipole interaction energy between two magnetic moments $\boldsymbol{\mu}_1$ and $\boldsymbol{\mu}_2$ separated by a vector $\mathbf{r}$ is given by [69]:

$$E = \frac{\mu_0}{4\pi r^3}\left[\boldsymbol{\mu}_1 \cdot \boldsymbol{\mu}_2 - \frac{3}{r^2}(\boldsymbol{\mu}_1 \cdot \mathbf{r})(\boldsymbol{\mu}_2 \cdot \mathbf{r})\right]. \tag{2.16}$$

This energy is minimized when the magnetic moments align parallel to the longest dimension of the sample, favoring magnetization along that axis. As such, this form of anisotropy is not intrinsic to the material but depends on its macroscopic shape.

Shape anisotropy is particularly significant in nanoscale systems, where domain formation is suppressed and the magnetization tends to remain nearly uniform. In the case of ultrathin films, as used in this thesis, the thickness is much smaller than the lateral dimensions, resulting in a strong demagnetizing field in the OOP direction. This effect confines the magnetization predominantly IP.

The associated shape anisotropy energy density in the thin film limit can be approximated as:

$$K_{\text{shape}} \approx \frac{1}{2}\mu_0 M_s^2, \tag{2.17}$$

where M_s is the saturation magnetization of the material. This term acts to favor IP magnetization.

For most metallic thin films used in this work, which are polycrystalline, shape anisotropy dominates the anisotropy landscape and often dictates the ground-state magnetization direction. To achieve PMA, an additional competing term favoring OOP alignment must overcome this shape-induced IP preference. In metallic systems, this is typically realized through interfacial contributions, as discussed in the following sections. By contrast, the insulating REIGs studied here can overcome shape anisotropy through strain-induced anisotropy, stabilizing PMA. This perpendicular orientation is essential for the controlled manipulation of DWs and for SOT experiments.

Magnetocrystalline Anisotropy

Magnetocrystalline anisotropy arises from the dependence of the spin–orbit interaction energy on the orientation of magnetization relative to the crystal lattice. In a crystalline solid, the atomic arrangement breaks rotational symmetry, making certain crystallographic directions energetically favorable for magnetization.

The strength and direction of this anisotropy depend on the symmetry of the crystal structure. For example, in cubic crystals like Fe or Ni, the easy axes often lie along the $\langle 100 \rangle$ or $\langle 111 \rangle$ directions, while in hexagonal close-packed (hcp) structures like Co, the easy axis lies along the c-axis.

In cubic systems, the lowest-order magnetocrystalline anisotropy energy density can be expressed as:

$$E_{\text{mc}} = K_1\left(\alpha_1^2\alpha_2^2 + \alpha_2^2\alpha_3^2 + \alpha_3^2\alpha_1^2\right), \tag{2.18}$$

where K_1 is the first-order anisotropy constant, and α_i are the direction cosines of the magnetization vector with respect to the crystallographic axes [69].

While magnetocrystalline anisotropy plays only a minor role in the polycrystalline metallic films studied in this thesis, it can become significant in garnet films, where epitaxial growth and lattice strain introduce sizable anisotropy contributions.

Magnetoelastic Anisotropy

Magnetoelastic anisotropy arises from the coupling between magnetization and lattice strain, a phenomenon known as magnetostriction. When a magnetic material is subjected to internal or external mechanical stress, its magnetic energy landscape changes, leading to anisotropic behavior. This effect becomes particularly significant in thin films, where lattice mismatch and thermal strain are common.

The magnetoelastic contribution to the anisotropy energy can be estimated as:

$$K_{\mathrm{ME}} = \frac{3}{2}\lambda_s \sigma, \tag{2.19}$$

where λ_s is the saturation magnetostriction coefficient, and σ is the IP stress. A positive (negative) λ_s indicates that tensile stress favors magnetization parallel (perpendicular) to the stress axis.

For garnet films grown epitaxially on (111)-oriented substrates, such as those used in this work, the expression becomes:

$$K_{\mathrm{ME}} = \frac{3}{2}\lambda_{111} \sigma_{\parallel}, \tag{2.20}$$

where λ_{111} is the magnetostriction constant along the (111) direction, and $\sigma_{\parallel}$ is the IP biaxial stress induced by the substrate. This stress typically originates from the lattice mismatch between the film and the substrate and can be estimated using Hooke's law:

$$\sigma_{\parallel} = \frac{Y}{1-\nu}\epsilon_{\parallel}, \tag{2.21}$$

where Y is Young's modulus, ν is Poisson's ratio, and $\epsilon_{\parallel}$ is the IP strain.

The strain $\epsilon_{\parallel}$ is defined as:

$$\epsilon_{\parallel} = \frac{a_{\mathrm{film}} - a_{\mathrm{bulk}}}{a_{\mathrm{bulk}}}, \tag{2.22}$$

where a_{film} and a_{bulk} are the IP lattice parameters of the strained film and its bulk counterpart. In the approximation of coherent epitaxial growth, where the film fully accommodates the substrate lattice, this expression is often replaced by [85]:

$$\epsilon_{\parallel} = \frac{a_{\mathrm{sub}} - a_{\mathrm{film}}}{a_{\mathrm{film}}}, \tag{2.23}$$

with a_{sub} the substrate lattice parameter.

Magnetoelastic anisotropy is especially relevant in magnetostrictive materials, such as REIGs, which exhibit large λ_{111} values. In these systems, epitaxial strain can generate strong perpendicular anisotropy, even in the absence of significant shape or magnetocrystalline contributions. Therefore, this anisotropy mechanism plays a central role in the behavior and design of the REIG-based heterostructures explored in this thesis.

Perpendicular Magnetic Anisotropy

PMA refers to the preferential alignment of the magnetization along the film normal rather than within the plane of the film. This effect is especially important in ultrathin ferromagnetic layers and multilayer heterostructures, where it can overcome the usually dominant IP shape anisotropy.

The effective magnetic anisotropy, K_{eff}, is typically expressed as the sum of a volume (bulk) term K_v and a surface (interfacial) term K_s:

$$K_{\mathrm{eff}} = K_v + \frac{2K_s}{t}, \tag{2.24}$$

where t is the ferromagnetic layer thickness. In most metallic ferromagnets, the bulk contribution K_v is negative, favoring IP magnetization, whereas the interfacial term K_s can be positive and promote OOP alignment. As the magnetic layer becomes thinner, the interfacial contribution grows in relative importance, potentially leading to PMA.

The concept of interfacial magnetic anisotropy was first introduced by Néel in 1954 [86] and experimentally verified by Gradmann and Müller in 1968 in NiFe films grown on Cu(111) [5]. Two decades later, Carcia *et al.* reported robust PMA in Pd/Co bilayers [7], followed by similar observations in Pt/Co multilayers [8] (Fig. 2.3). These discoveries not only advanced the fundamental understanding of PMA but also paved the way for its application in perpendicular magnetic recording, which reached large-scale commercialization in the mid-2000s through companies such as Toshiba and Seagate. The principles established during this period now guide the design of PMA in a broad range of materials, from metallic multilayers to insulating ferrimagnets such as REIGs, where perpendicular anisotropy plays a crucial role in DW dynamics, SOT switching, and efficient spin transport.

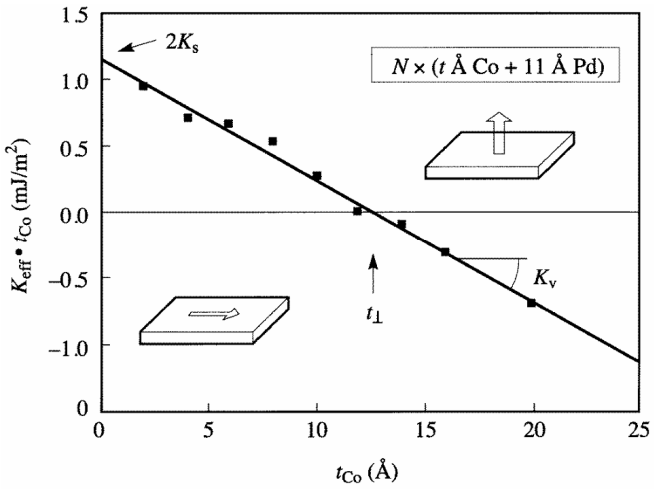

Figure 2.3: Perpendicular magnetic anisotropy revealed in Co/Pd multilayers when Co thickness was below ≈ 1.3 nm. Taken from [87]).

Microscopically, PMA often originates from interfacial effects that enhance SOC and break inversion symmetry. In metallic systems, two key mechanisms are typically involved:

- **Interface-induced anisotropy:** At the boundary between a FM and a HM or oxide (e.g., Co/Pt, CoFeB/MgO), strong SOC and orbital hybridization modify the electronic band structure, favoring perpendicular alignment of spins.
- **Crystal field effects:** In materials with uniaxial symmetry (e.g., hcp Co or strained epitaxial films), the crystalline environment itself stabilizes the perpendicular orientation of magnetic moments.

The first mechanism is particularly relevant to the final chapter of this thesis, which investigates Co/Pt/Co trilayers where the bottom, thicker Co layer exhibits IP anisotropy, while the top, ultrathin Co layer displays strong PMA. In this case, the PMA primarily arises from the asymmetric electronic environment at the Co/Pt interface, where hybridization between Co $3d$ and Pt $5d$

orbitals, combined with the large SOC of Pt, drives the OOP easy axis.

2.2 Magnetoelectric Transport in Solids

Magnetotransport refers to the study of how electric charge carriers move through a material under the combined influence of electric and magnetic fields. It provides powerful tools for probing the electronic and magnetic properties of solids, particularly in low-dimensional systems, semiconductors, and quantum materials. When a magnetic field is applied, the Lorentz force alters the trajectory of charge carriers, giving rise to measurable changes in electrical transport such as modified resistance or the appearance of transverse voltages.

A wide variety of magnetotransport phenomena exist, each revealing complementary aspects of a material's behavior. In classical systems, magnetoresistance describes the change in longitudinal resistance under an external field, while the Hall effect provides access to carrier density, carrier type, and mobility. In low-temperature or high-field regimes, quantum magnetotransport effects such as Shubnikov–de Haas oscillations and the quantum Hall effect emerge, reflecting quantized energy levels and the topological character of electronic states. These effects have proven essential for both fundamental condensed matter physics and the development of advanced electronic devices.

In the context of this thesis, we are primarily interested in magnetoelectric effects that occur when an electric current is injected into a normal metal subjected to an external magnetic field $\mathbf{B}_{\text{ext}}$, or a ferromagnetic material with a magnetization vector $\mathbf{M} = (m_x, m_y, m_z)$ of fixed orientation.

These effects form the experimental basis for detecting and quantifying changes in the magnetization direction of ferromagnets, especially those driven by SOTs. By monitoring the dependence of longitudinal and transverse voltages on $\mathbf{B}_{\text{ext}}$ and $\mathbf{M}$, one can extract detailed information on the underlying anisotropic transport mechanisms.

Throughout this work, the angular orientations of both the magnetization and the external field are expressed in spherical coordinates: $\mathbf{M} \equiv (\theta, \varphi)$ and $\mathbf{B}_{\text{ext}} \equiv (\theta_B, \varphi_B)$. The adopted coordinate system is illustrated in Fig. 2.4a. Fig. 2.4b shows a typical experimental geometry, in which both longitudinal (V) and transverse (V_H) voltages are measured simultaneously. Such measurements enable a comprehensive characterization of anisotropic magnetotransport and provide direct sensitivity to the orientation of $\mathbf{M}$ and its reorientation under external stimuli.

The electrical transport properties of a material can be described using the resistivity tensor $\boldsymbol{\rho}$, which relates the electric field components E_n to the charge current density components j_m, with $n, m = x, y, z$, via:

$$\begin{pmatrix} E_x \\ E_y \\ E_z \end{pmatrix} = \begin{pmatrix} \rho_{xx} & \rho_{xy} & \rho_{xz} \\ \rho_{yx} & \rho_{yy} & \rho_{yz} \\ \rho_{zx} & \rho_{zy} & \rho_{zz} \end{pmatrix} \begin{pmatrix} j_x \\ j_y \\ j_z \end{pmatrix}. \tag{2.25}$$

The diagonal components ρ_{xx}, ρ_{yy}, and ρ_{zz} describe the longitudinal resistivity along each principal axis. In three-dimensional cubic systems, these components are typically equal in the absence of magnetic fields. However, when an external magnetic field or magnetization is present, they become direction-dependent, giving rise to magnetoresistance effects.

The off-diagonal elements of the resistivity tensor represent the transverse resistivity. These components are generally antisymmetric, such that $\rho_{nm} = -\rho_{mn} = \rho_H$ for $n \neq m$. The associated phenomena, collectively referred to as Hall effects, describe the generation of a transverse electric field in response to a longitudinal current.

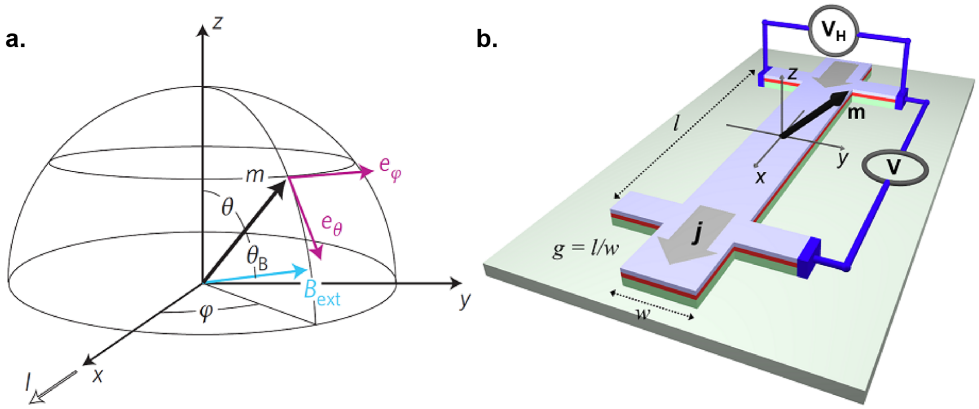

Figure 2.4: (a) Coordinate system and angular definitions used in this work, (b) typical experimental setup for simultaneous measurement of transverse (V_H) and longitudinal (V) voltages. Courtesy of C. O. Avci [unpublished].

In this work, magnetoresistance and Hall effects are quantified by measuring the corresponding voltages and dividing by the injected current. Specifically, we define the longitudinal resistance R as the voltage drop V along the current direction divided by the current I, and the transverse resistance R_H as the Hall voltage V_H (measured perpendicular to the current) divided by I:

$$R = \frac{V}{I}, \qquad R_H = \frac{V_H}{I}. \tag{2.26}$$

2.2.1 Longitudinal Magnetoresistance

Magnetoresistance refers to the change in the longitudinal electrical resistance of a sample when either the magnetization orientation or the applied magnetic field is varied. In metallic conductors, the most common contribution is the ordinary Lorentz magnetoresistance (OMR), while in magnetic conductors the anisotropic magnetoresistance (AMR) is typically stronger.

In HM/FM bilayers, an additional contribution arises from the spin Hall magnetoresistance (SMR). This effect originates from the interplay between the SHE in the HM and the reflection or absorption of spin currents at the interface with the magnetic layer. The SMR is particularly important in REIG-based heterostructures, where the magnetic layer is insulating and AMR is absent.

In this thesis, longitudinal transport measurements are employed not only to quantify magnetoresistance but also as a complementary probe to transverse (Hall) measurements. Together, these measurements enable the reconstruction of the full magnetization orientation during external field sweeps and current-induced switching experiments.

Ordinary Lorentz Magnetoresistance

The OMR, also known as Lorentz magnetoresistance, refers to the increase in longitudinal resistance that occurs when a magnetic field is applied to a conductor. This effect arises due to the Lorentz force acting on moving charge carriers, which causes them to follow cycloidal trajectories rather than straight paths. As a result, the effective path length increases, leading to enhanced resistive

scattering. The magnitude of this resistance increase scales with the square of the applied magnetic field:

$$\Delta R \propto B_{\text{ext}}^2. \tag{2.27}$$

OMR is a universal property of metals and semiconductors and is independent of the spin of the carriers. It is purely orbital in nature and does not require magnetic ordering.

The strength of the effect depends on the relative orientation of the magnetic field $\mathbf{B}_{\text{ext}}$ and the current density $\mathbf{j}$. It is maximized when the field is perpendicular to the current direction ($\mathbf{B}_{\text{ext}} \perp \mathbf{j}$) and minimized when the field is parallel ($\mathbf{B}_{\text{ext}} \parallel \mathbf{j}$) [88].

Although OMR is generally small in metals at room temperature due to short mean free paths, it can become significant in high-mobility systems, semiconductors, and at low temperatures.

Anisotropic Magnetoresistance

In magnetic materials, the most prominent magnetoresistance effect is the AMR. Unlike ordinary magnetoresistance, AMR depends on the orientation and magnitude of the magnetization $\mathbf{M}$, rather than the externally applied magnetic field, and it is generally much stronger than OMR in ferromagnets [89].

AMR arises from the interplay between SOC and the $3d$-states of transition metals. SOC couples the orbital angular momentum of the d-orbitals to their spin, which is in turn aligned with the magnetization in a ferromagnet. This coupling modifies the energy of the d-orbitals depending on their orientation relative to $\mathbf{M}$ [90]. Specifically, orbitals with lobes perpendicular to $\mathbf{M}$ experience a lowering of energy, while those parallel to $\mathbf{M}$ are shifted upward. This anisotropic modification of orbital energies affects the scattering of conduction s-electrons. These electrons can scatter into the partially filled d-states, which are less conductive. The probability of such scattering depends on the relative orientation of the current $\mathbf{j}$ and the magnetization $\mathbf{M}$. When $\mathbf{j} \parallel \mathbf{M}$, the scattering rate is higher, resulting in increased resistivity. In contrast, when $\mathbf{j} \perp \mathbf{M}$, the scattering is reduced, and resistivity is lower. This mechanism is illustrated in Fig. 2.5.

In polycrystalline materials, the AMR can be phenomenologically described by:

$$\rho_{xx} = \rho_0 + \rho_{\text{AMR}} m_x^2, \tag{2.28}$$

where ρ_0 is the resistivity when $\mathbf{M} \perp \mathbf{j}$, and ρ_{AMR} denotes the AMR amplitude. The m_x term corresponds to the component of the magnetization unit vector along the current direction.

Spin Hall Magnetoresistance

SMR is a magnetotransport effect observed in bilayer systems composed of an HM, such as Pt or Ta, in contact with a FM. In contrast to conventional magnetoresistance, SMR arises from the interplay between the SHE and the inverse spin Hall effect (ISHE) (that will be explained in Chapter 3) in the HM layer, mediated by spin current reflection and absorption at the HM/FM interface [92, 93].

When a longitudinal charge current $\mathbf{j}_c$ flows through the HM along the x-axis, the SHE generates a transverse spin current $\mathbf{j}_s$, with spin polarization $\boldsymbol{\xi} \propto \mathbf{z} \times \mathbf{j}_c$, directed toward the HM/FM interface. Depending on the relative orientation between the magnetization $\mathbf{m}$ of the FM and the spin polarization $\boldsymbol{\xi}$, this spin current can either be absorbed or reflected at the interface. If $\boldsymbol{\xi} \perp \mathbf{m}$, spin transfer torque leads to spin absorption into the FM, while for $\boldsymbol{\xi} \parallel \mathbf{m}$, the spin current is largely reflected

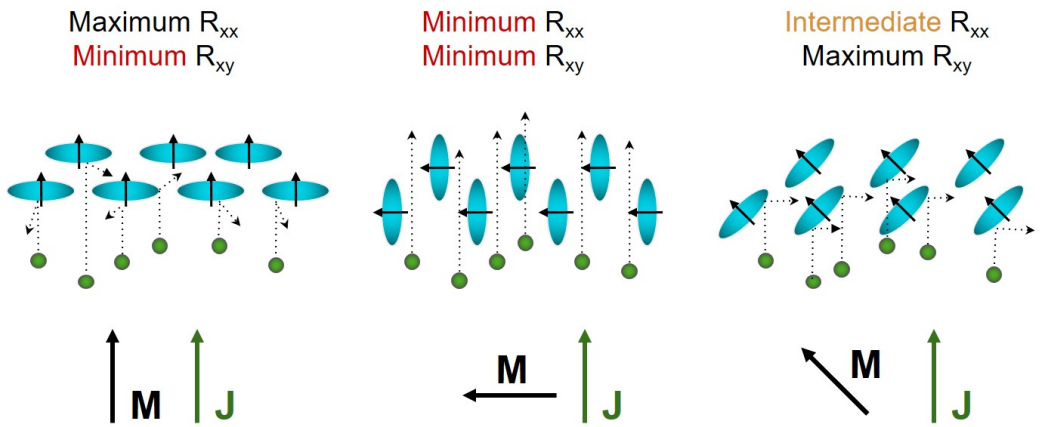

Figure 2.5: Intuitive explanation of the origin of the AMR (and the planar Hall effect, described in the next section). The orientation of the *d*-atomic orbitals (gray area) depends on the magnetization direction **M**. A higher scattering cross-section occurs for $\mathbf{M} \parallel \mathbf{j}$ (high resistance), while $\mathbf{M} \perp \mathbf{j}$ leads to lower resistance. When **M** and **j** are at 45°, a transverse charge accumulation arises due to preferential scattering, giving rise to the planar Hall effect. Adapted from [91].

back into the HM. This reflected spin current is converted back into a charge current via the ISHE, modifying the local charge distribution and thereby the longitudinal and transverse resistances of the HM.

This sensitivity of spin transmission to the magnetization direction leads to a measurable angular dependence of the resistance. As a result, SMR provides an all-electrical probe of magnetization orientation, even in insulating ferromagnets. This enables device architectures that do not require direct charge transport through the magnetic layer. In insulating FM/HM systems, SMR is typically the dominant magnetoresistive effect, since conventional magnetoresistance and Hall effects are absent.

Experimentally, SMR is quantified via angular-dependent longitudinal resistance measurements. The longitudinal resistance can be expressed as [94]:

$$R = R_0 + \Delta R^{\mathrm{SMR}} \sin^2\theta \sin^2\varphi, \tag{2.29}$$

where R_0 is the magnetization-independent longitudinal resistance, ΔR^{SMR} represents the longitudinal SMR amplitude, θ is the polar angle of **m** with respect to the z-axis, and φ the azimuthal angle in the sample plane.

The microscopic origin of SMR lies in the efficiency of spin transmission and reflection at the HM/FM interface, which is governed by the complex spin mixing conductance $G^{\uparrow\downarrow} = \mathrm{Re}[G^{\uparrow\downarrow}] + i\,\mathrm{Im}[G^{\uparrow\downarrow}]$. Its real part is related to coherent spin exchange across the interface, while the imaginary part reflects spin rotation effects, which give rise to transverse signals similar to Hall effects, as will be described in Section 2.2.2.

In this thesis, SMR plays a central role in characterizing REIG-based heterostructures. It provides a fully electrical probe of the magnetization direction without requiring a charge current to pass through the magnetic layer, thereby enabling the extraction of spin-transport parameters. The quality of the REIG/HM interface is fundamental for SMR and other spin-related phenomena [95].

2.2.2 Transverse Hall Effects

The family of Hall effects originates from the discovery of the classical Hall effect by Edwin Hall in 1879 [96]. As introduced earlier, Hall effects appear in the off-diagonal components of the resistivity tensor and manifest as a transverse voltage developing under a longitudinal current.

Although they share the same general measurement geometry, the underlying physical mechanisms of the different Hall effects can differ substantially. To distinguish among them, the original discovery is now referred to as the ordinary Hall effect (HE)[1].

The HE arises in nonmagnetic conductors and semiconductors and scales linearly with the magnitude and orientation of the applied external magnetic field. In ferromagnetic materials, additional contributions appear: the anomalous Hall effect (AHE) and the planar Hall effect (PHE), both of which depend solely on the magnetization vector $\mathbf{M}$ and not directly on the external field. These spin-dependent Hall effects originate from SOC and provide powerful probes of magnetic behavior in spintronic systems.

In HM/FM bilayers, the SMR can generate transverse voltages with the same symmetry as the AHE and PHE. In metallic heterostructures, the AHE typically dominates due to the metallic ferromagnet's strong spin-dependent scattering. In contrast, for REIG-based heterostructures, the relative magnitude of the SMR-induced AHE and the HE can be comparable, since the interfacial SMR-AHE signal is intrinsically weaker. The SMR-induced PHE, however, often exceeds the SMR-AHE by an order of magnitude in insulating systems, making it an especially sensitive probe of IP magnetization components.

Ordinary Hall Effect

The HE arises from the action of the Lorentz force $\mathbf{F}_L$ on moving charge carriers in the presence of an external magnetic field $\mathbf{B}$. The force is given by:

$$\mathbf{F}_L = q(\mathbf{E} + \mathbf{v} \times \mathbf{B}), \tag{2.30}$$

where q is the charge of the carrier, $\mathbf{v}$ is its velocity, and $\mathbf{E}$ is the electric field. The cross product $\mathbf{v} \times \mathbf{B}$ shows that the effect is maximized when the velocity and the magnetic field are perpendicular.

In the coordinate system defined in Fig. 2.4a, the HE is most prominent when $\mathbf{B} \parallel \mathbf{z}$ and current is injected along the x-axis, as shown in Fig. 2.4b. In this geometry, electrons experience a transverse deflection toward the sample edges, resulting in an accumulation of charge and the generation of a transverse electric field E_y. In steady state, this transverse field balances the Lorentz force:

$$E_y = \frac{j_x B_z}{ne}, \tag{2.31}$$

where j_x is the current density, B_z is the magnetic field component along z, n is the carrier density, and e is the elementary charge. The corresponding transverse resistivity is:

$$\rho_{xy} = \rho_{\mathrm{HE}} B_z, \tag{2.32}$$

with $\rho_{\mathrm{HE}} = \frac{1}{ne}$ defining the HE coefficient.

In ferromagnetic heterostructures and at low fields, the HE is typically negligible compared to other spin-dependent Hall effects.

[1] To avoid confusion, in this thesis the ordinary Hall effect (usually abbreviated OHE) will be called HE, to distinguish it from the orbital Hall effect introduced later.

Anomalous Hall Effect

In addition to the HE, ferromagnetic materials exhibit a much stronger transverse resistance known as the AHE. Unlike the HE, the AHE depends on the OOP component of the magnetization and arises from spin-dependent scattering processes influenced by SOC.

Although the AHE has been extensively studied, its precise microscopic origin remains the subject of ongoing research. As reviewed by Nagaosa et al. [97], three primary mechanisms are generally accepted: two extrinsic and one intrinsic. The intrinsic mechanism was first proposed by Karplus and Luttinger [98], who showed that SOC modifies the band structure of a FM in such a way that an electrical current induces an anomalous transverse velocity perpendicular to both the current direction and magnetization (Fig. 2.6c). This anomalous velocity gives rise to a transverse charge accumulation, independent of scattering. Because it arises purely from the Berry curvature of the occupied electronic bands, it is referred to as intrinsic.

The two extrinsic mechanisms are:

(i) Skew scattering, first identified by Smit in 1955 [99], results from asymmetric scattering of electrons by impurities due to SOC. Within a semiclassical Boltzmann transport framework, skew scattering breaks time-reversal symmetry, giving different probabilities for left- and right-handed scattering events. The transition probability from state n to n' is described by Fermi's golden rule:

$$W_{n\to n'} = \frac{1}{h} \left|\langle n|V|n'\rangle\right|^2 \delta(E_n - E_{n'}), \tag{2.33}$$

where V is the perturbation potential. In the presence of SOC, the time-reversal symmetry $W_{n\to n'} = W_{n'\to n}$ no longer holds. This asymmetry can be modeled as:

$$W_{\mathbf{k}\to\mathbf{k}'} = -\frac{1}{\tau_{\mathrm{SS}}}(\mathbf{k}\times\mathbf{k}')\cdot\mathbf{M}, \tag{2.34}$$

where $\mathbf{k}$ and $\mathbf{k}'$ are the incident and scattered wave vectors, $\mathbf{M}$ is the magnetization, and τ_{SS} is the average time between skew scattering events.

Intuitively, skew scattering can be understood as a Lorentz-like deflection caused by the Oersted field of the impurity acting on the electron's spin. For a spin-up electron passing to the right or left of a positively charged impurity, the interaction with the Oersted field bends the trajectory in a preferred direction, generating a net transverse voltage. This mechanism is also referred to as Mott-skew scattering and is proportional to the scattering lifetime.

(ii) Side jump, described by Smit in 1958 [100], is a quantum mechanical effect that occurs when an electron undergoes scattering without changing its wavevector. During the scattering process, the electron's wavepacket shifts laterally, producing a transverse displacement independent of the scattering rate. This mechanism is not captured by semiclassical theory and must be treated within a quantum transport framework.

The resistivity contribution due to the AHE is typically modeled as:

$$\rho_{xy} = \rho_{\mathrm{AHE}} m_z, \tag{2.35}$$

where ρ_{AHE} is the anomalous Hall coefficient and m_z is the OOP component of the magnetization unit vector.

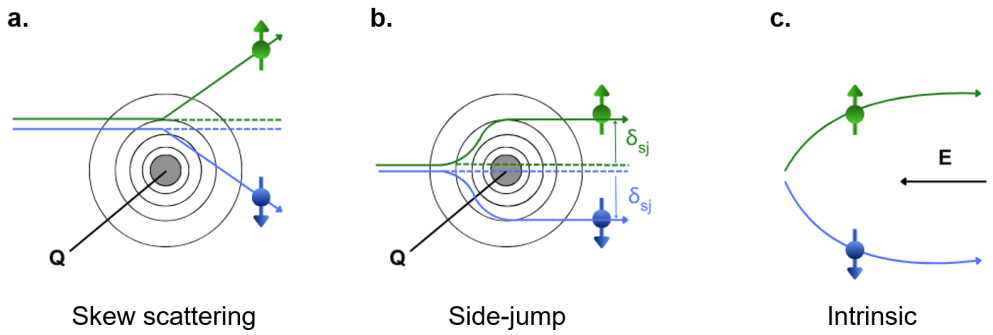

Figure 2.6: Mechanisms underlying the AHE and spin Hall effect (SHE, discussed in Section 3.1): (a) skew scattering, (b) side jump, and (c) intrinsic Berry curvature mechanism. Adapted from [97].

Planar Hall Effect

The PHE [101], although named similarly, is not a true Hall effect in the classical sense. Instead, it is the transverse manifestation of the AMR, and arises due to the same spin-orbit-induced anisotropic scattering mechanisms, as illustrated earlier in Fig. 2.5.

The PHE emerges when the IP magnetization is neither parallel nor perpendicular to the current direction, creating an effective asymmetry in scattering paths. This results in a transverse voltage even though the magnetic field is applied in the film plane.

The resistivity associated with the planar Hall effect is given by:

$$\rho_{xy} = \rho_{\mathrm{PHE}} m_x m_y, \tag{2.36}$$

where ρ_{PHE} is the planar Hall coefficient and m_x, m_y are the IP components of the normalized magnetization vector.

While the PHE is typically weaker than the AHE, it provides a valuable tool for determining the IP orientation of magnetization and complements AMR-based measurements in spintronic devices.

SMR-induced Hall Effects

In addition to the longitudinal magnetoresistance described earlier, SMR can also generate transverse voltage signals. These can be decomposed into two components:

- $R_{\mathrm{H}}^{\mathrm{SMR}}$: a planar-Hall-like transverse contribution.
- $R_{\mathrm{H}}^{\mathrm{SMR\text{-}AHE}}$: an anomalous-Hall-like transverse contribution induced by SMR.

The PHE-like term is the transverse counterpart of the longitudinal SMR, in the same way that the PHE accompanies AMR. In contrast, the AHE-like term originates from a different mechanism: the imaginary part of the spin-mixing conductance $G^{\uparrow\downarrow}$, which is associated with spin rotation upon reflection at the HM/FM interface. The real part of $G^{\uparrow\downarrow}$ governs the efficiency of coherent spin transfer (and thus both longitudinal and PHE-like SMR), whereas the imaginary part is responsible for generating the AHE-like transverse signal [94].

The normalized transverse resistances can be expressed as:

$$\frac{R_{\mathrm{H}}^{\mathrm{SMR}}}{R_{\mathrm{sq}}} = \theta_{\mathrm{SH}}^2 \frac{\lambda_{\mathrm{SD}}}{d_N} \cdot \mathrm{Re}\left[\frac{2\lambda_{\mathrm{SD}} G^{\uparrow\downarrow} \tanh^2\left(\frac{d_N}{2\lambda_{\mathrm{SD}}}\right)}{\sigma_N + 2\lambda_{\mathrm{SD}} G^{\uparrow\downarrow} \coth\left(\frac{d_N}{\lambda_{\mathrm{SD}}}\right)}\right], \tag{2.37}$$

$$\frac{R_{\mathrm{H}}^{\text{SMR-AHE}}}{R_{\mathrm{sq}}} = -\theta_{\mathrm{SH}}^2 \frac{\lambda_{\mathrm{SD}}}{d_N} \cdot \mathrm{Im}\left[\frac{2\lambda_{\mathrm{SD}} G^{\uparrow\downarrow} \tanh^2\left(\frac{d_N}{2\lambda_{\mathrm{SD}}}\right)}{\sigma_N + 2\lambda_{\mathrm{SD}} G^{\uparrow\downarrow} \coth\left(\frac{d_N}{\lambda_{\mathrm{SD}}}\right)}\right], \tag{2.38}$$

where λ_{SD} is spin-diffusion length of the HM, d_N the HM thickness, σ_N the HM conductivity, R_{sq} the sheet resistance of the HM, and θ_{SH} the spin Hall angle of the HM.

A large $\mathrm{Re}[G^{\uparrow\downarrow}]$ indicates efficient spin transmission, resulting in a strong longitudinal SMR and a relatively small $R_{\mathrm{H}}^{\text{SMR-AHE}}$. Conversely, a larger imaginary part enhances the SMR-induced AHE-like term.

In insulating-FM/HM systems, additional phenomena can produce transverse signals indistinguishable from a conventional AHE. A well-known example is the magnetic proximity effect (MPE) in Pt [102, 103], where interfacial exchange induces a finite magnetic moment in the HM layer. This magnetized region can generate an AHE-like signal even when the FM is insulating. Moreover, other interface-related mechanisms, such as spin-dependent scattering or Rashba-type SOC, can also produce transverse responses with identical symmetry, making the microscopic origin of the AHE signal in these systems complex and not straightforward to pinpoint. The interplay of these contributions will be discussed in more detail in the following chapters.

Measurement Geometry of Hall Effects

Considering the combined contributions of the ordinary, anomalous, and planar Hall effects (or their SMR counterparts), the total transverse Hall resistivity can be expressed in terms of the magnetization components and the external magnetic field as:

$$\rho_H = \rho_{\mathrm{AHE}} m_z + \rho_{\mathrm{PHE}} m_x m_y + \rho_{\mathrm{HE}} B_z, \tag{2.39}$$

where ρ_{AHE}, ρ_{PHE}, and ρ_{HE} are the anomalous, planar, and ordinary Hall resistivity coefficients, respectively.

To connect this expression to experimentally measurable quantities, the Hall voltage V_H is expressed as a function of the injected current I, leading to the total Hall resistance $R_H = V_H/I$. Introducing the angular dependence of the magnetization vector $\mathbf{M}$ and the external magnetic field $\mathbf{B}_{\mathrm{ext}}$, we obtain:

$$R_H = R_{\mathrm{AHE}} \cos\theta + R_{\mathrm{PHE}} \sin^2\theta \sin(2\varphi) + c_{\mathrm{HE}} B_{\mathrm{ext}} \cos\theta_B, \tag{2.40}$$

where R_{AHE} and R_{PHE} are the anomalous and planar Hall resistance amplitudes, c_{HE} is the ordinary Hall coefficient (in Ω/mT), θ and φ are the polar and azimuthal angles of $\mathbf{M}$, and θ_B is the polar angle of $\mathbf{B}_{\mathrm{ext}}$. These angles are defined in Fig. 2.4(a).

Measurement of R_{AHE}: An OOP field scan is performed with $\theta = 0°$, so that $\cos\theta = 1$ and $\sin\theta = 0$. This configuration maximizes the contribution from R_{AHE} while canceling R_{PHE}. The anomalous Hall signal is identified by a sign reversal when the magnetization switches from $+z$ to $-z$. In this geometry, the HE also contributes a signal proportional to the applied magnetic

field. For metallic systems, the HE is typically much smaller than the AHE and often negligible. In REIGs, however, the SMR-AHE signal is significantly smaller, and both effects can have comparable magnitude.

Measurement of R_{PHE}: To determine R_{PHE}, the magnetization is oriented IP ($\theta = 90°$) to suppress both the AHE and HE. An angle scan in the xy-plane is then performed by varying φ. The maximum R_{PHE} occurs at $\varphi = 45°$. In metallic systems, the PHE amplitude is usually smaller than the AHE, whereas in insulating systems it can be larger by up to an order of magnitude.

Chapter 3

Current-induced Torques in Magnetic Heterostructures

Contents

3.1 Origin of Spin Accumulation

To understand the spin-dependent phenomena explored in this thesis, including SOTs and SMR, it is first necessary to examine how spin accumulation arises at the interface between a HM and a FM or FI, and how this accumulation subsequently interacts with the magnetization.

In the heterostructures studied in this thesis, where current-induced effects are investigated, we focus on HM/FI bilayers. For simplicity, we consider only the *effective* magnetization of the FI (the net moment M resulting from the sum of the sublattice magnetizations). On the timescales relevant to SOT switching and DW depinning and motion, the different magnetic sublattices (three in the case of REIGs) respond collectively and can be treated as a single macrospin.

In the reference frame sketched in Fig. 2.4a, the interface lies in the xy-plane (normal to $\hat{z}$), and the charge current $\mathbf{j}$ flows along the $\hat{x}$-direction. Under these conditions, a non-equilibrium spin accumulation $\boldsymbol{\xi}$ develops along the $\hat{y}$-axis, perpendicular to both the interface normal and the current ($\boldsymbol{\xi} \propto \mathbf{z} \times \mathbf{j}$). This interfacial spin accumulation is the primary driver of SOTs. In this thesis, we focus

on two main mechanisms that can generate such spin accumulation: the REE and the SHE. Both rely on SOC in the presence of broken inversion symmetry and lead to a net spin polarization near the HM/FI interface when current flows[1]. More recently, a third mechanism has been recognized: the OHE. In this case, current flow generates a transverse flow of orbital angular momentum, which is subsequently converted into spin accumulation by SOC. The OHE thus provides an additional pathway for producing interfacial spin polarization.

In the following sections, we discuss the microscopic origins of the REE, the SHE, and the OHE. We then describe how the resulting nonequilibrium spin accumulation couples to the magnetization of the FM or FI layer, giving rise to SOTs capable of electrically manipulating the magnetization.

3.1.1 The Rashba-Edelstein Effect

The REE arises at surfaces or interfaces where structural inversion symmetry is broken. In a system with both inversion symmetry $E(\uparrow, \mathbf{k}) = E(\uparrow, -\mathbf{k})$ and time-reversal symmetry $E(\uparrow, \mathbf{k}) = E(\downarrow, -\mathbf{k})$, where $\uparrow\downarrow$ represent the spin of the electron moving in the solid and $\mathbf{k}$ is its wavevector, electrons exhibit spin degeneracy: $E(\uparrow, \mathbf{k}) = E(\downarrow, \mathbf{k})$. In this case, the energy dispersion of the free electrons is spin-degenerate and is given by:

$$E(k) = \frac{\hbar^2 k^2}{2m^*}, \tag{3.1}$$

where m^* is the effective mass of the electron. However, at a surface or interface, inversion symmetry is broken, lifting the spin degeneracy and modifying the dispersion relation. At such an interface, electrons experience an electric field $\mathbf{E} = E_0\mathbf{z}$ oriented perpendicular to the 2D surface. The magnitude of this interfacial field scales with atomic number Z and is particularly strong for heavy atoms.

Due to Lorentz transformations, a moving electron in this field perceives an effective magnetic field:

$$\mathbf{B}_\mathrm{R} = \frac{\mathbf{E} \times \mathbf{v}}{2c^2\sqrt{1 - \frac{v^2}{c^2}}}, \tag{3.2}$$

which couples with its spin. This leads to an additional term in the Hamiltonian [104]:

$$H_\mathrm{SO} = \frac{\Gamma\gamma\mu_B}{2c^2}(\mathbf{v} \times \mathbf{E}) \cdot \hat{\boldsymbol{\sigma}}, \tag{3.3}$$

where γ is the gyromagnetic ratio, $\hat{\boldsymbol{\sigma}}$ the Pauli vector, and $\Gamma = \sqrt{1 - v^2/c^2}$ is the Lorentz factor. This term can be rewritten in the familiar Rashba form:

$$\hat{H}_R = \alpha_R \mathbf{z} \cdot (\hat{\boldsymbol{\sigma}} \times \mathbf{k}), \tag{3.4}$$

where $\alpha_R = \frac{\gamma\hbar g\mu_B E_0}{2mc^2}$ is the Rashba constant. The material dependence of the effect is encoded in α_R, which includes the interfacial electric field E_0. This phenomenon, first described by Bychkov and Rashba in 1984 [105], is known as the Rashba effect. In 1990, Edelstein extended this concept to non-equilibrium conditions, demonstrating that an electric current can induce spin polarization in systems with Rashba SOC. This mechanism is now known as the Rashba–Edelstein effect [106].

A direct consequence of this Hamiltonian is spin–momentum locking: the electron spin $\hat{\boldsymbol{\sigma}}$, momentum $\mathbf{k}$, and surface normal $\mathbf{z}$ are mutually orthogonal. This causes the spin of the conduction

[1] Other mechanisms or interface symmetries can, in principle, produce spin accumulations with different polarization directions, but in the standard geometry considered here, the spin accumulation is oriented along $\mathbf{z} \times \mathbf{j}$.

electrons to lie IP, perpendicular to both **k** and **z**. When the Rashba constant is sufficiently large, the energy dispersion is significantly modified. The two spin bands split, and their dispersion is given by:

$$E_{\pm}(\mathbf{k}) = \frac{\hbar^2 k^2}{2m^*} \mp \alpha_R |\mathbf{k}|, \tag{3.5}$$

where + and − denote the two spin-split branches. This spin-dependent dispersion also modifies the Fermi surface, as illustrated in Fig. 3.1a, where two concentric contours represent the spin-split bands. When an IP current density $\mathbf{j_c}$ is applied (along $\hat{x}$), it generates an electric field $\mathbf{E} = \rho \mathbf{j_c}$ that causes both Fermi contours to shift rigidly in **k**-space by Δk. This shift leads to an imbalance in the spin population along $\hat{y}$, generating a net spin accumulation at the NM/FM interface (Fig. 3.1b).

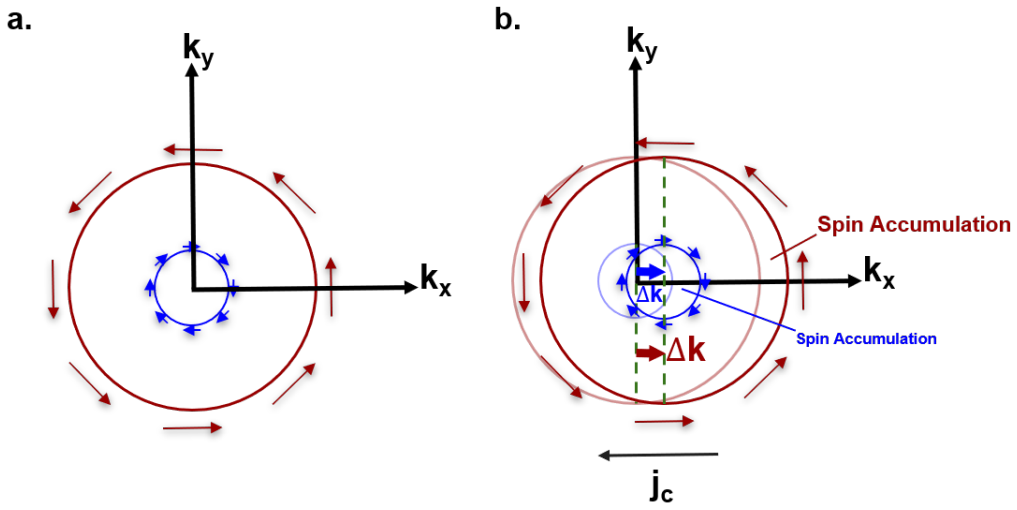

Figure 3.1: (a) Fermi contours of a Rashba system showing spin–momentum locking: spin orientation (red and blue arrows) is locked perpendicular to momentum. (b) When a current $\mathbf{j_c}$ is applied, both contours shift by Δk, leading to a net spin accumulation at the interface. Figure adapted from [107].

A more detailed theoretical treatment of the Rashba-induced spin accumulation, including the contribution from both spin bands, is presented by Miron *et al.* [108].

3.1.2 The Spin Hall Effect

In materials with strong SOC, a longitudinal charge current can generate a transverse spin current, a phenomenon called the spin Hall effect [109, 110, 111, 112]. The SHE is a bulk phenomenon and one of the main sources of spin accumulation in HM/FM heterostructures. Unlike the interfacial REE, the SHE originates from spin-dependent scattering and intrinsic band structure effects throughout the bulk of the material.

The term "Hall effect" is somewhat misleading here: whereas conventional Hall effects (ordinary and anomalous) produce a transverse charge imbalance and voltage, the SHE produces a transverse *pure spin current* with no net charge flow [113]. A pure spin current is the flow of spin angular momentum without a net electrical current, arising when spin-up and spin-down electrons move in opposite directions with equal magnitude so that their charge contributions cancel but their spin contributions add [114].

The spin polarization $\boldsymbol{\xi}$ of the accumulated spins is orthogonal to both the charge current $\mathbf{j}_c$ and the spin current $\mathbf{j}_s$ [115]. The generated spin current density can be expressed as:

$$\mathbf{j}_s = \frac{\hbar}{2e}\,\theta_{\mathrm{SH}}\,(\mathbf{j}_c \times \boldsymbol{\xi}), \tag{3.6}$$

where the spin Hall angle θ_{SH} is a dimensionless measure of the charge–to–spin conversion efficiency (see Table 3.1). Its sign sets the direction of spin accumulation at the HM/FM interface, and its magnitude reflects the strength of the effect in a given material.

Fig. 3.2a schematically illustrates spin accumulation from the SHE, while Fig. 3.2b shows the REE for comparison.

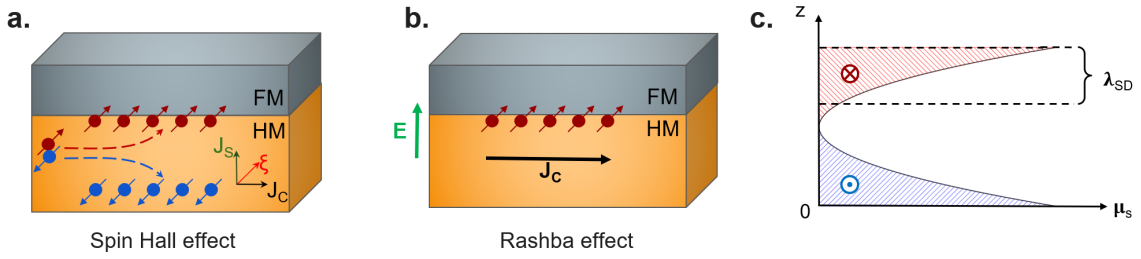

Figure 3.2: (a) In the SHE, a longitudinal charge current $\mathbf{j}_c$ in a NM with strong SOC produces a transverse spin current $\mathbf{j}_s$ and spin accumulation $\boldsymbol{\xi}$ at the NM/FM interface. (b) In the REE, an interfacial electric field $\mathbf{E}$ together with $\mathbf{j}_c$ induces a spin accumulation. (c) Spatial profiles of μ_s and λ_{SD} as a function of $\hat{z}$.

The microscopic mechanisms underlying the SHE mirror those of the AHE (see Section 2.2.2), and include *skew scattering*, *side jump*, and *intrinsic* contributions arising from the electronic band structure. In skew scattering, spin-up and spin-down electrons are deflected in opposite transverse directions by impurities; in side jump, spin-dependent displacements occur during scattering. In contrast to the AHE, here the system is nonmagnetic and contains equal populations of spin-up and spin-down electrons, so these opposite deflections yield a pure spin current without transverse charge buildup.

Although the SHE acts throughout the HM, a measurable spin accumulation appears only near the edges over a characteristic distance given by the spin diffusion length λ_{SD}, which is the average distance a non-equilibrium spin polarization travels before decaying due to spin-relaxation processes:

$$\frac{\delta^2 \mu_s}{\delta z^2} = \frac{\mu_s}{\lambda_{\mathrm{SD}}^2}, \tag{3.7}$$

with

$$\lambda_{\mathrm{SD}} = \sqrt{D_{\mathrm{diff}}\,\tau_{\mathrm{sf}}}, \tag{3.8}$$

where μ_s is the spin-dependent chemical potential, D_{diff} the diffusion constant, and τ_{sf} the spin-flip relaxation time. The spatial profile of μ_s and the characteristic decay over λ_{SD} are illustrated in Fig. 3.2c. Materials with strong SOC typically have short λ_{SD} (1–5 nm) because spin–phonon, spin–spin, and spin–orbit scattering rapidly randomize spin directions [116, 117, 118]. This makes λ_{SD} a critical parameter when studying HM layers with thickness comparable to or smaller than this scale, as explored later in this thesis.

The ISHE, the reciprocal process, converts a spin current into a transverse charge current via the same underlying mechanisms [119, 120, 121, 113], and plays an important role in effects such as SMR.

Table 3.1: Spin Hall Parameters of common metals used in spintronics

Material	ρ (Ω·m)$\times 10^{-8}$	λ_{SD} (nm)	θ_{SH}	**Ref.**
Au	2.44	30–60	0.012–0.1	[122], [123]
Cu	1.68	300–500	∼0	[124]
Pd	10.5	7–12	0.01	[125], [126]
Pt	25	1.5–5.3	0.05–0.11	[122], [126], [93]
Ta	13	2.7–5.1	-(0.006–0.02)	[127], [128]
β-W	195	1–4	-(0.24–0.49)	[129], [130]

3.1.3 The Orbital Hall Effect

For many years, the orbital angular momentum of electrons was considered irrelevant to non-equilibrium, current-induced phenomena. The prevailing view was that in solids, orbital angular momentum is strongly suppressed (or "quenched") by the combined effects of the crystal field and the hybridization of electronic states.

The crystal field, produced by the electrostatic potential of surrounding ions or atoms, breaks the spherical symmetry of an isolated atom. This reduced symmetry mixes atomic orbitals, transforming the pure spherical-harmonic states (which are eigenfunctions of orbital angular momentum in free atoms) into new combinations that, on average, carry no net orbital moment, a phenomenon known as orbital quenching.

Furthermore, in solids, atomic orbitals hybridize into extended Bloch states that are delocalized over many lattice sites. This spatial delocalization erases the localized character of the orbital moment, further reinforcing the quenching caused by the crystal field.

However, recent theoretical and experimental works have overturned this long-standing assumption. It is now clear that orbital angular momentum can persist in solids and actively contribute to transport phenomena. In particular, it can give rise to the OHE, in which an applied charge current generates a transverse flow of orbital angular momentum. Through SOC, this orbital flow can be partially converted into spin accumulation, providing an alternative pathway to spin-current generation beyond the conventional SHE and REE.

The possibility of a sizable OHE was already anticipated in 2008 by Tanaka, Kontani, and co-workers [40, 41], who predicted large orbital Hall conductivities in transition metals. At the time, these results attracted little attention. More recently, however, both theory and experiment have revived interest in the topic, showing that non-equilibrium orbital effects can be particularly strong in light transition metals such as V, Ti, Cr, and Mn, in some cases exceeding the typical spin Hall conductivity of the heavy metals traditionally used in spintronics [42, 43].

To illustrate the mechanism of the OHE without delving into the full theoretical formalism, we follow the toy model proposed in Ref. [42]. This model considers a tight-binding Hamiltonian for a cubic lattice containing only s and p orbitals, where electrons can hop between an s and a p orbital with a finite probability quantified by the inter-orbital hopping parameter γ_{sp}.

This hybridization produces an *orbital texture* in reciprocal space, meaning that the orbital character of electronic states depends on the crystal momentum $\mathbf{k}$. In this simplified picture, we can consider two bands, in which the inner (outer) band has predominantly radial (tangential) p-orbital

character (see Fig. 3.3a).

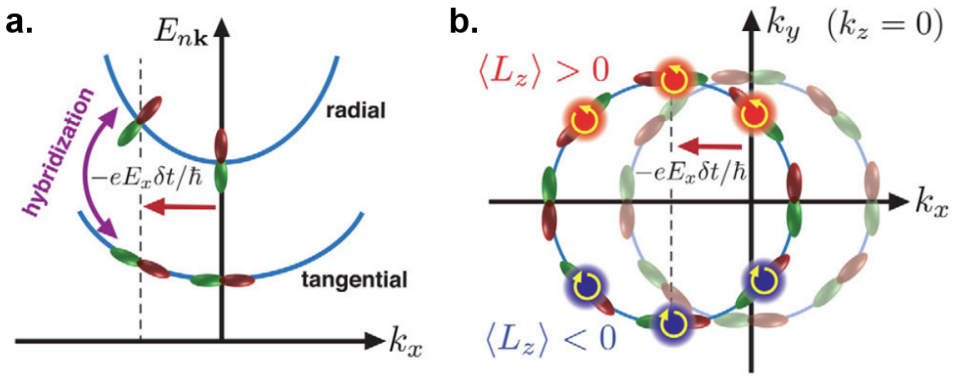

Figure 3.3: (a) Hybridization of the radial and tangential bands under an applied electric field generates perturbed states with finite orbital angular momentum. (b) Electrons occupying these states contribute to an orbital current transverse to $\mathbf{E}$, with orbital polarization $\mathbf{L} \propto \mathbf{E} \times \mathbf{k}$. Taken from Ref. [42].

Consider the outer tangential band. Because the orbital character varies with $\mathbf{k}$, the orbital angular momentum distribution is odd in momentum space: states at $+\mathbf{k}$ and $-\mathbf{k}$ carry opposite orbital moments. When an electric field $\mathbf{E}$ is applied, the Fermi surface shifts in momentum space, creating an imbalance between $+\mathbf{k}$ and $-\mathbf{k}$ states (Fig. 3.3b). The resulting non-equilibrium states acquire a radial component, leading to hybridization between the two bands and generating a finite orbital angular momentum for individual carriers.

Although the total orbital moment remains zero, electrons with opposite velocities along $\hat{y}$ (v_y) now carry opposite components of orbital angular momentum along $\hat{z}$ (L_z), producing a transverse orbital current:

$$j_L \propto v_y L_z. \tag{3.9}$$

By symmetry, the transported orbital angular momentum satisfies:

$$\mathbf{L} \propto \mathbf{E} \times \mathbf{k}, \tag{3.10}$$

ensuring that the orbital current flows perpendicular to the applied electric field, which is the hallmark of a Hall effect.

An intuitive (classical) picture is to imagine that conduction electrons, while drifting through the crystal, also circle around atomic sites. If the sense of rotation is systematically biased by the electric field, the net result is a transverse flow of orbital angular momentum, which is an orbital current.

From a microscopic viewpoint, the orbital texture in momentum space produces a finite *Berry curvature* in the orbital sector. This geometric property of the Bloch states is the intrinsic origin of the OHE and explains its transverse nature, in close analogy to the intrinsic SHE.

In this perspective, the OHE can be regarded as more fundamental than the SHE. Orbital texture mediated by inter-orbital hopping is ubiquitous in solids and does not require broken inversion symmetry or SOC. The SHE can then be viewed as a by-product of the OHE in materials where SOC converts orbital currents into spin currents. Historically, the SHE was identified earlier because spins couple directly to magnetization through exchange, making their effects easier to detect. In

contrast, orbital currents cannot interact directly with magnetization and must first be converted into spin accumulation via SOC. This conversion may occur within the OHE source material itself (if it is a heavy metal) or in an adjacent FM in metallic multilayers (see Fig. 3.4a). In the case of insulating ferrimagnets, such as the garnet-based systems studied in this work, an additional high-SOC spacer layer is conventionally required to convert orbital into spin current (see Fig. 3.4b), although this viewpoint has been challenged by recent publications [50].

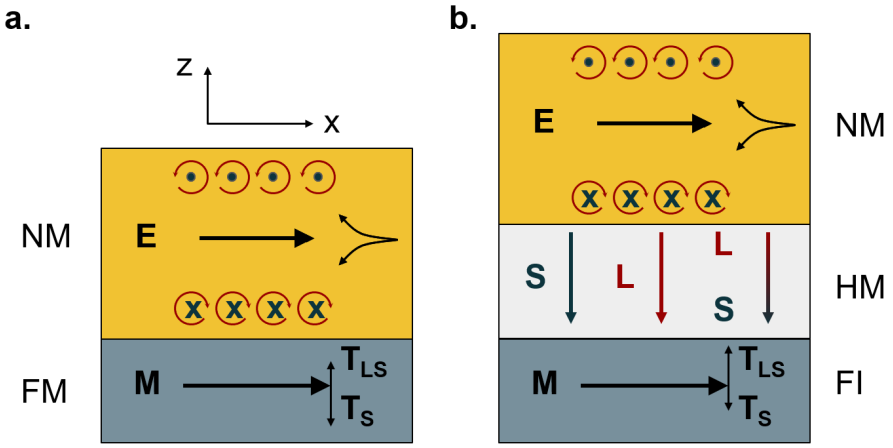

Figure 3.4: (a) An electric field **E** in a non-magnet generates an orbital current j_L^z with polarization along y, which via SOC also produces a spin current j_S^z. The resulting orbital (T_{LS}) and spin (T_{S}) torques act on the magnetization **M** of an adjacent FM. (b) A buffer layer can enhance T_{LS} by converting j_L into j_S before injection; in the case of a ferromagnetic insulator, this conversion requires a heavy-metal layer with strong SOC. Adapted from [131].

This extra conversion step makes OHE more challenging to isolate experimentally, as orbital and spin currents share the same symmetry and produce similar torques on the magnetization. Furthermore, due to the $L \to S$ conversion, even though the effective orbital Hall angle can exceed the spin Hall angle in many systems, its impact on magnetization is often weaker.

Despite these experimental challenges, several recent results strongly support the OHE picture: the observation of sizable SOTs and current-induced magnetization switching in devices containing $3d$ transition metals [132, 45, 133, 134, 135, 136, 137], the identification of an interfacial magnetoresistance of orbital origin [138], the optical detection of orbital accumulation in Ti [139], and the demonstration of orbital-current-driven control of insulating REIGs [45, 46, 47, 48, 49, 50], the latter being the subject of the following chapters.

3.2 Magnetization Dynamics Induced by Spin Accumulation

In this section, we examine how the spin accumulation introduced in the previous section, which arises at HM/FM interfaces, couples to the magnetization of the FM and gives rise to SOTs. These torques provide a direct pathway for electrical manipulation of magnetic order, forming the foundation of many spintronic technologies.

We begin by presenting the Landau–Lifshitz–Gilbert (LLG) equation, which describes the general dynamics of magnetization under effective magnetic fields. We then extend this framework to include

the contribution of nonequilibrium spin accumulation, which enters as an additional torque term that modifies both precession and damping. This extension naturally leads to the classification of distinct torque symmetries arising from interfacial SOC and the SHE.

Finally, we discuss how these torques can be harnessed to achieve deterministic magnetization switching and to drive the motion of magnetic DWs, two processes of central importance for this thesis and, more in general, for spin–orbitronic memory and logic devices.

3.2.1 LLG Equation and Spin Accumulation

The equilibrium orientation of the magnetization can be determined by minimizing the total free energy of the system using variational principles:

$$\delta E = \delta(E_{\text{ex}} + E_A + E_Z + E_D) = 0, \tag{3.11}$$

where E_{ex} denotes the exchange energy, E_A the anisotropy energy, E_Z the Zeeman energy, and E_D the demagnetizing energy.

In this work, we are primarily concerned with the magnetization dynamics when driven out of equilibrium. Its time evolution is described by the LLG equation [140]:

$$\frac{\partial \mathbf{M}}{\partial t} = -\gamma \mathbf{M} \times \mu_0 \mathbf{H}_{\text{eff}} + \alpha \mathbf{M} \times \frac{\partial \mathbf{M}}{\partial t}, \tag{3.12}$$

where α is the Gilbert damping constant, and $\mathbf{H}_{\text{eff}}$ the effective magnetic field incorporating all energy contributions. The first term describes precession of $\mathbf{M}$ around $\mathbf{H}_{\text{eff}}$, while the second term accounts for energy dissipation, aligning $\mathbf{M}$ with the field direction.

To include the effect of spin accumulation, consider a current flowing along $\mathbf{x}$ that generates a non-equilibrium spin accumulation $\boldsymbol{\xi}$ along $\mathbf{y}$ at the HM/FM interface. Since spin accumulation builds up on timescales much shorter than magnetization dynamics, it can be treated as quasi-static. Its effect is modeled as an additional effective field $\mathbf{B}_{\text{eff}} = J\boldsymbol{\xi}$, where J characterizes the exchange coupling between conduction electron spins and localized moments [141]. The modified LLG equation becomes:

$$\frac{\partial \mathbf{M}}{\partial t} = -\gamma \mathbf{M} \times (\mu_0 \mathbf{H}_{\text{eff}} + \mathbf{B}_{\text{eff}}) + \alpha \mathbf{M} \times \frac{\partial \mathbf{M}}{\partial t}. \tag{3.13}$$

Only the component of $\boldsymbol{\xi}$ perpendicular to $\mathbf{M}$ contributes to torque. This component can be decomposed as [141]:

$$J\boldsymbol{\xi}_{\perp} = a\,(\boldsymbol{\xi} \times \mathbf{M}) + b\,\boldsymbol{\xi}. \tag{3.14}$$

This decomposition is general and does not assume a specific orientation of $\boldsymbol{\xi}$. It expresses the component of spin accumulation perpendicular to $\mathbf{M}$ as a linear combination of two orthogonal directions in the plane normal to $\mathbf{M}$: one along $\boldsymbol{\xi}$ (after removing its projection on $\mathbf{M}$) and the other along $\boldsymbol{\xi} \times \mathbf{M}$. The term proportional to b corresponds to an effective field along $\boldsymbol{\xi}$, giving rise to the field-like (FL) torque $\mathbf{M} \times \boldsymbol{\xi}$. The term proportional to a lies along $\boldsymbol{\xi} \times \mathbf{M}$ and produces the damping-like (DL) torque $\mathbf{M} \times (\boldsymbol{\xi} \times \mathbf{M})$. In the typical geometry where $\mathbf{M}$ is along $\hat{z}$ and $\boldsymbol{\xi}$ along $\hat{y}$, this second component points along $\hat{x}$, which explains why the associated effective field of the DL torque rotates in the xz-plane as $\mathbf{M}$ tilts.

The DL term resembles the alternative form of the Gilbert damping torque:

$$\mathbf{T}_{\text{damp}} = \alpha' \mathbf{M} \times (\mathbf{M} \times \mathbf{H}_{\text{eff}}), \tag{3.15}$$

which is equivalent to the standard Gilbert form under small damping conditions [140]. These torques exhibit distinct symmetry under magnetization reversal, a property exploited in experimental separation techniques, as discussed in the next section [142].

3.2.2 Damping-like and Field-like Torques

Spin accumulation at the HM/FM interface generates two distinct SOT components with different physical characteristics. The action of a magnetic field $\mathbf{B}$ on a magnetic moment $\mathbf{M}$ produces a torque $\mathbf{T} = \mathbf{M} \times \mathbf{B}$, where $\mathbf{T}$ denotes the torque density, as $\mathbf{M}$ is expressed per unit volume. Consequently, the effective field corresponding to a torque can be formally written as $\mathbf{B}_{\text{eff}} = \mathbf{T} \times \mathbf{M}$ [20].

The FL torque is associated with an effective field aligned with the spin polarization direction $\boldsymbol{\xi}$ of the accumulated spins (typically along $\hat{y}$). It is expressed as:

$$\mathbf{T}_{\text{FL}} = T_{\text{FL}}(\mathbf{M} \times \boldsymbol{\xi}), \tag{3.16}$$

with the corresponding effective field:

$$\mathbf{B}_{\text{FL}} = B_{\text{FL}}\boldsymbol{\xi}. \tag{3.17}$$

For $\mathbf{M}$ along $\hat{z}$ and $\boldsymbol{\xi}$ along $\hat{y}$, $\mathbf{B}_{\text{FL}}$ points along $+\hat{y}$, while $\mathbf{T}_{\text{FL}}$ points along $\pm\hat{x}$, inducing a precession of $\mathbf{M}$ in the xz-plane.

The DL torque corresponds to an effective field perpendicular to $\boldsymbol{\xi}$, which rotates in the xz-plane as $\mathbf{M}$ tilts:

$$\mathbf{T}_{\text{DL}} = T_{\text{DL}}\, \mathbf{M} \times (\mathbf{M} \times \boldsymbol{\xi}), \tag{3.18}$$

with its associated effective field:

$$\mathbf{B}_{\text{DL}} = B_{\text{DL}}(\mathbf{M} \times \boldsymbol{\xi}). \tag{3.19}$$

For $\mathbf{M}$ along $\hat{z}$ and $\boldsymbol{\xi}$ along $\hat{y}$, $\mathbf{B}_{\text{DL}}$ points along $\pm\hat{x}$, while $\mathbf{T}_{\text{DL}}$ points along $\pm\hat{y}$, driving $\mathbf{M}$ toward or away from $\boldsymbol{\xi}$. This torque mimics Gilbert damping, promoting alignment of $\mathbf{M}$ with the spin polarization direction.

The FL torque is *odd* under magnetization reversal: $\mathbf{M} \to -\mathbf{M}$ changes the sign of $\mathbf{T}_{\text{FL}}$. This behavior is analogous to a Zeeman field. In contrast, the DL torque is *even* under magnetization reversal: $\mathbf{T}_{\text{DL}}$ remains unchanged when $\mathbf{M}$ flips. This distinction is crucial for experimental separation of the two components, for example, via harmonic Hall measurements, since odd and even symmetries produce different voltage signatures.

Since both torque magnitudes are proportional to the applied current, it is useful to define the spin–torque efficiencies:

$$\xi^{j}_{\text{DL, FL}} = \frac{2e}{\hbar} M_s t_F \frac{B_{\text{DL, FL}}}{j}, \tag{3.20}$$

where t_F is the ferromagnetic layer thickness. These parameters allow for a quantitative comparison of SOT strengths across different material systems. In an ideal scenario, characterized by a spin-transparent interface and negligible spin-memory loss, the DL torque efficiency ξ^{j}_{DL} approaches the bulk spin Hall angle of the HM.

However, there is ambiguity in defining the current density j, as some studies use the total average current, while others apply a parallel resistor model to separate contributions from each layer. Moreover, current inhomogeneity due to thickness variations or interfacial scattering can

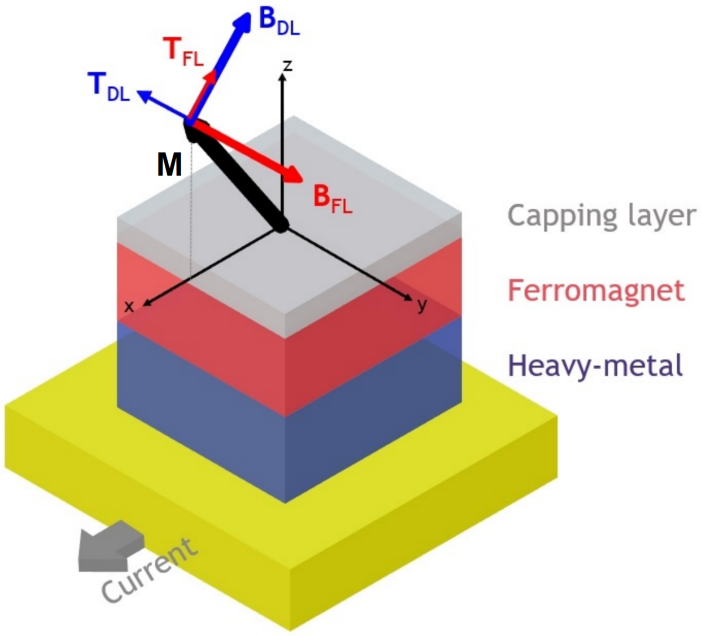

Figure 3.5: Torques and corresponding effective field directions in a trilayer structure composed of a heavy metal, a FM, and a capping layer. Courtesy of F. Binda.

distort the actual current distribution [143]. To address this, an alternative definition based on the electric field is sometimes preferred:

$$\xi^{E}_{\mathrm{DL,\,FL}} = \frac{2e}{\hbar} M_s t_F \frac{B_{\mathrm{DL,\,FL}}}{E} = \frac{\xi^{j}_{\mathrm{DL,\,FL}}}{\rho}, \tag{3.21}$$

where $E = \rho j$ is the applied electric field. This definition is independent of sample thickness and more convenient in voltage-controlled experiments. Within the framework of the SHE-driven SOT model, ξ^{E}_{DL} serves as an effective spin Hall conductivity.

3.2.3 Current-induced Magnetization Switching

A central application of SOTs is the current-induced switching of the magnetization in ferromagnetic layers [144]. This mechanism underpins SOT-MRAM, a promising technology offering fast switching speeds, high endurance, and CMOS compatibility [145].

In heterostructures with PMA, the magnetization is oriented along $\hat{z}$ at equilibrium. When a charge current flows along $\hat{x}$, a transverse spin accumulation $\boldsymbol{\xi}$ is generated along $\hat{y}$ via the SHE, REE, or OHE. In this configuration, the dominant torque responsible for switching is the DL torque:

$$\mathbf{T}_{\mathrm{DL}} \propto \mathbf{M} \times (\mathbf{M} \times \boldsymbol{\xi}). \tag{3.22}$$

Although $\mathbf{T}_{\mathrm{DL}}$ is finite for $\mathbf{M} \parallel \hat{z}$, it is *even* under magnetization reversal ($\mathbf{M} \to -\mathbf{M}$). Consequently, the energy landscape remains symmetric, and the switching outcome is probabilistic and thermally assisted rather than deterministic. To achieve reliable switching, a symmetry-breaking mechanism is required to lift the degeneracy between the $+\hat{z}$ and $-\hat{z}$ states.

A common approach is to apply an IP magnetic field H_{IP}, typically along the current direction ($\hat{x}$), which tilts $\mathbf{M}$ slightly away from $\hat{z}$ and biases the precessional trajectory. Fig. 3.6 illustrates this process: (a) initial PMA state; (b) magnetization tilt under H_{IP}; (c) application of $\mathbf{T}_{\mathrm{DL}}$ drives $\mathbf{M}$ toward reversal, assisted by the combined effective field; (d) after reversal, the two fields oppose each other, stabilizing the new state. Without symmetry breaking, $\mathbf{M}$ would relax randomly into either polarity.

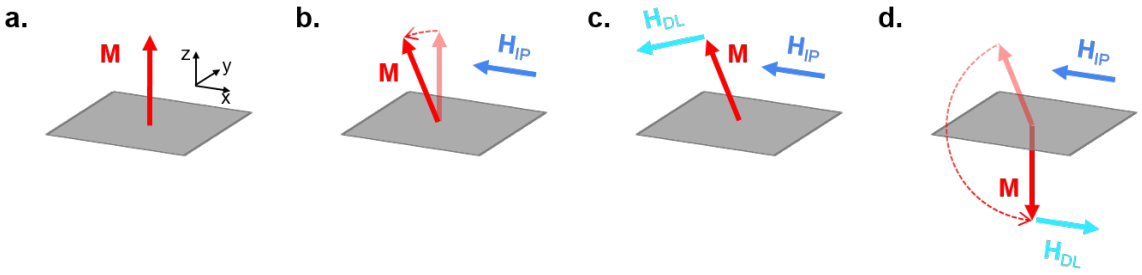

Figure 3.6: Schematic of SOT-induced switching in a PMA system: (a) initial state; (b) tilt under IP field H_{IP}; (c) DL torque drives reversal; (d) final stabilized state.

Symmetry breaking can also arise from internal mechanisms, such as interfacial or structural asymmetries [146, 147], or exchange bias from an adjacent antiferromagnet [148, 149]. Additionally, the IL-DMI in FM/HM/FM trilayers can bias the switching trajectory even without an external field [150, 151, 152]. Recent studies have explored further strategies for field-free switching [153, 154, 155, 156].

These mechanisms collectively lift the degeneracy between the two magnetization states, enabling deterministic switching driven by the DL torque. The critical switching current density j_c is a key performance metric, inversely proportional to the spin–torque efficiency (see Eq. 3.20). Materials with large spin Hall angles, such as Pt, β-W, or topological insulators, allow lower j_c, reducing energy consumption.

SOT Switching in Real Devices

The simplified macrospin picture is useful from a didactic perspective, but real devices, such as those studied in this thesis, with lateral dimensions of tens or hundreds of micrometers, are far larger than the scale where the macrospin approximation holds (approximately the domain wall width, typically below 10 nm depending on material properties) [157].

Outside the macrospin regime, magnetization reversal under SOT involves more complex processes influenced by several factors, including DMI, inhomogeneous current distribution, device geometry, defects, pinning sites, and non-uniform magnetization states.

A widely observed mechanism, and the one relevant to this work, is switching via domain nucleation and propagation. This process is often thermally assisted due to Joule heating from the injected current [158, 159]. Current injection in the HM reduces the effective anisotropy through heating while simultaneously generating the DL torque. These effects together increase the probability of nucleating a reversed domain, typically at a defect site where the energy barrier is lower [160]. Once nucleated, the reversed domain expands across the ferromagnetic layer, driven primarily by the DL torque, ultimately leading to full magnetization reversal.

The efficiency of this process depends on the DW structure. The DL torque couples effectively only to Néel-type DWs, as it does not act on magnetization aligned along $\hat{y}$. Therefore, an IP magnetic field is often required: in the case of Bloch walls, it transforms them into Néel walls, while in systems with interfacial DMI, it breaks the fixed chirality, enabling domain expansion rather than rigid translation. Understanding the conditions for domain nucleation and DW dynamics under SOT is thus essential for a complete description of SOT-induced switching. These aspects will be analyzed in detail in the next chapter.

The timescale of the current pulse is another critical parameter. Depending on the pulse duration, the switching mechanism can range from fully thermally activated to thermally assisted (the regime explored in this thesis) and, at ultrashort timescales (nanoseconds or below), to nearly pure SOT-driven switching [161]. Fig. 3.7, adapted from Ref. [161], illustrates the dependence of the critical current density on the pulse duration, highlighting these different regimes.

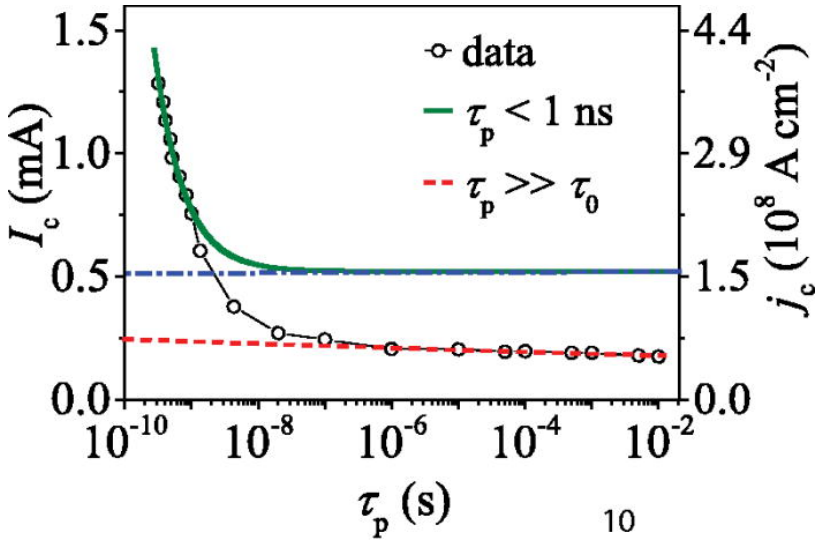

Figure 3.7: Dependence of the critical current density for SOT switching on the pulse duration, showing the transition from thermally dominated to SOT-dominated regimes. Taken from [161]).

Chapter 4

Chiral Magnetic Interactions and Domain Walls

Contents

4.1 The Dzyaloshinskii–Moriya Interaction

The DMI plays a central role in this thesis, as the work primarily focuses on chiral magnetic structures in both magnetic insulator/HM bilayers and fully metallic heterostructures. In this section, I present the theoretical foundations of DMI, addressing both intralayer and interlayer cases, with emphasis on the aspects most relevant to the systems investigated in this work.

4.1.1 Intralayer Dzyaloshinskii-Moriya Interaction

The intralayer DMI is an antisymmetric interaction that causes the spins of neighboring atomic sites to align perpendicularly to each other. Its origins date back to the 1950s, when scientists sought to

explain the weak ferromagnetism observed in certain antiferromagnets, such as α-Fe_2O_3, as well as the carbonate compounds $MnCO_3$ and $CoCO_3$. In 1957, Dzyaloshinskii applied Landau's second-order phase transition theory to demonstrate that the spontaneous magnetization in α-Fe_2O_3 was due to a spin-canting state of the material [162]. He showed that, under specific temperature and pressure conditions, the material transitions from a purely antiferromagnetic phase to a spin-canted phase, resulting in a small net total magnetic moment.

DMI leads to canting or spiraling spin structures and is a crucial mechanism for understanding chiral non-trivial magnetic textures. In thin films and multilayer structures where inversion symmetry is inherently broken at the interfaces, the DMI forms chiral Néel DWs. Unlike conventional Bloch walls, these DWs are characterized by a fixed sense of rotation, which can be exploited for efficient current-driven DW motion in spintronic devices. Moreover, the balance between DMI, exchange interactions, and anisotropy stabilizes magnetic skyrmions, which are promising for low-power, next-generation magnetic memory and logic devices due to their small size, stability, and manipulability.

Superexchange-based DMI

Two years after Dzyaloshinskii's paper, Moriya explained this canting through an anti-symmetric interaction that arises in the presence of SOC and inversion symmetry breaking in magnetic crystals [163, 164]. From second-order perturbative corrections to the superexchange interaction, he formulated formally the DMI interaction as:

$$\hat{H}_{\mathrm{DMI}} = \mathbf{D}_{ij} \cdot (\mathbf{S}_i \times \mathbf{S}_j), \tag{4.1}$$

where S_i and S_j are the spins of two adjacent atoms, and $\mathbf{D}_{ij}$ is the Dzyaloshinskii-Moriya vector, determined by SOC and structural asymmetry between sites i and j. The cross-product between spins favors a chiral arrangement, where the rotation direction depends on $\mathbf{D}_{ij}$.

In this view, magnetic ions interact indirectly through virtual hopping of electrons mediated by an intermediate non-magnetic anion (e.g., oxygen). When SOC is introduced on the magnetic sites, the resulting exchange is no longer symmetric. This mechanism is prevalent in bulk non-centrosymmetric magnetic crystals such as B20 compounds (MnSi, FeGe), where global inversion symmetry is absent. The superexchange-based DMI stabilizes long-period spin helices and skyrmion lattices in these systems [165].

RKKY-based DMI in Conductors

A theory of DMI for conducting ferromagnets emerged in 1976 when Smith suggested that the scattering of conduction electrons with non-magnetic impurities could introduce an asymmetric term to the RKKY mechanism [77, 166].

This picture was developed further by Fert and Levy in 1980 [167] who formulated a three-site model (schematic shown in Fig. 4.1), where DMI arises from electron exchange between two magnetic atoms (e.g., 3*d* elements) with a spin–orbit scattering event occurring at a nearby heavy non-magnetic atom (e.g., Pt, Ir). The spatial asymmetry of the setup, along with strong SOC on the non-magnetic site, breaks inversion symmetry and induces a chiral exchange interaction.

Fert extended this idea in 1990 to interfaces between a magnetic metal and a HM with strong SOC [168], where the symmetry is intrinsically broken. This so-called *interfacial* DMI sparked

significant interest in the scientific community [165] due to the flexibility of working with interfaces rather than bulk materials, the ability to use ultrathin films, and the potential to tune the interaction by modifying the ferromagnetic or HM layer.

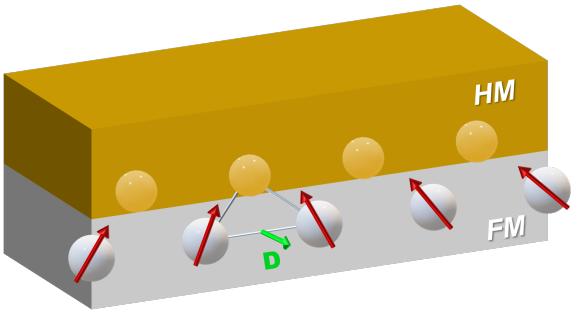

Figure 4.1: Schematic representation of the three-site model for interfacial DMI. A HM atom (gold) interacts with two neighboring ferromagnetic atoms (gray), inducing a fixed chirality in their spins (red arrows) along the direction of the DMI vector (green arrow).

Comparison and Material Relevance

The fundamental distinction between the two mechanisms lies in the nature of the mediating process: virtual electron hopping in insulating systems versus itinerant electron scattering in conducting systems. Identifying the dominant DMI mechanism in a given material is essential for tailoring chiral magnetic textures. In this thesis, DMI is investigated in both fully metallic heterostructures (such as Pt/Co) and magnetic-insulator/HM bilayers, where the microscopic origin of DMI is less straightforward and will be examined in detail in the following chapters.

DMI Energy

In a simple system with two adjacent spins along the $\hat{x}$-axis and the DMI vector $\mathbf{D}_{ij} = \begin{pmatrix} 0 \\ D_{ij} \\ 0 \end{pmatrix}$ pointing in the $\hat{y}$-direction, the DMI Hamiltonian simplifies to:

$$\hat{H}_{\mathrm{DMI}} = D_{ij} \left(S_i^z S_j^x - S_i^x S_j^z \right), \tag{4.2}$$

This form highlights the chiral nature of the interaction, where the energy is minimized when the spins are canted in a counterclockwise rotation. The lowest energy configuration $-D_{ij}S^2$ is achieved when spin i points along $\hat{z}$ and spin j points along $-\hat{x}$, or in any equivalent rotation.

It is significant to express the DMI energy density as a function of the continuous magnetization $\mathbf{m}(\mathbf{r})$ that varies smoothly as a function of position $\mathbf{r}$. We can consider a chain of spins along the $\hat{x}$-direction, where each spin S_i interacts with two neighboring spins located at sites $i-1$ and $i+1$, both a distance a apart, with the DMI vector $\mathbf{D_{ij}}$ aligned along the $\hat{y}$-axis. The Hamiltonian of spin S_i interacting with its neighbors through DMI is [169]:

$$\hat{H}_{\mathrm{DMI}} = D_{ij} \left(S_{i-1}^z S_i^x - S_{i-1}^x S_i^z \right) + D_{ij} \left(S_i^z S_{i+1}^x - S_i^x S_{i+1}^z \right), \tag{4.3}$$

which can be simplified as

$$\hat{H}_{\mathrm{DMI}} = 2D_{ij}a\left(S_i^z\left(\frac{S_{i+1}^x - S_{i-1}^x}{2a}\right) - S_i^x\left(\frac{S_{i+1}^z - S_{i-1}^z}{2a}\right)\right), \tag{4.4}$$

and assuming that D_{ij} is constant for all sites and that the spins vary smoothly, we approximate the differences as derivatives:

$$\hat{H}_{\mathrm{DMI}} = 2D_{ij}a\left(S_i^z\frac{\partial S^x}{\partial x_i} - S_i^x\frac{\partial S^z}{\partial x_i}\right). \tag{4.5}$$

Now, replacing the discrete spins $\mathbf{S}$ with the continuous magnetization $\mathbf{m}$, we can express the DMI energy density U_{DMI} as

$$U_{\mathrm{DMI}}(\mathbf{r}) = D\left(m_z\frac{\partial m_x}{\partial x} - m_x\frac{\partial m_z}{\partial x}\right), \tag{4.6}$$

where $\mathbf{D} = 2\mathbf{D}_{ij}/a^2$ is the micromagnetic DMI vector in units of J/m^2 [170].

In conclusion, the DMI introduces a fundamental modification to the exchange interaction in magnetic systems due to the interplay of broken inversion symmetry and SOC This leads to the emergence of non-collinear, chiral spin configurations, which are central to the behavior of DWs and other topologically non-trivial magnetic textures.

4.1.2 Interlayer Dzyaloshinskii–Moriya Interaction

So far, DMI has been discussed as a short-range, intralayer interaction between neighboring spins. In contrast, long-range interactions such as interlayer exchange coupling allow for novel magnetic configurations in multilayered systems, enabling functionalities not easily achievable otherwise [84, 171]. Recent theoretical [172] and experimental [173, 174] works have shown that DMI can also arise between magnetic layers separated by a non-magnetic spacer. This so-called interlayer DMI arises from SOC in the spacer and structural inversion asymmetry across the stack, which generates an antisymmetric exchange interaction between the magnetic layers, with a well-defined chirality (see Fig. 4.2).

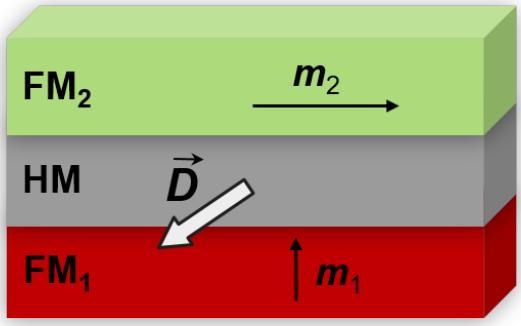

Figure 4.2: Schematic representation of IL-DMI, where the magnetizations of two ferromagnetic layers (black arrows), separated by a HM spacer, are coupled chirally. The direction of the IL-DMI vector is indicated by the white arrow.

IL-DMI is phenomenologically similar to intralayer DMI, but it acts globally on uniform magnetizations, opening new routes for magnetic control in multilayer devices [175, 150]. Microscopically, IL-DMI can be viewed as an extension of the three-site Fert–Levy model, involving two magnetic atoms in separate layers coupled via spin–orbit scattering at a non-magnetic site in the spacer. Depending on the symmetry and thickness of the spacer, the resulting DMI vector may favor twisted spin alignments between layers, leading to complex three-dimensional chiral textures.

IL-DMI has been demonstrated using various spacer layers, including Ru [173, 174], Pt [176], Pd [177], Ir [178], and Ag [179]. In most of these systems, IL-DMI exhibits an oscillatory behavior as a function of spacer thickness, similar to the RKKY interaction. This has been confirmed by first-principles calculations [180], and supports the interpretation of IL-DMI as the antisymmetric counterpart of interlayer RKKY exchange. In this picture, SOC modifies the spin susceptibility of conduction electrons across the spacer, introducing an additional exchange term proportional to $\vec{S}_i \times \vec{S}_j$. As with conventional DMI, this antisymmetric term requires both SOC and broken inversion symmetry, and leads to chiral coupling between the magnetic layers.

4.2 Magnetic Domains and Domain Walls

In this section, magnetic domains are introduced from an energetic perspective, demonstrating their formation and equilibrium conditions. We then examine how the presence of DMI modifies DWs' structure, before analyzing their dynamics under applied currents or magnetic fields in the following section. DWs have already been mentioned in the context of current-induced switching and will play a central role throughout this thesis.

4.2.1 Energetics of Magnetic Domains

In ferromagnetic materials, the competition between different energy contributions leads to the spontaneous formation of magnetic domains, regions where the magnetization is uniformly aligned. The main energies involved are the magnetic exchange, which favors parallel spin alignment; the magnetic anisotropy, which defines preferred directions (easy and hard axes) for the magnetization; and the demagnetizing energy, which arises from the stray magnetic fields produced by a uniformly magnetized body and is energetically unfavorable [69, 68].

If only exchange interactions were present, the lowest energy configuration would be one in which all spins are uniformly aligned (as shown in Fig. 4.3a). However, this would generate strong stray fields and increase the demagnetizing energy. To reduce this energy, the system divides into multiple domains with different magnetization directions, thereby minimizing the net external field (Fig. 4.3b). To completely cancel the stray field, the system further minimizes energy by forming closure domains, small domains rotated by 90° (Fig. 4.3c).

The formation of magnetic domains introduces DWs, which are transition regions where the magnetization gradually rotates from one domain orientation to another. These walls increase the system's exchange energy, since neighboring spins are no longer perfectly aligned, and also contribute to the anisotropy energy when the magnetization deviates from the easy axis. As a result, the equilibrium domain configuration reflects a compromise among minimizing exchange, anisotropy, and magnetostatic energies.

Depending on the material properties and geometric constraints, two primary types of DWs can

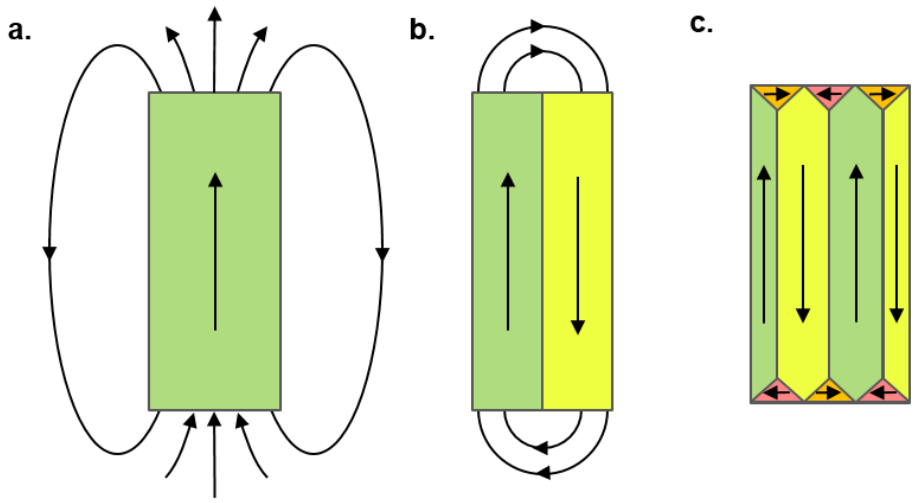

Figure 4.3: Schematic representation of magnetic domain configurations: (a) single-domain state with uniform magnetization; (b) multi-domain state reducing stray fields; (c) formation of closure domains to further minimize demagnetizing energy.

form. In Bloch walls, the magnetization rotates within the plane of the wall. In contrast, Néel walls feature a rotation of the magnetization perpendicular to the wall plane. The two configurations are depicted in Fig. 4.4.

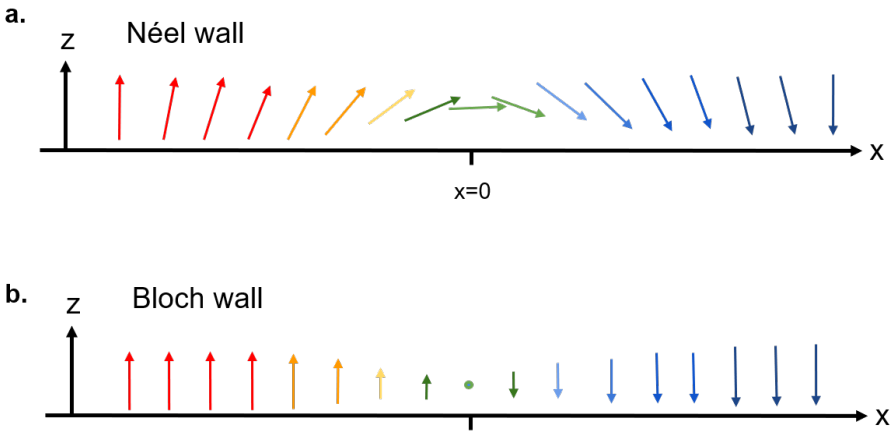

Figure 4.4: Schematic representation of Néel (a) and Bloch (b) DWs.

Bloch Domain Wall Width and Energy

To understand the nature of magnetic domains and DWs, it is useful to estimate the width and energy of a Bloch wall by balancing the competing contributions of exchange and anisotropy energies, following the approach in Ref. [69].

Consider two neighboring spins $\mathbf{S}_1$ and $\mathbf{S}_2$ separated by an angle θ. The exchange energy is:

$$E_{\text{ex}} = -2J\mathbf{S}_1 \cdot \mathbf{S}_2 = -2JS^2 \cos\theta \approx JS^2\theta^2, \tag{4.7}$$

for small θ. In a 180° Bloch wall, the magnetization rotates by π over N atomic sites, so $\theta \approx \pi/N$. The total exchange energy across the wall is then:

$$E_{\text{ex}}^{\text{wall}} \approx JS^2 \frac{\pi^2}{N}. \tag{4.8}$$

Expressed as an energy per unit area (dividing by a^2, where a is the lattice spacing):

$$\sigma_{\text{ex}} = \frac{JS^2\pi^2}{Na^2}. \tag{4.9}$$

A uniaxial anisotropy introduces an energy penalty for spins deviating from the easy axis. Assuming an energy density $E_K = K_{\text{eff}} \sin^2\theta$, where K_{eff} is the effective anisotropy, the total anisotropy energy across the wall is approximately:

$$\sum_{i=1}^{N} K_{\text{eff}} \sin^2\theta_i \approx \frac{N}{\pi} \int_0^{\pi} K_{\text{eff}} \sin^2\theta \, d\theta = \frac{NK_{\text{eff}}}{2}. \tag{4.10}$$

The DW energy per unit area is:

$$\sigma_{\text{BW}}(N) = \frac{JS^2\pi^2}{Na^2} + \frac{NK_{\text{eff}}a}{2}. \tag{4.11}$$

Minimizing with respect to N gives:

$$N = \pi S \sqrt{\frac{2J}{K_{\text{eff}}a^3}}. \tag{4.12}$$

The corresponding DW width is:

$$\Delta_{\text{DW}} = Na = \pi \sqrt{\frac{A}{K_{\text{eff}}}}, \tag{4.13}$$

where $A = 2JS^2/a$ is the exchange stiffness. The equilibrium wall energy per unit area is:

$$\sigma_{\text{BW}} = 4\sqrt{AK_{\text{eff}}}. \tag{4.14}$$

The Bloch wall width Δ_{DW} reflects the competition between exchange, which favors a gradual rotation (wide wall), and anisotropy, which favors alignment with the easy axis (narrow wall). Strong exchange (A large) produces wide walls, while strong anisotropy (K_{eff} large) produces narrow walls. For typical Co/Pt systems with $A \sim 10^{-11}\,\text{J/m}$ and $K_{\text{eff}} \sim 10^6\,\text{J/m}^3$, Δ_{DW} is on the order of 5–10 nm.

In the absence of chiral interactions, Bloch walls are generally favored in thin films with PMA, as they minimize stray fields. However, as discussed in the next section, the presence of DMI stabilizes Néel walls with a fixed chirality, profoundly altering DW structure and dynamics.

4.2.2 Influence of DMI on Domain Walls

The introduction of the DMI favors spin configurations with a well-defined chirality. This stems from the antisymmetric nature of DMI, which energetically prefers a specific rotational sense between neighboring spins. In systems with PMA and *interfacial* DMI, the combination of broken inversion symmetry at the interface and strong SOC leads to a preferred direction of spin rotation across the

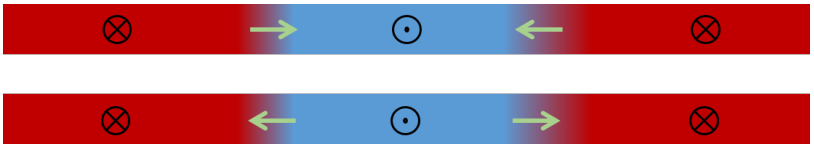

Figure 4.5: The DMI fixes the chirality of Néel DW, and the magnetization at the center of the wall consistently points toward one of the domains. The top diagram illustrates a left-handed Néel wall, while the bottom one shows a right-handed configuration.

DW. This results in the stabilization of chiral Néel walls, where the rotation sense (left-handed or right-handed, see Fig. 4.5) is determined by the sign of the DMI constant D.

In the micromagnetic approximation, for a DW oriented along the $\hat{x}$-direction, the interfacial DMI energy density U_{DMI} is given by Eq. 4.6. This energy is minimized when the magnetization rotates within the xz-plane with a fixed chirality, characteristic of a Néel wall. In contrast, Bloch walls, where the magnetization rotates around the $\hat{y}$-axis, do not couple to this DMI term and are thus energetically unfavorable in the presence of interfacial DMI. Therefore, DMI acts as an effective chiral field that stabilizes Néel walls with a specific sense of rotation. This has significant consequences for spintronic applications, as chiral Néel walls can be efficiently moved by SOTs. The overall reduced domain wall energy density in the presence of DMI becomes:

$$\sigma_{\mathrm{D}} = 4\sqrt{AK_{\mathrm{eff}}} - \pi D. \tag{4.15}$$

The first term represents the intrinsic energy cost of forming a domain wall, while the second term reflects the energy gain from stabilizing a chiral Néel configuration. A sufficiently large D can significantly lower σ_{D}, favoring the formation of compact, mobile domain walls and even skyrmions.

In real systems, however, the DW structure can adopt an intermediate configuration between Bloch and Néel. This occurs when the DMI strength is insufficient to fully stabilize a Néel wall. Thiaville et al. [170] defined a critical DMI strength above which a pure Néel wall becomes energetically favored:

$$D_{\mathrm{c}} = \frac{4\Delta K}{\pi}, \tag{4.16}$$

where $\Delta = \sqrt{\frac{A}{K_{\mathrm{eff}}}}$ is the DW parameter and $K = N_x \mu_0 M_s^2/2$ is the magnetostatic shape anisotropy that favors the Bloch wall, with N_x the demagnetizing coefficient of the wall.

As illustrated in Fig. 4.6, when $D < D_{\mathrm{c}}$, the DW tends to retain a Bloch-like configuration. As D increases beyond this threshold, the spins gradually reorient from a Bloch profile toward a fully chiral Néel configuration, passing through mixed intermediate states.

4.2.3 Magnetic Skyrmions

In addition to stabilizing chiral Néel DWs, the DMI can also support the formation of magnetic skyrmions, particle-like spin textures stabilized by the interplay of exchange, DMI, anisotropy, and dipolar interactions. These structures are characterized by a swirling spin configuration with a non-zero topological charge $Q = \pm 1$, which measures how many times the magnetization wraps around in all directions as you move across the plane. Intuitively, this means the spin texture forms a complete "twist" that cannot be undone without breaking the configuration, making skyrmions topologically protected. This protection grants them remarkable stability against moderate perturbations such

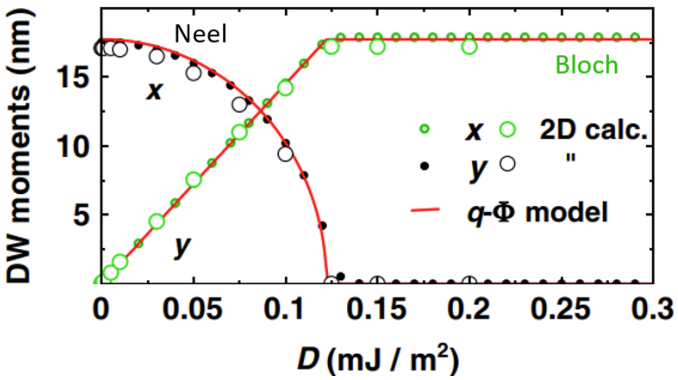

Figure 4.6: DW magnetic moments for different DMI strengths D. Increasing D favors a transition from Bloch-like to Néel-like DW configurations. Taken from [170].

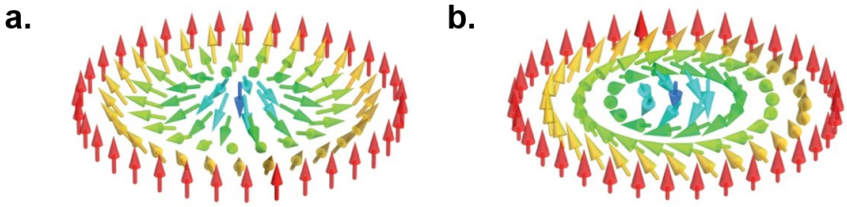

Figure 4.7: Sketch of (a) Néel-type and (b) Bloch-type skyrmions. Taken from [181].

as defects, thermal fluctuations, or external fields, distinguishing them from conventional magnetic domains.

A skyrmion can be visualized as a DW wrapped into a circular configuration (see Fig. 4.7). Analogous to DWs, skyrmions can exhibit either Bloch-type or Néel-type spin textures, depending on the type of DMI present in the system. They can be extremely compact, with diameters ranging from a few nanometers to several hundreds of nanometers, making them highly attractive for high-density spintronic applications.

Skyrmions were first predicted and observed in B20-type chiral magnets such as MnSi and FeGe, where bulk DMI stabilizes helical spin structures and skyrmion lattices [182, 183]. More recently, interfacial DMI in ultrathin ferromagnetic films has enabled the stabilization and manipulation of isolated skyrmions at room temperature [184], as well as their high-speed electrical control [185], thereby sparking significant interest in their technological potential [186]. Among the most promising applications is the skyrmion racetrack memory [181], where a train of skyrmions is shifted along a nanotrack by electrical current pulses, similar to DW racetrack memory but with potentially lower energy consumption and higher density. Other proposed uses include logic gates, probabilistic computing, and neuromorphic architectures, leveraging the topological and nonlinear properties of skyrmion dynamics.

Despite their promise, several challenges remain before skyrmion-based devices can become practical. These include ensuring thermal stability at the nanoscale, achieving reliable and deterministic nucleation and deletion, and mitigating the skyrmion Hall effect, which causes undesired transverse

motion under current.

4.3 Domain Wall Dynamics

In this thesis, we are primarily interested in the behavior of domains and DWs under the application of an electrical current. This includes phenomena such as SOT-induced switching and the study of DMI through DW depinning. To build a solid foundation for understanding current-induced DW motion (CIDWM) and its dynamics, it is instructive to first analyze the simpler case of field-driven DW motion in a ferromagnet with PMA.

4.3.1 Field-Driven DW Motion and Walker Breakdown

Consider a 180° Bloch DW separating two domains magnetized along the $\hat{z}$ direction, and an external magnetic field $\boldsymbol{H}_{\text{ext}} \parallel \boldsymbol{z}$ is applied. According to the LLG equation (see Chapter 3), this external field induces a precessional torque $\boldsymbol{m} \times \boldsymbol{H}_{\text{ext}}$ as well as a damping torque $\boldsymbol{m} \times \frac{d\boldsymbol{m}}{dt}$ on the local magnetization.

The damping term acts in a straightforward manner, tending to align the spins within the DW along the direction of the applied field. As a result, the domain with magnetization aligned with $\boldsymbol{H}_{\text{ext}}$ expands, effectively moving the DW.

The precessional torque, on the other hand, initially rotates the magnetization inside the Bloch wall toward the Néel configuration. This transformation alters the internal structure of the wall and generates an additional demagnetizing field due to the appearance of magnetic charges in the Néel state. This new internal field then induces further torques via the LLG dynamics, eventually driving the magnetization out of the wall plane in the direction of the external field.

In this dynamic regime, the precessional and damping torques cooperate to produce steady and efficient DW motion. The DW velocity under such a field can be expressed as [187, 188]:

$$v_{\text{DW}} = \mu H_{\text{ext}} = \frac{\gamma_0 \Delta}{\alpha} H_{\text{ext}}, \tag{4.17}$$

where μ is the DW mobility and $\gamma_0 = |\gamma|\mu_0$. The velocity is linearly proportional to the applied field H_{ext} and increases with larger Δ or smaller α.

However, when the applied field exceeds a critical threshold, the DW tilts beyond an angle of $\pi/4$, and the precessional torque can no longer be fully balanced by damping. At this point, the internal magnetization of the wall enters a continuous precessional regime, alternating between Bloch and Néel configurations. This phenomenon is known as the Walker breakdown [189], and it results in a significant reduction of the average wall velocity due to the oscillatory internal motion, as shown in Fig. 4.8.

The Walker field can be derived as:

$$H_W = \frac{\alpha}{\gamma \Delta}, \tag{4.18}$$

and the average velocity becomes:

$$v_{\text{DW}} \propto \alpha^2 \mu H_{\text{ext}}, \tag{4.19}$$

which is significantly lower than below the Walker threshold.

Walker breakdown has been experimentally observed in various ferromagnetic systems, including perpendicularly magnetized permalloy and Co/Pt multilayers [190, 191].

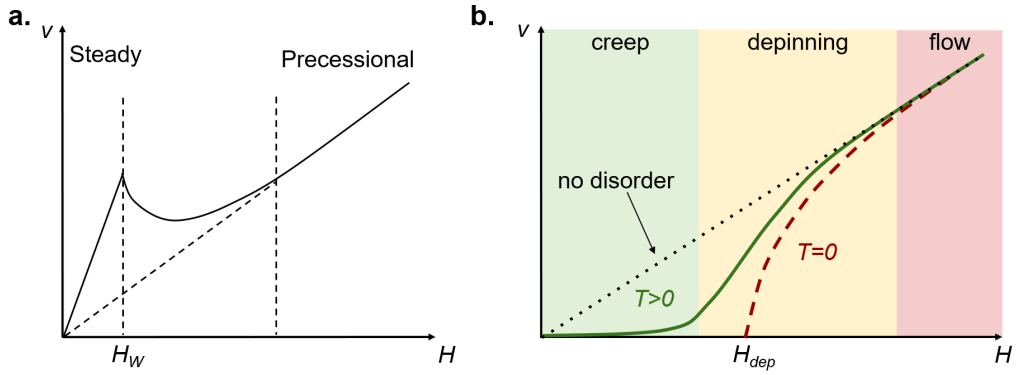

Figure 4.8: (a) DW velocity as a function of the externally applied magnetic field H in the absence of pinning. The steady and precessional regimes are separated by the Walker breakdown at H_w. (b) At low fields, the creep, depinning, and flow regimes can be distinguished depending on the excitation energy and the characteristic depinning field H_{dep}. Adapted from [190].

DW Motion at Low Fields

At low applied fields, DW motion deviates from the ideal linear flow regime described earlier. Depending on the relative strength of the external field H_{ext} and the pinning potential landscape, three main dynamical regimes can be identified and are shown in Fig. 4.8b [192]:

- **Creep regime:** For fields well below H_{dep}, DW motion is governed by thermally activated hopping between pinning sites. The wall advances very slowly, with its velocity following an exponential dependence on the field:

$$v_{\text{DW}} \propto \exp\left[-\left(\frac{H_0}{H_{\text{ext}}}\right)^{\mu}\right], \tag{4.20}$$

  where H_0 is a characteristic field and μ is a universal exponent (typically $\mu = 1/4$ for 1D interfaces in 2D disordered media). This so-called *creep law* has been experimentally validated in a wide range of materials [190].

- **Depinning (thermally activated) regime:** When H_{ext} is comparable to H_{dep}, the DW intermittently overcomes local pinning sites with the aid of thermal fluctuations. The motion becomes stochastic, and the velocity exhibits a nonlinear but continuous dependence on field. In this regime, the activation over energy barriers dominates the dynamics, and the wall moves via thermally assisted jumps.

- **Flow regime:** When H_{ext} is significantly larger than the depinning field H_{dep}, the DW moves freely through the material without being hindered by defects or inhomogeneities. In this regime, the wall velocity is proportional to the applied field and follows the linear expression given by Eq. (4.17), independent of the energy landscape.

The transition between creep, depinning, and flow regimes underpins the behavior of DWs in practical spintronic devices, especially in the presence of disorder or edge roughness.

Field-Driven Néel Walls

In systems with strong DMI, the internal structure of the DW is stabilized in a Néel configuration rather than the conventional Bloch type. The DMI acts as an effective IP magnetic field that fixes the chirality of the DW and energetically favors a uniform Néel texture across the film.

This stabilization has a crucial consequence: it suppresses the internal magnetization precession responsible for Walker breakdown in conventional systems. As a result, the Walker field is significantly increased, extending the steady-flow regime of DW motion to higher applied fields. The Walker field becomes [170, 193]:

$$H_{\mathrm{W}} \sim \frac{\pi \alpha H_{\mathrm{DMI}}}{2} = \frac{\pi \alpha D}{2 M_s \Delta}, \tag{4.21}$$

where the DMI effective field is given by $H_{\mathrm{DMI}} = D/(\mu_0 M_s \Delta)$, and sets the scale of the Walker threshold.

Interestingly, unlike simulations that include precession, real systems with strong DMI often show suppressed DW precession above the Walker field, resulting in velocity saturation [194]. In this DMI-stabilized regime, the DW velocity at Walker breakdown becomes:

$$v_{\mathrm{DW}} = \frac{\pi}{2} \gamma_0 H_{\mathrm{DMI}} \Delta = \frac{\pi \gamma D}{2 M_s} \tag{4.22}$$

and can be used to quantify the strength of DMI. This expression shows that, in the presence of strong DMI, DW velocity is directly proportional to the DMI strength. Consequently, materials with large D not only stabilize homochiral Néel walls but also enable efficient and fast field-driven DW motion in the steady regime.

4.3.2 Spin Torque-induced Domain Wall Motion

The injection of an electrical current into a ferromagnetic material can drive DW motion via STT, a mechanism rooted in the exchange of angular momentum between spin-polarized conduction electrons and local magnetic moments.

When a current flows through a nonmagnetic metal, the electron spins are randomly oriented, resulting in zero net spin polarization. In contrast, when current passes through a FM such as Co, Ni, or Fe, conduction electrons become spin-polarized due to spin-dependent scattering. This spin polarization aligns preferentially with the local magnetization direction, as spin-up and spin-down electrons experience different resistivities. The degree of spin polarization P is defined as:

$$P = \frac{\rho_- - \rho_+}{\rho_- + \rho_+}, \tag{4.23}$$

where ρ_- and ρ_+ are the resistivities for spin-up and spin-down electrons, respectively.

As these spin-polarized electrons traverse a DW, their spin direction must adapt to the local magnetization texture. This gradual rotation of spin orientation results in a torque on the local magnetic moments, conserving total angular momentum. This process, known as the adiabatic STT, causes the DW to move in the direction of electron flow.

However, adiabatic STT alone is often insufficient to sustain DW motion against internal demagnetizing fields and damping. A second contribution, referred to as the non-adiabatic STT, arises due to spin mistracking at the DW interface. In this process, spin misalignment between conduction

electrons and the local magnetization leads to partial spin reflection, generating momentum transfer that exerts a force on the DW. This mechanism has a DL symmetry and is essential for initiating and sustaining DW motion below intrinsic threshold currents.

The generalized LLG equation incorporating both adiabatic and non-adiabatic STT contributions is written as [195, 196, 197]:

$$\frac{d\mathbf{m}}{dt} = -\gamma\,\mathbf{m}\times\mathbf{H}_{\text{eff}} + \alpha\,\mathbf{m}\times\frac{d\mathbf{m}}{dt} - (\mathbf{u}\cdot\nabla)\mathbf{m} + \beta\,\mathbf{m}\times(\mathbf{u}\cdot\nabla)\mathbf{m}, \tag{4.24}$$

where the third and fourth terms correspond to the adiabatic and non-adiabatic STT, respectively, and β is the dimensionless non-adiabatic STT coefficient. The spin drift velocity $\mathbf{u}$ is given by:

$$\mathbf{u} = \frac{gP\mu_B}{2eM_s}\mathbf{j}_e. \tag{4.25}$$

In the purely adiabatic regime, DW motion requires a threshold current to overcome intrinsic pinning and initiate precessional motion. By contrast, the inclusion of non-adiabatic torques ($\beta \neq 0$) enables CIDWM even below this threshold, allowing for more efficient control of magnetic textures [198, 199].

Overall, STT provides a robust mechanism for electrically driven DW motion, though its efficiency is typically lower than that of SOT-based approaches. Nonetheless, it remains a foundational concept in understanding current-induced magnetization dynamics.

4.3.3 Spin Orbit Torques on Chiral Domain Walls

As discussed in Chapter 3, injecting an electrical current into an HM layer generates SOTs. Compared to STT, SOT provides a more efficient mechanism for CIDWM. In the STT regime, the angular momentum transfer is limited to $\hbar/2$ per electron. In contrast, SOTs originate from spin currents generated in the HM layer via the SHE or interfacial REE, and their magnitude is governed by the SOC strength and the spin transparency of the HM/FM interface. For instance, in the widely studied Co/Pt heterostructure, SOT-driven DW velocities exceeding ~ 300 m/s have been demonstrated [21, 200, 201], whereas STT-driven motion in single Co layers reaches speeds an order of magnitude lower [202, 203]. Nevertheless, in some optimized systems such as Mn_4N, STT-driven velocities up to ~ 3 km/s have been reported, thanks to high spin polarization and low M_s [204, 205].

The interplay between SOT and DMI is critical in determining both the efficiency and direction of DW motion. In HM/FM systems with PMA, interfacial DMI stabilizes chiral Néel walls, which couple strongly to the DL term, the dominant torque responsible for DW motion [170, 206, 207].

When the wall magnetization lies along the $\hat{x}$-axis, the DL torque acts as an effective field, driving the DW along or against the current direction depending on the sign of the spin Hall angle θ_{SH} and the DMI constant D. Due to the geometry of the DL torque and the chirality of the Néel walls, domain motion results in a rigid shift of the entire domain, which is essential for technologies such as racetrack memory proposed by Parkin [65]. The ability of SOT to move domains without deformation and in a direction controlled by the current is a fundamental technological advantage.

A schematic of the DL torque acting on a domain with chiral Néel DWs is shown in Fig. 4.9.

To model these dynamics, the one-dimensional collective coordinate approach describes the DW using two parameters: its position $q(t)$ and internal angle $\phi(t)$, defined in Fig. 4.10.

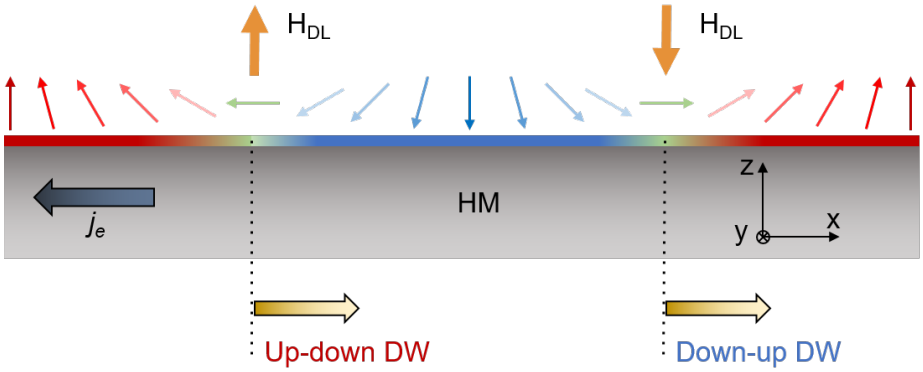

Figure 4.9: Schematic illustration of DL torque acting on a domain with chiral Néel DWs. The direction of DW motion depends on the sign of the spin Hall angle and the DMI constant.

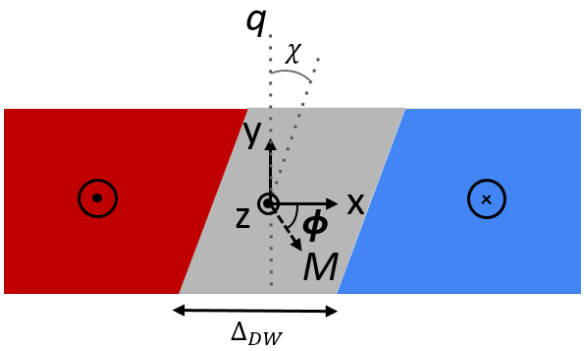

Figure 4.10: Schematic representation of the collective coordinates used to describe DW dynamics. q is the DW position, Φ is the azimuthal angle of the magnetization vector $\vec{M}$ projected onto the xy-plane, Δ_{DW} represents the DW width, and χ is the tilting angle of the DW. Adapted from [208].

Including SOT and DMI contributions in the LLG equation leads to the following coupled equations of motion [170, 196]:

$$\begin{aligned} \dot{\phi} + \alpha \frac{\dot{q}}{\Delta} &= \gamma H_{\mathrm{DL}} \cos\phi, \\ \frac{\dot{q}}{\Delta} - \alpha\dot{\phi} &= \gamma \left(-H_K \sin\phi\cos\phi + H_{\mathrm{DMI}} \sin\phi\right), \end{aligned} \tag{4.26}$$

where H_K is the IP wall anisotropy field, and H_{DL} is the effective DL torque field:

$$H_{\mathrm{DL}} = \frac{\hbar\theta_{\mathrm{SH}} j}{2eM_s t_F}. \tag{4.27}$$

The DMI term H_{DMI} pins the internal angle ϕ to 0 or π, stabilizing a Néel structure with a well-defined chirality. This alignment optimizes the torque efficiency, allowing deterministic and efficient DW motion.

In the steady-state regime (neglecting pinning and inertia), the DW velocity simplifies to:

$$v = \Delta\gamma \frac{H_{\mathrm{DL}} H_{\mathrm{DMI}}}{\sqrt{H_{\mathrm{DL}}^2 + \alpha^2 H_{\mathrm{DMI}}^2}} = \frac{v_D}{\sqrt{1 + \left(\frac{j_D}{j}\right)^2}}, \tag{4.28}$$

where $v_D = \Delta\gamma H_{\mathrm{DMI}} = \frac{\gamma\pi D}{M_s}$ is the maximum DW velocity, and

$$j_D = \frac{2\alpha t_F e D}{\hbar\theta_{\mathrm{SH}}\Delta} \tag{4.29}$$

is the characteristic current scale needed to reach this velocity.

This expression reveals that the maximum DW velocity increases with the DMI strength D, and is enhanced in systems with low M_s. The sign of motion depends on both D and θ_{SH}, highlighting their symmetry-breaking role.

When a longitudinal IP magnetic field H_{IP} is applied, it effectively modifies the DMI field. If H_{IP} is aligned with H_{DMI}, the total effective field becomes $H_{\mathrm{tot}} = H_{\mathrm{DMI}} + H_{\mathrm{IP}}$, enabling ultrafast DW motion [30, 51]. Conversely, when H_{IP} cancels H_{DMI}, the DW velocity drops to zero as the wall transitions to a Bloch configuration, which is insensitive to DL torque [200, 201, 170]. This property is used to quantify the DMI strength in this thesis.

In summary, the combination of SOT and DMI provides an efficient, scalable, and field-free means to manipulate chiral DWs in PMA heterostructures. This mechanism underpins next-generation spintronic devices such as racetrack memories, offering fast, deterministic, and low-power magnetic control.

4.4 Experimental Techniques for DMI Characterization

The DMI is a key factor in the advancement of spintronic technologies, making it essential to accurately determine both the magnitude and sign of the DMI constant D across various material systems. Achieving reliable and precise measurements is therefore of critical importance.

Although the number of studies on DMI has grown significantly in recent years, a wide range of measurement techniques are employed, often leading to inconsistent and non-comparable results. In many cases, different methods yield conflicting values of D for nominally identical systems. Moreover, discrepancies can arise even when the same technique is applied to similar stacks, or when different techniques are used on the same sample [209]. These inconsistencies highlight the ongoing challenge of DMI quantification and the need for standardized approaches within the scientific community.

This thesis contributes to this effort by focusing on the quantification of DMI in REIG/HW heterostructures, addressing both the measurement challenges and the broader issues associated with current methodologies.

In this section, we draw upon the recent and thorough review by Kuepferling *et al.* [208], which outlines the principal techniques used to measure DMI, along with respective advantages and limitations. Special attention is given to the methods most relevant to the experimental work presented in this thesis. In their review, the authors identify three main categories of experimental techniques for quantifying the DMI: DW methods, spin-wave methods, and SOT methods. DW methods determine the DMI constant D by analyzing DW velocity or DW energy under varying conditions. Spin-wave methods extract D by measuring the nonreciprocal behavior of propagating spin waves. SOT methods infer D based on torque characteristics. These categories differ significantly in terms of the assumptions required and the physical quantities they probe. Each method has its own advantages and limitations and may be better suited for specific material systems.

Domain-wall Methods

Among the DW-based techniques, several approaches are commonly used: current-driven DW motion, field-driven DW motion (in both creep and flow regimes), equilibrium stripe domain patterns, magnetic stripe annihilation, nucleation field measurements, stray field imaging, and DW internal structure imaging.

The current-driven DW motion method quantifies interfacial DMI by measuring the velocity of DWs in lithographically patterned wires under applied current and IP magnetic fields. The DMI field is extracted from the IP field value at which DW motion is suppressed or reversed, accounting for current-induced torques. A slightly modified version based on the estimation of the DW depinning field is used in this thesis.

The field-driven DW motion method determines the DMI by measuring DW velocity in continuous films under perpendicular and IP magnetic fields. The DMI field is extracted from the IP field value at which the velocity reaches a minimum, typically analyzed in the creep regime with MOKE.

The nucleation field method estimates the DMI by analyzing asymmetries in domain nucleation under IP magnetic fields, typically at the edges of patterned structures. The DMI modifies the DW energy, affecting the nucleation barrier, and the DMI constant is extracted by fitting thermally activated nucleation models.

The stray field imaging method uses nitrogen-vacancy (NV) magnetometry to measure the magnetic stray field profile across DWs. The Zeeman shift in the NV center reveals the DW structure, from which the DMI strength and sign can be inferred, particularly in samples with low DMI where Bloch and Néel walls are distinguishable.

While each method has its own advantages and limitations, DW-based techniques generally require accurate estimation of several magnetic parameters (e.g. the exchange parameter A), which can be challenging. These methods are best suited for materials with PMA and are less applicable to IP magnetized systems. Additionally, the dependence of DW velocity on the IP field does not always follow a simple linear trend, especially in current-driven configurations. Nevertheless, these methods allow for the determination of both the magnitude and chirality of the DMI and are particularly effective for ultrathin films with PMA and systems with very low DMI values, such as the REIG heterostructures studied in this thesis.

Spin-Wave Methods

The most common method to quantify DMI, especially in metallic systems, is Brillouin Light Scattering (BLS). Other spin-wave-based techniques include time-resolved MOKE (TRMOKE), propagating spin-wave spectroscopy (PSWS), and spin-polarized electron energy loss spectroscopy (SPEELS).

The BLS method quantifies DMI by measuring the frequency asymmetry between Stokes and anti-Stokes peaks arising from nonreciprocal surface spin waves (Damon–Eshbach modes) propagation. The wavevector is tuned via the incident light angle, and the DMI constant is extracted from the frequency shift, which is linear in wavevector. BLS does not require sample patterning and is relatively insensitive to defects. The other spin-wave techniques also exploit spin-wave nonreciprocity to extract DMI, but typically require patterned structures, specialized setups, or ultrahigh vacuum conditions, and are less commonly used than BLS.

Spin-wave methods allow for a straightforward quantification of both the magnitude and chirality of DMI. While they require knowledge of material-dependent parameters, they do not require esti-

mation of the exchange stiffness, which is often a source of uncertainty in other methods. Contrary to common belief, spin-wave methods are not limited to systems with IP magnetization. However, in the Damon–Eshbach geometry, commonly used for DMI characterization, an IP magnetic field is applied to align the magnetization IP, which is necessary for observing nonreciprocal spin-wave propagation. These techniques are generally more suitable for metallic systems with higher thickness and stronger DMI. For this reason, they are not well-suited for REIGs with low DMI and strong PMA, such as those studied in this thesis.

Spin-Orbit Torque Methods

SOT methods quantify DMI by measuring current-induced shifts in the OOP hysteresis loop under applied IP magnetic fields. The DMI field is extracted from the field value at which the DW magnetization aligns with the IP field, enabling domain expansion. This shift is attributed to the DL torque generated by spin accumulation at the interface.

These methods are straightforward to implement; however, similar to DW methods, they rely on accurate knowledge of material parameters such as M_s and A, and are only applicable to systems with PMA and square hysteresis loops. Additionally, they cannot determine the sign of the DMI.

Due to their simplicity and compatibility with insulating systems, SOT methods are particularly useful for probing DMI in magnetic insulator heterostructures. However, their sensitivity is limited for ultrathin films with very low DMI, such as the REIG systems studied in this thesis. Moreover, the shift of the hysteresis loop is not always reliable, as domain nucleation and expansion can be influenced by thermal effects and may not be reproducible.

A comparative summary of the DMI quantification methods, including their main advantages and limitations, is presented in Table 4.1.

Table 4.1: Summary of experimental techniques for DMI quantification.

Method	**Advantages**	**Limitations**
Domain-Wall	Determines both magnitude and sign of DMI; applicable to materials with PMA; direct imaging of domain structures.	Sensitive to pinning and thermal effects; requires accurate magnetic parameters; high IP fields needed for large DMI values.
Spin-Wave	High precision and reproducibility; less affected by defects and pinning; differential measurement reduces systematic errors.	Requires IP magnetization, limiting applicability in PMA systems; low signal-to-noise ratio in ultrathin films; limited wavevector range in some setups.
SOT	Simple and direct measurement of DMI field; compatible with magnetic insulators.	Cannot determine chirality; requires accurate magnetic parameters; sensitive to Joule heating and current-induced effects; requires PMA and square hysteresis loops.

Finally, Fig. 4.11 illustrates the typical ranges of DMI strength and magnetic layer thickness

where each method is most effective[210]. DW and SOT methods are better suited for ultrathin films with low DMI, with DW techniques offering higher accuracy at the lowest limits. In contrast, spin-wave methods are more reliable and straightforward for thicker samples with stronger DMI.

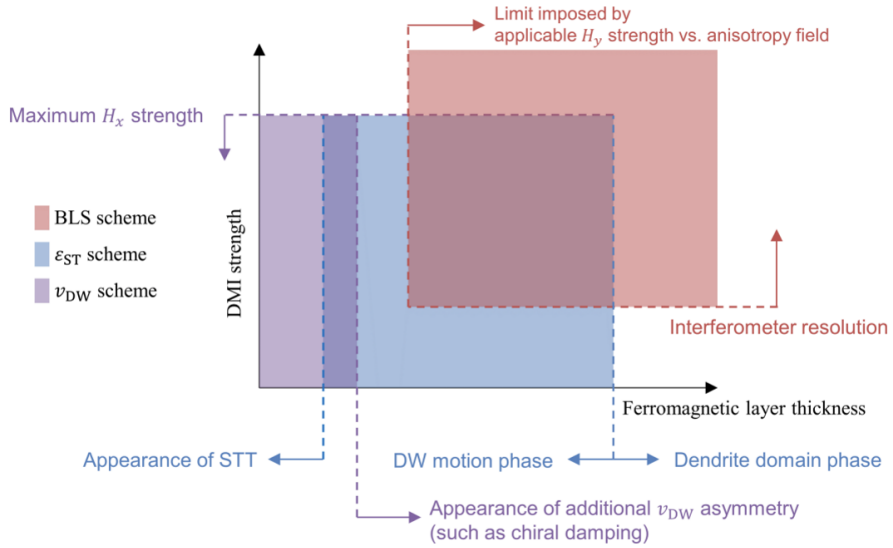

Figure 4.11: Comparison of the applicability range of DMI quantification methods as a function of magnetic layer thickness and DMI strength. Taken from [210].

Chapter 5

Thin Films Growth and Characterization

Contents

This chapter presents the main experimental techniques and materials employed throughout this thesis. It begins with an overview of the in-house sputtering system used for the growth of all thin films investigated in this work, including both oxide-based and metallic heterostructures.

Subsequent sections describe the device fabrication processes, which involve photolithography, lift-off, and etching techniques, as well as the Hall measurement setups utilized for the electrical and magnetic characterization of the devices.

The second section provides an overview of the crystalline and magnetic properties of REIGs, with particular emphasis on the origin of PMA in these systems. A detailed characterization of the deposition method and properties of terbium iron garnet ($Tb_3Fe_5O_{12}$, TbIG) thin films is also reported, as TbIG constitutes the primary material studied in this thesis. Finally, the last section offers a brief introduction to the metallic systems and their deposition processes.

5.1 Methods

5.1.1 Sputtering Deposition System

Thin film deposition in this work was carried out using a custom-configured magnetron sputtering system from AJA International (Orion Series UHV). Sputtering is a physical vapor deposition (PVD) technique widely employed for the growth of both metallic and oxide thin films due to its excellent uniformity, scalability, and industrial compatibility.

In a typical sputtering process, a plasma is ignited by applying a high voltage to a target (the material to be deposited) in the presence of an inert working gas, usually argon (Ar). The ionized Ar atoms (Ar^+) are accelerated towards the target, ejecting atoms from its surface through momentum transfer. These atoms travel through the vacuum chamber and condense onto a substrate, forming a thin film. When reactive gases such as oxygen (O_2) are introduced, the process becomes reactive sputtering, enabling the deposition of oxide materials from metallic or compound targets.

The AJA sputtering system used in this thesis consists of two interconnected vacuum chambers: one dedicated to the deposition of metals and magnetic heterostructures, and the other for oxide deposition (see Fig. 5.1). Samples can be transferred between the two chambers without breaking the vacuum, enabling the fabrication of oxide/metal heterostructures with preserved interface quality and minimal contamination, an essential requirement for high-performance spintronic devices. This dual-chamber configuration allows in-situ growth of complex heterostructures composed of insulating garnet films and metallic overlayers, which is crucial for studying interfacial spin transport phenomena. In particular, clean interfaces are vital to preserve effects such as spin mixing conductance, SOTs, and interfacial properties, such as the DMI studied in this thesis, all of which are highly sensitive to interface roughness, oxidation, and contamination.

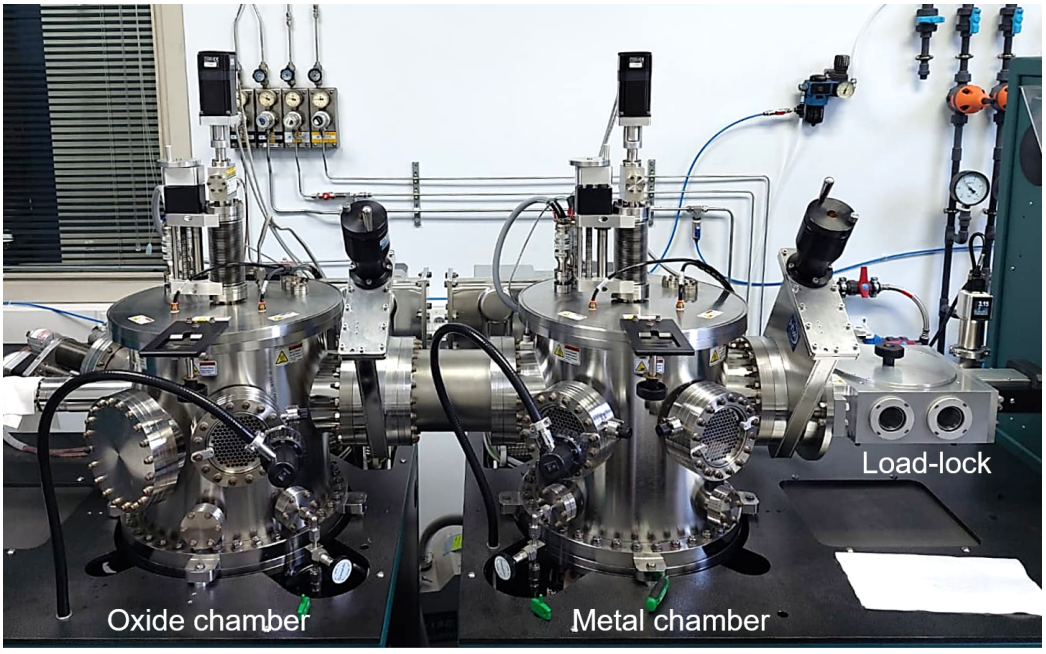

Figure 5.1: Photograph of the sputtering system used in this thesis. On the left the oxide chamber, in the middle the metal chamber and on the right the load-lock.

The metal chamber is equipped with multiple DC magnetron guns and is primarily used for the deposition of metallic and ferromagnetic layers. It enables precise control over layer thickness and supports the fabrication of complex multilayer stacks. DC sputtering is well-suited for conductive materials and allows for fast deposition rates. The oxide chamber is dedicated to RF sputtering, primarily for the growth of complex oxide thin films such as REIGs. RF power is required when using insulating targets to prevent charge accumulation during deposition. Reactive sputtering is commonly employed in this chamber, utilizing an Ar/O_2 gas mixture.

Both chambers are equipped with resistive heaters capable of reaching temperatures up to 850 ^{o}C, enabling the growth of high-crystallinity epitaxial films. The heaters apply heat to the sample holder, which transfers it to the substrate through direct contact. Consequently, the actual substrate temperature is lower than the heater setpoint; however, a conversion table provided by the manufacturer is used to determine the substrate temperature. All temperatures reported in this thesis refer to the substrate temperature.

Ar is used as the sputtering gas in both chambers, while a controlled O_2 flow is introduced during oxide deposition to ensure stoichiometric composition and stabilize the desired crystalline phases.

Additionally, the system includes a load-lock chamber, which allows sample introduction and removal without compromising the vacuum conditions in the deposition chambers.

All REIG thin films discussed in this thesis were deposited using RF sputtering in the oxide chamber. Subsequent metallic layers, such as Pt, were deposited in-situ in the metal chamber via DC sputtering, ensuring atomically clean and abrupt REIG/metal interfaces. Deposition details are provided in the next sections.

5.1.2 Device Fabrication

Device fabrication was carried out in the ICMAB cleanroom (NANOQUIM) using standard optical lithography techniques. First, a positive photoresist was spin-coated onto the film surface using an SMA AC 6000 spinner, followed by a soft bake on an SBS hotplate at 75 °C for 1 minute.

Two types of fabrication methods were employed: etching and lift-off. Both used the same positive photoresist, and pattern definition was achieved using a maskless lithography system (Micro-Writer ML3, Durham Magneto Optics Ltd.), which enabled selective UV exposure of the photoresist. With a positive photoresist, the areas exposed to light become soluble and are removed during development. The sample was developed at room temperature for 1 minute to remove the exposed regions, then rinsed in water for another minute to stop the development process and prevent overexposure, which could result in poorly defined device edges.

Etching was performed on the full heterostructure grown in situ. Although this method is more time-consuming than lift-off, it offers the advantage of creating devices on complete heterostructures, preserving perfect interfaces. Additionally, the magnetic area is confined to the active device, which improves repeatability and significantly increases the coercivity of individual devices compared to the full film. This increase is typically due to the reduced number of nucleation sites in smaller structures. For etching, the regions outside the desired structures were exposed and removed, leaving only the device area protected by the photoresist. Reactive ion etching (RIE) was carried out at ICN2 to remove the REIG/metal stack in the exposed areas. The etching was performed at 6 mTorr of Ar, with a power of 200 W for 15 minutes, ensuring complete removal of the film in the patterned regions. Finally, the photoresist was removed using a 20-second ultrasonic bath in acetone and isopropanol.

All garnet-based structures were defined using this etching process.

In contrast, fully metallic devices or additional fabrication steps (e.g., contact pads) were defined via lift-off, which is a simpler and faster procedure. In this case, the desired pattern was directly exposed on the substrate. After development at room temperature for 1 minute, the exposed regions were removed, leaving the device area open to air. The sample was then placed in the sputtering system for metal deposition. Lift-off was completed by sonicating the sample in acetone for 30 seconds to remove the photoresist. While this method is quicker, it does not allow for high-temperature deposition, and the interface between the substrate (or the first deposited layer) and the metal comes into contact with air, which can compromise interface sharpness and cleanliness. To mitigate this, a gentle plasma cleaning (10 W for 30 seconds) is typically performed before deposition.

Two main device geometries are used throughout this thesis and are shown in Fig. 5.2. Fig. 5.2a shows the full layout, designed in CleWin, of the device optimized for MOKE measurements. It consists of a DW track, 10 µm in width and 120 µm in length, which provides optimal optical contrast. These dimensions have been adjusted over the course of this work, with the width being particularly critical: it allows for the formation of sharp DWs transverse to the track, which is essential for DMI measurements (as discussed later), while also ensuring clean magnetic contrast. Background-subtracted MOKE images are highly sensitive to vibrations, and if the track is too narrow, the proximity of the device edges can cause the magnetic signal to be overwhelmed by noise. More details are provided in the chapter dedicated to MOKE measurements.

Fig. 5.2b shows an optical microscope image of a fabricated device, highlighting the active region. The transverse arm enables electrical measurements on the same structure and, as described in Chapter 7, allows decoupling of current injection paths.

The second geometry, shown in Fig. 5.2c, consists of a standard Hall bar with a channel width of 7.5 µm and a length of 30 µm, optimized for magnetoelectrical transport measurements. These devices include transverse Hall arms to enable both longitudinal and transverse resistance measurements. Fig. 5.2d presents an optical micrograph of a real device, showing the current injection line (the widest) and two transverse Hall arms used to measure the signals described in Chapter 2.

5.1.3 Electrical Measurements

Electrical and magneto-optical measurements were performed by wire-bonding the devices onto custom-fabricated PCBs, designed to be compatible with our sample holders and electrical setup. The wire-bonding process was carried out using a wedge–wedge wire bonder (WestBond manual bonder 7476E-79), employing 25 μm diameter aluminum wire.

During the course of this thesis, I was responsible for the maintenance of the wire bonder, which included training new students and researchers, purchasing and replacing wire, and performing regular maintenance procedures.

Hall Measurement Setup

The main setup used for electrical characterization is a home-built Hall effect measurement platform comprising the following components (see Fig. 5.3):

- A GMW5403 electromagnet capable of producing magnetic fields up to 2 T.

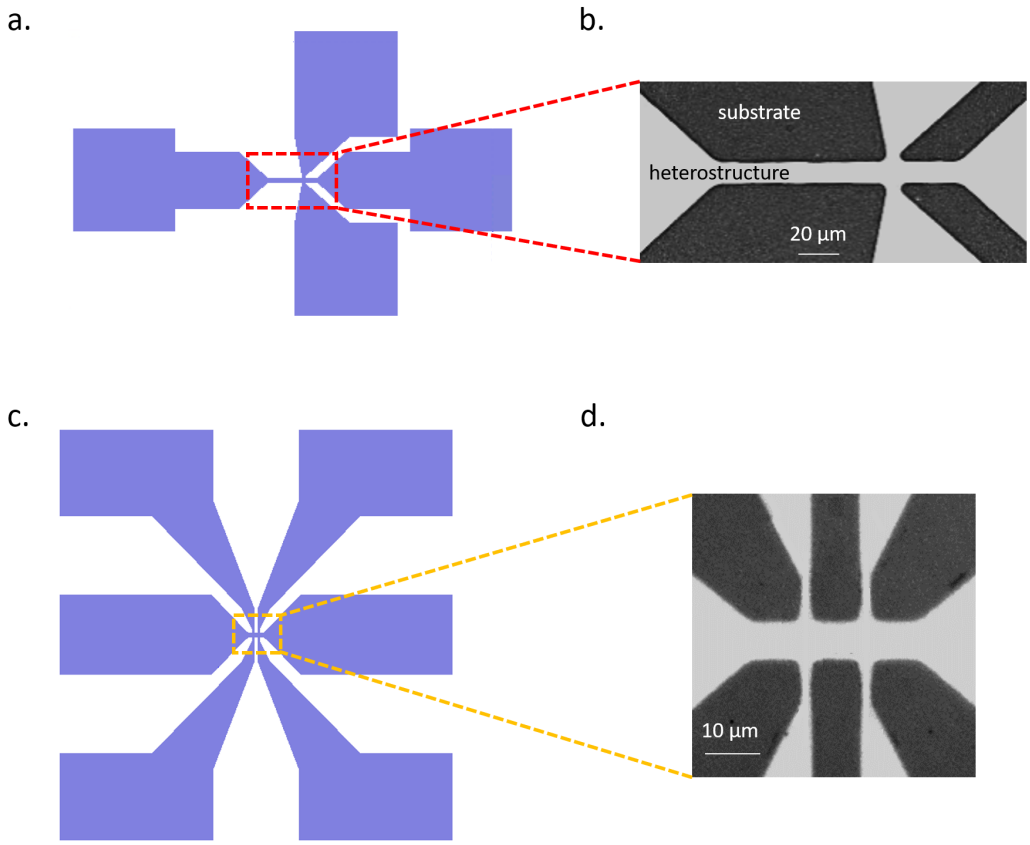

Figure 5.2: (a) CleWin design of the DW device for MOKE measurements. (b) Optical microscope image of the active region of the DW device. (c) Layout of a standard Hall bar for electrical transport measurements. (d) Optical image of a fabricated Hall bar showing current and voltage lines.

- A motorized rotation stage (Standa 8MR151) allowing field angle scans in the xy, yz, and zx planes with angular resolution of 0.075 degrees.
- A custom-designed PCB-compatible chip carrier, enabling quick swapping of devices between configurations (0°, 45°, 90°, 135° field orientation).
- A homemade switchbox allowing flexible routing of the voltage and current lines, optimized for dual orientation (0° and 90°) without requiring re-bonding.
- A Zurich Instruments MFLI lock-in amplifier (500 kHz bandwidth) used to perform low-noise voltage measurements at a reference frequency (normally $f = 1092$ Hz).

For most measurements, an AC current was injected into the device using the internal voltage source of the lock-in amplifier, or an external current source (Keithley 6221). For standard AHE and SMR measurements, currents on the order of 1 mA or lower were typically used to minimize Joule heating and avoid thermal effects.

First-harmonic signals (ω) were recorded to extract the Hall resistance, defined as $R_H = V_H/I$, where V_H is the measured Hall voltage and I is the excitation current.

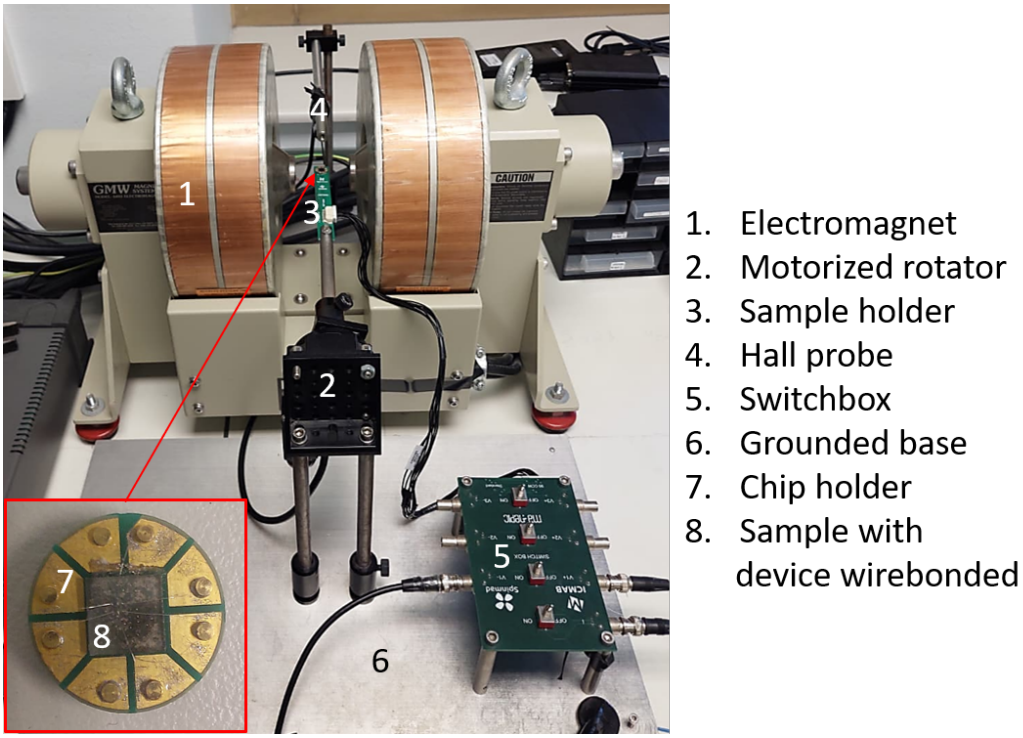

Figure 5.3: Photograph of the Hall setup with all the components described.

Measurement Configurations

Hall bar devices were characterized under the following conditions:

- **Anomalous Hall Effect:** OOP field scans (H_z) were performed at fixed temperature to extract R_{AHE}, coercivity H_c, and switching symmetry.
- **Spin Hall Magnetoresistance:** Longitudinal resistance R_{xx} and transverse R_{xy} were measured while sweeping the field direction IP and OOP.
- **Angle-Resolved Measurements:** The sample was rotated in controlled angular sweeps in the xy, yz, or zx planes to characterize the angular dependence of magnetoresistance and torque-related signals (not performed in the projects presented in this thesis).
- **Temperature-Dependent Studies:** For selected devices, low-temperature AHE and magnetoresistance measurements were conducted in a Physical Property Measurement System (PPMS) in the range 50-300 K, with field up to 9 T.

5.2 Rare-Earth Iron Garnets

As introduced throughout this thesis, the primary focus of this work is on REIGs, a family of insulating ferrimagnetic oxides. Their general chemical formula is $Re_3Fe_5O_{12}$, where Re represents a trivalent rare-earth ion such as yttrium (Y), terbium (Tb), or thulium (Tm). This chapter presents

the crystalline and magnetic properties of REIGs, concluding with a detailed description of the growth and characterization of TbIG, the specific REIG investigated in this thesis.

While REIGs exhibiting PMA have only recently gained prominence in the field of spintronics, their significance in magnetism dates back several decades. These materials were first introduced in the 1950s [211, 212]. In the following years, extensive investigations by Pauthenet, Gilleo, Geller, and Kittel significantly advanced the understanding of their crystal structure, stoichiometry, and magnetic interactions. This foundational work established the basis for their integration into magneto-optical technologies, most notably in magnetic bubble memory devices developed during the 1980s [213], where garnets demonstrated exceptional suitability.

In the context of spintronics, REIGs stand out due to their exceptional properties. They typically exhibit low Gilbert damping and long magnon diffusion lengths, which facilitate efficient spin current generation and nonlocal transport [214, 215, 216]. Moreover, their high electrical resistivity makes them ideal candidates for insulating spintronic platforms. REIGs also offer tunable magnetic characteristics, such as saturation magnetization and magnetocrystalline anisotropy, which can be engineered via chemical composition or strain [217, 218]. Their oxide nature imparts high robustness against thermal degradation, oxidation, and aging.

Recent advances have further elevated the technological relevance of REIGs. The demonstration of ultrathin REIG films with PMA [219, 220], along with the ability to manipulate magnetization via SOTs [25] and detect it through SMR [92], has paved the way for integrating these materials into practical spintronic devices. As a result, REIGs now represent a fertile ground for the development of robust, low-power, and efficient next-generation spintronic technologies [24].

5.2.1 Crystal Structure of REIGs

As stated before, REIGs have the general chemical formula $Re_3Fe_5O_{12}$ where Re is a trivalent rare-earth ion, and are ferrimagnetic oxides that crystallize in a highly symmetric cubic structure. This structure is fundamental to their magnetic behavior and suitability for spintronic applications.

The garnet unit cell is large, containing 160 atoms, and features a complex arrangement of oxygen anions and three distinct cation sites:

- Dodecahedral sites (c-sites), occupied by 24 rare-earth ions (Re^{3+}) with 8 Oxygen neighbors, which do not contribute significantly to the net magnetization in many cases (e.g., YIG).
- Octahedral sites (a-sites), occupied by 16 Fe^{3+} ions with 6 Oxygen neighbours
- Tetrahedral sites (d-sites), occupied by 24 Fe^{3+} ions with 4 Oxygen neighbours

A schematic representation of the REIG unit cell highlighting the c, a, and d sites is shown in Fig. 5.4.

5.2.2 Magnetic Properties of REIGs

The magnetic behavior of REIGs originates from superexchange interactions (see Chapter 2) between Fe^{3+} ions, mediated by oxygen anions. These ions occupy the octahedral (a) and tetrahedral (d) sublattices and are antiferromagnetically coupled. However, due to the unequal number of Fe^{3+} ions in the two sublattices, the system exhibits a nonzero net magnetic moment, resulting in ferrimagnetism.

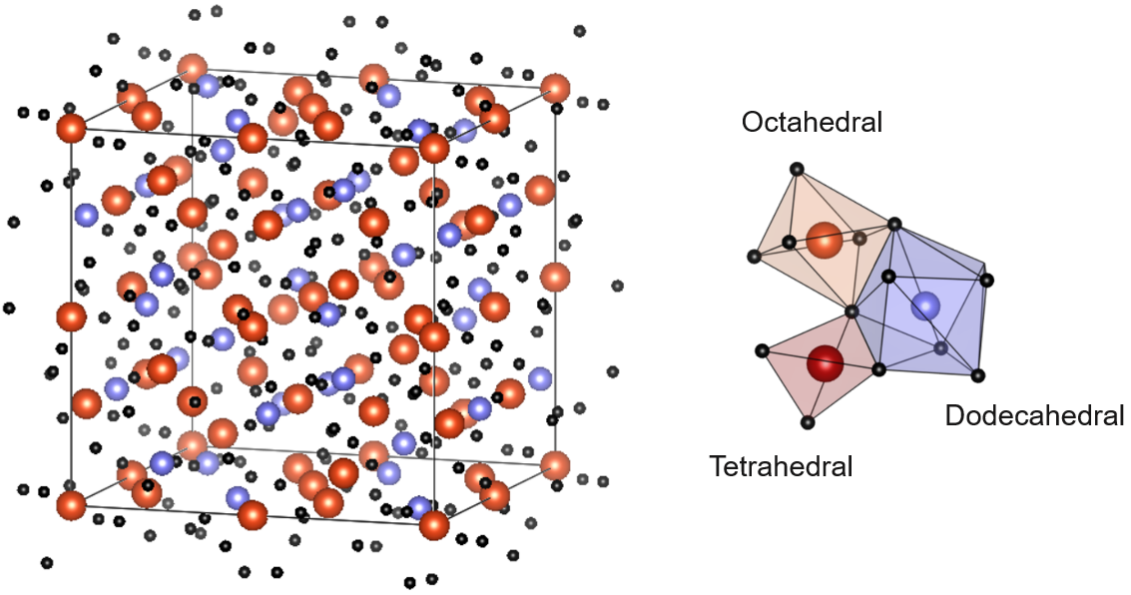

Figure 5.4: Crystal structure of a REIG visualized using VESTA software. Red/orange spheres represent Fe atoms, while blue spheres represent Re atoms. The three primary cation sites are indicated: dodecahedral (c), octahedral (a), and tetrahedral (d). Courtesy of S. Damerio.

Due to the structural complexity of the garnet unit cell and the diversity of magnetic interactions, the sublattice magnetizations are more accurately described within the framework of molecular field theory. In this model, each magnetic ion experiences an effective "molecular" field arising from its neighboring ions, capturing both intra- and inter-sublattice exchange couplings [221, 222, 223].

In garnets with non-magnetic rare-earth ions (e.g., yttrium in YIG), the net magnetization is given by [71]:

$$M_{\text{tot}} = M(\text{Fe}^{3+})_{\text{tetra}} - M(\text{Fe}^{3+})_{\text{octa}}, \tag{5.1}$$

where $M(\text{Fe}^{3+})_{\text{tetra}}$ and $M(\text{Fe}^{3+})_{\text{octa}}$ are the magnetic moments of the tetrahedral and octahedral Fe^{3+} sublattices, respectively. When the rare-earth ion Re^{3+} is magnetic (e.g., in TbIG or TmIG), it contributes to the total magnetization through coupling with the Fe^{3+} sublattices. The expression for the net magnetization becomes:

$$M_{\text{tot}} = M(\text{Fe}^{3+})_{\text{tetra}} - M(\text{Fe}^{3+})_{\text{octa}} - M(Re^{3+})_{\text{dodeca}}, \tag{5.2}$$

where $M(Re^{3+})_{\text{dodeca}}$ is the contribution from the rare-earth ions occupying the dodecahedral sites. This typically results in a reduced net magnetization compared to non-magnetic REIGs such as YIG.

Importantly, the exchange interaction between rare-earth ions (Re–Re) is much weaker than that involving Fe ions (Fe–Fe and Fe–Re), owing to the highly localized and shielded nature of the 4f electrons in rare-earth elements, which limits orbital overlap and magnetic coupling.

Due to the distinct temperature dependencies of the Fe and Re sublattice magnetizations, REIGs exhibit a nontrivial evolution of net magnetization as a function of temperature, as shown in Fig. 5.5. In particular, a specific temperature, known as the magnetic compensation temperature (T_{MC}), may

occur at which the opposing sublattice magnetizations cancel each other exactly, leading to zero net magnetization.

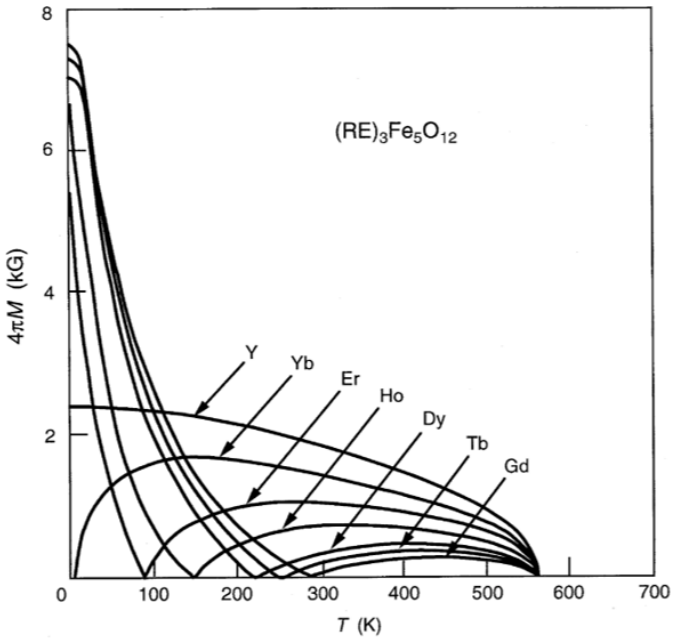

Figure 5.5: Temperature-dependent magnetization curves for several REIGs, showing how different rare-earth ions modify the magnetic compensation temperature and overall magnetization behavior. Taken from [221].

The value of T_{MC} depends on the specific rare-earth ion. For example, in GdIG or TbIG it may lie close to room temperature, while in YbIG or ErIG it occurs near 0 K. These compensation points are technologically relevant: at T_{MC}, the REIG behaves effectively as an antiferromagnet, eliminating stray fields and enabling applications in high-density magnetic memory. Moreover, it facilitates efficient SOT switching due to the vanishing net magnetization [224].

In addition to magnetic compensation, a second temperature can emerge, the angular momentum compensation temperature (T_{A}). At T_{A}, the net angular momentum of the sublattices cancels, even though the net magnetization may be nonzero. The difference between T_{MC} and T_{A} arises from the variation in the Landé g-factors among different ions occupying distinct crystallographic sites. The gyromagnetic ratio $\gamma = g\mu_B/\hbar$ links the magnetic moment to angular momentum. While Fe^{3+} has $g \approx 2$, similar to the free electron, rare-earth ions typically exhibit different g-values due to strong SOC and orbital contributions.

As a result, even when the sublattice magnetizations cancel at T_{MC}, their angular momenta may not, and vice versa. The angular momentum compensation point is associated with ultrafast magnetization dynamics, divergent domain wall mobility, and the emergence of ultrafast, nanoscale spin textures [62, 225, 226]. Since T_{A} is generally higher than T_{MC}, it opens an additional regime for tuning the dynamic response of ferrimagnetic systems.

Finally, the presence and exact values of T_{MC} and T_{A} are highly sensitive to multiple parameters, including cation distribution across sublattices, stoichiometry, film thickness, strain, and deposition method. Accurate control of these factors is essential for harnessing compensation effects in device

applications.

5.2.3 REIGs Thin Films with PMA

In this work, we deposit ultrathin films of REIGs (especially TbIG, see Section 5.2.4) using RF magnetron sputtering. The typical thickness of the studied films is below 10 nm, with the thickest sample reaching 50 nm and the thinnest nominally 3 nm. All the samples exhibit PMA, a key property for efficient spintronic devices. Achieving PMA in REIG thin films requires a careful balance of the various anisotropy contributions discussed in Chapter 2.

The total effective anisotropy energy K_{eff} of a REIG thin film grown epitaxially along the [111] direction (as in this work) can be expressed as [227, 220]:

$$K_{\text{eff}} = \frac{K_1}{12} - \frac{3}{2}\lambda_{111}\sigma_{[111]} + \frac{1}{2}\mu_0 M_s^2 + K_G, \tag{5.3}$$

where:

- K_1 is the first-order cubic magnetocrystalline anisotropy constant. The factor 1/12 accounts for the projection onto the [111] growth axis
- λ_{111} is the saturation magnetostriction coefficient along the [111] direction
- $\sigma_{[111]}$ is the uniaxial stress projected along the [111] direction, derived from the IP strain
- $\frac{1}{2}\mu_0 M_s^2$ represents the shape anisotropy energy, which always favors IP magnetization
- K_G is the growth-induced anisotropy, accounting for factors introduced during epitaxial growth, such as chemical segregation, defect formation, and non-stoichiometry.

To quantify the IP stress, we first compute the IP strain due to lattice mismatch:

$$\varepsilon_{\parallel} = \frac{a_{\text{sub}} - a_{\text{film}}}{a_{\text{film}}}, \tag{5.4}$$

and then convert strain to stress using elastic constants as [219]:

$$\sigma_{\parallel} = 6C_{44} \cdot \frac{C_{11} + 2C_{12}}{C_{11} + 2C_{12} + 4C_{44}} \cdot \varepsilon_{\parallel}. \tag{5.5}$$

This biaxial IP stress can be projected along the [111] axis to obtain the uniaxial stress $\sigma_{[111]}$ relevant to magnetoelastic coupling. This projection assumes elastically isotropic behavior and that the film is coherently strained.

The shape anisotropy term $\frac{1}{2}\mu_0 M_s^2$ contributes positively to the total anisotropy energy, thus opposing PMA by favoring IP magnetization. Consequently, to achieve PMA ($K_{\text{eff}} < 0$), the strain-induced magnetoelastic anisotropy must overcome this demagnetizing energy.

Thanks to the relatively large values of λ_{111} for many REIG compounds (e.g., TbIG with $\lambda_{111} \approx 12 \times 10^{-6}$), PMA can be obtained even for moderate compressive strain. This strain is controlled through careful choice of lattice-mismatched substrates. A wide variety of commercially available garnet substrates with tailored lattice parameters makes this approach highly versatile. Moreover, the ability to tune the strain anisotropy enables engineering of PMA across different thicknesses and compositions [228].

5.2.4 Sputtering Growth and Characterization of TbIG

In this work, the material of choice is TbIG, a REIG distinguished by its high magnetic compensation temperature, large positive magnetostriction coefficient λ, and relatively low saturation magnetization at room temperature. These properties make TbIG an excellent platform for investigating spintronic phenomena near compensation and for enabling room-temperature SOT applications with PMA.

REIGs explored in spintronics are commonly grown by pulsed laser deposition (PLD) [229, 230], which enables atomically smooth surfaces and high-quality epitaxial films. Magnetron sputtering has also been successfully employed to grow REIGs [231], with recent advancements showing that off-axis sputtering can further improve crystalline quality [232].

Although PLD remains the most established technique for achieving perfect epitaxy, in this work we adopt RF magnetron sputtering due to its greater technological relevance and flexibility for co-sputtering different materials simultaneously. Sputtering is more compatible with industry-scale fabrication processes, offers easier integration with standard CMOS platforms, and enables deposition over large-area wafers.

An additional advantage of RF sputtering is the ability to perform *in-situ* deposition of metallic overlayers immediately after garnet growth, without breaking vacuum. This is particularly important for spintronic devices, as the garnet/metal interface plays a crucial role in interfacial spin transport properties, such as spin mixing conductance, interfacial DMI, and spin pumping efficiency. Maintaining clean and abrupt interfaces is essential for maximizing these effects and achieving reproducible, high-performance spintronic behavior.

The first observation of PMA in TbIG was reported in 2008 by Kumar et al. [233], who demonstrated that a 250 nm-thick epitaxial TbIG film grown on a (110)-oriented $Gd_3Ga_5O_{12}$ (GGG) substrate using PLD exhibited OOP magnetization due to strain-induced anisotropy. Over the last decade, interest has shifted to ultrathin TbIG films (thickness < 10 nm), particularly those grown on GGG substrates with (111) or (001) orientations [51, 220, 234, 29, 235]. More recently, Li et al. [236] systematically studied how substrate-induced strain, using alternative garnet substrates such as NGG, YSGG, and GSGG, can be used to tune the compensation temperature and enhance PMA.

The sputtered growth method employed in this thesis builds upon the protocol optimized by our group, as reported by Damerio et al. [237], who first demonstrated the growth of TbIG thin films with robust PMA using RF sputtering. Their work enabled the fabrication of high-quality 20 nm films exhibiting clear magnetic anisotropy and epitaxial ordering. Building on this foundation, I extended the method to cover a broader range of thicknesses, achieving epitaxial growth and strong PMA in TbIG films ranging from 3 nm to 50 nm. All samples used in this thesis, regardless of thickness, exhibit consistent properties such as PMA, M_s, surface roughness, and crystalline quality, confirming the reliability and reproducibility of the growth process. Furthermore, these results demonstrate the scalability of the method and its potential for integration into future spintronic technologies and devices.

Sputtering Growth

The ultrathin TbIG films were grown from a stoichiometric ceramic target onto GGG(111) substrates by RF magnetron sputtering. Substrates were first cleaned in an ultrasonic bath (10 min each in

acetone and isopropanol), followed by in-situ low-power Ar plasma etching (30 W, 3 mTorr, 60 s) to remove surface contaminants and adsorbed gases.

The deposition was carried out at 800 °C in an Ar:O_2 atmosphere with a 30:2 ratio, at a total pressure of 3 mTorr and a target-to-substrate distance of 150 mm. The deposition rate was approximately 0.4 nm/min under an applied RF power of 150 W.

TbIG has a large positive saturation magnetostriction along the [111] direction ($\lambda_{111} = 12\times10^{-6}$) [238]. This means that compressive IP strain (i.e., when the substrate has a smaller lattice constant than the film) favors OOP magnetization. GGG has a lattice constant of $a_{\mathrm{GGG}} = 12.383$ Å, while TbIG has $a_{\mathrm{TbIG}} = 12.460$ Å [228]. The resulting IP compressive strain is:

$$\varepsilon_{\parallel} = \frac{a_{\mathrm{GGG}} - a_{\mathrm{TbIG}}}{a_{\mathrm{TbIG}}} = -0.62\%. \tag{5.6}$$

This strain, combined with the high λ_{111}, contributes significantly to the magnetoelastic anisotropy and is one of the key factors enabling PMA in these sputtered TbIG films.

As a reference, we report here the characterization of the 20 nm-thick TbIG film grown using the optimized sputtering procedure described earlier.

Structural Characterization

The crystal structure was analyzed using X-ray diffraction (XRD) in a Bragg–Brentano geometry with Cu K-α radiation ($\lambda = 1.5406$ Å). A $2\theta - \omega$ scan was collected around the (444) reflections of both the film and the GGG substrate, which appear at approximately 51°. The resulting diffraction pattern is shown in Fig. 5.6a.

The XRD pattern shows a sharp TbIG (444) Bragg peak, confirming high-quality garnet growth with no secondary phases. This indicates that the high-temperature RF sputtering conditions effectively stabilize the garnet structure.

The TbIG (444) peak of the film appears at a lower angle than the bulk reference position ($d_{444}^{\mathrm{bulk}} = 1.7984$ Å^{-1}, shown as a vertical black line in Fig. 5.6a). This shift indicates OOP lattice expansion caused by compressive IP strain. From this, the OOP spacing is calculated as $d_{444} = 1.8411$ Å^{-1}, corresponding to an OOP strain:

$$\varepsilon_{444} = \frac{d_{444} - d_{444}^{\mathrm{bulk}}}{d_{444}^{\mathrm{bulk}}} = \frac{1.8411 - 1.7984}{1.7984} \approx 2.37\%. \tag{5.7}$$

Furthermore, the full width at half maximum (FWHM) of the TbIG (444) peak is 0.336°, indicating a highly coherent crystalline film with low defect density and good epitaxial quality.

To further confirm the epitaxial strain state, a reciprocal space map was acquired around the asymmetric (642) reflection, as shown in Fig. 5.6b. The vertical alignment of the film and substrate peaks confirms that the film is fully strained to the substrate. Since the IP lattice constant of the film matches that of the GGG substrate, the IP strain can be estimated using:

$$\varepsilon_{\parallel} = \frac{d_{1\bar{1}0} - d_{\mathrm{bulk}}}{d_{\mathrm{bulk}}}, \tag{5.8}$$

where $d_{1\bar{1}0}$ is the IP spacing measured from the substrate, and d_{bulk} is the relaxed value for bulk TbIG. This gives a compressive IP strain of approximately -0.419%. As expected, this compressive strain leads to elongation of the unit cell in the OOP direction, resulting in a shift of the film peak toward lower q_z values, as seen in the XRD image.

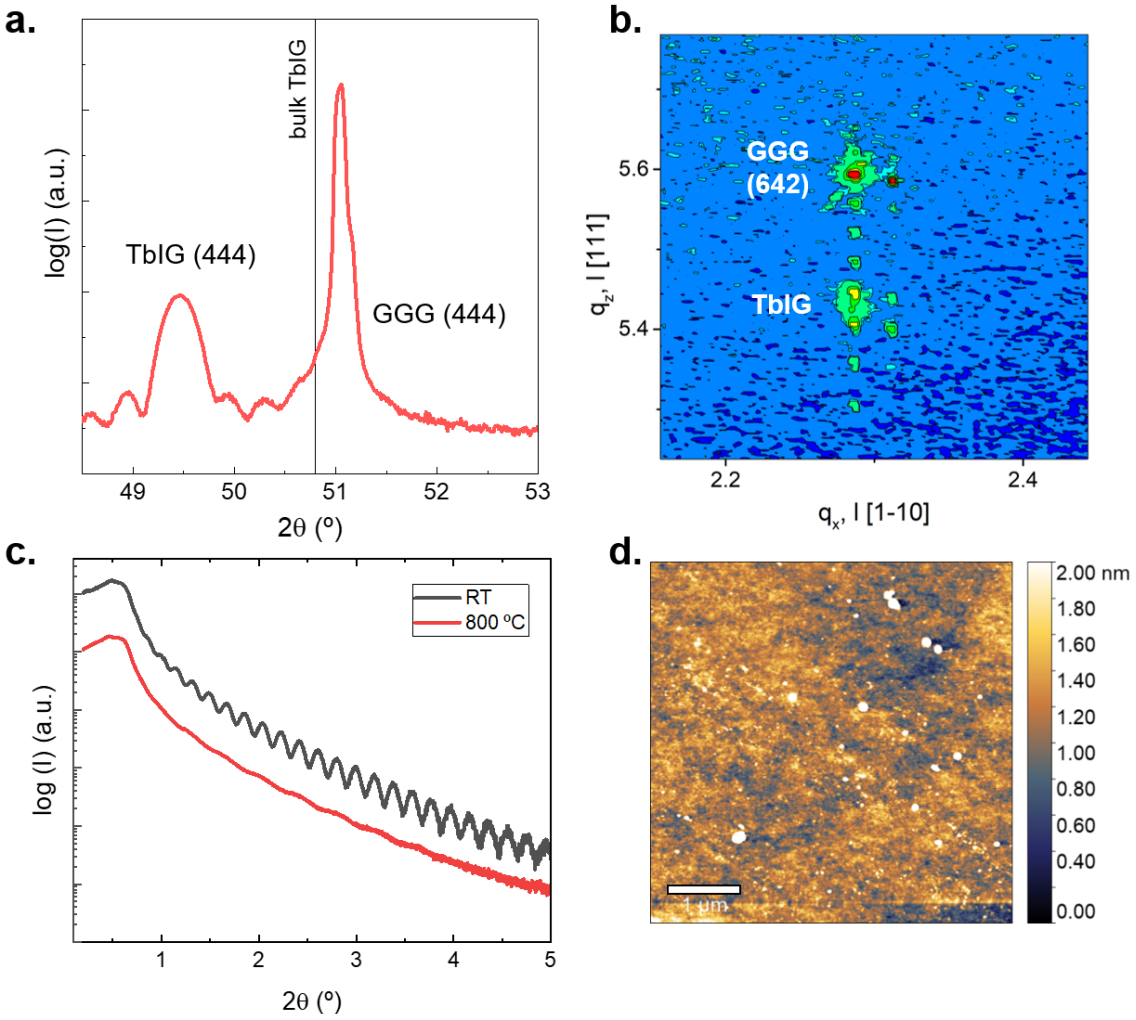

Figure 5.6: (a) $2\theta - \omega$ scan around the (444) reflections of GGG and TbIG. The TbIG peak appears at lower angles than the bulk value (black line). (b) Reciprocal space map around the asymmetric (642) reflection, confirming that the film is fully strained to the substrate. (c) XRR scans of a high-temperature-grown sample (red) and a room-temperature-grown sample (black), used to calibrate the deposition rate and determine the precise thickness. (d) AFM image of the TbIG surface, showing a flat morphology with RMS roughness of 120 pm. Courtesy of S. Damerio.

The film thickness was determined by X-ray reflectivity (XRR), shown in Fig. 5.6c. The high-temperature-grown sample (black curve) exhibits very weak Kiessig fringes due to its epitaxy and extremely smooth interface with GGG. To calibrate the deposition rate and extract precise thickness, a RT reference sample was also analyzed (red curve), which shows pronounced fringes suitable for quantitative fitting.

The surface morphology was characterized by atomic force microscopy (AFM) in dynamic tapping mode. As shown in Fig. 5.6d, the film exhibits a flat surface with a root-mean-square (RMS) roughness of approximately 120 pm, confirming the high surface quality essential for spintronic interface engineering.

These measurements confirm the high quality of TbIG growth achieved via high-temperature RF sputtering. A detailed Scanning Transmission Electron Microscopy (STEM) and Electron Energy Loss Spectroscopy (EELS) analysis, presented in Chapter 7 and 8, further supports the presence of epitaxial ordering, strain in the TbIG layer, and sharp interfaces.

Magnetic Characterization

The magnetic properties of the continuous TbIG films were characterized using both optical and magnetometry techniques. The results presented here correspond to the same GGG/TbIG (20 nm) sample described previously.

First, magnetic hysteresis and anisotropy were investigated using a home-built MOKE setup in polar geometry, sensitive to the OOP component of the magnetization (for more details on the MOKE setup, see Chapter 6). Fig. 5.7a shows the hysteresis loop obtained by sweeping an OOP magnetic field. The loop is perfectly square with 100% remanence and a coercive field of $H_c = 500$ Oe, indicating strong PMA.

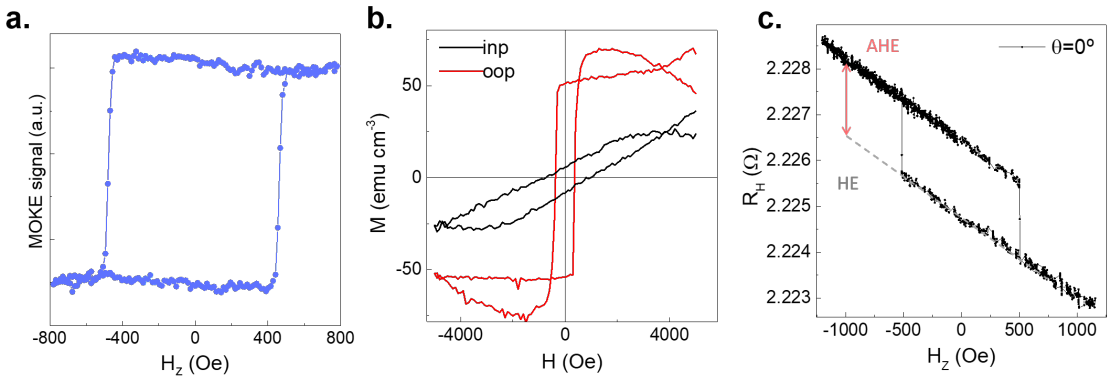

Figure 5.7: (a) MOKE hysteresis loop showing a square shape with 100% remanence and high coercivity. (b) SQUID M–H loops for IP (black) and OOP (red) geometries, confirming the PMA of TbIG. (c) R_{AHE} as a function of OOP magnetic field H_z, showing contributions from both AHE and HE of the TbIG/Pt bilayer. Courtesy of S. Damerio.

Room temperature magnetization vs. field (M–H) loops were also measured using a superconducting quantum interference device (SQUID) magnetometer. Fig. 5.7b shows representative IP and OOP measurements. The OOP loop displays sharp switching and a low saturation magnetization of approximately 50 emu/cm^3, consistent with the film being near its magnetic compensation temperature T_{MC}. The small non-magnetic bumps are likely due to background signals from the substrate. In contrast, the IP magnetization only reaches 20 emu/cm^3 under the same field range, reinforcing the presence of strong PMA. The M–H loops are particularly challenging to analyze due to the low saturation magnetization of our sample, over an order of magnitude smaller than that of metallic ferromagnets, and the significant paramagnetic contribution from the GGG substrate. Nevertheless, a comparison between the IP and OOP loops clearly reveals the PMA character of TbIG. The hysteresis curve is well-defined, allowing us to extract a reasonably accurate value for the saturation magnetization.

To probe interfacial spin transport, Pt Hall bar devices were fabricated on continuous TbIG

films. Electrical measurements were conducted at room temperature in the Hall setup described in Section 5.1.3. A sinusoidal current of 0.5 mA (rms) at $\omega = 1092$ Hz was injected through the Pt layer. The first harmonic Hall voltage V_H was recorded and the Hall resistance calculated as $R_H = V_H/I$.

AHE measurements were used to evaluate the spin transport properties of the Pt/TbIG interface. In these bilayers, the AHE primarily originates from the imaginary component of the spin mixing conductance and manifests via SMR, as discussed in Chapter 2. Fig. 5.7c shows the AHE resistance R_{AHE} measured as a function of OOP magnetic field H_z (i.e., $\theta = 0°$). The square hysteresis loop confirms PMA, and the coercivity matches that measured by MOKE, indicating no change of magnetic properties during lithography or Pt deposition. The AHE amplitude at room temperature is $R_{\mathrm{AHE}} = 0.8$ mΩ, in good agreement with prior reports on PLD-grown TbIG/Pt films [220, 235].

The temperature dependence of the magnetization of TbIG was investigated using a PPMS in the 50–300 K range under a swept magnetic field up to 10 kOe. Fig. 5.8a shows the temperature-dependent coercivity for a TbIG film grown at 750 °C. A similar trend was observed for a sample grown at 800 °C, with both exhibiting a magnetic compensation temperature $T_{\mathrm{M}} \approx 190$ K, significantly lower than the bulk value of 248 K.

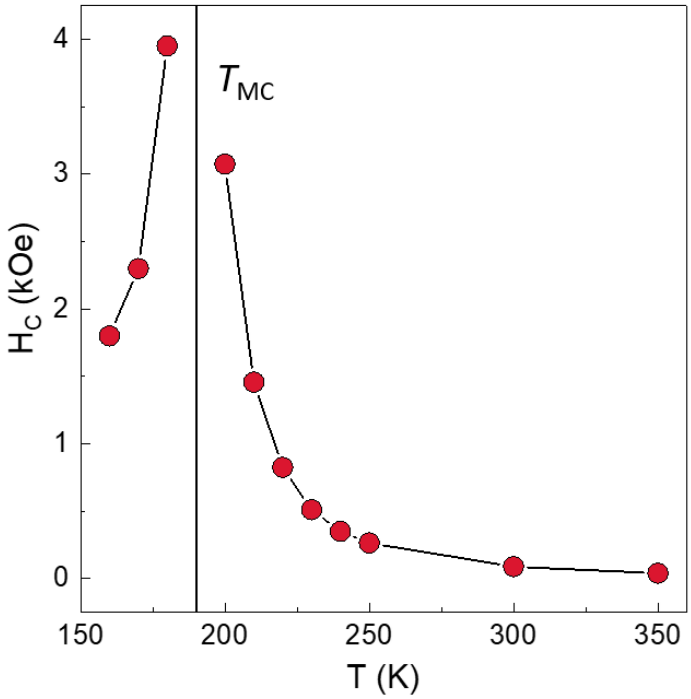

Figure 5.8: Temperature dependence of the coercivity of TbIG measured with PPMS, identifying the compensation temperature $T_{\mathrm{MC}} = 190$ K. Courtesy of S. Damerio.

5.3 Metallic Thin Films

While the primary focus of this thesis is on insulating REIG thin films, metallic multilayers play a crucial supporting role in enabling spintronic functionality. These layers, typically composed of

platinum (Pt), cobalt (Co), tungsten (W), titanium (Ti), and copper (Cu), were deposited via DC sputtering at room temperature under low-power conditions (typically 50 W), and serve as essential components in heterostructures designed for spin transport studies.

The integration of metallic layers is motivated by their ability to generate and detect spin currents through mechanisms such as the SHE, SOT, and SMR. In particular, Pt is widely used due to its strong SOC and high spin Hall angle, making it an effective spin current source when interfaced with garnet films like TbIG. For example, Pt overlayers were deposited directly onto TbIG films to form Hall bar structures, enabling electrical probing of magnetization via the AHE. These measurements provided insight into interfacial spin transport and confirmed the presence of PMA in the garnet layer.

Although detailed structural and magnetic characterization of the metallic layers was not pursued in this work, their inclusion was essential for fabricating functional spintronic devices. Based on STEM analysis presented in Chapters 7 and 8, we expect the metallic layers to grow polycrystalline under room-temperature sputtering conditions.

To quickly and reliably assess the quality of the metallic thin films, we primarily rely on resistivity measurements and comparisons with literature values. For Pt, the resistivity strongly depends on thickness in ultrathin (< 1 nm) films (see Chapter 8), but for thicker (> 2 nm) films, we measure a resistivity of $\rho_{\mathrm{Pt}} \approx 26\ \mu\Omega \cdot \mathrm{cm}$, consistent with reported values [122].

W films present a particular challenge, as sputtered W can crystallize in either the α- or β-phase, or as a mixed phase, each exhibiting significantly different physical properties. Based on the efficient SOT switching observed in our devices (see Chapter 7), we expect our W films to be predominantly in the β-phase, in agreement with previous studies [239]. The α-phase has a relatively low resistivity ($\rho_{\alpha\text{-W}} = 5.3\ \mu\Omega \cdot \mathrm{cm}$), while the β-phase shows much higher values ($\rho_{\beta\text{-W}} = 150\text{–}300\ \mu\Omega \cdot \mathrm{cm}$) [240]. Although direct resistivity measurements of W were not feasible due to device geometry, we compared two-point resistances of TbIG/W and TbIG/Pt devices with identical geometries. The W-based devices exhibited approximately five times higher resistance than the Pt-based ones, suggesting a W resistivity of $\rho_{\mathrm{W}} \approx 130\ \mu\Omega \cdot \mathrm{cm}$. This value is consistent with the β-phase and significantly higher than the α-phase, supporting our conclusion.

In Chapter 8, we also estimate the resistivity of Ti layers for different thicknesses, with "bulk-like" Ti showing $\rho_{\mathrm{Ti}} \approx 100\ \mu\Omega \cdot \mathrm{cm}$, again in agreement with sputtered thin films reported in the literature [241].

The metallic multilayers were grown either on standard $\mathrm{Si/SiO_x}$ substrates or directly on garnet films, depending on the device architecture. While optimization of metallic film properties was beyond the scope of this thesis, their role in spintronic measurements and device integration is fundamental.

Chapter 6

Design and Implementation of a Custom MOKE Microscope

Contents

My first challenge as a PhD candidate was to design and build a custom MOKE setup. I devoted much of my first year to this task, purchasing components, and then designing, assembling, and optimizing the system. The first magnetic signal detected with this setup, measured on an old Co/Pt Hall bar after months of persistent effort, marked not only a key milestone in my thesis but also a deeply meaningful moment in my personal journey.

This MOKE setup became the primary measurement tool for this work, with most of the results presented in this thesis relying on it. Over time, it has also become a core instrument in the laboratory, routinely used by other PhD students and postdoctoral researchers, and contributing to several recently published high-impact papers. The development of this setup closely mirrored the evolution of my thesis: I never truly stopped working on it. Over the years, I continuously refined it, implementing automated measurement programs and introducing physical upgrades such as motorized stages, a black box, cryostat integration, and the addition of various complementary instruments.

This chapter is divided into two sections. The first introduces the fundamental principles of the Kerr effect and the operating principles of the setup. The second provides a step-by-step account of the construction process, explaining the design choices made along the way. The abundance of

practical details is intended as a guide for anyone who will work with this setup in the future, offering both procedural instructions and insight into the reasoning behind them.

6.1 Theoretical Introduction to Kerr Effect

The discovery of the magneto-optic effect began with early efforts to find links between light and electric fields. Initial studies were unsuccessful until 1845, when Michael Faraday applied a magnetic field instead of an electric one and observed that it could rotate the polarization of light passing through a material, revealing a fundamental interaction between light and magnetism [242]. This breakthrough was further advanced in 1877 by *Rev.* John Kerr, who discovered that light reflecting off a magnetized surface experiences a change in polarization. This phenomenon, now known as the magneto-optic Kerr effect, is described in his seminal works [243, 244]. The MOKE technique has since become a straightforward yet powerful tool for studying magnetic properties, particularly in thin films and it plays a crucial role in areas such as data storage technology. When awarded the Royal Medal in 1898, Kerr described its apparatus as *"Simple it may be, but not ineffectual; rude, but not crude."* [245]. This statement captures the technique's simplicity and effectiveness, which continue to make it indispensable in modern magnetism and spintronics research [246, 247, 248].

In summary, when linearly polarized light strikes the surface of a magnetized sample, the reflected beam acquires an additional polarization component. As a result, it becomes elliptically polarized, with its principal axes (a, b) rotated by an angle proportional to the direction and intensity of the magnetization [245, 249, 250, 251, 252, 253]. The complex Kerr angle, Φ_K, can then be defined as:

$$\Phi_K = \theta_K + i\xi_K, \tag{6.1}$$

where θ_K represents the Kerr rotation, and ξ_K corresponds to the Kerr ellipticity. Together, these parameters fully characterize the reflection of a linearly polarized beam from a magnetic surface [254].

6.1.1 Macroscopic Description of Kerr Effect

To describe magneto-optic effects such as the Kerr and Faraday effects, we first need to establish the basics of optical phenomena, beginning with the wave equation. This discussion is adapted from the book *Magnetic Microscopy of Layered Structures* by W. Kuch, R. Schäfer, P. Fischer, and F. U. Hillebrecht [254].

6.1.1.1 Wave Equation

Light, as an electromagnetic wave, can be described starting from Maxwell's equations, which relate the electric and magnetic fields:

$$\begin{aligned} \nabla \cdot \boldsymbol{D} &= \rho, \\ \nabla \cdot \boldsymbol{B} &= 0, \\ \nabla \times \boldsymbol{E} &= -\dot{\boldsymbol{B}}, \\ \nabla \times \boldsymbol{H} &= \boldsymbol{j} + \dot{\boldsymbol{D}}, \end{aligned} \tag{6.2}$$

where $\boldsymbol{D}$ is the electric displacement field, $\boldsymbol{B}$ the magnetic flux density, $\boldsymbol{E}$ the electric field vector, and $\dot{\boldsymbol{B}}$ and $\dot{\boldsymbol{D}}$ the time derivatives of $\boldsymbol{B}$ and $\boldsymbol{D}$, respectively. The quantities ρ and $\boldsymbol{j}$ represent the electric charge and current densities, which act as sources of the electromagnetic field.

The electric displacement field $\boldsymbol{D}$ and the electric field $\boldsymbol{E}$ are connected via:

$$\boldsymbol{D} \equiv \varepsilon_0 \boldsymbol{\varepsilon}\, \boldsymbol{E} \equiv \varepsilon_0 \boldsymbol{E} + \boldsymbol{P}, \tag{6.3}$$

where $\boldsymbol{P}$ is the polarization density, $\boldsymbol{\varepsilon}$ the (generally tensorial) permittivity, and ε_0 the vacuum permittivity. Similarly, the magnetic flux density $\boldsymbol{B}$ and the magnetic field $\boldsymbol{H}$ are related through:

$$\boldsymbol{B} \equiv \mu_0 \boldsymbol{\mu}\, \boldsymbol{H} \equiv \mu_0 (\boldsymbol{H} + \boldsymbol{M}), \tag{6.4}$$

where $\boldsymbol{M}$ is the magnetization vector, $\boldsymbol{\mu}$ the permeability tensor, and μ_0 the vacuum permeability. In the optical and near-infrared frequency ranges, $\boldsymbol{\mu}$ is often approximated as unity because spins cannot follow the rapidly oscillating magnetic field of light. In contrast, $\boldsymbol{\varepsilon}$ is strongly frequency-dependent, and thus incorporates absorption, dispersion, and magneto-optical effects.

Starting from Maxwell's equations and incorporating Ohm's law:

$$\boldsymbol{j} = \boldsymbol{\sigma} \boldsymbol{E}, \tag{6.5}$$

which connects the current density to the electric field via the conductivity tensor $\boldsymbol{\sigma}$, we can derive a general wave equation for the electric field. From Maxwell's curl equations, we write:

$$\begin{aligned} \nabla \times (\nabla \times \boldsymbol{E}) &= \nabla \times (-\dot{\boldsymbol{B}}) = -\mu_0 \boldsymbol{\mu} (\nabla \times \dot{\boldsymbol{H}}) \\ &= -\mu_0 \boldsymbol{\mu} \frac{\partial}{\partial t} (\boldsymbol{j} + \dot{\boldsymbol{D}}) = -\mu_0 \boldsymbol{\mu} \left(\boldsymbol{\sigma} \frac{\partial \boldsymbol{E}}{\partial t} + \varepsilon_0 \boldsymbol{\varepsilon} \frac{\partial^2 \boldsymbol{E}}{\partial t^2} \right). \end{aligned} \tag{6.6}$$

In non-conductive (dielectric) media, the term proportional to the permittivity $\boldsymbol{\varepsilon}$ dominates in the wave equation. This enables electromagnetic waves to propagate through the material with minimal attenuation, as the lack of free charges prevents significant energy dissipation. In contrast, in conductive media, the term involving the electrical conductivity $\boldsymbol{\sigma}$ becomes dominant. This leads to the generation of conduction currents, which absorb and dissipate the energy of the electromagnetic wave, resulting in attenuation and hindering efficient wave propagation.

Rewriting Eq. 6.6 yields:

$$\nabla (\nabla \cdot \boldsymbol{E}) - \nabla^2 \boldsymbol{E} + \mu_0 \boldsymbol{\mu} \left(\boldsymbol{\sigma} \frac{\partial \boldsymbol{E}}{\partial t} + \varepsilon_0 \boldsymbol{\varepsilon} \frac{\partial^2 \boldsymbol{E}}{\partial t^2} \right) = 0, \tag{6.7}$$

where we can assume the solution to be a plane wave which is harmonic in both time t and position $\mathbf{r}$:

$$\mathbf{E} = E^0 e^{i(\mathbf{k} \cdot \mathbf{r} - \omega t)}. \tag{6.8}$$

Here $\mathbf{k}$ is the wave vector, ω is the angular frequency, and E^0 the the amplitude of the electric field. The wave number $|\mathbf{k}|$ relates to the refractive index n by:

$$|\mathbf{k}| = n k_0, \quad \text{with} \qquad k_0 = \frac{\omega}{c_0} = \frac{2\pi}{\lambda_0}, \tag{6.9}$$

with k_0 and λ_0 representing the wave propagation number and wavelength in vacuum and c_0 is the speed of light in a vacuum, defined as:

$$c_0 = \frac{1}{\sqrt{\varepsilon_0 \mu_0}}. \tag{6.10}$$

In any material, the wave propagation number becomes $|\mathbf{k}| = \frac{\omega}{v}$, defining the speed of light in the medium as:

$$v = \frac{1}{n} c_0, \tag{6.11}$$

implying an inverse proportionality between wave velocity and refraction index.

The Maxwell's equations for a plane wave can be simplified using the following algebraic relations:

$$\begin{aligned} \text{Divergence:} \quad & \nabla\cdot \rightarrow i\mathbf{k}\cdot, \\ \text{Curl:} \quad & \nabla\times \rightarrow i\mathbf{k}\times, \\ \text{Time Derivative:} \quad & \frac{\partial}{\partial t} \rightarrow -i\omega. \end{aligned} \tag{6.12}$$

Substituting these into Maxwell's equations gives the following system of algebraic amplitude equations:

$$\begin{aligned} \mathbf{k}\cdot\mathbf{D} &= -i\rho \\ \mathbf{k}\cdot\mathbf{B} &= 0 \\ \mathbf{k}\times\mathbf{E} &= \omega\mathbf{B} \\ \mathbf{k}\times\mathbf{H} = -i\mathbf{j} - \omega\mathbf{D} &= -\omega\varepsilon_0\left(\boldsymbol{\varepsilon} + i\frac{\boldsymbol{\sigma}}{\varepsilon_0\omega}\right)\mathbf{E}. \end{aligned} \tag{6.13}$$

Introducing the effective complex permittivity:

$$\tilde{\boldsymbol{\varepsilon}} = \boldsymbol{\varepsilon} + i\frac{\boldsymbol{\sigma}}{\varepsilon_0\omega}, \tag{6.14}$$

we rewrite the wave propagation vector as:

$$\tilde{\mathbf{k}} = \mathbf{k}' + i\mathbf{k}'', \tag{6.15}$$

where $\mathbf{k}'$ and $\mathbf{k}''$ are real vectors. Using these algebraic relationships, the generalized wave equation (Eq. 6.7) can be expressed as:

$$(\tilde{\mathbf{k}}\cdot\mathbf{E})\tilde{\mathbf{k}} - \tilde{\mathbf{k}}^2\mathbf{E} + \mu_0\varepsilon_0\boldsymbol{\mu}\omega^2\tilde{\boldsymbol{\varepsilon}}\mathbf{E} = 0, \tag{6.16}$$

where $\tilde{\mathbf{k}}^2 = \tilde{\mathbf{k}}\cdot\tilde{\mathbf{k}}$. Finally, assuming $\mu = 1$, and introducing the complex refractive index $\tilde{n}$:

$$\tilde{n} = |\tilde{\mathbf{k}}|/k_0 = \sqrt{\frac{\tilde{\mathbf{k}}\cdot\tilde{\mathbf{k}}}{k_0^2}}, \tag{6.17}$$

we can rewrite Eq. 6.16 as a system of three linear equations for the three vector components E_i of the **E**-field:

$$\frac{\tilde{k}_i(\tilde{\mathbf{k}}\cdot\mathbf{E})}{k_0^2} - \tilde{n}^2 E_i + \sum_{j=1}^{3}\tilde{\varepsilon}_{ij}E_j = 0. \tag{6.18}$$

The system of linear equations (6.18) has non-trivial solutions for E when the determinant of the coefficient matrix vanishes. These solutions are known as eigenmodes, and describe the propagation of light waves in the medium. This gives rise to a characteristic equation that relates the components k_i of the wave vector $\mathbf{k}$ to the elements of the dielectric tensor. Once the values of k_i, representing the allowed propagation directions, are determined, the corresponding electric field amplitudes of the propagating waves can be obtained as solutions to equation (6.18).

6.1.1.2 Polarized Light and Jones Vectors

Before discussing the solutions of (6.18), it is useful to establish a formalism to describe polarized light. Light is described as a transverse electromagnetic wave characterized by an electric field **E** and a magnetic field **H**, which are perpendicular to each other and to the direction of wave propagation, represented by **k**. The electric field interacts strongly with matter and is conventionally used to describe the polarization of light. Assuming propagation in the $\hat{z}$-direction, the **E**-vector lies in the xy-plane and can be expressed using the components E_x and E_y as:

$$E_j(z,t) = \mathrm{Re}\left(e_j E_j^0 \exp[i(k_z z - \omega t)]\right), \quad j = \{x, y\}, \tag{6.19}$$

where $E_j^0 = E_j^{\max} \exp[i\delta_j]$ represents the amplitude and phase retardation δ_j of the respective component.

The **E**-vector describes an elliptic trajectory over time, forming a polarization ellipse in the xy-plane. This ellipse is fully characterized by:

- The ratio between the maximal values of the electric field in $\hat{y}$- and $\hat{x}$-directions, expressed by $\tan\Omega = \frac{|E_y^{max}|}{|E_x^{max}|}$.
- The phase shift δ, defined as the phase difference between the $\hat{x}$ and $\hat{y}$ components: $\delta = \delta_y - \delta_x$.
- The amplitude A, which defines the "size" of the elliptical vibration: $A = \sqrt{a^2 + b^2}$.
- The azimuth θ, which is the angle between the major axis of the ellipse and the $\hat{x}$-direction.
- The ellipticity ξ, which is the ratio of the minor to major axes of the ellipse, defined as $\tan\xi = b/a$.
- The handedness, determined using the right- or left-hand rule relative to the wave vector **k**.

These quantities are illustrated in Fig. 6.1, where two linearly polarized partial waves, vibrating along the $\hat{x}$- and $\hat{y}$-directions and shifted in phase, combine to generate an elliptically polarized wave.

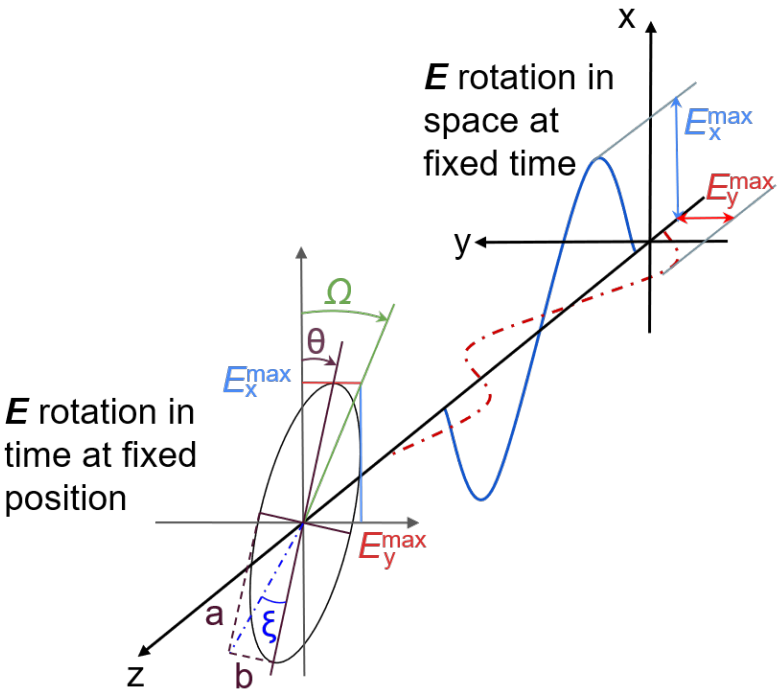

Figure 6.1: Visualization of right-handed elliptically polarized light generated by the superposition of two phase-shifted partial waves polarized in the (x, z)- and (y, z)-planes. The plot shows the spatial and temporal evolution of the electric field vector $\mathbf{E}$. The polarization ellipse displayed has a negative azimuth θ and a positive ellipticity ξ, following the conventional definition in optics. Adapted from [254].

Special polarization states include linear polarization, where the components are in phase ($\delta = m\pi$) and the ellipse degenerates into a straight line, and circular polarization, when the amplitudes of E_x and E_y are equal, with a phase shift of $\delta = \pm\pi/2$, resulting in a circular trajectory.

An efficient way to describe the polarization state of the light is through the Jones formalism [255], where the electric field vector is expressed by the Jones vector:

$$\mathbf{J} = \begin{pmatrix} E_x \\ E_y \end{pmatrix} = \begin{pmatrix} |E_x| e^{i\delta_x} \\ |E_y| e^{i\delta_y} \end{pmatrix}, \tag{6.20}$$

where the spatial and temporal phase is omitted since it is common for both components. Using this formalism, the normalized Jones vector for a linearly polarized wave with the electric field oscillating along a given specific direction is represented as:

$$\mathbf{J_{lin}} = \begin{pmatrix} \cos\alpha_{\mathrm{pol}} \\ \sin\alpha_{\mathrm{pol}} \end{pmatrix}, \tag{6.21}$$

where α_{pol} is the azimuth angle of the $\mathbf{E}$ vector with respect to the $\hat{x}$-axis. From this, the particular cases of waves polarized along the $\hat{x}$ or $\hat{y}$ axes can be described as:

$$\mathbf{J_x} = \begin{pmatrix} 1 \\ 0 \end{pmatrix} \quad \text{and} \quad \mathbf{J_y} = \begin{pmatrix} 0 \\ 1 \end{pmatrix}. \tag{6.22}$$

Finally, the general expression for elliptic polarization can be derived from eq. (6.20) as:

$$\mathbf{J}_{\text{elp}} = E_x^{\max} e^{i\delta_x} \begin{pmatrix} 1 \\ \frac{E_y^{\max}}{E_x^{\max}} e^{i(\delta_y - \delta_x)} \end{pmatrix} = E_x^{\max} e^{i\delta_x} \begin{pmatrix} 1 \\ \frac{\sin\Omega}{\cos\Omega} e^{i\delta} \end{pmatrix} = \begin{pmatrix} \cos\Omega \\ \sin\Omega e^{i\delta} \end{pmatrix}. \tag{6.23}$$

From this, recalling the conditions stated earlier, we can derive the normalized Jones vector for right- and left-circularly polarized light as:

$$\mathbf{J}_R = \frac{1}{\sqrt{2}} \begin{pmatrix} 1 \\ -i \end{pmatrix} = \frac{1}{\sqrt{2}} (\mathbf{J}_x - i\mathbf{J}_y) \tag{6.24}$$

$$\mathbf{J}_L = \frac{1}{\sqrt{2}} \begin{pmatrix} 1 \\ i \end{pmatrix} = \frac{1}{\sqrt{2}} (\mathbf{J}_x + i\mathbf{J}_y), \tag{6.25}$$

where we rely on the fact that $\mathbf{J}_x$ and $\mathbf{J}_y$ are normalized and orthogonal, allowing their use as a new basis. This shows that circularly polarized light is a superposition of two linearly polarized waves along $\hat{x}$ and $\hat{y}$ with equal amplitudes and a phase shift of $\pm\frac{\pi}{2}$.

6.1.1.3 The Dielectric Permittivity Tensor

The dielectric permittivity tensor $\boldsymbol{\varepsilon}$ relates the electric field vector $\mathbf{E}$ of incident light to the induced dielectric displacement vector $\mathbf{D}$ in a material, as expressed in eq. (6.3). In non-magnetic materials, $\boldsymbol{\varepsilon}$ can be decomposed as follows:

$$\boldsymbol{\varepsilon} = \boldsymbol{\varepsilon_0} + \boldsymbol{\varepsilon}_{\text{br}} + \boldsymbol{\varepsilon}_{\text{oa}}, \quad \text{with} \quad \boldsymbol{\varepsilon_0} = \begin{pmatrix} \varepsilon_{\text{iso}} & 0 & 0 \\ 0 & \varepsilon_{\text{iso}} & 0 \\ 0 & 0 & \varepsilon_{\text{iso}} \end{pmatrix}. \tag{6.26}$$

Here, $\boldsymbol{\varepsilon_0}$ is the isotropic permittivity with ε_{iso} being the isotropic dielectric constant, $\boldsymbol{\varepsilon}_{\text{br}}$ describes crystalline birefringence and $\boldsymbol{\varepsilon}_{\text{oa}}$ accounts for optical activity, including effects such as rotation of the polarization plane. When $\boldsymbol{\varepsilon_0}$ is the only contributor, $\mathbf{D}$ aligns with $\mathbf{E}$, resulting in no rotation of the polarization plane. However, effects like polarization rotation or ellipticity require non-zero off-diagonal elements in $\boldsymbol{\varepsilon}$, arising from $\boldsymbol{\varepsilon}_{\text{oa}}$ or other contributions.

In ferro- and ferrimagnetic materials, for a cubic crystal, $\boldsymbol{\varepsilon}$ can be expressed as:

$$\begin{aligned} \boldsymbol{\varepsilon} = \varepsilon_{\text{iso}} & \begin{pmatrix} 1 & -iQ_V m_3 & iQ_V m_2 \\ iQ_V m_3 & 1 & -iQ_V m_1 \\ -iQ_V m_2 & iQ_V m_1 & 1 \end{pmatrix} + \\ & \begin{pmatrix} B_1 m_1^2 & B_2 m_1 m_2 & B_2 m_1 m_3 \\ B_2 m_1 m_2 & B_1 m_2^2 & B_2 m_2 m_3 \\ B_2 m_1 m_3 & B_2 m_2 m_3 & B_1 m_3^2 \end{pmatrix}, \end{aligned} \tag{6.27}$$

where m_i are the components of the magnetization vector $\mathbf{m}$. In this expression, Q_V denotes the Voigt magneto-optical constant, which is typically associated with linear magneto-optical phenomena such as the Kerr and Faraday effects. The constants B_1 and B_2 represent parameters related to the intrinsic Voigt effect, a magneto-optical phenomenon that is proportional to the square of the magnetization and is observable only at normal incidence [256].

6.1.1.4 Description of Polar Kerr Effect

We now return to the solutions of Eq. 6.18. For simplicity (and because this case is relevant to the present thesis) we consider the polar geometry, in which the light incidence, magnetization, and surface normal vector are all aligned along the $\hat{z}$-axis of the cubic coordinate system. Under these conditions, the only non-zero components are $m_3 = m_z = |\mathbf{m}|$ and $k_3 = k_z = |\mathbf{k}|$. Inserting the magneto-optical tensor (6.27) into the wave equation (6.16) and accounting for the polar geometry, we obtain a system of three equations for the Cartesian components of the vector field amplitude. The characteristic equation is derived by setting the determinant of the coefficient matrix to zero, leading to the solutions:

$$k_z^2 = k_0^2 \varepsilon_{\mathrm{iso}} (1 \pm Q_V). \tag{6.28}$$

Assuming $|Q_\mathrm{V}| << 1$, the wave vector k_z can be approximated as:

$$k_z \approx \pm k_0 \sqrt{\varepsilon_{\mathrm{iso}}} \left(1 \pm \frac{Q_V}{2}\right), \tag{6.29}$$

describing waves propagating in the forward (+) and retrograde (−) directions. In both cases, substituting Eq. 6.29 into the equations for the vector field amplitude to the solutions:

$$E_\mathrm{y}^0 = \pm i E_\mathrm{x}^0, \tag{6.30}$$

which describes left- and right-circularly polarized waves for plus and minus signs, respectively, as described in Section 6.1.1.2.

Considering a wave propagating in the positive ($+k_\mathrm{z}$) direction and assuming $k_\mathrm{z} = nk_0$ (as shown in Eq. (6.9)), the representation of the refractive indices of left- (n_+) and right-circularly (n_-) polarized electromagnetic waves can be expressed as:

$$n_\pm = \sqrt{\varepsilon_{\mathrm{iso}}}(1 \pm Q_\mathrm{V}/2). \tag{6.31}$$

This solution demonstrates that for light propagating along the direction of the magnetization, the normal modes are two oppositely rotating circularly polarized waves, where the magnetic material has refractive index $n_+ = \sqrt{\varepsilon_{\mathrm{iso}}}(1+Q_\mathrm{V}/2)$ for left-circularly polarized radiation and $n_- = \sqrt{\varepsilon_{\mathrm{iso}}}(1-Q_\mathrm{V}/2)$ for right-circularly polarized radiation. In the case of non-magnetic material Q_V is zero and thus $n_+ = n_-$ and any polarization state could propagate in the crystal, feeling an isotropic refractive index $n = \sqrt{\varepsilon_{\mathrm{iso}}}$. Considering an absorptive medium, (n_+) and (n_-) become complex quantities:

$$n_\pm = n'_\pm + i n''_\pm, \tag{6.32}$$

where $n'_\pm$ and $n''_\pm$ are the real components representing the refractive index and the extinction coefficient, respectively.

To describe the Kerr effect, we consider reflected light, described by Fresnel's equations [255, 257]:

$$\begin{aligned} r_{\mathrm{pp}}^{ij} &= \left(\frac{E^{\mathrm{refl}}}{E^{\mathrm{in}}}\right)_\mathrm{p} = \frac{n_i \cos\vartheta_j - n_j \cos\vartheta_i}{n_i \cos\vartheta_j + n_j \cos\vartheta_i}, \\ r_{\mathrm{ss}}^{ij} &= \left(\frac{E^{\mathrm{refl}}}{E^{\mathrm{in}}}\right)_\mathrm{s} = \frac{n_i \cos\vartheta_i - n_j \cos\vartheta_j}{n_i \cos\vartheta_i + n_j \cos\vartheta_j}, \end{aligned} \tag{6.33}$$

where r_{pp}^{ij} and r_{ss}^{ij} are the reflection coefficients for p- and s-polarized light, respectively, E^{refl} and E^{in} the components of the respective direction to the total **E**-field and the indices i and j denote the

two media (air and ferromagnet in this case). For normal incidence ($\vartheta_i = \vartheta_j = 90°$) and assuming n_i= 1 (air), the Fresnel relations for each of the circular components become:

$$r(n_+) = \frac{1-n_+}{1+n_+} \qquad \text{and} \qquad r(n_-) = \frac{1-n_-}{1+n_-}. \tag{6.34}$$

Taking into consideration the complex nature of $n_\pm$ and the electric field of a circularly polarized wave (described in Sec. 6.1.1.2) the reflection coefficients can be expressed as functions of the $\hat{x}$ and $\hat{y}$ components:

$$r(n_+) = r_x + ir_y \qquad \text{and} \qquad r(n_-) = r_x - ir_y, \tag{6.35}$$

which leads to:

$$r_x = \frac{1}{2}[r(n_+) + r(n_-)] \qquad \text{and} \qquad r_y = \frac{1}{2}i[r(n_+) - r(n_-)]. \tag{6.36}$$

These expressions simplify to:

$$r_x = \frac{1-\bar{n}}{1+\bar{n}} \equiv N, \tag{6.37}$$

$$r_y = \frac{-i\bar{n}Q_\mathrm{V}}{(1+\bar{n})^2} \equiv K. \tag{6.38}$$

Here, $\bar{n} = \frac{1}{2}(n_+ + n_-) = \sqrt{\varepsilon_\mathrm{iso}}$ represents the average complex refractive index, N the regular Fresnel reflectance and K the Kerr coefficient.

Finally, taking as example an incident linearly polarized light along the $\hat{x}$-axis $\mathbf{E} = \begin{pmatrix} E_\mathrm{x}^\mathrm{in} \\ 0 \end{pmatrix}$ reflecting off a magnetic surface, a $\hat{y}$-component is generated in the reflected light:

$$\begin{pmatrix} E_\mathrm{x}^\mathrm{refl} \\ E_\mathrm{y}^\mathrm{refl} \end{pmatrix} = \begin{pmatrix} r_\mathrm{xx} & r_\mathrm{xy} \\ r_\mathrm{yx} & r_\mathrm{yy} \end{pmatrix} \begin{pmatrix} E_\mathrm{x}^\mathrm{in} \\ 0 \end{pmatrix} = \begin{pmatrix} r_\mathrm{xx}E_\mathrm{x}^\mathrm{in} \\ r_\mathrm{yy}E_\mathrm{x}^\mathrm{in} \end{pmatrix} = \begin{pmatrix} NE_\mathrm{x}^\mathrm{in} \\ KE_\mathrm{x}^\mathrm{in} \end{pmatrix} \equiv \begin{pmatrix} R_\mathrm{N} \\ R_\mathrm{K} \end{pmatrix}, \tag{6.39}$$

where r_xx corresponds to r_x and r_yy to r_y. Thus, a linearly polarized impinging light wave generates a reflected wave with a small transverse component due to the differences in n_+ and n_-. The reflected light can be described by the *regular Fresnel component* R_N, which retains the polarization of the incident light, and the *Kerr component* R_K, which arises due to the Kerr effect. These two components are generally out of phase, resulting in elliptically polarized reflected light with ellipticity ξ_K and azimuth θ_K. The complex Kerr angle Φ_K is given by:

$$\frac{R_\mathrm{K}}{R_\mathrm{N}} = \frac{K}{N} \approx \Phi_\mathrm{K} = \theta_\mathrm{K} + i\xi_\mathrm{K} = -i\frac{\bar{n}Q_\mathrm{V}}{1-\bar{n}^2} \tag{6.40}$$

The rotation of reflected light primarily originates from the imaginary part of the off-diagonal elements of the magneto-optical matrix, while the ellipticity arises from the real part. Hence, reflection-induced rotation requires a non-vanishing imaginary part, which implies absorption.

6.1.2 Microscopic Description of Kerr Effect

While the classical macroscopic description of the Kerr effect provides a comprehensive phenomenological understanding, its microscopic origin requires examining the coupling between the electric field of light and the electron spin within a magnetic medium via the SOC.

This was first proposed in 1932 by Hulme [258], who recognized that the large Faraday rotation observed in ferromagnetic materials originates from the SOC, that couples the electron's spin to its motion. The SOC links the magnetic moment of an electron to its motion through the magnetic field

experienced as the electron moves within the electric field of a medium. In ferromagnetic materials, the unbalanced population of electron spins generates an effective magnetic vector potential that influences the electrons' motion, thereby connecting magnetic and optical properties. Nonetheless, Hulme was unable to fully account for the magnitude of magneto-optical effects. A complete theoretical explanation had to wait until 1955, when Argyres [250] successfully derived these effects using perturbation theory.

In simpler terms, the Kerr effect can be attributed to optical transitions within the valence band energy regime, requiring the simultaneous presence of exchange splitting and spin-orbit splitting. Considering the case of the polar Kerr effect, we must first examine the selection rules for electric-dipole transitions to determine which transitions are permitted:

- Energy: $E_\mathrm{f} - E_\mathrm{i} = \hbar\omega$, which states that the difference between energies of the final (E_f) and initial (E_i) electron states equals the absorbed photon energy ($\hbar\omega$, where ω is the photon frequency);

- Momentum: $k^e_\mathrm{f} = k^e_\mathrm{i}$, due to the negligible momentum of the photon $\hbar\omega/c \approx 0$, the momentum of the electron does not change between initial (k^e_i) and final (k^e_f) state (vertical transitions in k-space);

- Electron spin: $\Delta s = 0$, the spin of the electron is preserved as the impinging photon has no spin;

- Orbital momentum: $\Delta l = \pm 1$, the photon has angular momentum $1\hbar$, therefore only $s \leftrightarrow p$, $p \leftrightarrow d$ etc. transitions are allowed;

- Orbital momentum along quantization axis (magnetic number): $\Delta m = \pm 1$, where the sign depends on the photon helicity (- for circularly left polarized light and + for circularly right polarized light).

Fig. 6.2a illustrates a general transition in a ferromagnet, from an occupied d-state to an unoccupied p-state. These states are depicted as horizontal lines and are labeled according to their orbital and spin quantum numbers, $|lm\updownarrow\rangle$. The exchange splitting (Δ_ex) separates the energy of the levels for spin down ($\downarrow$, majority, left) and spin up ($\uparrow$, minority, middle). In addition, the SOC further lifts the degeneracy of states with different m. Transitions corresponding to left (right)-circular polarization are portrayed in red (green), where only the transitions with $\Delta m = -1$ ($\Delta m = +1$) are allowed. The two different resulting absorption spectra for the two helicities are shown schematically on the right-hand side of Fig. 6.2a. By removing the exchange interaction (Fig. 6.2b) or the SOC (Fig. 6.2c), the absorption spectra become degenerate for the two helicities, eliminating the dichroism effect.

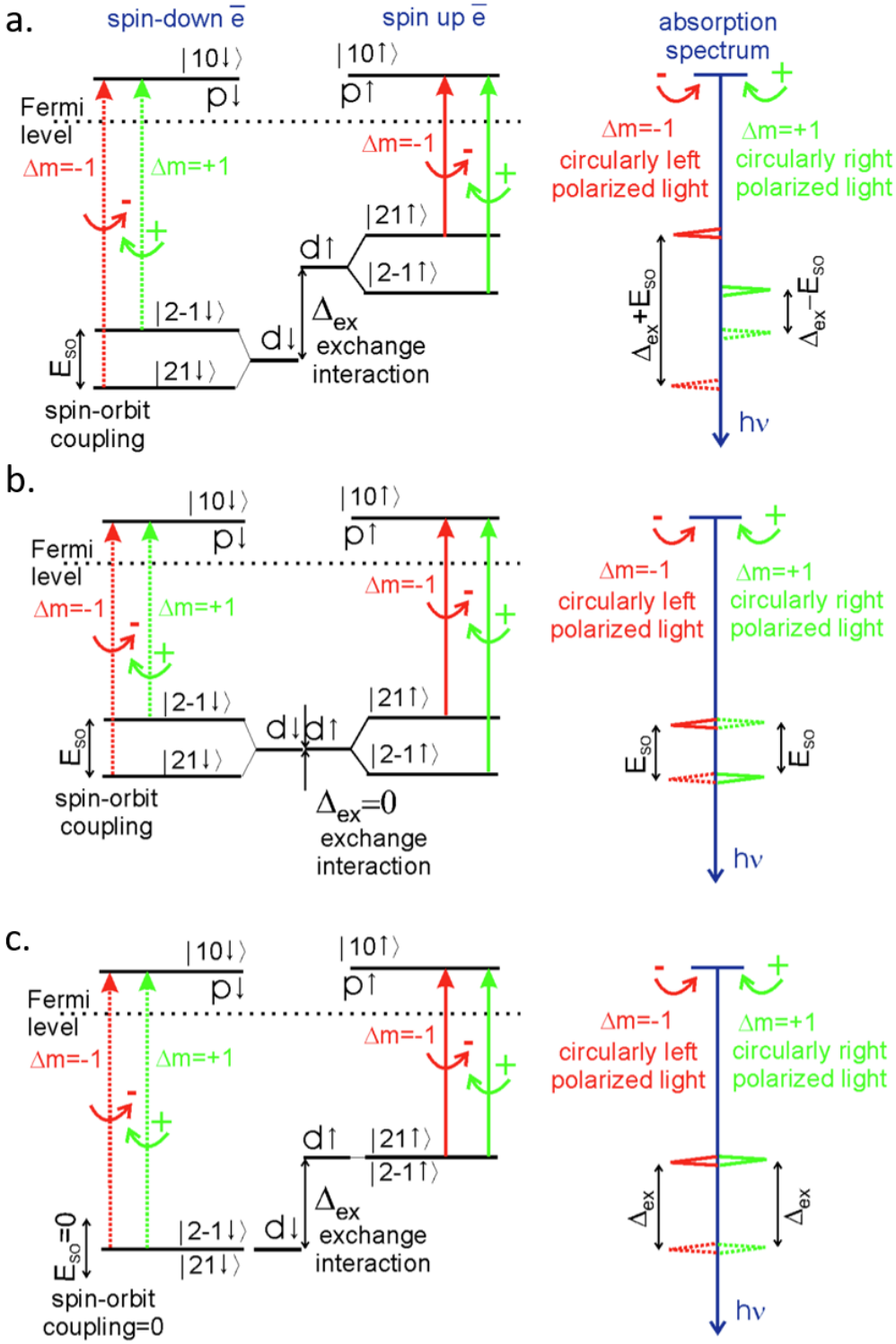

Figure 6.2: Microscopic origin of the Kerr effect illustrated through electric-dipole transitions in a ferromagnetic material. (a) Transitions from exchange-split d-states to unoccupied p-states are shown, with SOC lifting the degeneracy of orbital states. (b) In the absence of exchange splitting, the spectra for both helicities become degenerate. (c) Similarly, without spin-orbit coupling, the dichroism vanishes. Taken from [259].

6.1.3 Intuitive (Lorentz) Description of Kerr Effect

The last method to describe the Kerr effect, and probably the easiest for understanding the different geometries and symmetries (see Section 6.1.3.1), is based on the *Lorentz concept*. When a light wave propagates through a medium, its electric field induces motion in the medium's electrons. Right circularly polarized light causes electron motion in the same rotational sense, and vice versa. The two cases are degenerate if no magnetic field or magnetization is present in the medium. However, when magnetization or magnetic field is present, the Lorentz force acts on the moving electrons, reducing the radius for left circular motion and expanding the radius for right circular motion. This difference leads to distinct dielectric constants, thereby generating a Faraday or Kerr effect.

This can also be demonstrated by considering the dielectric law, Eqs. (6.3) and (6.27), and rewriting it as:

$$\mathbf{D} = \varepsilon_0 n^2 [\mathbf{E} + iQ_\mathrm{V}(\mathbf{m} \times \mathbf{E})], \tag{6.41}$$

where it becomes evident that the electric field of the incident light interacts with the magnetization vector $\mathbf{m}$ in the same symmetry as the Lorentz force acting on the light-induced electron motion. Thus, when Q_V is nonzero, it induces a rotation in the vibrational plane, and the $\mathbf{D}$-vector acquires a different polarization than the $\mathbf{E}$-vector.

In this scenario, a magnetization-dependent contribution to the $\mathbf{D}$-vector is generated only when the cross product $\mathbf{m} \times \mathbf{E}$ is nonzero, imposing constraints on the possible symmetries of the Kerr effect.

6.1.3.1 Geometries of Kerr Effect

For instance, considering light incident at an oblique angle on a sample with perpendicular magnetization, it will induce oscillatory motion in the electrons parallel to its plane of polarization. In the absence of magneto-optical effects, this oscillatory motion would result in emitted light with the same polarization ($\mathbf{R}_\mathrm{N}$). However, when the Lorentz force is accounted for, a small component of vibrational motion perpendicular to both the direction of magnetization and the plane of polarization of the light arises. This secondary motion, proportional to the "Lorentz velocity" $\mathbf{v}_\mathrm{Lor} = -\mathbf{m} \times \mathbf{E}$, gives rise to the Kerr (secondary) amplitude $\mathbf{R}_\mathrm{K}$. The superposition of these two amplitudes ultimately leads to the magnetization-dependent polarization rotation, which constitutes the Kerr effect.

The Kerr effects are traditionally categorized into three primary geometries: polar, longitudinal, and transverse, based on the relative orientation of the magnetization, the polarization direction of the incident light, and the plane of light incidence.

- *Polar effect*: This configuration occurs when the magnetization is oriented perpendicular to the sample surface. It is independent of the polarization direction of the incident light and reaches its maximum intensity at normal incidence ($\vartheta = 0°$). This technique is employed throughout this thesis, as the focus lies on probing the perpendicular component of the magnetization.

- *Longitudinal effect*: This configuration arises when the magnetization lies parallel to the sample surface and along the plane of incidence. It produces a magneto-optical rotation for both light polarized parallel and perpendicular to the plane of incidence, with opposite rotation senses in the two cases. The effect is only observable at oblique incidence ($\vartheta \neq 0°$).

- *Transverse effect*: This configuration occurs when the magnetization lies parallel to the sample surface but perpendicular to the plane of incidence. It results in changes in the intensity of the reflected light, rather than its polarization state, and is typically more challenging to detect.

These effects are schematically shown in Fig. 6.3 for (a) polar configuration (b) and (c) longitudinal and (d) transverse configuration. In the figure the reflected normal and Kerr component are highlighted.

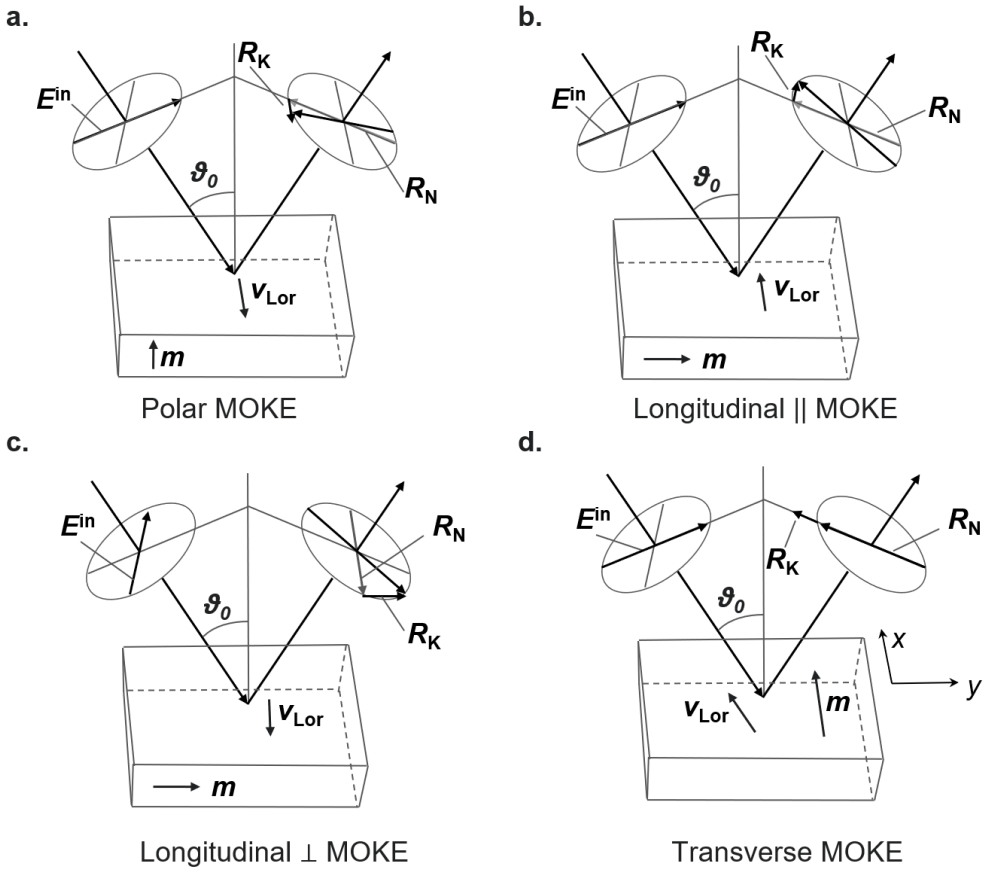

Figure 6.3: Illustration of the basic magneto-optical rotation effects. $\mathbf{R_N}$ denotes the regularly reflected electric field amplitude, while $\mathbf{R_K}$ represents the magneto-optical contribution generated by the Lorentz motion v_{Lor}. Shown are the cases of (a) polar incidence, (b) longitudinal parallel, (c) longitudinal perpendicular, and (d) transverse geometry. In the transverse case, only parallel polarization yields an effect; hence no Kerr contribution is shown. Adapted from [254].

In all three geometries, the Kerr effect induces a variation of light that is linearly proportional to the magnetization component parallel to the reflected light beam. When the magnetization direction is reversed, the Kerr rotation also inverts, forming the basis for detecting magnetic domains.

6.2 Development of a Wide-Field MOKE Microscope

As introduced at the beginning of the Chapter, one of the first major tasks in this work was the construction of a wide-field (also referred to as bright-field) MOKE microscope. The following section describes the setup in detail, outlining the choice of components, their specifications, and their specific roles within the system. Although the optical layout of a MOKE microscope is conceptually straightforward, the signals it detects are extremely small: typical Kerr rotation angles are on the order of milliradians for standard ferromagnets, and even smaller for the ferrimagnetic insulators investigated in this thesis. This makes careful component selection, precise optical alignment, and thorough calibration essential for achieving reliable measurements.

Two complementary MOKE setups were developed during my PhD: a wide-field (WF-MOKE) system and a laser-based (L-MOKE) system. I personally designed and built the WF-MOKE from scratch, while also contributing to the development and optimization of the L-MOKE. These setups differ in light sources, detection schemes, and operational modes, and serve distinct purposes in this work. The WF-MOKE operates exclusively in the polar configuration, while the L-MOKE can be used in both longitudinal and polar configurations, making it sensitive to both IP and OOP magnetization components.

The L-MOKE uses a tightly focused laser beam to probe the sample, with a Charge Coupled Device (CCD) detector measuring the contrast changes induced by magneto-optical effects. The measurement area is defined by the laser spot size, which typically ranges from a few millimeters to a few microns in diameter, depending on whether an objective lens is used. The coherence and high intensity of the laser source enhance sensitivity, allowing the detection of very small Kerr rotations. However, the small illuminated area means that mapping extended regions requires scanning, which can be time-consuming. Although low-power lasers are used in our setup to avoid sample heating, high-intensity illumination in general may alter sensitive materials.

In contrast, the WF-MOKE employs a collimated light source, in this case, an LED, to illuminate a large area of the sample. The reflected light is captured by an imaging system with a CMOS camera, enabling the simultaneous observation of magnetic structures over wide areas. This approach allows real-time visualization of domain patterns, skyrmions, and their evolution under external stimuli such as magnetic fields or electrical currents. The trade-off is lower sensitivity compared to the laser-based system, due to the lower intensity and coherence of the LED source. Spatial resolution is also limited by the imaging optics and the light wavelength, making it difficult to resolve sub-micron features. Additionally, illuminating large areas can increase background noise or introduce optical artifacts.

In summary, the L-MOKE setup provides high sensitivity and spatial resolution for localized magnetic measurements, while the WF-MOKE setup offers a wide field of view for dynamic, large-area magnetic imaging. Together, they form a versatile toolkit that has been central to the experimental work presented in this thesis. The two setups, shown in their preliminary configurations, are presented in Fig. 6.4.

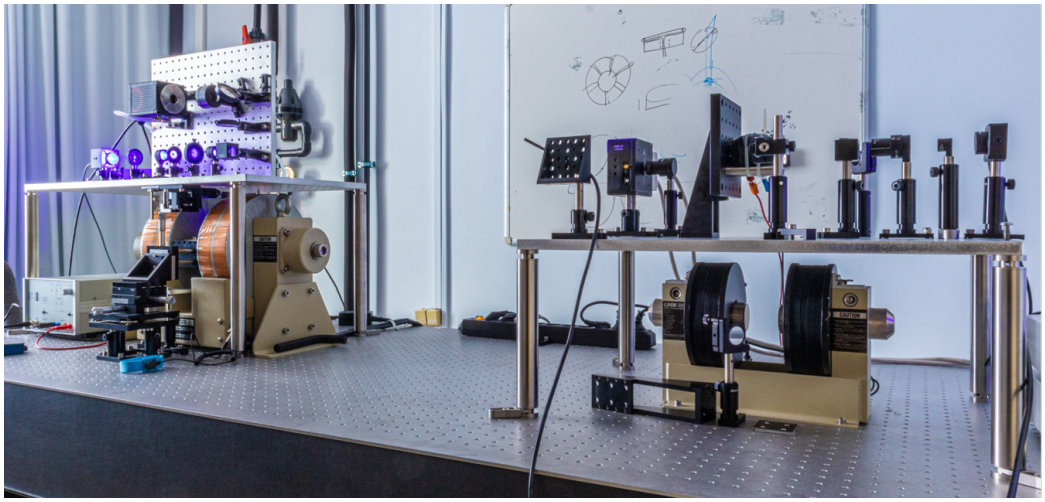

Figure 6.4: Photograph of the MOKE setups in their initial configurations: WF-MOKE (left) and L-MOKE (right).

6.2.1 Setup

In general, the main components of a MOKE setup, common to both WF-MOKE and L-MOKE, are:

- **The light source**, generates the probing light used to illuminate the sample.
- **The polarizer**, sets the polarization state of the incident light beam.
- **The magnetic surface**, The sample under analysis, which reflects the light and induces the Kerr component.
- **The analyzer**, a second polarizer that isolates the Kerr signal from the reflected light.
- **The detector**, measures the intensity of the final light beam to quantify the Kerr effect.

The home-built WF-MOKE setup described in this work incorporates these fundamental components along with additional elements to ensure an optimal signal-to-noise ratio and minimize artifacts in the measurements. Below, all components and their respective functions are detailed, with reference to Fig. 6.5 for a general schematic representation. In the figure, the blue light represents the "illumination light path", referring to the beam before it interacts with the magnetic sample. The yellow light depicts the "image-forming light path," which carries the Kerr angle information after reflection from the sample.

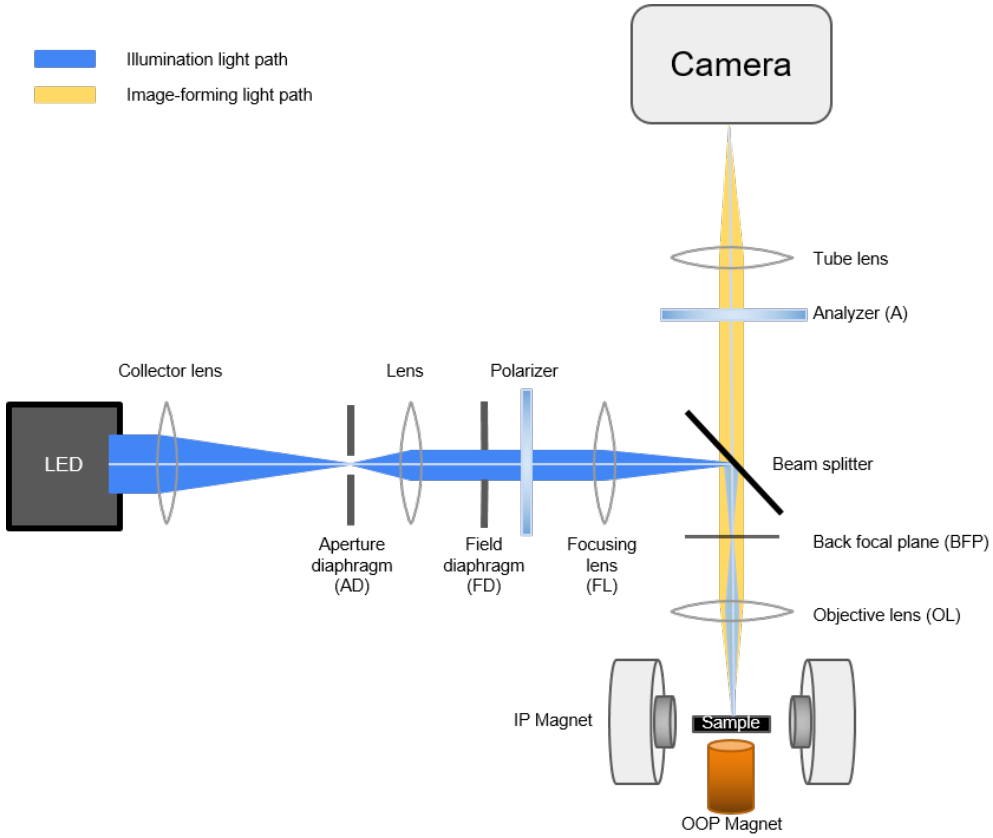

Figure 6.5: Schematic picture of the MOKE setup, where all components are shown. In blue is highlighted the illuminating light path while in yellow the image-forming one.

At the very beginning of our MOKE[1] setup, an LED light source (Prizmatix Mic-LED-455L, 100 mW) emits blue light with $\lambda = 455 \pm 24$ nm. The blue light was specifically chosen to enhance the Kerr signal when analyzing ferrimagnetic iron garnets. For ferrimagnetic insulators, the simplified description in Section 6.1.2 no longer fully applies, as the behavior in complex materials is significantly more intricate. Nevertheless, the underlying physics remains consistent. For example, in materials like TbIG, white light would probe the three sublattices with nearly equal intensity. Because these sublattices are antiferromagnetically coupled, the overall signal is significantly reduced. Thus, while the precise color of the light source is less critical, avoiding white light is essential.

The output light of the LED is collimated, meaning the emitted light rays are parallel to one another. Directly at the output of the LED, a collector lens (Thorlabs AC254-100-A-ML) focuses the LED light onto the aperture diaphragm (AD) (Thorlabs ID25/M). The AD is used to regulate the total intensity of the illumination light as well as the Kerr configuration. By positioning the AD either centered or off-centered, the microscope can probe different magnetization components, as will be explained in detail later.

Subsequently, a lens with the same focal length f as the collector lens is used to collimate the light beam such that it travels through the field diaphragm (FD) (Thorlabs ID25/M), which filters stray light, and the polarizer (Thorlabs LPVISE100-A) as a bundle of parallel beams. In this 'infinity'

[1]From this point onward, WF-MOKE will be referred to simply as MOKE for clarity.

space, additional optical components such as reflector mirrors, polarizers, and compensators can be incorporated with a straightforward design, without introducing image distortion. The polarizer used in this setup has a moderate extinction ratio of approximately 2000:1 (for λ=455 nm), where the extinction ratio is defined as the ratio of the transmitted light in the principal polarization mode to that in the orthogonal polarization mode. While high-end polarizers typically achieve extinction ratios of 100,000:1 or higher, the chosen polarizer is sufficient to resolve the desired magnetic contrast. Thus, a more expensive alternative is not deemed necessary at this stage.

For the polar MOKE, the direction of polarization is not critical, as *s*- or *p*-polarized light at normal incidence behaves the same way. The polarized light is then focused by the focusing lens (FL) (Thorlabs AC254-200-A-ML), which produces an image of both the AD and of the LED matrix on the back focal plane (BFP) of the objective (Mitutoyo M Plan Apo SL 20x). This configuration is needed to generate the so-called Köhler illumination, which ensures uniform illumination while preventing the formation of an image of the light source on the sample surface (see Section 6.2.1.3). A non-polarizing beam splitter (Thorlabs LPVISE100-A) is introduced between the FL and the objective. The choice of the objective was mainly guided by three factors: the infinity-correction, that is, the light rays emerge from the objective in parallel bundles from every azimuth and are projected to infinity, the 20x magnification, which allows full observation of the devices used in this thesis in a single image while still resolving the magnetic structures in our samples (on the order of microns), and the extremely long working distance, which is 30.5 mm. This long working distance is essential to keep the objective as far from the sample as possible, thus avoiding the influence of magnetic field lines on the objective and the potential creation of spurious signals.

Finally, the light is focused onto the sample, where it is reflected and acquires a Kerr rotation. The reflected light emerges elliptically polarized and is transmitted again through the objective and the non-polarizing beam splitter before reaching the second polarizer (Thorlabs LPVISE100-A), known as the analyzer, which is placed in a crossed configuration relative to the first one (more details on how to obtain the Kerr signal are provided in Section 6.2.1.2). This arrangement eliminates most of the reflected light. The transmitted light then propagates through the tube lens (Thorlabs TTL200-A), which focuses the beam onto the water-cooled CMOS camera (Hamamatsu Orca-Flash4.0 C13440).

This entire structure is mounted on two levels, one horizontal and one vertical, to accommodate a large IP magnetic field (GMW 5403) of up to approximately 150 mT.[2] Additionally, a smaller, home-made OOP coil is used, capable of generating fields up to 180 mT. To achieve this configuration, a custom breadboard with a circular hole of 5x5 cm^2 has been purchased from Standa. In this setup, the beam splitter is positioned so that the split light travels vertically through the hole before reaching the objective. The sample is placed flat on a holder, positioned atop the OOP magnet and between the IP coils. The reflected light then continues vertically until it reaches the camera. This design offers the advantage of securely positioning the sample between the coils while maintaining stability due to gravitational support. However, it limits the operations in only the polar mode, as in this geometry, it is impossible to reach an incident angle large enough to generate longitudinal signal.

Finally, in a second step, the entire setup was enclosed within a custom-built black box, designed

[2]In principle, this magnet can produce fields as strong as 2 T, but due to the geometry of our MOKE setup and the instability of certain components (e.g., the objective) at high fields, the maximum IP field is limited for safety reasons.

with openings at the front and back to allow easy access to the sample and facilitate adjustments to the coils and Hall probe for precise measurement of the applied magnetic field. This box significantly improved measurement quality by eliminating stray light interference, ensuring that external illumination does not affect the Kerr signal. Additionally, it enhanced the accessibility and usability of the MOKE setup, as it eliminated the need to darken the entire laboratory. This modification enables multiple experimental setups to operate simultaneously without interference. Furthermore, the black box provides thermal insulation, reducing the impact of external temperature fluctuations and allowing the system to reach thermal equilibrium more quickly, thereby minimizing noise in the measurements. A picture of the final configuration of the MOKE setup, with all the components explained, is shown in Fig. 6.6.

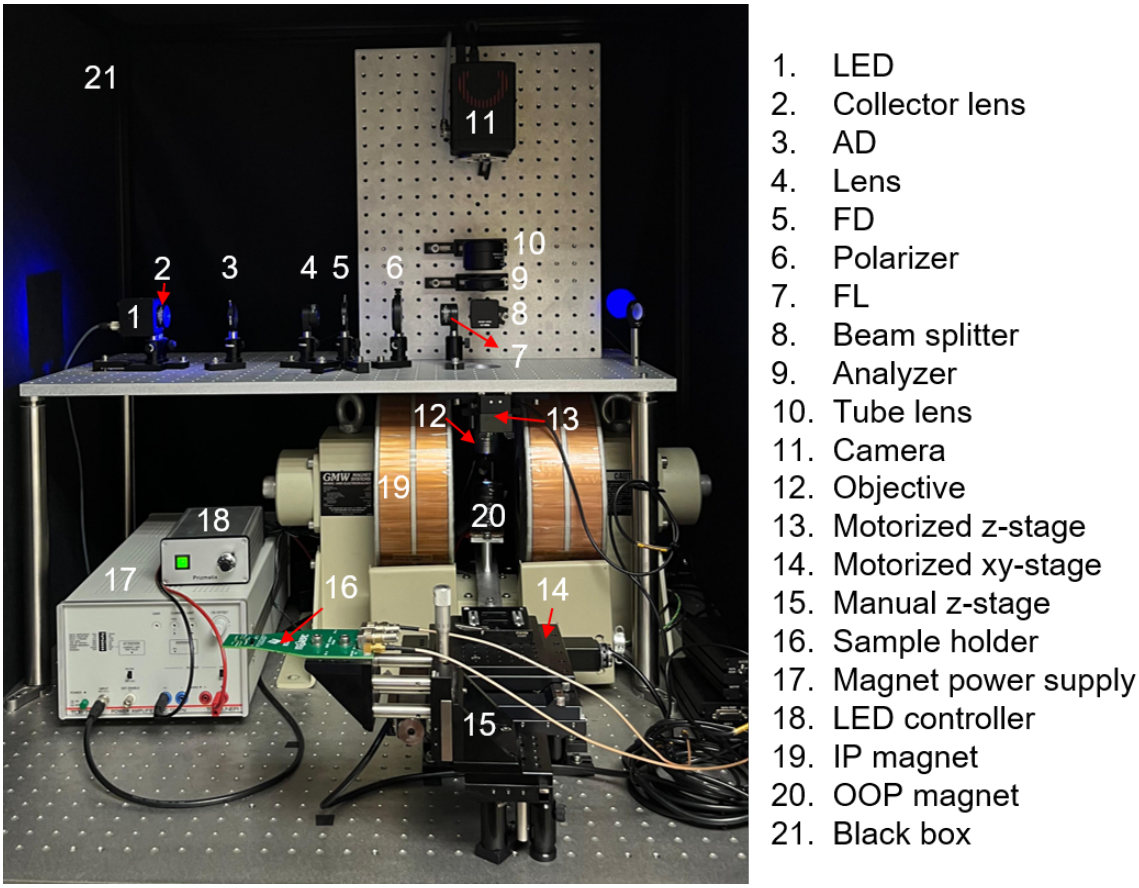

Figure 6.6: Photograph of the final configuration of the MOKE setup, with the black box, motorized stages, and all components explained.

6.2.1.1 Maltese Cross

As explained before, in our configuration, the FL forms an image of the AD on the BFP of the objective. When observing the colonoscopic image under crossed polarizers (i.e., with the polarizer and analyzer set to extinction configuration), a characteristic Maltese cross pattern appears, as shown in Fig. 6.7 [260]. This pattern arises because wide-field microscopy uses a converging light bundle rather than a collimated beam. As a result, off-axis rays experience different polarization

changes upon reflection, preventing complete extinction by the analyzer. The positioning of the AD is, therefore, crucial. As illustrated in Fig. 6.7, allowing only central rays to pass results in a polar MOKE configuration. However, for longitudinal and transverse MOKE, the AD must be off-centered to selectively permit oblique rays, enabling the detection of the IP magnetization component.

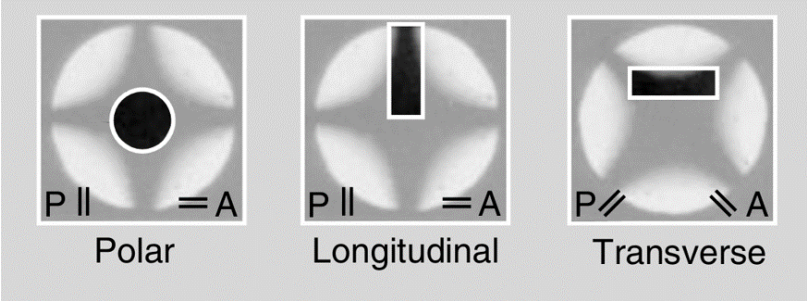

Figure 6.7: Representation of the Maltese cross pattern obtained from crossed polarizers, indicating the regions of the light beam selected to measure polar, longitudinal, or transverse MOKE. Taken from [261].

6.2.1.2 Kerr Contrast and Signal

The relative angle between the polarizer and the analyzer is crucial for obtaining the Kerr signal. In the polar MOKE configuration (Fig. 6.8a), when the polarizer and analyzer are perfectly crossed, the transmitted light intensity remains uniform, making magnetic domains indistinguishable. However, if the polarizer is rotated by a small skew-angle α, (comparable to the Kerr rotation θ_K), the intensity contrast between opposite Kerr rotations becomes visible (Fig. 6.8b). One domain appears darker while the other reaches maximum intensity.

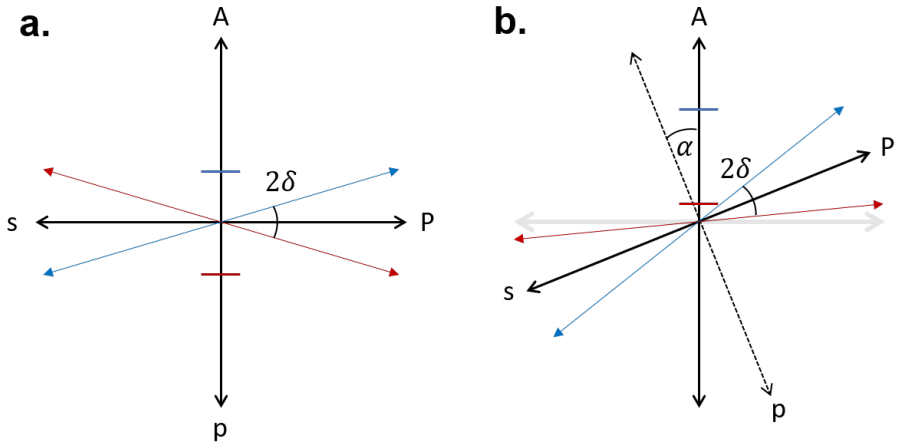

Figure 6.8: Schematic illustration of the effect of introducing a small skew angle to the crossed-polarizer configuration. (a) For perfectly crossed polarizers, Kerr rotation in either direction increases the transmitted intensity by the same amount. (b) A small skew angle lifts this degeneracy, enhancing image contrast and SNR.

To estimate an optimal value of α for maximizing contrast [262], we define the microscope contrast C as the ratio of the maximum change in the intensity that occurs during a full rotation of

magnetization ΔI over the intensity of the reflected light off of the sample I_0:

$$C \equiv \frac{\Delta I}{I_0}. \tag{6.42}$$

This contrast is limited by the quality of the polarizer and, specifically, by their extinction ratio η [263], given by:

$$\eta \equiv \frac{I_\mathrm{r}}{I_0}, \tag{6.43}$$

where I_r is the intensity leakage through ideally crossed polarizers. Thus, the transmitted light intensity I through the analyzer set at an angle α from the cross-polar setting is defined by the Malus law:

$$I = I_0 \sin^2(\alpha) + I_\mathrm{r}. \tag{6.44}$$

If now we consider a Kerr rotation θ_K produced at reflection, this becomes:

$$I = I_0 \sin^2(\alpha + \theta_\mathrm{K}) + I_\mathrm{r}. \tag{6.45}$$

Considering a small α, the contrast simplifies to:

$$C = \frac{\Delta I}{I_0} \approx \frac{2\alpha\theta_\mathrm{K} + \theta_\mathrm{K}^2}{\alpha^2 + \eta}. \tag{6.46}$$

Maximizing C by solving $\frac{dC}{d\alpha} = 0$ gives the optimal skew angle:

$$\alpha_\mathrm{m} = \frac{\theta_\mathrm{K}}{2}\left(\sqrt{1 + \frac{\eta}{\theta_\mathrm{K}^2}} - 1\right). \tag{6.47}$$

For very small Kerr rotations ($\theta_\mathrm{K} \ll 4\eta$), the approximation

$$\alpha_\mathrm{m} \approx \sqrt{\eta}, \tag{6.48}$$

is valid and the maximum contrast is given by:

$$C = \frac{\theta_\mathrm{K}}{\sqrt{\eta}}. \tag{6.49}$$

From these results, we conclude that contrast improves with lower extinction ratios. Knowing η of our polarizers, we estimate an optimal skew angle of $\alpha_\mathrm{m} \approx 1°$. This provides a theoretical starting point, but experimental fine-tuning is necessary due to real-world optical imperfections and setup variations.

6.2.1.3 Köhler Illumination

Wide-field microscopes employ the Köhler illumination technique, introduced in 1893 by August Köhler from Carl Zeiss corporation, to obtain homogeneously illuminated images with maximum resolution. The ideal illumination source for a microscope would be a point-like source, but this is not feasible in practice. Real illumination sources are neither point-like nor uniform, which can impact image quality. For instance, the LED used in this work is actually an LED matrix, which generates high power but does not produce inherently uniform illumination. To mitigate this issue, the optical components in the light-forming path can be aligned in a specific manner to ensure the light source is completely defocused on the sample. This configuration provides a consistent magneto-optical contrast across the entire viewing field [264, 265].

To better understand Köhler illumination, we must first introduce some fundamental concepts of optics.

Thin Lenses and Diaphragm When describing light propagation in geometrical optics, it is represented in terms of rays, which indicate the direction of light propagation. In the absence of obstacles, rays travel in a straight line. However, when a lens is placed in their path, reflection and refraction occur, causing the rays to bend depending on the type of lens.

In MOKE microscopes, simple thin lenses are used. These lenses are characterized by two diopters, which are the surfaces where light transitions from one medium to another. These surfaces can be plane, spherical, convergent, or divergent, and they are defined by their radii of curvature, R_1 and R_2. A thin lens is one in which the distance d between its two diopters is negligible compared to R_1 and R_2 (see Fig. 6.9)

A thin lens is characterized by its focal length f, which is defined as:

$$f = \frac{n_1}{n_2 - n_1} \frac{R_1 R_2}{R_2 - R_1}, \tag{6.50}$$

where n_1 is the refractive index of the medium where the light rays initially propagate (e.g., air), and n_2 is the refractive index of the lens. The focal length f represents the distance from the center of the lens at which the image of an infinitely distant object is formed (i.e., where parallel rays converge). Conversely, an object placed at a distance f from the lens will produce parallel rays, forming its image at infinity.

The lenses used in this work are all converging lenses, which have a positive focal length ($f > 0$), one or two convex surfaces, and are thicker at the center than at the edges. In contrast, diverging lenses have a negative focal length ($f < 0$) and are thinner at the center.

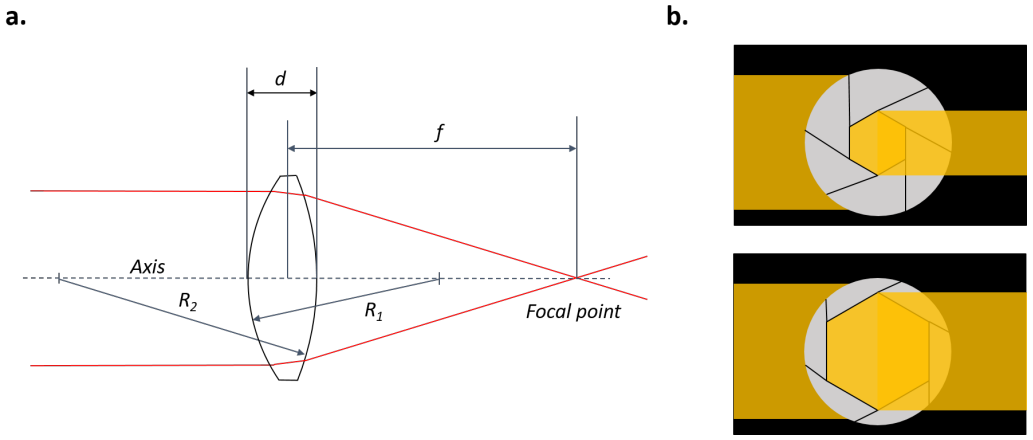

Figure 6.9: (a) Schematic of a converging thin lens. (b) Schematic of a diaphragm illustrating how it blocks part of the light bundle.

Another optical component shown in Fig. 6.9b, is the diaphragm, which is much simpler than lenses. It controls the amount of light passing through by adjusting its aperture, allowing more or less light into the system.

Conjugated Planes and Alignment From the previous paragraph, we understand that a lens can either generate a collimated beam of light from an object or form an image of the object, depending on its position relative to the focal plane f. To achieve uniform illumination across

the field of view, the optical components must be aligned so that an image of the light source is positioned at the back focal plane of the objective. In this configuration, the objective produces a defocused light beam, ensuring even illumination of the specimen (Fig. 6.10a).

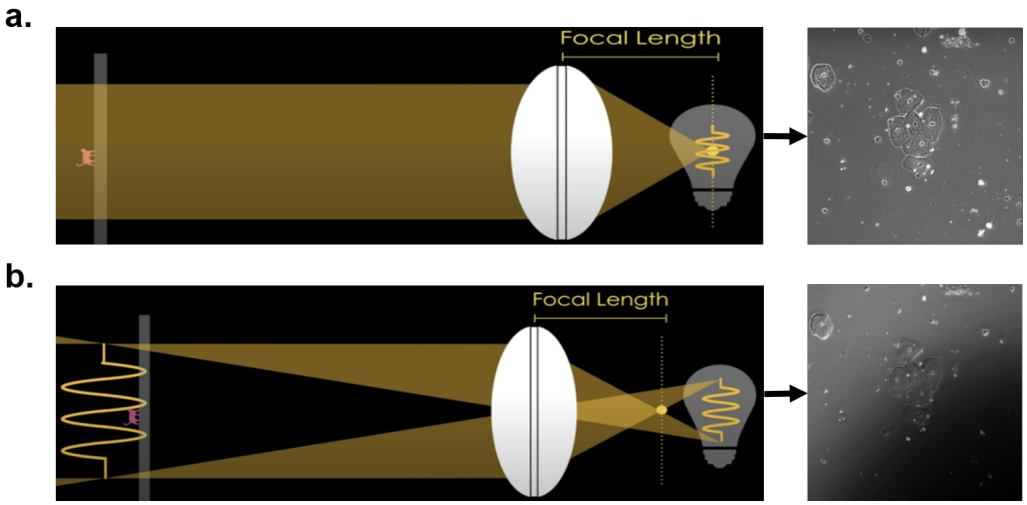

Figure 6.10: (a) Köhler illumination with uniform field. (b) Improper illumination when the filament image is focused on the specimen. Adapted from [266].

When a microscope sample is illuminated this way, the light source is completely out of focus at the sample plane, meaning each point of the illumination source is evenly spread over the entire field of view. Conversely, if the light source is positioned outside the focal plane, the lens will form a visible image of the filament. If this filament image is focused on or near the specimen, the field of view will be unevenly illuminated, leading to unwanted artifacts (Fig. 6.10b).

To better understand this, it is useful to introduce the concept of conjugate planes. For simplicity, we use a transmitted light microscope as an example, but the same principles apply to reflected light microscopes, such as those used in MOKE microscopy. In Köhler illumination, the conjugate planes along the illumination path (Fig. 6.11a) include the source plane, the AD (condenser), the BFP of the objective, and the region beyond the eyepiece. Meanwhile, the conjugate planes in the image-forming path (Fig. 6.11b) include the FD, the focused specimen, the intermediate image plane, and the retina (or, in our case, the camera sensor).

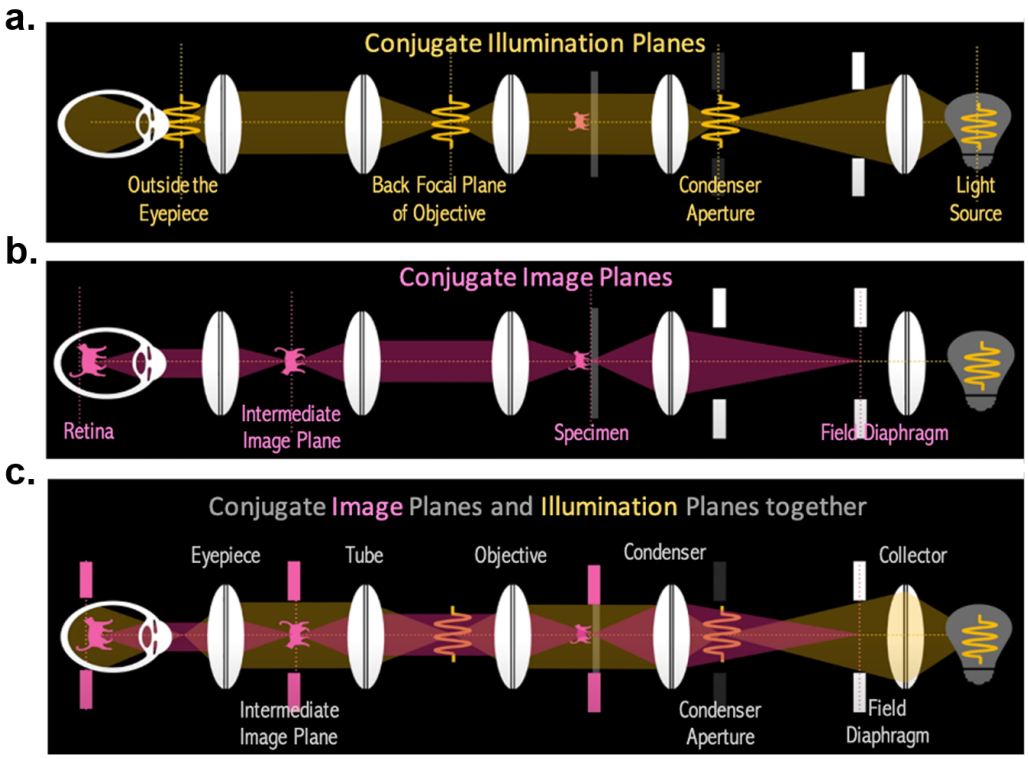

Figure 6.11: (a) Conjugate planes in the illumination path, (b) in the image path, and (c) combined. Taken from [266].

A key property of conjugate planes is that if a second object is introduced at any conjugate plane, its image will be overlaid with the existing image at all subsequent conjugate planes. In a properly aligned microscope, these two distinct sets of conjugate focal planes are referred to as the illumination plane and the image plane. To achieve Köhler illumination, all optical elements must be precisely positioned at the focal points of their respective conjugate planes.

When properly aligned, Köhler illumination ensures that the light source and its images remain in focus within the illumination planes. This means that the image of the FD will be superimposed over the specimen image, as both belong to the same set of conjugate image planes. This property can be used to verify whether the AD is correctly positioned: in an aligned system, the AD forms an image of the FD at the specimen plane while simultaneously providing defocused illumination.

The two iris-type diaphragms (AD and FD) play a crucial role in achieving Köhler illumination. The AD, which is conjugate with the light source, controls the angle of the light rays reaching the specimen, a critical factor in Kerr microscopy. Meanwhile, the FD, conjugate with the specimen, regulates the size of the illuminated area, ensuring that only the desired region is exposed to light.

6.2.1.4 Camera

The Kerr signals in normal ferromagnets are weak, but in the REIGs used in this work, they are even weaker due to the material's transparency and low saturation magnetization. To address this and obtain a clear Kerr signal, a high-performance sCMOS (scientific Complementary Metal-Oxide-Semiconductor) camera, combined with a powerful light source, is required. Introduced in 2009 [267],

sCMOS technology builds on CMOS sensor design and fabrication techniques, offering significant advantages over traditional CMOS and CCD sensors. CCD cameras provide high sensitivity but suffer from slow sampling speeds, and traditional CMOS cameras offer high frame rates at the cost of reduced dynamic range. In contrast, sCMOS image sensors combine extremely low noise, high frame rates, wide dynamic range, high quantum efficiency, high resolution, and a large field of view. These characteristics make sCMOS sensors ideal for high-fidelity and quantitative scientific imaging in low-light conditions [268].

These performance differences arise from their underlying sensor technologies. CCD sensors rely on a photoactive layer where photons generate electron-hole pairs, with charge transferred pixel by pixel to a readout node for voltage conversion. In CMOS sensors, each pixel contains its own photodiode and amplifier, allowing charge conversion into voltage directly at each pixel and enabling parallel readout rather than serial transfer across the chip. sCMOS further enhances performances by implementing advanced noise reduction techniques, such as dual amplifiers for each pixel (one optimized for low noise and high sensitivity, and the other for high dynamic range) along with multiple readout channels that facilitate high frame rates while maintaining a wide dynamic range [268, 269].

Camera Noise and Quantum Efficiency The detection limit of the camera is mostly determined by the dark current, the readout noise and its Quantum Efficiency (QE).

Dark current is an intrinsic noise source in photosensitive devices, arising from thermally generated charge carriers even in the absence of external illumination. While this noise cannot be eliminated, it can be minimized through sensor cooling and reduced exposure time, making it negligible in most cases. The associated dark noise N_{dark} is given by:

$$N_{\text{dark}} = I_{\text{dark}} \cdot t_{\text{exp}}, \tag{6.51}$$

where I_{dark} is the dark current and t_{exp} is the exposure time. In our MOKE measurements, the use of a water-cooled sensor and short exposures ($t_{\text{exp}} \approx 0.02$ s) effectively minimizes dark current contributions.

Readout noise arises from charge-to-voltage conversion within the sensor's amplifiers, incorporating contributions from amplifier noise, quantization noise, and variations in readout electronics. It is typically quantified as the RMS noise in electrons:

$$N_{\text{readout}} = \sigma_{\text{readout}}, \tag{6.52}$$

where σ_{readout} is the standard deviation of readout noise. For the ORCA-Flash4.0 V3 camera used in this setup, the readout noise is as low as 0.8 electrons (median) or 1.4 electrons (RMS) [270], which is significantly lower than the signal levels typically measured and markedly better than those of conventional CCD cameras. As a hardware-dependent characteristic, readout noise is fixed for a given sensor design and cannot be modified by the user.

Finally, the QE is the ratio of the number of photoelectrons generated in a sensor to the number of incident photons at a given wavelength. It essentially quantifies a sensor's ability to convert incident photons into photoelectrons and is defined as:

$$QE(\lambda) = \frac{\text{Number of electrons generated}}{\text{Number of incident photons}} \times 100\%, \tag{6.53}$$

where λ is the wavelength of the incident light. Fig. 6.12a shows the QE of the ORCA-Flash4.0 as a function of wavelength, reaching the exceptionally high efficiency of nearly 70% at the operating wavelength used in this work.

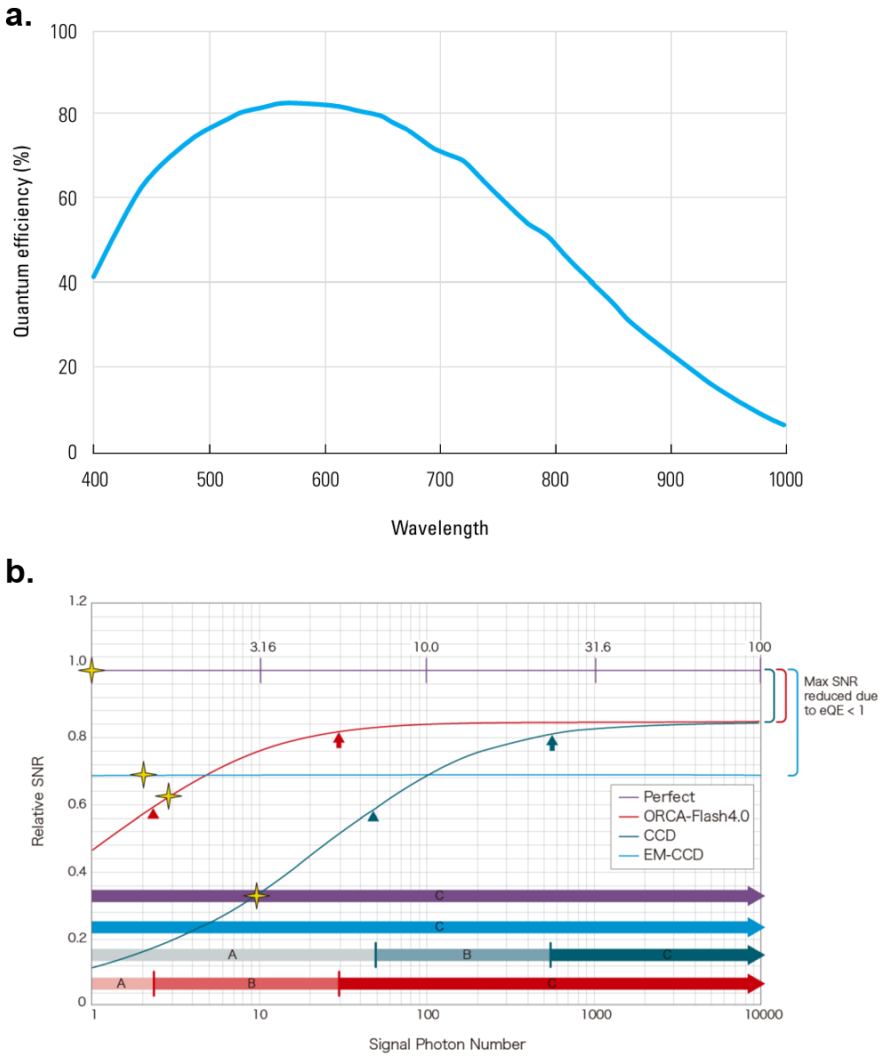

Figure 6.12: (a) Quantum efficiency of the ORCA-Flash4.0 vs. wavelength. Adapted from [270]. (b) SNR comparison across light intensity regimes for different cameras. Taken from [271].

The signal-to-noise ratio (SNR) is then defined as:

$$SNR = \frac{N_{\text{signal}}}{F_{\text{n}}\sqrt{N_{\text{signal}} + N_{\text{dark}} + N_{\text{readout}}^2}}, \tag{6.54}$$

where N_{signal} is the number of detected photoelectron, given by $N_{\text{signal}} = QE \cdot N_{\text{photons}}$, with N_{photons} the number of impinging photons. The noise factor F_{n} accounts for excess noise introduced by the sensor, typically $F_{\text{n}} \approx 1$ for CCD and CMOS sensors.

Fig. 6.12b compares the SNR across different light intensity regimes for various cameras. The purple line represents the theoretical SNR of an ideal camera, with stars marking the SNR = 1

threshold. The graph identifies three distinct regions: (A) a low-light regime dominated by readout noise, defining the lower sensitivity boundary; (B) an intermediate regime where readout noise and QE collectively influence SNR; and (C) a high-light regime where QE is the primary limiting factor. The ORCA-Flash4.0 sCMOS camera transitions into the noise-dominated region at significantly lower photon counts than CCDs, highlighting its superior low-light performance. In contrast, EM (Electron Multiplier) CCD cameras exhibit a relatively flat SNR curve but suffer an overall SNR reduction due to a noise factor of $F_{\mathrm{n}} \approx 1.41$ [271].

6.2.1.5 Detection of Kerr Signal

Although our setup incorporates a high-performance camera, a powerful LED light source, Köhler illumination, and an optimized skew angle between the polarizer and analyzer (as described so far), the detection of the Kerr signal still demands careful attention. Both the measurement process and the subsequent post-processing require additional steps to ensure reliable signal acquisition and interpretation.

Differential Image To enhance the Kerr signal and enable its detection, WF-MOKE setups commonly employ a differential imaging mode. In this technique, the sample magnetization is first saturated in one direction (UP or DOWN for polar MOKE), and an initial reference image is acquired. Subsequent images are then subtracted from this reference. Ideally, in the absence of noise, drift, and vibrations, the differential image would appear uniformly black, with bright regions emerging only when a magnetic domain reverses under an opposite applied field. This method significantly enhances contrast by orders of magnitude but has a major drawback: extreme sensitivity to drift and vibrations.

Non-magnetic structures within the image, such as devices or surface contaminants, become highly prominent if the reference image shifts slightly between acquisitions. This misalignment introduces strong edge contrast artifacts, often overshadowing the Kerr signal itself. These artifacts become particularly problematic when studying micrometer-sized magnetic structures, where edge effects can obscure the regions of interest. Consequently, the effective resolution of the magnetic signal is often lower than the optical resolution of the objective lens (see 6.2.1.6 for a more quantitative analysis).

Minimizing vibrations and drifts and avoid long measurements is therefore critical, as even small drifts can severely impact the signal. The primary sources of vibrations include:

- *Environmental*: people walking in the lab, elevators, vibrations transmitted from adjacent rooms or floors, etc.
- *Instrumental*: power supplies, mechanical pumps, cooling systems, etc.
- *Building*: structural, cooling/heating systems, etc.

While the main sources of drift comprise:

- *Mechanical*: Sample holder movement or instability, expansion/contraction of mounting materials, loose screws or misaligned components in the setup, etc.
- *Thermal*: temperature fluctuations in the lab affecting optical components, LED matrix heating, heat from current in magnetic coils, etc

- *Electronic*: slow variations in detector gain or response, instability in power supplies or voltage sources, camera sensor warm-up effects, etc.

To effectively reduce vibrations in the setup is a challenging task. The simplest actions include firmly securing all optical and mechanical components, avoiding the use of unnecessary power supplies or pumps during critical measurements, enclosing the setup in a black box, and replacing manual stages with motorized ones, which offer greater mechanical stability. A significant improvement is expected from upgrading the optical table legs from passive to active damping, a procedure currently in progress.

Bit Depth The last step to optimize contrast is tuning the bit depth (BD) of the camera. This parameter determines the number of bits each pixel uses to convert the analog signal ($N_{electrons}$) into a digital value, which is then displayed as an image on the computer. It corresponds to the number of grayscale levels the camera can show. If the BD is 1, each pixel can only be black or white. If the BD is 2, each pixel can represent $2^2 = 4$ different levels of grey. The ORCA-Flash4.0 camera can operate with a BD of 16, meaning it can distinguish 65,536 different grayscale levels. While this maximizes the ability to capture the full dynamic range (the difference between the highest and lowest signals that can be displayed), it makes it nearly impossible for the human eye to distinguish between very similar gray levels, requiring post-processing contrast enhancement.

To observe the Kerr contrast in real time, the effective BD used for display is usually reduced (typically to 8 or 9). This allows small Kerr signal variations to be mapped onto a more visually distinguishable grayscale range. However, this approach has drawbacks, such as increased risk of image saturation and amplified random noise. Nonetheless, it is useful for real-time imaging. When saving images, the full 16-bit depth is preserved, and external programs (such as ImageJ) can be used to analyze contrast more precisely.

Real-time Digital Image Processing To minimize noise and maximize the Kerr signal in our measurements, we have implemented real-time digital image processing in our custom LabView code (see Section 6.2.2 for details on the development and functionality of the program). Fig. 6.13a shows the raw differential image of a sharp magnetic domain, where distinguishing the contrast between the UP and DOWN states is nearly impossible. The linear profile along the yellow line, shown in Fig. 6.13e, does not reveal any variation in the MOKE signal. This is because, in the raw image, the contrast has been saturated during post-processing with IMAGEJ, while the line profile was taken from the unprocessed image. The same applies to all images in Fig. 6.13.

The most straightforward technique is averaging over a certain number of images. While this significantly reduces noise and enhances the overall SNR, it also drastically lowers the frame rate (from 12 frames per second with no averaging to 0.5 frames per second with an average of 50 frames). To quantify this effect, we consider a signal S with an associated noise variance σ^2. If the same signal is sampled n times, the total signal measured S_{T} is given by [272]:

$$S_{\mathrm{T}} = \sum_{i=1}^{n} S_i \approx n \cdot S_1, \tag{6.55}$$

where we assume the signal remains constant over the measurement ($S_1 \approx S_2 \approx \cdots \approx S_n$). The

total variance σ_{T}^2 associated with the summed signal is:

$$\sigma_{\mathrm{T}}^2 = \sum_{i=1}^{n} \sigma_i^2 \approx n \cdot \sigma_1^2, \tag{6.56}$$

where we again assume all variances are similar. The total RMS noise is then:

$$\sigma_{\mathrm{T}} = \sqrt{n}\sigma_1. \tag{6.57}$$

Finally, the SNR is given by:

$$SNR = \frac{S_{\mathrm{T}}}{\sigma_{\mathrm{T}}} = \frac{nS_1}{\sqrt{n}\sigma_1} = \sqrt{n}\frac{S_1}{\sigma_1}, \tag{6.58}$$

demonstrating that the total SNR improves by a factor of $\sqrt{n}$. This effect is evident in Fig. 6.13b and 6.13f, where the magnetic contrast becomes visible to the naked eye and the line profile shows a distinct jump, despite the remaining noise.

In addition to averaging, a convolution-based filtering procedure has been implemented. This method applies a predefined or user-defined matrix to recalculate each pixel's value as a weighted sum of its neighboring pixels. Depending on the matrix size and weights, this process can enhance contrast, blur the image, or highlight edges. In our LabVIEW setup, we primarily use a predefined 3×3 matrix. The impact of this filtering is shown in Fig. 6.13c and 6.13g, where the contrast and SNR are visibly improved.

Furthermore, a built-in LabVIEW low-pass filter (LPF) is applied to suppress high-frequency noise and smooth abrupt intensity variations. This operates similarly to a convolution but is optimized for enhanced image quality. Since our measurements focus on magnetic structures in equilibrium or undergoing slow magnetization changes, high-frequency components in the image are predominantly noise. The LPF effectively suppresses these components, reducing random fluctuations and improving clarity. Additionally, by averaging pixel values with their neighbors, the LPF smooths sharp transitions, making the image appear less pixelated and more visually coherent. This effect is demonstrated in Fig. 6.13d and 6.13h, where the contrast becomes significantly sharper, and the SNR reaches its highest level.

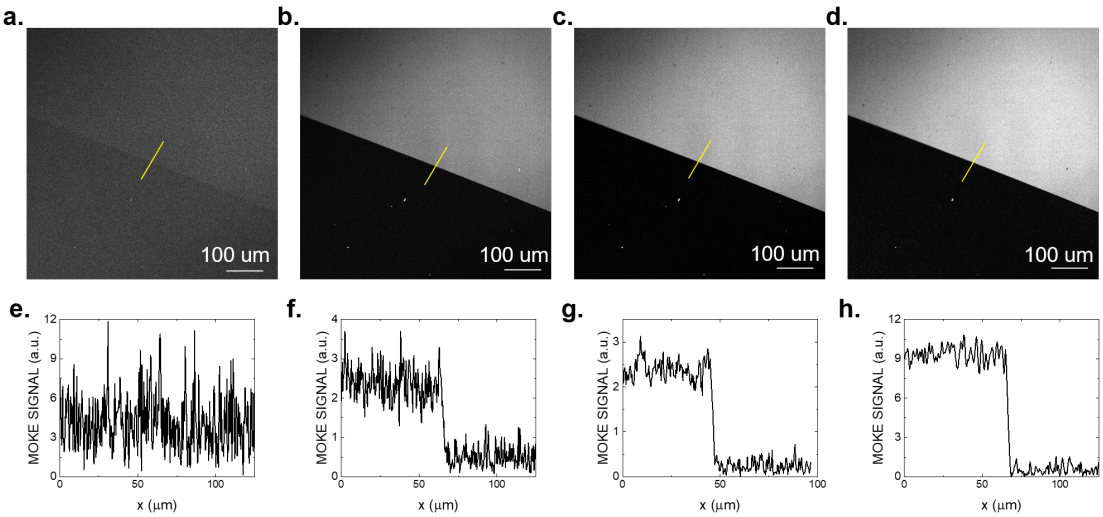

Figure 6.13: (a–d) MOKE images of a sharp magnetic domain with increasing SNR, and (e–h) corresponding line profiles along the yellow line. (a,e) no processing; (b,f) averaging; (c,g) convolution; (d,h) low-pass filter.

Finally, Fig. 6.14 compares the SNR across the four different measurement approaches, demonstrating an overall improvement by a factor of 50 between the first (differential image only) and the final fully optimized image.

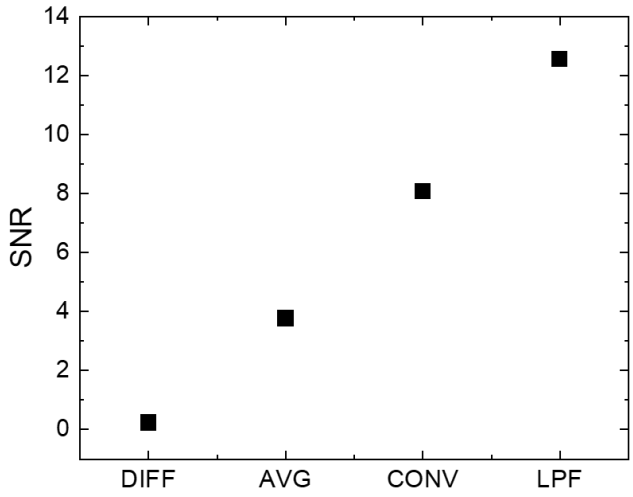

Figure 6.14: SNR calculated from the images in Fig. 6.13, showing an order-of-magnitude increase when all enhancements are applied.

6.2.1.6 Objective and Resolution

The objective used in this setup has a magnification of 20× and a numerical aperture (NA) of 0.28. The NA is a dimensionless number that quantifies the acceptance cone of an objective, determining its light-gathering ability and resolution. In an ideal optical system, the lateral resolution is fundamentally limited by the wavelength of the incoming light (λ) and the NA of the objective:

$$d_0 = \frac{\lambda}{2NA} = 812.5\text{nm} \tag{6.59}$$

for the described setup. In this case, the limiting factor is the relatively low NA, which is a trade-off required due to the long working distance of the objective, essential for building the custom setup.

To determine the actual resolution of the system, we first measured the physical size corresponding to a single pixel in the real image. This was achieved by analyzing a known reference pattern and using the relation:

$$\Delta x_{\text{pixel}} = \frac{lenght}{N_{\text{pixels}}} = 335\text{nm}, \tag{6.60}$$

resulting in a total field of view (FOV) of approximately $686 \times 686\mu\text{m}^2$.

Finally, by examining the line profiles in Fig. 6.13, we measured the step change in contrast in the MOKE signal. By counting the number of pixels between the minimum and maximum contrast levels, the optical resolution was determined to be approximately $\approx 1.5\mu$m.

6.2.1.7 Holder Design

The sample holder implemented in the MOKE setup was designed to enable real-time electrical measurements. It consists of two custom-designed PCB components: the chip holder and the base.

Fig. 6.15a shows the base mounted on the z-stage. It includes two BNC and two SMA connectors, allowing simultaneous connection to up to four instruments. Two of these lines are specifically designed with a $50\,\Omega$ impedance and incorporate an optional $50\,\Omega$ parallel resistance to the device, optimizing performance for nanosecond pulse measurements.

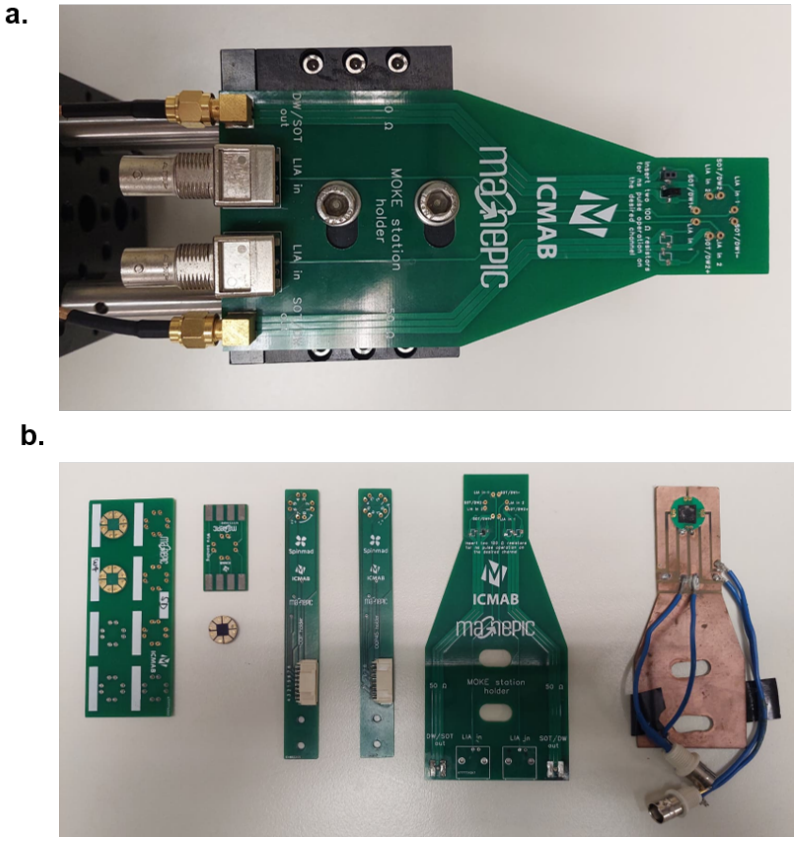

Figure 6.15: (a) MOKE base mounted on the z-stage. (b) PCB components implemented in the lab, including storage PCB, wirebonding PCB, chip holders for Hall setup (OOP, IP 0°, 45°, 90°, and 135°), MOKE base, and the previous MOKE holder for comparison.

The chip holder features eight gold contact pads that can be connected to the device via wire bonding. Each pad is soldered to a male pin, which connects to the base through female pins. This design ensures both electrical connectivity and mechanical stability, with connectors carefully selected for robustness.

The chip holder is compatible with various laboratory setups, including Hall effect measurements, ensuring a smooth and efficient workflow. Fig. 6.15b illustrates several PCB components developed in the lab. These include storage and wirebonding PCBs, multiple chip holders for different angular configurations in Hall setups, the MOKE base, and the previous MOKE holder for comparison. This PCB set was designed and developed collaboratively by myself and another PhD student, who generated the printable files. Several iterations were necessary to identify suitable male/female connectors that provide both mechanical stability and reliable electrical contact.

6.2.2 LabVIEW Program

A significant portion of the development time was dedicated to creating and optimizing the LabVIEW program used to control the camera, motorized stages, power supplies, LED, Hall probe, and external instruments. The program is structured into three main modules: LIVE, HYSTERESIS, and POSITION.

The LIVE module (Fig. 6.16 a) enables real-time visualization of both the optical and magnetic (background-subtracted) images of the sample under the microscope. Several image processing tools are available to enhance image quality, including averaging, background subtraction, convolution filtering, low-pass filtering, and bit depth adjustment. The exposure time is user-selectable, with a typical setting of 0.02 s. Magnetic fields (both IP and OOP) can be applied in various modes: as DC fields, pulsed (down to millisecond durations), or using a demagnetization function.

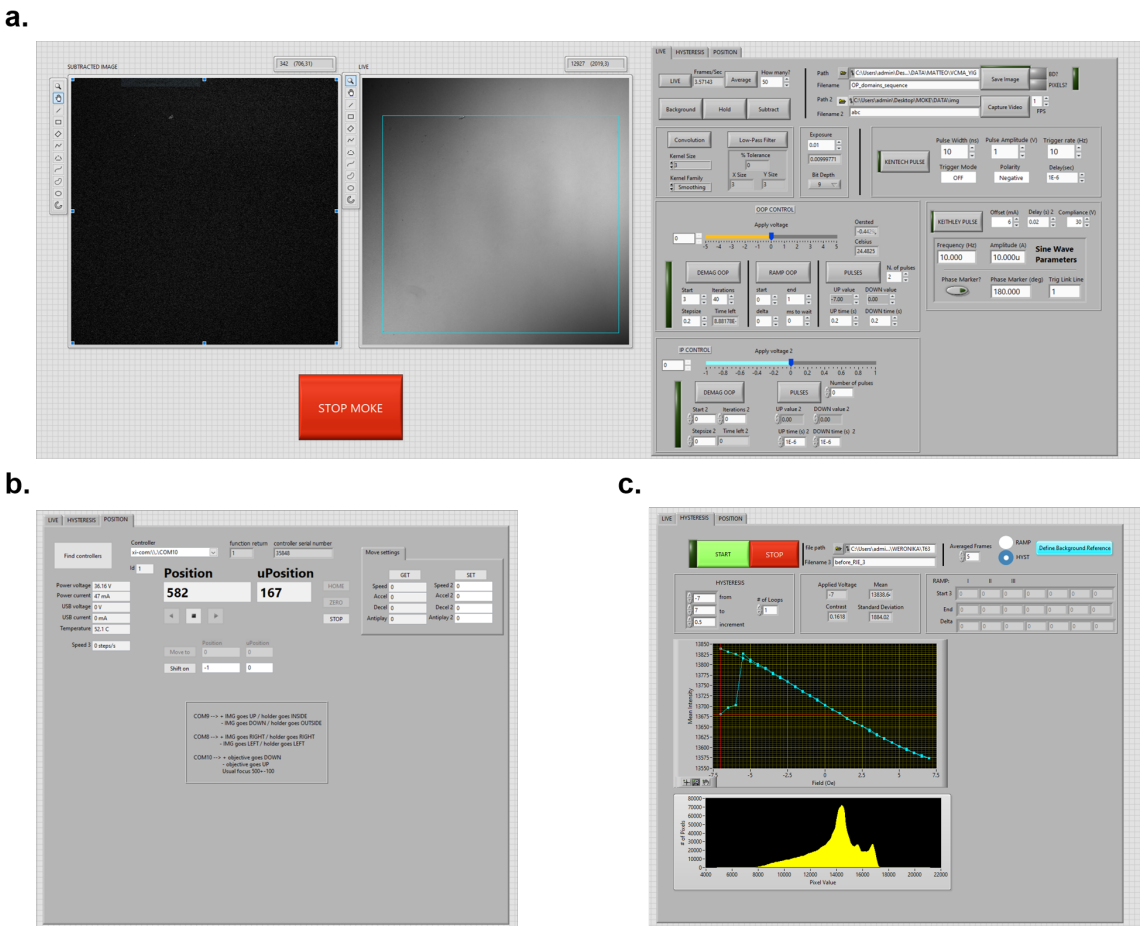

Figure 6.16: LabView user interface of the main MOKE program: (a) LIVE mode for parameter setup and magnetic image display, (b) motor control panel, and (c) hysteresis/ramp control section.

The demagnetization function applies alternating positive and negative pulses of decreasing amplitude. It serves two purposes: (i) when the maximum field amplitude exceeds the sample's coercivity, it can fully demagnetize the sample, allowing the observation of domain structures in the remanent state; (ii) when the amplitude remains below the sample's coercivity, the function demagnetizes the iron core of the magnet, reducing unwanted stray OOP fields that could interfere with sensitive measurements.

The IP field is particularly useful for electrical experiments such as SOT switching, DW depinning, and DW motion. Additionally, the program allows the application of current pulses via a Keithley 6221 (up to 100 mA, millisecond scale) and voltage pulses via a Kentech pulser (as short as

1 ns and up to 50 V amplitude). These capabilities are essential for studying fast magnetic dynamics.

Finally, the program includes options to save both the live and subtracted images simultaneously, with the ability to select the bit depth of the subtracted image. Saving in full 16-bit resolution preserves detailed magnetic information, which can later be extracted through post-processing. Video recording at various frame rates is also supported.

The POSITION module (Fig. 6.16 b) allows the user to control the motorized stages along the x, y, and z axes. These stages are essential for navigating across the sample and precisely focusing on its surface, all fully remotely. This remote control capability not only enhances ease of use but also reduces vibrations during measurements, improving image stability and quality.

The HYSTERESIS module (Fig. 6.16c) enables the analysis of a specific Region of Interest (ROI) while applying an OOP magnetic field, either through a linear ramp or a predefined hysteresis function. Once the measurement is initiated, the software plots the mean pixel intensity within the ROI as a function of the applied magnetic field. This functionality provides quantitative insight into the magnetic behavior of the sample, complementing the more qualitative observations obtained from the LIVE module.

To enhance flexibility, the module allows the user to perform either a full hysteresis loop or a series of connected ramps with variable step sizes. This is particularly useful for probing regions near critical OOP fields, such as around the coercive field, where finer resolution is beneficial. Since acquiring a full hysteresis loop can be time-consuming (taking up to several minutes depending on the averaging and total number of points), this modular approach helps reduce measurement time and minimizes time-dependent drift effects.

Furthermore, several fully automated programs have been implemented to make repetitive and time-consuming measurements more feasible and reproducible. These automation tools significantly enhance experimental efficiency and consistency. More details about one such automated program can be found in the Appendix of Chapter 7.

6.2.3 Cryostat Integration

During this thesis, a custom-made cryostat was designed and procured in collaboration with the company INSTEC. The system was specifically tailored to fit within the MOKE setup and to be compatible with existing electrical measurement protocols, offering up to four electrical connections.

The cryostat consists of three main components. The first is a mobile sample holder, designed to facilitate sample mounting and wire bonding. This holder can be detached for preparation and then connected to the main chassis via a custom cable for measurement. The second component is the main chassis, which is actively water-cooled to ensure thermal stability across a wide temperature range. It includes connections to both the temperature control system and external electronics, and has been designed to fit seamlessly into the custom MOKE setup (Fig. 6.17a). The third component is a lid featuring a precision optical window, aligned to allow the incident beam to reach the sample and the reflected Kerr signal to be collected during MOKE experiments (Fig. 6.17b).

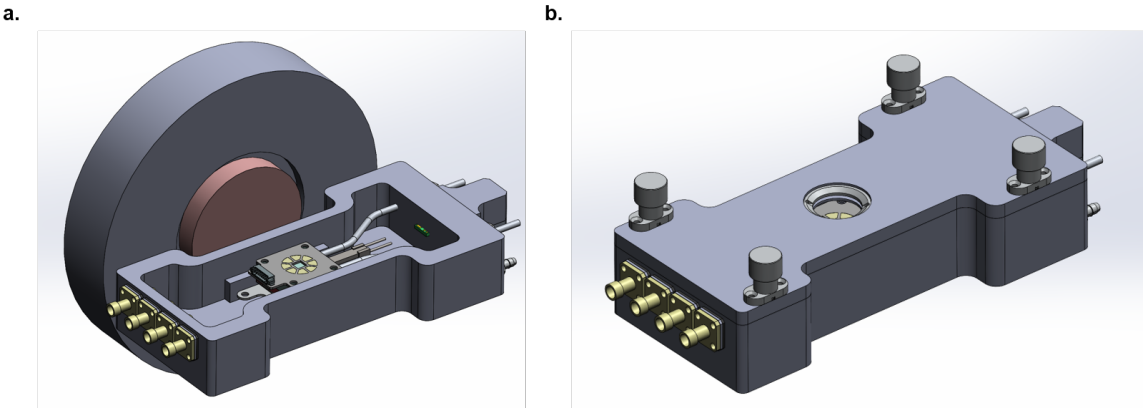

Figure 6.17: 3D renderings of the cryostat: (a) main chassis positioned within the IP magnets; (b) cryostat with the lid on, showing the optical window.

The system enables operation across a temperature range from −190°C (using liquid nitrogen) to 400°C, with a temperature stability of ±0.01°C. Temperature regulation is provided by the Instec mK2000 precision temperature controller, which supports programmable heating and cooling rates, as well as remote control via external software. Cooling is delivered by a dedicated LN_2 unit consisting of a 3-liter Dewar, cryogenic pump, ported lid, and insulated tubing.

Although the cryostat is currently integrated into one of the electrical Hall effect measurement setups, further upgrades are required for its implementation in the MOKE system. Specifically, a new custom sample mount must be designed to ensure mechanical compatibility and optical alignment within the MOKE geometry. In addition, the existing OOP magnetic coils will need to be replaced or upgraded. Due to the cryostat's bulk, the distance between the sample and the magnet increases significantly, requiring stronger magnetic fields to effectively control magnetization, especially at low temperatures.

These improvements are scheduled for the near future. Once implemented, they will enable temperature-dependent MOKE studies on magnetic garnet films, including access to the magnetization compensation point. This will open the door to exploring rich spintronic phenomena such as zero-moment spin dynamics, enhanced SOTs, and ultrafast DW motion in compensated ferrimagnets.

Chapter 7

Study of Dzyaloshinskii–Moriya Interaction at TbIG/Heavy Metal Interfaces

Contents

This work is adapted from a publication authored by the candidate and published in *Advanced Functional Materials* [61]. It builds directly upon the theoretical framework established in the previous chapters, where the microscopic origins of the DMI and its influence on DWs and spin textures were discussed. In the present chapter, these concepts are applied experimentally to TbIG-based heterostructures, providing a concrete demonstration of how interfacial symmetry breaking and SOC manifest in real materials.

In particular, we investigate the interfacial DMI in the ferrimagnetic insulator TbIG, examining its dependence on the film thickness and on different NM overlayers. By correlating the DMI with interfacial spin transport measurements and atomically resolved electron microscopy, we identify the TbIG/NM interface as the dominant source of DMI in these structures. Furthermore, the insertion

of a Cu spacer layer is shown to substantially modify the interfacial DMI, an effect attributed to a long-range interaction between TbIG and the Cu/NM interface. Complementary DFT calculations on analogous structures qualitatively support these experimental findings and the proposed interpretation.

Altogether, these results provide new insight into the origin and tunability of interfacial DMI in ferrimagnetic insulators, offering a pathway to engineering chiral spin interactions in complex oxide heterostructures. Beyond their fundamental relevance, the findings hold direct implications for the design of next-generation spintronic devices based on DWs and skyrmions.

The remainder of this chapter is organized as follows: Section 7.2 introduces the preparation and characterization of the TbIG/NM heterostructures. Section 7.4.1 presents the thickness dependence of the DMI and its correlation with magnetic anisotropy. Section 7.4.2 discusses the role of Cu spacers and compares Pt and W overlayers, supported by structural characterization. Section 7.4.3 summarizes the DFT calculations and their relation to the experiments. Finally, Section 7.5 provides the conclusions and perspectives of this study.

7.1 Background

Chiral magnetic interactions have attracted enormous attention in recent years, both for the richness of the underlying physics and for their potential in next-generation spintronic technologies [273, 274, 275, 276, 277]. Among these interactions, the DMI occupies a central place. This antisymmetric exchange interaction underlies a wealth of chiral spin textures, including Néel DWs [170, 278], magnetic skyrmions [181, 183], and even more exotic structures such as hopfions [279, 280].

The coexistence of DMI and SHE in FM/HM systems such as CoFeB/W or Co/Pt, in which interfacial DMI stabilizes chiral spin textures while the HM provides strong SHE enables efficient current-induced manipulation of magnetic textures, including SOT-driven magnetization switching [281, 282], DW motion [206, 200], and skyrmion dynamics [283].

More recently, attention has expanded from metallic systems to magnetic insulators, and in particular to the family of REIGs [28, 51, 56, 52]. This work mostly focuses on REIGs, which are especially attractive for spintronics owing to their tunable magnetic anisotropy, low damping, and unique optical properties, all of which can be engineered through strain, stoichiometry, and composition [221]. When combined with heavy metals, REIGs allow for the electrical manipulation of magnetization via SOTs [24, 284], opening pathways to efficient insulator-based spintronic devices. Understanding and controlling DMI in REIG-based heterostructures is thus a fundamental step toward the development of such devices.

Despite intensive research on prototypical REIGs such as $Y_3Fe_5O_{12}$ (YIG) and $Tm_3Fe_5O_{12}$ (TmIG), the reported values of the interfacial DMI vary widely, sometimes by more than an order of magnitude even within the same material system [285]. This lack of consistency stems from both experimental and material challenges: different measurement techniques rely on different assumptions—ranging from DW depinning [51, 52], AHE analysis [56, 57, 59], Brillouin light scattering [55, 36], or NV magnetometry [28], and REIG growth conditions can strongly affect stoichiometry, strain, and interface quality [209, 208]. As a result, both the magnitude and the microscopic origin of interfacial DMI in REIGs remain under debate. In particular, whether the dominant contribution originates at the substrate/REIG interface [28, 51, 52, 27, 53, 54, 55] or at the REIG/HM interface [56, 57, 58, 59, 54, 60, 36] is still unresolved. A summary of the main literature is provided in a

table in Appendix 7.A.

In this context, TbIG represents a particularly promising yet scarcely explored REIG for the study of interfacial DMI. TbIG grown on $Gd_3Ga_5O_{12}$ (GGG) substrates exhibits PMA due to compressive strain [220]. It also possesses one of the highest magnetic compensation temperatures among REIGs, with bulk $T_{MC} \approx 248$ K [221]. In ultrathin films, however, T_{MC} can be tuned over a wide range, from about 190 K [237] to above 350 K [220, 286], through growth method, strain, stoichiometry, and thickness [220, 237, 287, 288]. At compensation, ferrimagnets behave dynamically like antiferromagnets, supporting ultrafast magnetization dynamics [226, 62]. The ability to achieve and tune T_{MC} near room temperature makes TbIG a unique candidate for chiral spintronic applications, where interfacial DMI plays a decisive role.

In this chapter, we present a systematic study of the interfacial DMI in TbIG/HM heterostructures. The effective DMI field (H_{DMI}) is quantified using current- and field-driven DW depinning measurements across a range of TbIG thicknesses (1.9–7.9 nm). We find that the DMI energy density D scales with the inverse TbIG thickness, confirming its interfacial nature. Combining these results with interfacial spin transport measurements, EELS, and high-angle annular dark-field scanning transmission electron microscopy (HAADF-STEM), we identify the TbIG/HM interface as the primary source of DMI. Interestingly, insertion of a Cu spacer between TbIG and Pt reduces the DMI by about 70%, while the same Cu insertion between TbIG and W enhances the DMI by about 40%. This striking contrast suggests the presence of additional, non-local contributions to the DMI in TbIG, a conclusion further supported by DFT calculations. Our findings reveal new pathways to engineer interfacial DMI in REIG-based heterostructures and provide a foundation for the design of chiral spintronic devices based on TbIG.

7.2 TbIG Thin Film Characterization

Heterostructure and Device Preparation

TbIG thin films with nominal thicknesses of 3, 4, 5, 7, and 9 nm were deposited on (111)-oriented GGG substrates by r.f. magnetron sputtering, following the optimized growth recipe described in Chapter 5. Due to intermixing at the GGG/TbIG interface, a magnetically dead layer of approximately 1.1 nm is formed, as determined in Section 7.2. Unless otherwise specified, the effective magnetic thicknesses, obtained by subtracting this dead layer, will be used throughout the discussion.

The NM overlayers consisted of Pt(4 nm), Cu(1.5 nm)/Pt(4 nm), W(4 nm)/Ti(2.5 nm), and Cu(1.5nm)/W(4 nm)/Ti(2.5 nm), where the Ti layer serves as a capping layer to prevent oxidation of W. These were deposited *in situ* by d.c. magnetron sputtering at room temperature without breaking the vacuum. For electrical and magneto-optical measurements, Hall bar devices incorporating DW tracks and Hall arms were fabricated by optical lithography and reactive ion etching (Fig. 7.1). No additional contact layers were deposited afterward.

Perpendicular Magnetic Anisotropy and Compensation Temperature

TbIG layers grow under compressive strain on GGG (111) substrates, which stabilizes PMA, as discussed in Chapter 5. The magnetization reversal was first probed by polar MOKE microscopy.

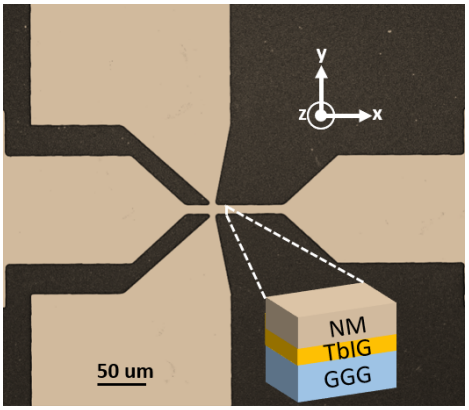

Figure 7.1: Optical micrograph of a Hall bar device used for MOKE and electrical measurements. The heterostructure composition is shown in the inset, and the coordinate system is indicated in the top right.

Fig. 7.2a (left axis) shows the Kerr rotation signal for a TbIG(2.9 nm)/Pt(4 nm) film as a function of an OOP magnetic field H_z. The square hysteresis loop, with nearly 100% remanence and coercive field of about 30 mT, confirms robust PMA. The corresponding Hall resistance R_H, measured on a patterned device in the same field geometry (Fig. 7.2a, right axis), reproduces the hysteresis and originates from SMR-AHE [25]. This signal is analogous to the AHE in metallic ferromagnets, but reduced in magnitude due to the insulating character of TbIG.

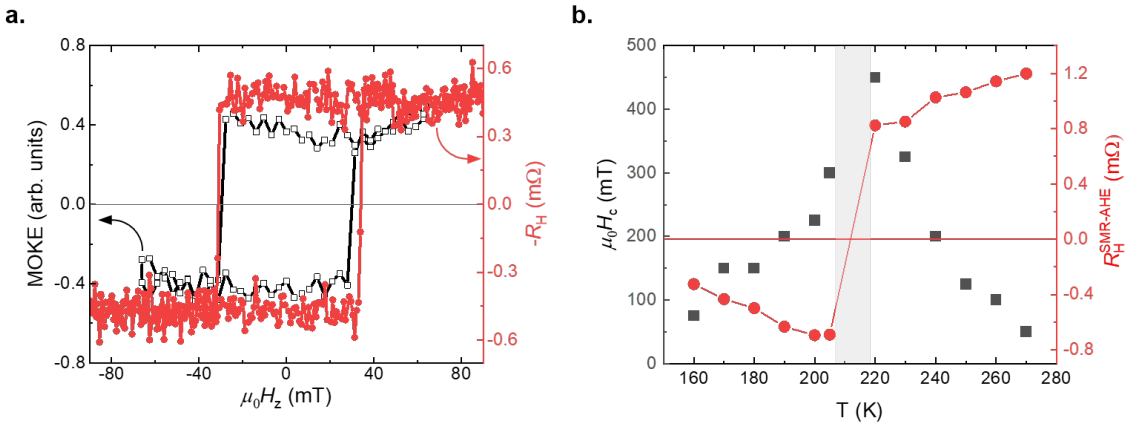

Figure 7.2: (a) OOP hysteresis loops measured by MOKE (black squares, left axis) and SMR-AHE (red dots, right axis) for TbIG(2.9 nm)/Pt(4 nm), confirming PMA. (b) Compensation temperature T_M estimated from the coercive field (black squares, left axis) and from the sign change of the SMR-AHE signal (red dots, right axis).

The magnetic compensation temperature of sputtered TbIG was measured on GGG/TbIG(5.9 nm)/Pt(1.2 nm)/Ti(10 nm) using a PPMS (Fig. 7.2b). A series of OOP hysteresis loops were recorded at different temperatures ranging from 100 K to 280 K, and both the coercivity and the SMR-AHE amplitude were quantified. From the divergence of the coercivity H_c (black squares, left axis), we estimate $T_{MC} \approx 215$ K, in agreement with previous reports [237]. A concurrent sign reversal in the SMR-AHE signal (red dots, right axis) further confirms the compensation, reflecting the change of

dominant magnetic sublattice across T_{MC}.

Magnetic Anisotropy Field

To quantify the PMA, we measured R_H under an IP magnetic field H_x. In this configuration, R_H probes the OOP magnetization component, which rotates coherently into the plane as the field increases. Ideally, it is not possible to completely cancel the OOP component of the field, but as long as the angle remains small, it does not affect the measurement significantly and, in fact, helps ensure its reliability. A representative measurement is shown in Fig. 7.3a (black curve), together with a macrospin simulation (orange curve) (details on the Scilab simulations can be found in Appendix 7.B).

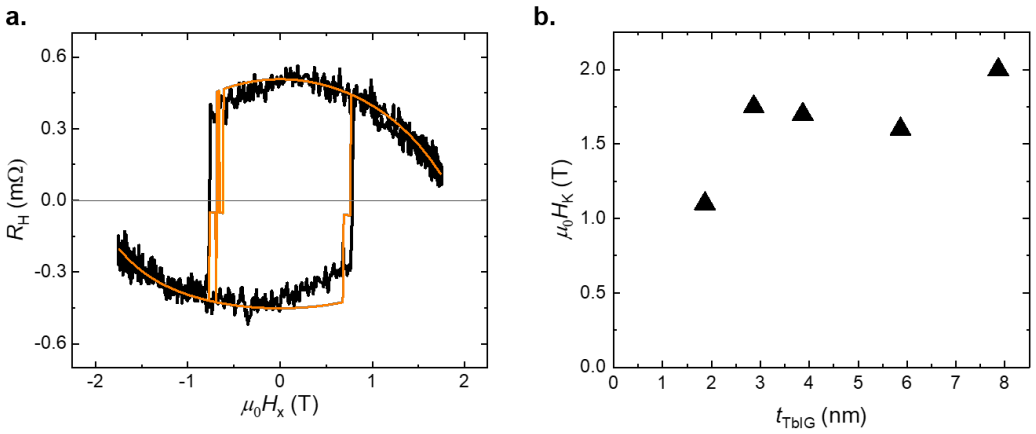

Figure 7.3: (a) IP field sweep of the Hall resistance R_H used to extract the effective anisotropy field H_K. The orange curve shows the macrospin simulation. (b) Effective anisotropy field H_K as a function of TbIG thickness. Error bars are smaller than the marker size.

In this geometry, the Hall resistance is primarily determined by the SMR-AHE contribution, which depends on the z-component of the magnetization. Ideally, this signal decreases monotonically from its maximum at $H_x = 0$ to zero at high fields, where the magnetization lies fully IP. In practice, however, slight misalignments introduce a small SMR contribution, which we include in the simulations to reproduce the experimental asymmetry.

The macrospin simulations were implemented in a custom SciLab code, where the equilibrium magnetization orientation is obtained by minimizing the total torque due to the external field and the anisotropy field. By varying the anisotropy field parameter, we reproduce the experimental data and extract the effective anisotropy field:

$$H_K = \frac{2K_{\mathrm{eff}}}{\mu_0 M_s}, \tag{7.1}$$

where K_{eff} is the effective anisotropy constant. The extracted values of H_K for all TbIG thicknesses are summarized in Fig. 7.3b. We find that H_K is consistently above 1 T and increases with increasing TbIG thickness, confirming strong and thickness-dependent PMA in our films.

Current-Induced Switching

The finite R_H signal observed in Fig. 7.2a demonstrates substantial spin current transfer into TbIG. To evaluate the efficiency of the resulting SOTs, we performed current-induced switching experiments [25]. Fig. 7.4a shows a representative loop for TbIG(5.9 nm)/Pt(4 nm). An IP bias field H_x was applied to break symmetry, after which current pulses of 8 ms duration with decreasing amplitude were injected. The critical switching current density was determined as $j_c = 0.9 \times 10^{11}$ A/m^2 under an applied field of 260 mT.

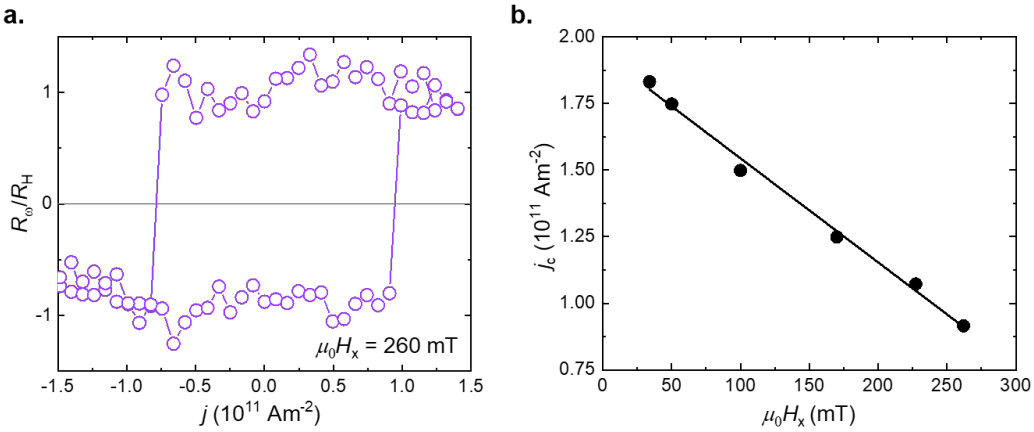

Figure 7.4: (a) Current-induced switching loop under an IP bias field of 260 mT for TbIG(5.9 nm)/Pt(4 nm). (b) Critical switching current density j_c as a function of the IP magnetic field H_x. A linear fit highlights the expected trend.

The dependence of j_c on H_x is shown in Fig. 7.4b. As expected, j_c decreases linearly with increasing IP field, consistent with the progressive reduction of the switching barrier [289]. Despite the longer pulse duration employed in our measurements (8 ms), the extracted switching current densities are consistent with those reported for significantly shorter pulses (200 μs) [29]. This supports the high efficiency of SOTs in our heterostructures, although thermal activation effects may contribute to the observed switching behavior.

Saturation Magnetization

The saturation magnetization M_s of all samples was measured at room temperature using SQUID magnetometry. Fig. 7.5a shows a representative M–H loop for TbIG(2.9 nm). Due to the noisy signal, M_s was determined by averaging the up and down branches, with the noise amplitude providing an estimate of the error.

The extracted M_s values are summarized in Fig. 7.5b for films of varying thicknesses, alongside a 50 nm reference. A clear reduction of M_s is observed for thinner films, consistent with previous reports on garnets [31]. A hyperbolic tangent fit yields a critical thickness of approximately 10 nm, above which the films recover bulk-like behavior. In the thick-film limit, we obtain $M_s \approx 74$ kA/m, notably higher than the bulk tabulated value of 20 kA/m [220]. This discrepancy correlates with the reduced T_{MC} of our films [237], which leads to an enhanced M_s at room temperature.

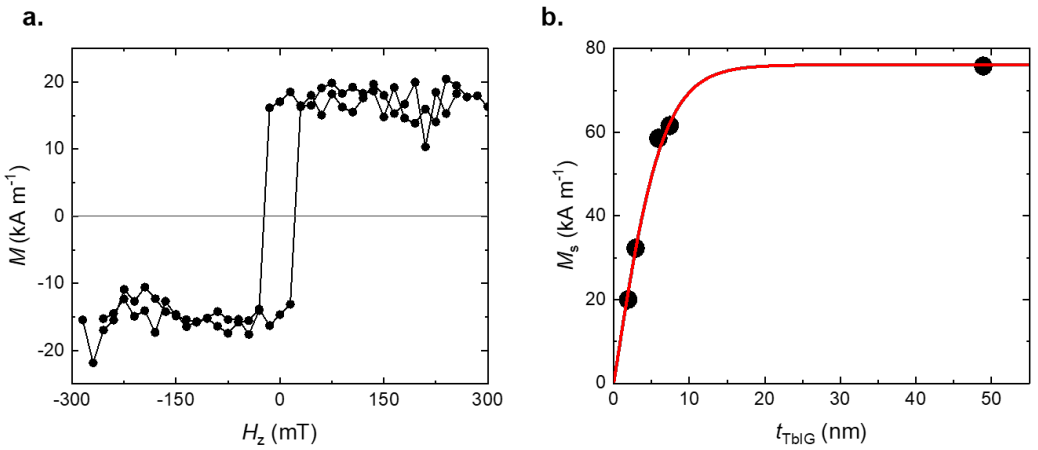

Figure 7.5: (a) Example M–H loop of TbIG(2.9 nm) measured by SQUID. M_s was estimated by averaging the saturation values of the up and down branches. (b) Saturation magnetization M_s as a function of TbIG thickness. The red line is a *tanh* fit to the data.

Exchange Stiffness Estimation

The exchange stiffness constant (A) is a key micromagnetic parameter that governs the characteristic length scales of spin textures such as DWs and skyrmions. Direct determination of A in ultrathin ferrimagnetic insulator films, however, is notoriously difficult due to the extremely low magnetic volume and the consequent limitations of standard magnetometry close to the ordering temperature (T_N). For this reason, we adopted an indirect estimation method based on the approach originally proposed by Slonczewski [290].

The method relies on scaling the exchange stiffness of TbIG relative to that of YIG using the following expression:

$$A_{\mathrm{TbIG}}(T, T_N) = A_{\mathrm{YIG}} \times \frac{T_{N,\mathrm{TbIG}} - T}{T_{N,\mathrm{YIG}} - T}, \tag{7.2}$$

where T is the measurement temperature, here fixed at room temperature ($T = 300$ K). The constants $A_{\mathrm{YIG}} = 4.15\ \mathrm{pJ\,m^{-1}}$ and $T_{N,\mathrm{YIG}} = 560$ K are taken from the literature [291]. The only unknown in this relation is $T_{N,\mathrm{TbIG}}$, the Curie temperature of the TbIG films.

Direct determination of $T_{N,\mathrm{TbIG}}$ via $M_s(T)$ measurements using SQUID magnetometry is impractical in our case, as the extremely low signal-to-noise ratio near T_N prevents reliable extrapolation. Instead, we use the SMR-AHE as a proxy. Although SMR-AHE does not directly measure M_s, its amplitude scales with the interfacial magnetization and is expected to vanish when $M_s \to 0$, i.e., as $T \to T_N$. This makes it a suitable indirect probe of $T_{N,\mathrm{TbIG}}$.

Fig. 7.6a shows exemplary transverse resistance (R_H) measurements as a function of temperature for a TbIG(2.9 nm) sample. The SMR-AHE signal decreases progressively with increasing temperature and eventually vanishes above 380 K, where the easy axis reorients from OOP to IP. In Fig. 7.6b, the normalized $R_H^{\mathrm{SMR-AHE}}$ values for all investigated TbIG/Pt samples are plotted. By fitting the rapid decay of $R_H^{\mathrm{SMR-AHE}}$ with the expression

$$R_H^{\mathrm{SMR-AHE}} = a \times (T - T_N)^{\beta}, \tag{7.3}$$

we extract the Curie temperatures T_N for each thickness (Fig. 7.6c, left axis). These T_N values are then used in Slonczewski's relation to calculate A_{TbIG} at room temperature (Fig. 7.6c, right axis).

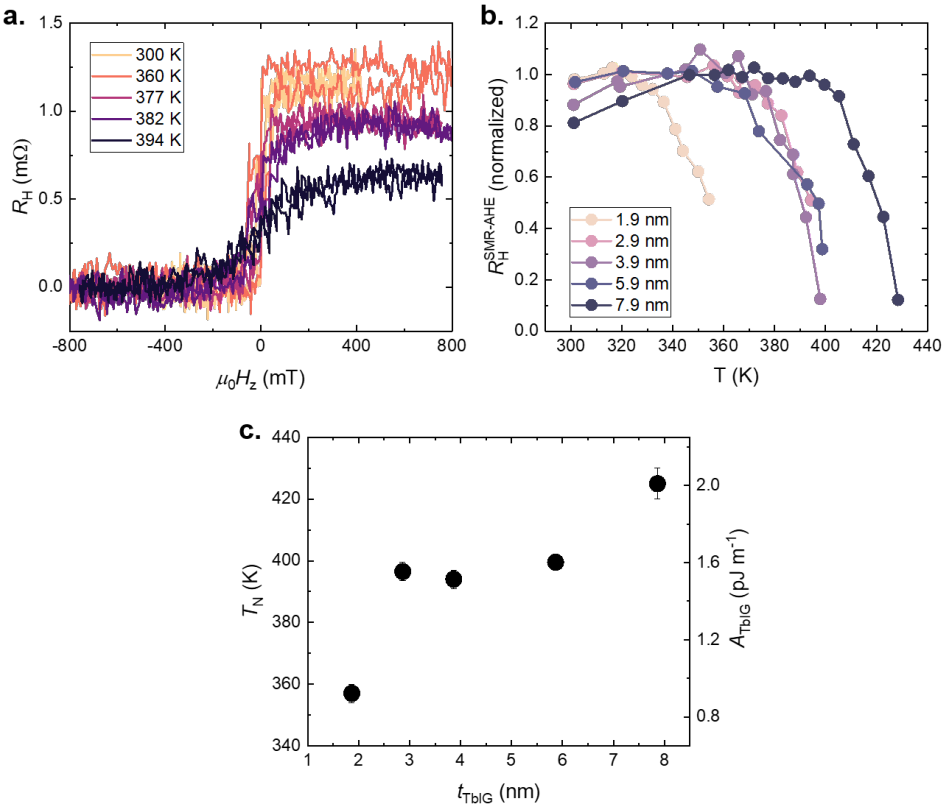

Figure 7.6: (a) Transverse resistance measured for the TbIG(2.9 nm) sample at different temperatures, showing the progressive suppression of the SMR-AHE signal with increasing T. (b) Normalized SMR-AHE resistance as a function of T for the TbIG/Pt series, from which T_N is extracted. (c, left axis) Extracted T_N values as a function of TbIG thickness. (c, right axis) Exchange stiffness A_{TbIG} calculated using the extracted T_N values and Slonczewski's formula.

In summary, by combining SMR-AHE thermometry with Slonczewski's scaling relation, we obtain reliable estimates of the exchange stiffness A_{TbIG} for ultrathin TbIG films. This approach allows us to circumvent the limitations of direct SQUID magnetometry and provides thickness-dependent A values that are essential for the quantitative analysis of DMI and DW dynamics in the following sections.

Structural Analysis

The interfacial DMI is highly sensitive to both the bulk crystallinity and the interface quality of the magnetic layers [292, 293]. To address this, we characterized the structural properties of TbIG films and their interfaces with GGG and Pt by HAADF-STEM and EELS. The STEM measurements were performed by M. Villa and J. Gasquez and the sample studied was deposited by S. Damerio.

Cross-section samples for STEM experiments were prepared using a focused ion beam (FIB)

system (Thermo Fischer Scios 2) at 30 kV and 16 kV for thinning and polishing steps, respectively, followed by final cleaning steps at low voltages of 5 kV and 2 kV. Prior to this, a 15 nm protective carbon layer was deposited by thermal evaporation using a High Vacuum Sputter Coater (Leica ACE 600) to prevent initial FIB-ion damage. HAADF-STEM imaging was performed using a double aberration-corrected Thermo Fischer Scientific Spectra 300 electron microscope operated at 300 kV and equipped with a Schottky field emission gun (X-FEG) and a Gatan GIF Continuum K3 electron energy loss spectrometer.

Fig. 7.7a displays a cross-sectional HAADF-STEM image of a representative GGG/TbIG(30 nm)/Pt(4 nm) heterostructure. The TbIG layer is observed to grow epitaxially in the single-phase cubic garnet structure across the entire field of view. This is highlighted in the orange-framed inset, where the atomic lattice of TbIG viewed along the [-110] direction is superimposed. The GGG/TbIG interface shows excellent structural continuity, with no evidence of relaxation or misfit dislocations, indicating fully strained growth.

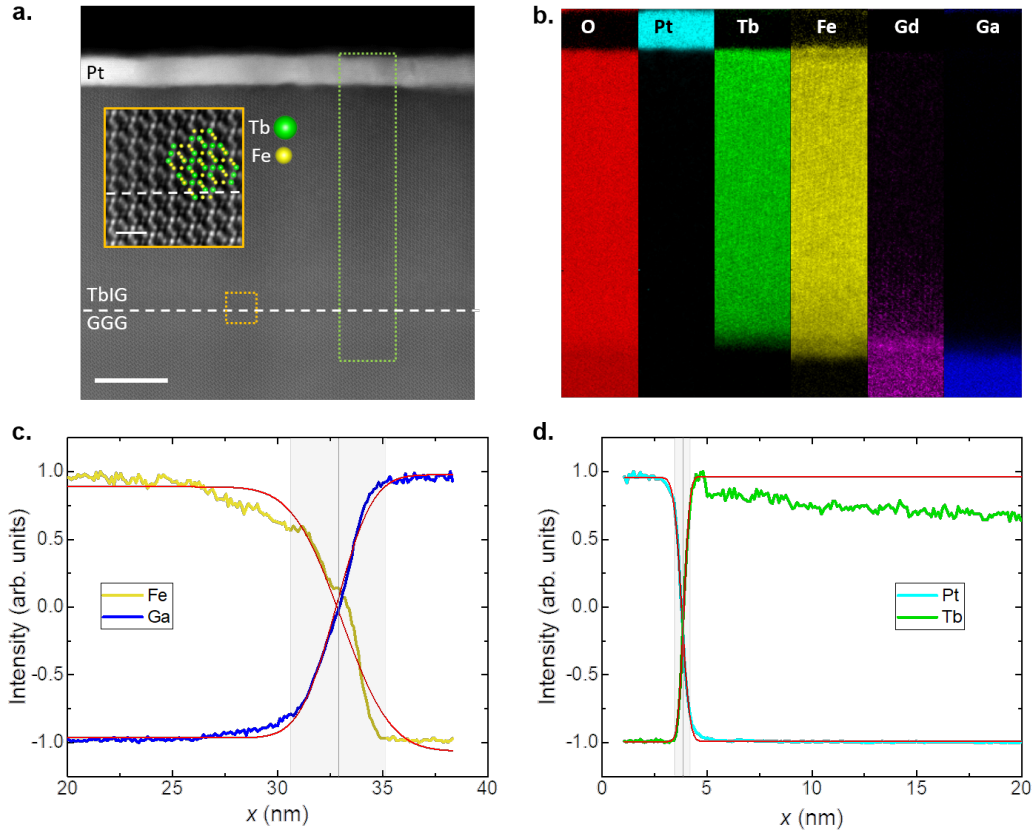

Figure 7.7: (a) Cross-sectional HAADF-STEM image of the GGG/TbIG(30 nm)/Pt(4 nm) heterostructure, confirming the high-quality epitaxy of TbIG and the sharp interface with the Pt overlayer. The orange inset shows the atomic-resolution view of the substrate/film interface, with a superimposed structural model along the [-110] zone axis. The green dashed rectangle marks the region where EELS elemental maps were acquired. (b) EELS elemental maps of the selected region. (c,d) Concentration profiles of Fe/Ga at the bottom interface and Pt/Tb at the top interface, respectively. Solid red lines are error-function fits used to estimate the total intermixing thickness (shaded area). Scale bar: 10 nm in (a), 1 nm in inset.

The EELS elemental maps acquired in the region marked in green (Fig. 7.7b) reveal the elemental distributions across the interfaces. At the bottom interface, substantial intermixing of Fe and Ga is observed. Since Ga^{3+} is a small, non-magnetic ion that can occupy both octahedral and tetrahedral sites typically filled by Fe^{3+}, this substitution locally disrupts the magnetic network. By fitting the Fe and Ga line profiles (Fig. 7.7c) with an error function, the total intermixed thickness at the GGG/TbIG interface is estimated to be 4.5 ± 0.9 nm. While we do not have direct evidence of the magnetization state of the intermixed layer, we assume that Ga substitution significantly degrades the magnetic ordering, resulting in a region with negligible net magnetization. This assumption is motivated by the fact that Ga^{3+} ions dilute the magnetic Fe^{3+} lattice and disrupt superexchange interactions. We acknowledge, however, that the intermixed region could exhibit more complex magnetic behavior, such as paramagnetism or antiferromagnetic coupling with TbIG, similar to what has been reported for $Gd_3Fe_5O_{12}$-like phases at YIG/GGG interfaces. In the absence of direct magnetic characterization, we conservatively treat this region as effectively nonmagnetic for the purpose of estimating the magnetic thickness. Assuming that half of the intermixed zone on the TbIG side is nonmagnetic, we deduce an effective magnetic dead layer thickness of 1.1 ± 0.2 nm. This value is consistent with previous reports [287] and is used throughout this thesis to correct the effective magnetic thickness of TbIG films.

Intermixing at the upper TbIG/Pt interface is far less pronounced. The Pt and Tb concentration profiles (Fig. 7.7d) yield an intermixed region of only 0.7 ± 0.1 nm. Given its small value (approximately six times smaller than that of the GGG/TbIG interface), this contribution is considered negligible for the magnetic properties of the films. It is also consistent with expectations based on ionic size, as Pt atoms are more likely to occupy the larger dodecahedral sites nominally filled by Tb^{3+}.

Interestingly, the Tb and Gd maps reveal significant interdiffusion across the entire TbIG layer thickness, with Gd from the substrate gradually diffusing into TbIG up to the surface in contact with Pt (Fig. 7.8). However, since both ions occupy equivalent crystallographic sites in the garnet structure and have comparable magnetic moments [221], this intermixing is expected to have only a minor influence on the net magnetic response. The dominant effect of interdiffusion on magnetism thus arises from Fe/Ga mixing at the substrate interface, which is responsible for the observed magnetic dead layer.

In summary, STEM-EELS analysis demonstrates that TbIG films grow epitaxially on GGG with excellent structural quality, but intermixing at the lower interface introduces a well-defined magnetic dead layer. In contrast, the upper TbIG/Pt interface remains sharp. These findings confirm that the effective magnetic thickness of sputtered TbIG must be corrected for interfacial intermixing, a critical step for the quantitative analysis of interfacial DMI presented in the following sections.

7.3 DMI Quantification Based on Domain Wall Depinning

To quantify the DMI effective field, we used the DW depinning method that exploits the unique property that the damping-like SOT interacts predominantly with the Néel component (i.e., parallel to x) of the DW's internal spins [170, 200].

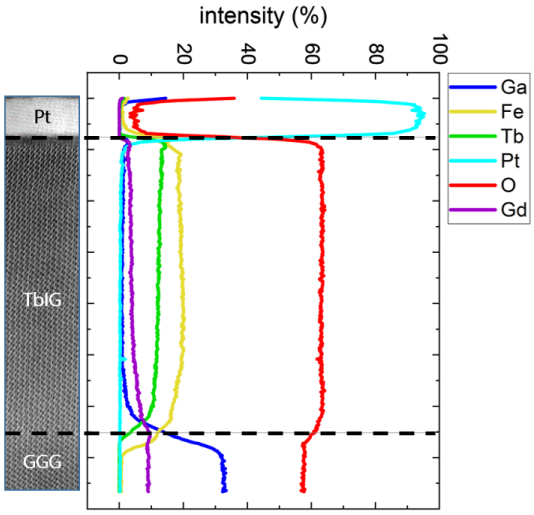

Figure 7.8: Complete EELS elemental maps of GGG/TbIG(30 nm)/Pt(4 nm). Horizontal dashed lines mark the top and bottom interfaces. The maps illustrate elemental distributions across the heterostructure and highlight the contrast between strong Ga/Fe intermixing at the bottom interface and the sharp Pt/Tb interface at the top. Gd diffusion across the entire TbIG layer is also visible.

Experimental Procedure

As a representative example, we describe here the typical experimental procedure applied to a TbIG(2.9 nm)/Pt(4 nm) device. First, a reversed domain is created by SOT switching with a current pulse flowing through the track and splitting into the Hall arms. The sample magnetization is initially saturated in one direction by applying an OOP magnetic field larger than the coercivity for 400 ms. Then, a reversed domain is generated by applying a constant IP magnetic field along the x-axis and injecting a current pulse of duration $t_{p,c} = 20$ ms. When the injected current splits into the Hall arms, the SOT switching stops, leaving behind a DW precisely at the position where the current path diverges. The DW stabilizes at the nearest natural pinning site, and this procedure is repeated multiple times to ensure reproducibility.

The deterministic character of SOT switching guarantees that the DW forms consistently at the edge of the Hall cross (Fig. 7.9a). For the depinning measurements, we inject a low-amplitude d.c. current I along the bar, together with an IP bias field (H_x), while sweeping an OOP field (H_z). The depinning field H_{dep} is defined as the field at which the DW escapes its initial pinning site (Fig. 7.9b). An example of a depinning event, corresponding to a jump in MOKE intensity, is shown in Fig. 7.9c. A detailed description of the automated Labview routine used for these measurements is given in Appendix 7.C.

Current-Induced Contributions to the Depinning Field

The injected current I is expected to influence H_{dep} in two ways: *i*) it increases the device temperature and hence lowers H_{dep}; and *ii*) it exerts a damping-like SOT field H_{DL} on the DW, provided that the DW has a Néel component. The first effect is quadratic in current and independent of

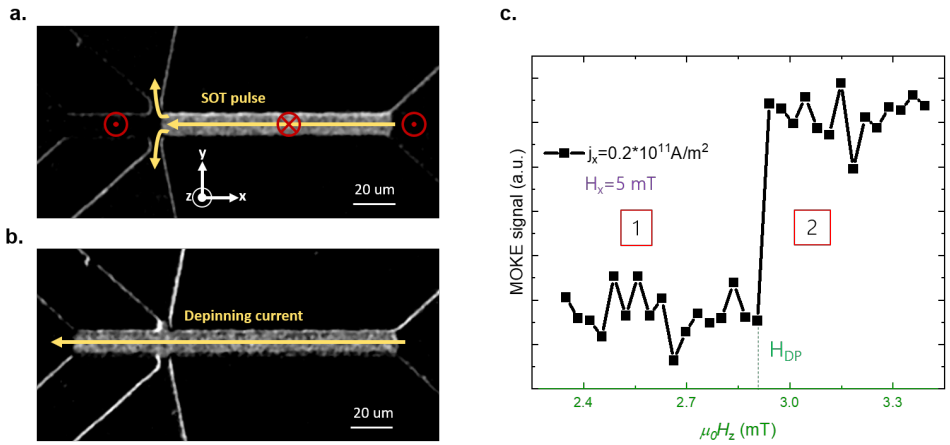

Figure 7.9: (a) Generation of the DW used for H_{DMI} quantification observed with MOKE. A d.c. pulse (indicated by blue arrows) is injected into the current line and split in the Hall bars, generating an opposite (bright) domain due to SOT. (b) Depinning of the DW after injecting a d.c. depinning current and an IP field along the x-axis, and ramping the OOP field. (c) Exemplary depinning event recorded with the automated Labview program, where H_{dep} is defined as the field needed to depin the DW formed in (a) and marked by a jump in MOKE signal.

the injection direction and hence can be modeled by an effective thermal field $H_{\mathrm{T}} \propto I^2$. In contrast, the SOT effect is linear in current $H_{\mathrm{DL}} \propto I$ and depends on the injection direction. The combined effect (H_{T}+H_{DL}) yields a deviation in H_{dep} as a function of the injected current, characterized as $\Delta H_{\mathrm{dep}} = H_{\mathrm{dep}}^{\mathrm{I=0\ mA}} - H_{\mathrm{dep}}$. Fig. 7.10a shows the measurements of ΔH_{dep} in the range of -16.2 $< \mu_0 H_{\mathrm{x}} <$ 11.8 mT, with each data point representing the average of 20 depinning measurements to ensure reliability. By extracting the linear component from the data shown in Fig. 7.10a, we find the effective H_{DL} acting on the DW. This analysis explicitly takes into account the differential effects between positive and negative currents, thereby minimizing the influence of external factors, such as pinning strength, local (or global) anisotropies, or defects, ensuring accurate and unbiased measurements. Furthermore, contributions from the Oersted field can be excluded, as it reaches a maximum of $\sim$ 0.2 mT in our samples with the maximum applied current, significantly lower than the DMI effective field and Bloch anisotropy fields.

Fig. 7.10b shows the dependence of H_{DL} on the current density (j) for various H_{x} bias fields. We recall that the torque acting on the DW is proportional to the x-component of the DW's internal spin. By defining the angle of the DW's internal spin (red arrow) on the x-y plane (Ψ) as shown in Fig. 7.10c, H_{DL} is expected to be maximum (minimum) when Ψ is 0^{o} (90^{o}). The equilibrium angle Ψ is determined by the interplay between the Bloch anisotropy field (H_{Bloch}, blue arrow) and the DMI effective field H_{DMI} (black arrow), which are along the y- and x-axis, respectively. Consequently, H_{x} either adds up or acts against H_{DMI}, depending on their relative orientation. When H_{DMI} = -H_{x}, the DW assumes a Bloch orientation ($\Psi = 90^{\mathrm{o}}$) and H_{DL} becomes negligible. This condition provides us with an accurate estimation of both the magnitude and direction of H_{DMI} for the device under test.

Fig. 7.10d shows the dependence of the normalized H_{DL}, defined as ξ^{DL}, on H_{x} for both the up-down (black squares) and down-up (red dots) DWs. We observe that ξ^{DL} has an opposite action

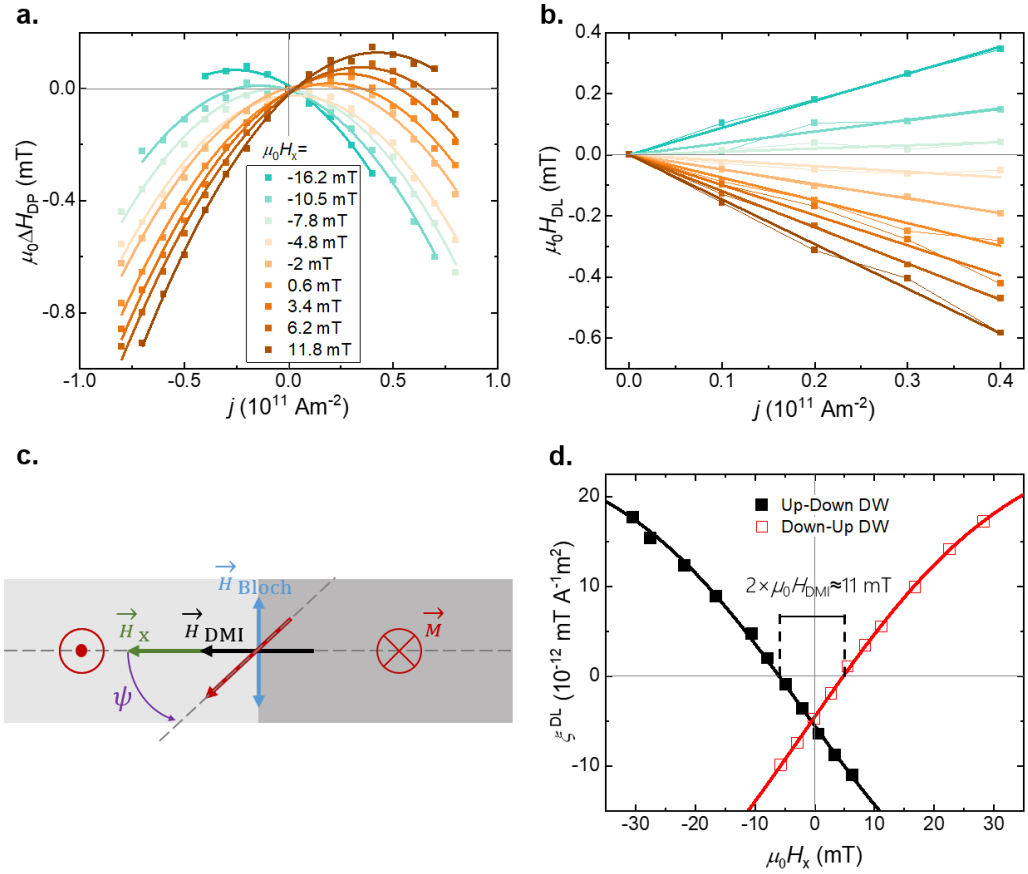

Figure 7.10: (a) OOP depinning field applied to depin the generated DW in Fig. 7.10 for various d.c. currents and IP fields along the x-axis. Both linear and a quadratic contribution, distinct for each H_x, are visible. (b) Fitting of the linear (SOT) contribution extracted from (a). (c) The fitted values from (b) plotted as a function of H_x, allow us to estimate where the efficiency of the DL-torques (ξ^{DL}) goes to zero, thus determining the value of H_{DMI} for both up-down (black) and down-up (red) DWs.

in these two DW configurations. The finite effect of H_{DL} on the DW at $H_x = 0$ mT (i.e., the y-axis intercept) confirms the Néel character of the DWs. At -5 mT (+5 mT) ξ^{DL} becomes zero for the up-down (down-up) DWs. These values identify as the H_{DMI} for the respective DWs in this device.

Analytical Model and Interpretation

To better interpret our results, we follow the description presented in Refs. [294, 51], where the damping-like torque efficiency ξ^{DL} can be analytically expressed as

$$\xi^{DL} = \frac{\pi}{2}\xi_0^{DL}\cos\Psi, \tag{7.4}$$

with Ψ the angle between the DW internal magnetization and the x-axis. The dependence of Ψ on the IP field H_x can be obtained from the 1D DW model with DMI [170], where the DW surface energy density σ is written as

$$\frac{\sigma}{2\Delta\mu_0 M_s} = \frac{1}{2}H_k\cos^2(\Psi) - \frac{\pi}{2}H_{DMI}\cos(\Psi) - \frac{\pi}{2}H_x\cos(\Psi) - \frac{\pi}{2}H_y\sin(\Psi) + H_\perp, \tag{7.5}$$

with Δ the DW parameter, H_k the DW shape anisotropy field and $H_\perp$ the perpendicular anisotropy field. Minimization of σ with respect to Ψ yields an analytical relation for $\cos\Psi$, and hence $\xi^{\mathrm{DL}}(H_x)$. Since $\cos\Psi$ corresponds to the x-component of the DW moment (m_x), the SHE provides a direct probe of the DW configuration under IP fields:

$$\cos(\Psi) = m_x = \begin{cases} +1 & \text{if } H_{\mathrm{DMI}} + H_x > H_{\mathrm{Bloch}} \\ \frac{H_{\mathrm{DMI}}+H_x}{H_{\mathrm{Bloch}}} & \text{if } -H_{\mathrm{Bloch}} < H_{\mathrm{DMI}} + H_x < H_{\mathrm{Bloch}}, \\ -1 & \text{if } H_{\mathrm{DMI}} + H_x < -H_{\mathrm{Bloch}} \end{cases} \tag{7.6}$$

where we have defined $H_{\mathrm{Bloch}} = \frac{2}{\pi} H_k$.

The expected behavior is illustrated schematically in Fig. 7.11. In the absence of DMI ($H_{\mathrm{DMI}} = 0$, Fig. 7.11a), the DW is purely Bloch-type at $H_x = 0$, yielding $\xi^{\mathrm{DL}} = 0$. Applying an IP field progressively rotates the DW spins towards a Néel configuration, and ξ^{DL} increases until it saturates at $H_x = H_{\mathrm{Bloch}}$. When $H_{\mathrm{DMI}} < H_{\mathrm{Bloch}}$ (Fig. 7.11b), the DW has a finite Néel component already at $H_x = 0$, leading to $\xi^{\mathrm{DL}} \neq 0$. In this case, applying H_x in the same direction as H_{DMI} enhances ξ^{DL}, while applying it in the opposite direction reduces it, reaching $\xi^{\mathrm{DL}} = 0$ when $H_x = -H_{\mathrm{DMI}}$. This regime corresponds to our experimental samples. Finally, for $H_{\mathrm{DMI}} > H_{\mathrm{Bloch}}$ (Fig. 7.11c), the DW is stabilized in a fully Néel configuration already at $H_x = 0$, giving a saturated $\xi^{\mathrm{DL}} = \xi_0^{\mathrm{DL}}$; only a counteracting IP field can reduce the efficiency.

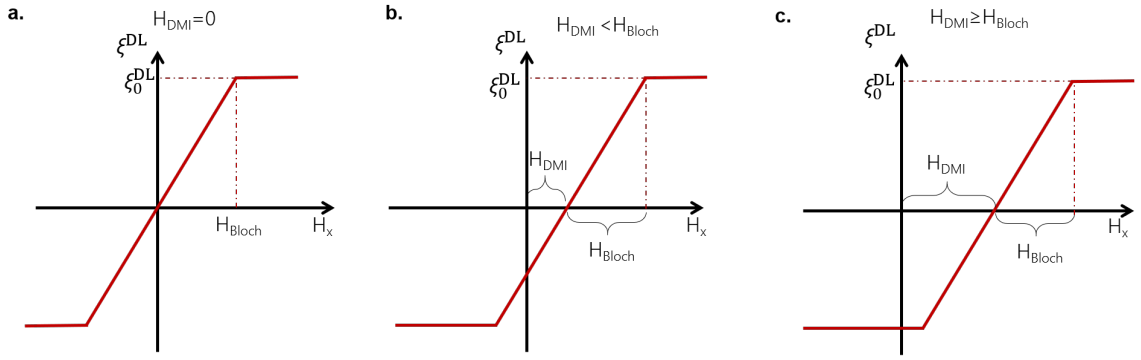

Figure 7.11: Sketch of the expected ξ^{DL} for the case (a) $H_{\mathrm{DMI}} = 0$, (b) $H_{\mathrm{DMI}} < H_{\mathrm{Bloch}}$ and (c) $H_{\mathrm{DMI}} > H_{\mathrm{Bloch}}$ for a DOWN-UP DW.

Experimental Results

In Fig. 7.12a and 7.12b, we compare the expected behavior of $\xi^{\mathrm{DL}}(H_x)$ with the experimentally extracted values for TbIG (2.9 nm). To test the consistency of the model, we repeated the measurements for DWs of both polarities (UP–DOWN and DOWN–UP) moving along both $+x$ and $-x$ directions for the TbIG(2.9 nm) sample. The results are fully reciprocal: H_{DMI} reverses sign depending on the DW polarity, but its absolute value remains unchanged. This confirms that H_{DMI} can be reliably obtained from the field at which ξ^{DL} crosses zero. The only notable deviation is that ξ^{DL} does not fully saturate at the largest accessible fields. We attribute this not to intrinsic physics, but to experimental constraints, as the maximum available H_x in our setup does not reach the values required to drive the DW fully into the Néel configuration in this sample.

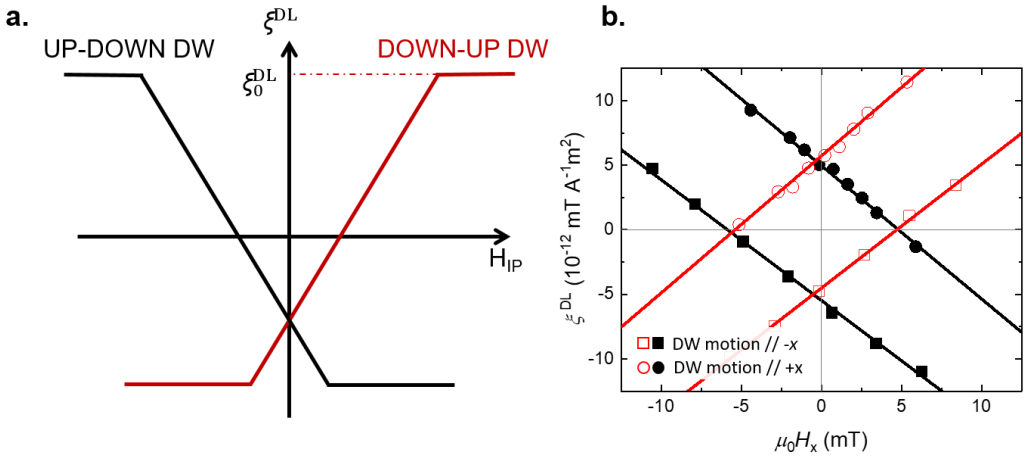

Figure 7.12: (a) Schematic illustration of the expected ξ^{DL} for the case $H_{DMI} < H_{Bloch}$, shown for both UP-DOWN (black) and DOWN-UP (red) DW configurations. (b) Corresponding measurements for TbIG (2.9 nm), where both types of DWs are driven along $+x$ and $-x$, and only the linear regime is displayed.

This approach provides a particularly robust method for extracting H_{DMI}. Unlike bubble-expansion measurements, which can be influenced by pinning, creep, and thermal activation, the torque-efficiency method relies on the internal configuration of the DW and its direct response to IP fields. Since ξ^{DL} is sensitive only to the Néel component of the DW moment, the point where ξ^{DL} vanishes offers a clear and model-independent signature of the effective H_{DMI}. This makes the method less prone to extrinsic effects and allows a more reliable quantification of interfacial DMI in our TbIG heterostructures.

Device-Specific Offsets

It is worth noting that in some devices, the data for UP–DOWN and DOWN–UP DWs exhibit a small rigid offset. For instance, in Fig. 7.13 the measurement on TbIG(5.9 nm)/Pt shows that the two curves do not intersect exactly at zero field, indicating that the SOT efficiency ξ^{DL} differs slightly between the two DW polarities. This is also reflected in the extracted values of H_{DMI}, where we obtain $\mu_0 H_{DMI,\,UP-DOWN} = -2.8$ mT and $\mu_0 H_{DMI,\,DOWN-UP} = 0.9$ mT. In such cases, the effective H_{DMI} is taken as the average of the two values.

This offset is a recurring observation, although it does not follow a systematic trend. Repeated measurements on the same device consistently reproduce the same offset (in both magnitude and sign), whereas measurements across different devices yield offsets of varying magnitude and sign (see Fig. 7.18). These findings suggest that the effect is device-specific rather than arising from global contributions such as the SHE, Oersted fields, or other extrinsic sources. A more complete measurement of all four branches (UP-DOWN and DOWN-UP DW under both positive and negative current) would help disentangle these asymmetries and remove contributions from possible experimental bias or setup asymmetry. However, in our case, the offset is small and consistent across repeated measurements, and does not significantly affect the extracted H_{DMI}. We hypothesize that the origin of the offset lies in local asymmetries intrinsic to individual devices, such as variations in DW shape, local pinning potentials, edge roughness, or fabrication imperfections. Similar offsets

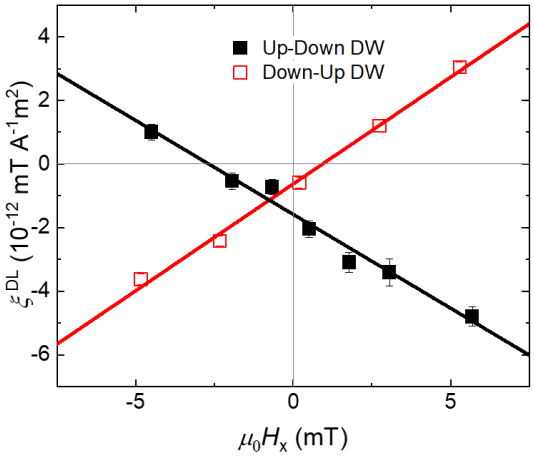

Figure 7.13: H_{DMI} quantification for the sample GGG/TbIG(5.9 nm)/Pt(4 nm). The efficiency of ξ^{DL} at zero field shows a slight offset and the curves for UP-DOWn and DOWN-UP domains are not symmetrical

have been reported in the literature, although they are often less visible due to the larger DMI fields typically studied. In our case, the small DMI values and the limited field range make such offsets more apparent, whereas in other studies, full $\xi^{\mathrm{DL}}(H_x)$ curves and fitting procedures may mask them.

Crucially, the magnitude of the offset is typically smaller than the extracted H_{DMI}, and comparisons across devices confirm that it does not significantly affect the estimation of H_{DMI}. Therefore, we conclude that this offset is a secondary effect and that our method provides a reliable determination of the interfacial DMI field.

Chirality

Finally, we determine the sign of the DW chirality in our samples by analyzing the sign of the IP field required to cancel the motion of UP-DOWN and DOWN-UP Néel DWs. This indicates a specific sense of rotation (clockwise in our case), consistent with a right-handed chirality in our TbIG/Pt heterostructures, following the convention established in Ref. [208]. This observation contrasts with the left-handed chirality typically associated with interfacial DMI at the bottom GGG/TbIG interface, as reported in Ref. [51].

Assuming that the GGG/TbIG interface contributes a left-handed DMI, as observed in other garnet systems, our results suggest that the DMI contribution from the top TbIG/Pt interface is stronger and dominates the net DMI in our samples. However, we emphasize that the sign of the DMI at the GGG/TbIG interface in our specific samples is not directly known and may differ due to variations in growth conditions and interface quality. Therefore, while our data are consistent with a dominant positive DMI contribution from the TbIG/Pt interface, this interpretation remains tentative.

This hypothesis is supported by structural considerations: the GGG/TbIG interface is diffuse, which may reduce its effectiveness in generating DMI [292], whereas the TbIG/Pt interface is sharp and likely more efficient in contributing to interfacial DMI. Additionally, Ref. [28] demonstrates that the left-handed DMI from a substrate/TmIG interface can be compensated by an oppositely signed DMI from a Pt overlayer, reinforcing the idea that both interfaces can contribute with opposite

chirality. Depending on factors such as growth method, material choice, and interface sharpness, one interface may dominate the net DMI even in structurally similar heterostructures. Further evidence supporting this scenario is presented in the following section.

7.4 Results

7.4.1 Thickness Dependence of the DMI

To investigate the physical origin of the interfacial DMI in TbIG/Pt heterostructures, a systematic study was conducted on the dependence of DMI on the thickness of the TbIG layer, while maintaining a constant Pt overlayer. Fig. 7.14a presents the measured effective DMI field, H_{DMI}, for TbIG thicknesses ranging from 1.9 to 7.9 nm. As anticipated for an interfacial phenomenon, thinner films exhibit stronger DMI fields, whereas thicker films show a reduction in H_{DMI}. The maximum value, $\mu_0 H_{\mathrm{DMI}} = 5.6 \pm 0.9$ mT, is observed for the 2.9 nm sample, in agreement with previous reports on TbIG systems [51], albeit for thicker films. Error bars represent the standard deviation from multiple measurements for each thickness.

Quantification of the DMI energy density D requires knowledge of the saturation magnetization M_{s}, the effective PMA field H_{K}, and the DW width Δ_{DW}, as detailed below.

Fig. 7.14b shows the calculated DW width Δ_{DW} as a function of t_{TbIG}, using the relation $\Delta_{\mathrm{DW}} = \pi\sqrt{A/K_{\mathrm{eff}}}$ [170], where A is the exchange stiffness and K_{eff} is the effective PMA energy, defined as $K_{\mathrm{eff}} = \mu_0 M_{\mathrm{s}} H_{\mathrm{K}}/2$. These parameters were extracted from experimental measurements discussed in Section 7.2. As expected, Δ_{DW} decreases with increasing TbIG thickness, consistent with the observed increase in M_{s} and H_{K}.

Fig. 7.14c presents the DMI energy density D, calculated using $D = H_{\mathrm{DMI}}\mu_0 M_{\mathrm{s}}\Delta$ [170], plotted against $1/t_{\mathrm{TbIG}}$. The data exhibit a linear trend, confirming the interfacial nature of the DMI. The highest value, $D = 1.33 \pm 0.07$ μJ m^{-2}, is obtained for the 2.9 nm sample, in agreement with literature values [51, 52].

To further analyze the interface contribution, the normalized DMI energy $D_{\mathrm{s}} = D{\cdot}t_{\mathrm{TbIG}}$ is plotted in Fig. 7.14d (left y-axis, black data points). We find that D_{s} does not show an apparent correlation with t_{TbIG} and fluctuates between 1.5 and 3.5 fJ m^{-1} with a mean value of 2.4 fJ m^{-1}. Assuming that the DMI in our structures originates from the TbIG/Pt interface, as evidenced in Section 7.3, it is likely correlated with other interface-related phenomena [295, 296]. In Fig. 7.14d (right y-axis, red data points), we plot the amplitude of the SMR-AHE ($R_{\mathrm{H}}^{\mathrm{SMR\text{-}AHE}}$), as measured in Fig. 7.2, normalized by the longitudinal resistance (R_{xx}) as a function of t_{TbIG}. These two datasets show a strong qualitative agreement, although not a strict one-to-one correlation. $R_{\mathrm{H}}^{\mathrm{SMR\text{-}AHE}}$ is driven by the combined action of SHE, a bulk property of Pt and expected to be constant through all samples, and the interfacial spin mixing conductance, which is highly sensitive to the microscopic details of the TbIG/Pt interface. There is pertinent evidence that the interfacial DMI is correlated with the spin mixing conductance due to their common link to the SOC [297, 298]. Thus, microscopic defects such as grain boundaries (see Fig. 7.15) could affect both quantities similarly. We argue, therefore, that the correlation between D_{s} and $R_{\mathrm{H}}^{\mathrm{SMR\text{-}AHE}}$ provides further confirmation of the TbIG/Pt interface being the predominant origin of DMI in our structures, even if a contribution from the substrate cannot be fully excluded at this stage. While experimental uncertainties may influence individual data points, the consistent trend observed across both datasets is statistically unlikely to

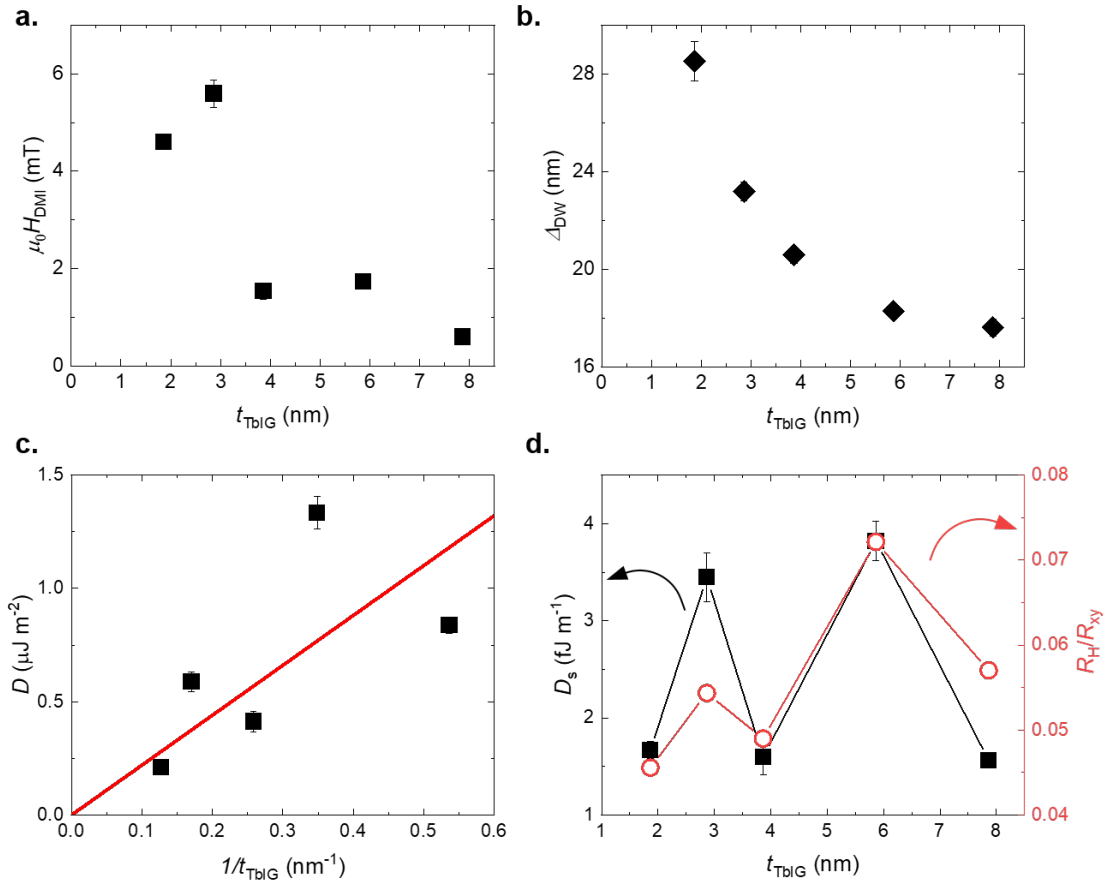

Figure 7.14: Thickness dependence of DMI in TbIG/Pt heterostructures. (a) Effective DMI field H_{DMI} as a function of TbIG thickness t_{TbIG}. (b) DW width Δ_{DW} calculated from experimental parameters. (c) DMI energy density D plotted against $1/t_{\mathrm{TbIG}}$, with a linear fit (red line). (d) Normalized DMI energy $D_{\mathrm{s}} = D \cdot t_{\mathrm{TbIG}}$ (black squares, left axis) and normalized SMR-AHE resistance $R_{\mathrm{H}}^{\mathrm{SMR\text{-}AHE}}/R_{\mathrm{xx}}$ (red open dots, right axis).

arise purely by coincidence, further supporting a common interfacial origin.

Fig. 7.15a displays a high-resolution HAADF-STEM image of the GGG/TbIG(30 nm)/Pt(4 nm) heterostructure. The image confirms high-quality epitaxial growth of TbIG on GGG, but also reveals grain boundaries within the TbIG layer, highlighted by white arrows. These boundaries span the full thickness of the film and are associated with grooves and contrast variations extending from the Pt surface to the substrate interface.

Such defects may contribute to sample-to-sample variations in R_{H} and D_{s}, as they locally degrade the TbIG/Pt interface quality. This is illustrated in Fig. 7.15b, where enhanced intermixing is observed at a grain boundary. In contrast, Fig. 7.15c shows a region with a sharp and well-defined interface, free of significant intermixing. These observations underscore the importance of local structural variations in determining macroscopic, interface-sensitive quantities such as DMI and spin transport efficiency.

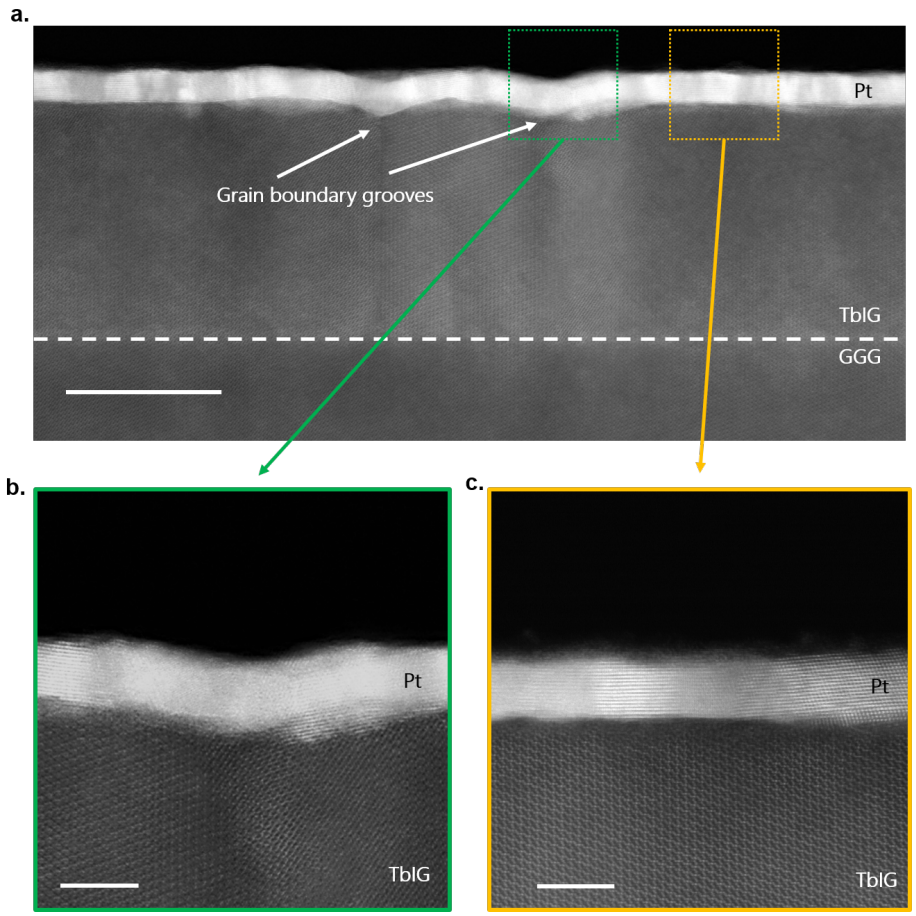

Figure 7.15: (a) Large field-of-view HAADF image of the GGG/TbIG(30 nm)/Pt(4 nm) stack, showing sharp Pt interface and grain boundaries in TbIG (white arrows). (b) Zoomed atomic-resolution image of a grain boundary region with enhanced intermixing. (c) Zoomed image of a sharp TbIG/Pt interface with minimal intermixing. Scale bars: 20 nm (a), 5 nm (b,c).

7.4.2 Nonmagnetic Metal Dependence of the DMI

To investigate the role of nonmagnetic metals on interfacial DMI in TbIG, we compared different NM overlayers and studied the effect of inserting a thin Cu spacer layer ($t_{\mathrm{Cu}} = 1.5$ nm). The TbIG thickness was fixed to 2.9 nm, corresponding to the thickness where the TbIG/Pt interface exhibited the largest DMI. Cu is a light metal with negligible SOC and is therefore expected to induce very weak DMI [296]. This is confirmed by DFT calculations performed for Co/Cu bilayers (Fig. 7.16a, details in Sec. 7.4.3), where the total and layer-resolved DMI contributions are nearly zero. While we recognize that comparing metal/metal interfaces (Co/Cu) with metal/oxide interfaces (TbIG/Cu) involves fundamentally different interfacial physics, the Co/Cu system serves as a useful reference for assessing the role of SOC and interfacial symmetry in DMI generation.

Moreover, a Cu spacer fully covers the TbIG surface and prevents direct exchange with the NM grown on top. AFM scans (Fig. 7.16b,c) confirm that 1.5 nm of Cu produces continuous coverage with only a slight increase in roughness (from 180 pm for bare TbIG to 280 pm for TbIG/Cu). This

is well below the Cu thickness, ensuring continuity. However, as uncapped Cu oxidizes easily, these results must be interpreted with caution.

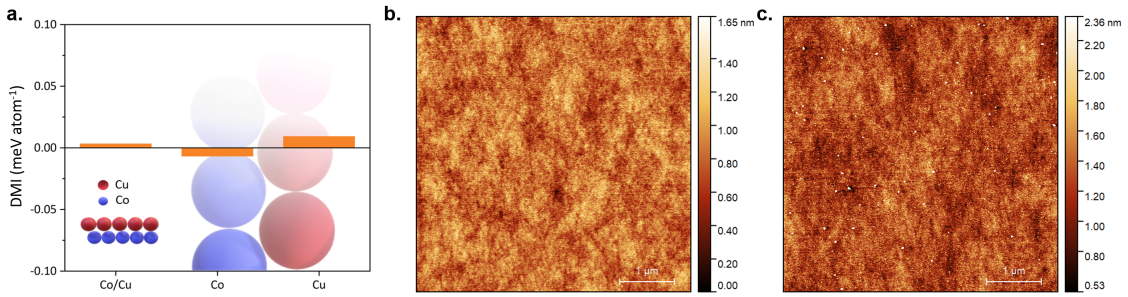

Figure 7.16: (a) Layer-resolved DMI in Co/Cu bilayers from DFT, showing negligible contributions. (b) AFM of GGG/TbIG(2.9 nm). (c) AFM of GGG/TbIG(2.9 nm)/Cu(1.5 nm). Both surfaces show comparable roughness, confirming continuous Cu coverage.

Pt and Cu/Pt Interfaces

Fig. 7.17a summarizes the extracted DMI energies D for different NM overlayers. Comparing TbIG/Pt with TbIG/Cu/Pt, we observe a threefold reduction of D, rendering the DMI nearly negligible in the latter. This confirms that the TbIG/Pt interface is the dominant DMI source in this system, and that Cu insertion suppresses the interfacial interaction [226].

The small positive DMI observed in GGG/TbIG/Cu/Pt could, in principle, originate from several sources. If the DMI from the top interface is fully suppressed, a residual positive contribution could arise from the bottom GGG/TbIG interface. However, literature suggests that DMI at GGG/TbIG is typically negative (or negligible due to strong intermixing in our case). Another possibility is a remanent TbIG/Pt interaction if the Cu spacer is not sufficiently thick to fully eliminate it. This scenario is unlikely, however, as DMI is generally highly sensitive to direct interfacial contact. A third possibility, which aligns more closely with the behavior observed in W-based samples discussed later, involves a non-local contribution from the Cu/Pt interface to the total DMI, and will be discussed in the next Sections.

W and Cu/W Interfaces

A contrasting and puzzling scenario emerges when replacing Pt with W overlayers. The TbIG/W interface produces a slightly larger DMI compared to TbIG/Pt, in opposition to the trend observed in metallic multilayers, where Pt usually exhibits stronger DMI than W [298]. In REIGs, however, it has been reported that the Topological Hall effect (THE) is more pronounced for W than for Pt [57], suggesting that W can induce sufficient DMI to stabilize skyrmions, and that skyrmion formation is more favorable in W-capped REIGs.

Furthermore, in models where the sign of SOC, such as the Levy-Fert model, determines the sign of the DMI, Pt and W are expected to produce opposite DMI signs, as frequently reported in the literature [208]. The discrepancy in our data may stem from the fact that the Levy-Fert model is not directly applicable to oxide/metal interfaces, as it assumes both materials are conductive

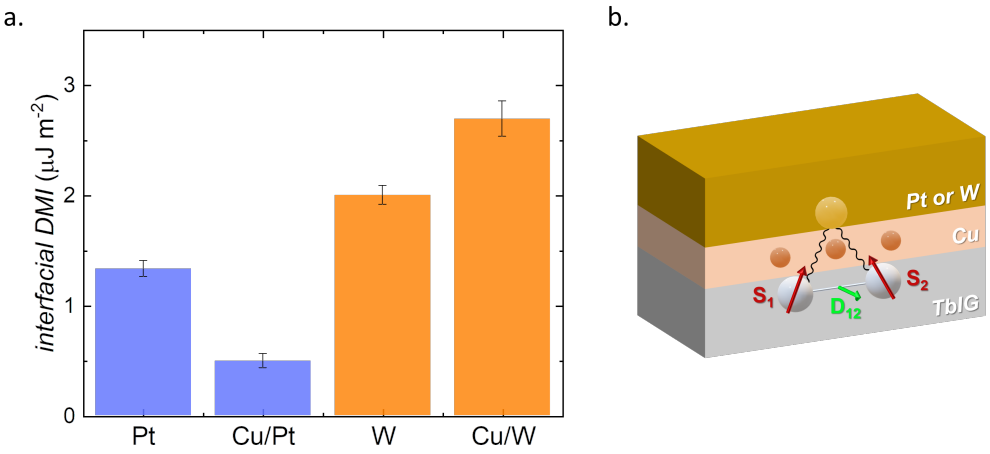

Figure 7.17: (a) DMI energy density D for different NM overlayers. Inserting Cu reduces D in TbIG/Pt but enhances it in TbIG/W. (b) Sketch of the proposed non-local contribution to DMI, mediated by the top Cu/NM interface.

and the interface is atomically sharp. In contrast, the TbIG/HM interface is known to be structurally and electronically complex. The TbIG/W interface, in particular, appears more intricate than TbIG/Pt. W tends to intermix more strongly with TbIG, and preliminary studies on TbIG/W samples deposited at high sputtering power (200 W) revealed no SOTs, indicating a degraded interface. Additionally, antiferromagnetically coupled MPE have been reported in TbIG/W systems at lower temperatures compared to TbIG/Pt [299]. W is also more prone to oxidation than Pt, potentially forming a thin WOx layer at the interface, which could introduce an additional source of DMI. While the observation of positive DMI in the W-capped samples is unexpected, we argue that it is not unphysical. Rather, it reflects the rich and complex interfacial physics at play, which may include intermixing, oxidation, and proximity-induced effects that go beyond conventional models.

Interestingly, inserting Cu between TbIG and W does not suppress the DMI, but instead enhances it by nearly 40%, opposite to the behavior observed for Cu/Pt. Given this counterintuitive result, extensive measurements were performed on multiple devices and deposition runs, consistently confirming the enhancement and ruling out experimental artifacts or growth-related variations. Fig. 7.18 summarizes the measurements of H_{DMI} in W-based devices. The SOT efficiency is reversed compared to Pt samples, consistent with the opposite spin Hall angle of W. Nevertheless, the sign of H_{DMI} remains unchanged, with positive values for UP–DOWN and negative values for DOWN–UP DWs, indicating that the chirality of the interaction is preserved. Two stacks of TbIG/W were studied, grown at different times: TbIG(2.9 nm)/W(4 nm)/Ti(2.5 nm) (Fig. 7.18a) and TbIG(2.9 nm)/W(4 nm)/Cu(1.5 nm)/Ti(2.5 nm) (Fig. 7.18b). Despite differences in preparation, the extracted H_{DMI} values are similar. The addition of a Cu overlayer before Ti only served to adjust device resistance and did not affect the quantification, as nonlocal DMI is not expected to act through a thick W layer.

The TbIG/Cu/W case was studied in two stacks: TbIG(2.9 nm)/Cu(1.5 nm)/W(4 nm)/Ti(2.5 nm) (Fig. 7.18c), and TbIG(2.9 nm)/Cu(1.5 nm)/W(4 nm). For the former, two devices were fully char-

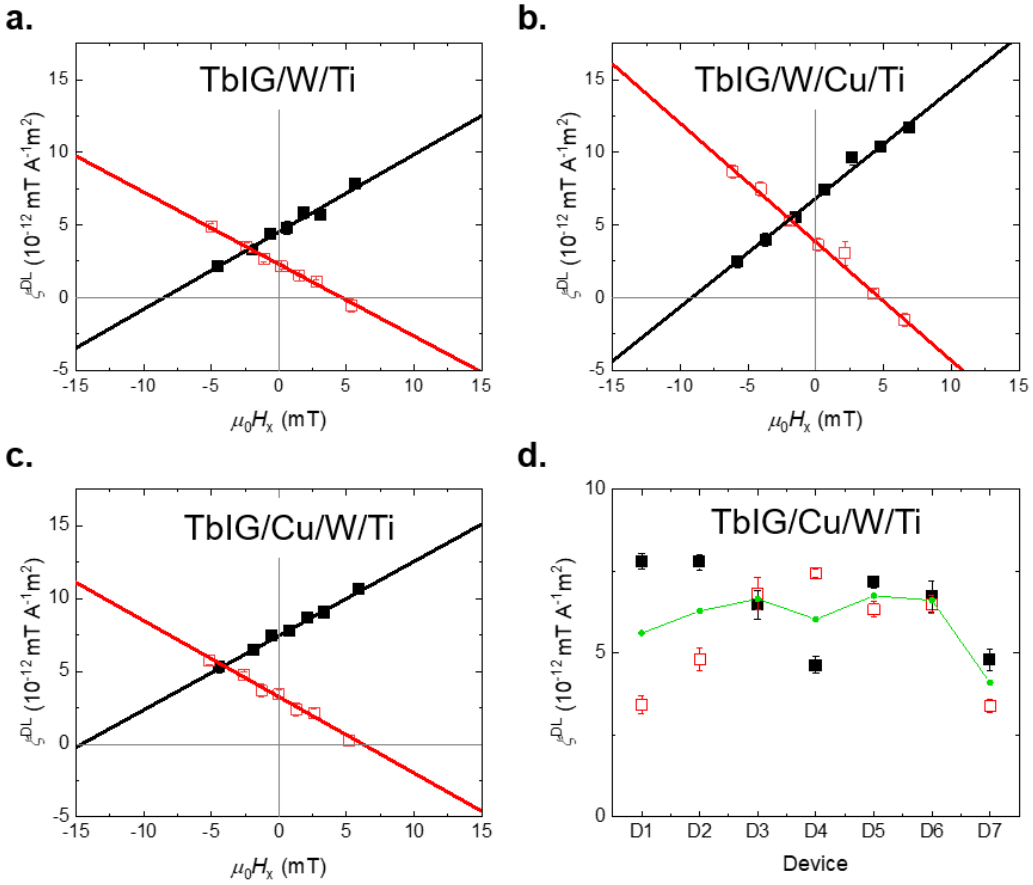

Figure 7.18: Measurements of H_{DMI} are shown for the following samples: (a) TbIG/W/Ti, (b) TbIG/W/Cu/Ti, and (c) TbIG/Cu/W/Ti. dc) Offset values for seven different devices measured from the TbIG/Cu/W/Ti sample are presented, showing the efficiency of the torques (ξ^{DL}) for UP-DOWN and DOWN-UP domains at zero field. While the offset varies across devices, its mean value (indicated by the green dot in the figure) remains constant, suggesting a similar H_{DMI} across all devices.

acterized, yielding consistent H_{DMI} values. In addition, the SOT efficiencies at zero field were extracted for several devices (Fig. 7.18d). The average ξ^{DL}, defined as the mean of $\xi^{\mathrm{DL}}_{\mathrm{UP-DOWN}}$ and $\xi^{\mathrm{DL}}_{\mathrm{DOWN-UP}}$, remained constant across devices (green dots in Fig. 7.18d), indicating reproducibility of the DMI values. The second stack, studied on a single device, gave results in agreement with the first one. Differences in capping layers do not influence the DMI extraction, as the main effect is a partial oxidation of the W layer in the uncapped stack, effectively reducing its metallic thickness.

Overall, these results demonstrate that the DMI at TbIG/W interfaces is robust and even enhanced by the insertion of a Cu spacer, in sharp contrast to the suppression observed for Cu/Pt. This robustness, together with the reproducibility across multiple devices, highlights the distinct role of W in governing interfacial interactions in REIG-based heterostructures.

Long-Range Contributions to DMI

The results summarized in Fig. 7.17a cannot be rationalized by models that attribute the DMI solely to a single source, such as the local TbIG/NM interface, the GGG/TbIG interface, or a possible

bulk structural gradient. For instance, the stacks GGG/TbIG/Cu/Pt and GGG/TbIG/Cu/W are nominally equivalent in terms of local interfaces, yet they yield the smallest and the largest DMI values, respectively. This striking contrast indicates that the interfacial DMI in TbIG is not governed exclusively by direct contact interfaces, but is instead modified by long-range contributions involving non-local interfaces such as Cu/Pt and Cu/W.

We propose that the magnetic layer can sense the presence of a remote (secondary) interface through a spacer with weak spin–orbit coupling, such as Cu, which mediates an additional contribution to the DMI generated by the primary interface (Fig. 7.17b). Possible mechanisms include RKKY-type interactions or quantum-well states within the spacer, whereby the electronic structure of one interface is modified by the other. Such interactions are reminiscent of interlayer DMI observed in FM/NM/FM trilayers [173, 174, 176], where no direct contact is required to mediate an exchange interaction. However, a comparable mechanism involving an FM and a remote NM interface that modifies the *interfacial* DMI has not been previously established.

In metallic multilayers, such long-range contributions are typically masked by the much stronger interfacial DMI. In contrast, for REIG systems the interfacial DMI is intrinsically weaker (up to three orders of magnitude smaller than in metallic counterparts), allowing non-local interactions to become competitive. Within this framework, the contrasting behavior of Cu/Pt and Cu/W stacks can be understood as the result of such long-range effects, which alter the balance of interfacial interactions in a spacer-dependent manner. These findings point toward a new degree of freedom for engineering DMI in insulating ferrimagnets, highlighting the role of non-local electronic interactions in addition to direct interfacial coupling.

In light of this interpretation, we argue that the small positive DMI observed in TbIG/Cu/Pt arises from an additional contribution mediated by the non-local Cu/Pt interface. Unfortunately, this contribution cannot be quantified, as the magnitude and sign of the GGG/TbIG and remanent TbIG/Pt DMI remain unknown. The DMI observed in TbIG/Cu/W follows the same reasoning. In this case, however, the contribution from the Cu/W interface appears to be both positive and substantial, as none of the other plausible configurations of DMI (in terms of sign and magnitude) can account for the observed increase relative to the TbIG/W sample.

7.4.3 Density Functional Theory Calculations

To gain qualitative insight into the role of non-local interfaces in modifying interfacial DMI, we carried out DFT calculations in collaboration with *C. Deger* and *E. Demiroglu* from Marmara University (Istanbul, Türkiye). These simulations were designed to complement the experimental results by clarifying whether a remote Cu/NM interface can significantly alter the interfacial DMI. Because a full TbIG unit cell contains 160 ions and is computationally prohibitive for converged DFT calculations, we adopted a simplified model system: a Co monolayer interfaced with Pt, Cu/Pt, W, and Cu/W. Although this substitution cannot capture the full complexity of TbIG, it provides a tractable minimal model for isolating interfacial effects. Since the DMI is known to be highly localized at FM/NM interfaces, this approach retains the essential physics and allows meaningful comparison with experiments.

The calculations employed the constrained spin method implemented in the Vienna *ab-initio* simulation package (VASP) [300, 301], following established approaches used for FM/NM interfaces [302, 303]. Exchange-correlation effects were treated within the PBE generalized gradient approxima-

tion, and the projector augmented-wave method was used for the electron–ion interaction [304, 305]. A plane-wave cutoff of 400 eV and a Γ-centered k-point grid with a separation of 0.03 2π Å^{-1} were employed [306]. Structural relaxations were performed until forces were below 1 meV/Å, and electronic steps converged to 10^{-5} eV. Using the constrained spin method [307], clockwise (CW) and counterclockwise (CCW) spin textures were imposed, and the DMI was obtained from the total energy difference between these two configurations in the presence of SOC.

Fig. 7.19a summarizes the calculated DMI values. For the reference systems, Co/Pt and Co/W exhibit similar DMI magnitudes of approximately 2 meV/atom, consistent with previous DFT studies [303, 308]. Introducing Cu as a spacer, however, produces opposite effects depending on the adjacent NM: in Co/Cu/Pt, the DMI is strongly reduced and even changes sign, whereas in Co/Cu/W it is enhanced compared to Co/W. These trends qualitatively reproduce our experimental findings, where Cu insertion suppresses the DMI in TbIG/Pt but amplifies it in TbIG/W.

Fig. 7.19b and 7.19c show the layer-resolved DMI contributions for all systems studied. In these calculations, the DMI is evaluated by imposing a spin spiral (i.e., a fixed chirality) in the ferromagnetic layer and computing the energy response of the system. This allows the extraction of DMI contributions from individual atomic layers, including both the FM and HM regions. The total DMI is then obtained by summing these layer-resolved contributions. This approach provides insight into how different layers, especially those near the interface, contribute to the overall DMI, and how the presence of a spacer like Cu modifies the interfacial electronic structure and spin-orbit interactions.

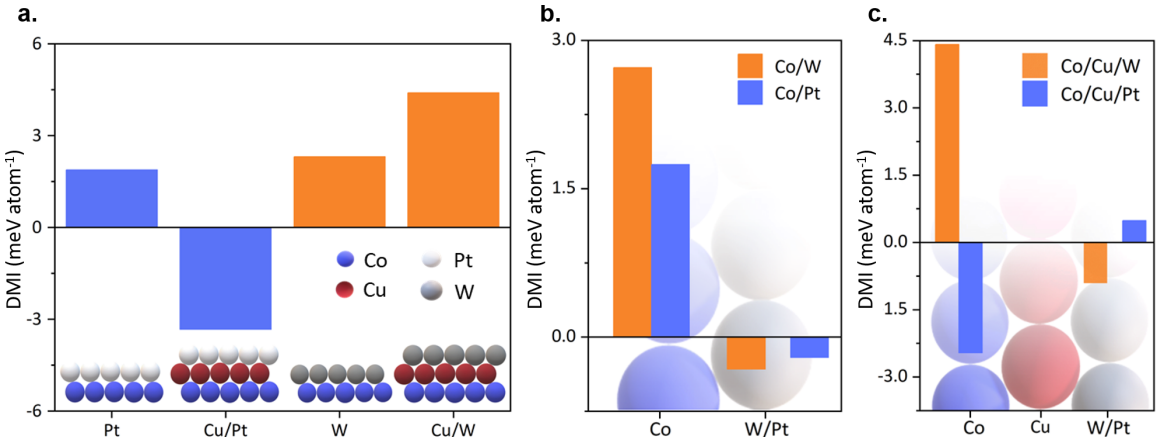

Figure 7.19: DFT-calculated interfacial DMI. (a) DMI values (in meV/atom) for Co/Pt, Co/Cu/Pt, Co/W, and Co/Cu/W interfaces. (b) Layer-resolved DMI contributions in Co/W and Co/Pt systems. (c) Layer-resolved DMI contributions in Co/Cu/W and Co/Cu/Pt systems.

It is important to note that differences between the model and the experimental structures, such as the choice of FM, layer thicknesses, and the possible contributions from the bulk TbIG and the bottom TbIG/GGG interface, mean that quantitative agreement is not expected. In particular, a sign reversal at the top interface predicted by DFT would appear experimentally only as a reduction in magnitude, since the measured signal reflects the sum of all contributions. Nevertheless, the qualitative agreement between experiment and DFT strongly supports the proposed scenario of a long-range DMI contribution mediated by non-local interfaces.

7.5 Conclusions

In this chapter, we investigated the interfacial DMI in TbIG-based heterostructures, focusing on the dependence on the magnetic layer thickness and on the choice of NM overlayers. We demonstrated that the DMI originates predominantly from the TbIG/NM interface, with values comparable to those reported in the literature. The thickness dependence confirmed its interfacial character, as the magnitude of the interaction decreases with increasing TbIG thickness.

A key result of this study is the contrasting role of Cu spacers: while the insertion of Cu between TbIG and Pt suppresses the DMI almost completely, the insertion of Cu between TbIG and W enhances it by about 40%. This striking difference cannot be explained solely by local interface effects. Instead, our results indicate that the interfacial DMI in TbIG is substantially influenced by long-range interactions involving non-local NM/NM interfaces.

This interpretation is supported by first-principles DFT calculations on simplified Co/NM and Co/Cu/NM systems, which reproduce the opposite Cu-induced trends observed experimentally. Although the model system differs from TbIG, the calculations provide qualitative evidence that the presence of a secondary NM interface can modify the interfacial DMI through non-local mechanisms.

Overall, these findings demonstrate that the DMI in TbIG-based heterostructures can be tuned not only by direct interface engineering but also by exploiting the influence of remote interfaces. This mechanism, not previously proposed or observed, suggests alternative routes for controlling chiral spin textures such as DWs and skyrmions in magnetic insulators, and offers new opportunities for designing more efficient SOT devices.

Appendix 7.A: Summary of DMI in REIGs

Table 7.1: Summary of reports on interfacial DMI in REIGs.

Material (nm)	**Growth**	**Origin DMI**	**Method**	D (μJ/m^2)	**Chirality**	**Ref**
sGGG/TmIG(2)/HW HM=Pt, W, Ta, Au	Off-axis sputtering	TmIG/HM	SH-THE Hall measurement	YES[1]	-	[57]
GGG/YIG(7) GGG/YIG(10)	Sputtering	GGG/YIG	Chiral spin waves velocity BLS	$D = 16$ $D = 14.2 \pm 4.2$	-	[55]
sGGG/TmIG(8.3)/Pt sGGG/TmIG(8.3)	PLD	sGGG/TmIG	NV magnetometry DW velocity	$D = -2 \pm 2$ $D = -5.3 \pm 1.8$	LEFT LEFT	[28]
GGG/TmIG(5.1)/Pt(4) GGG/TbIG(7.1)/Pt(4) GGG/TbIG(7.1)/Cu(2)/Pt(4)	PLD	GGG/ReIG	DW depinning	$D = -2$ $D = -1.4$ $D = -1.4$	LEFT LEFT LEFT	[51]
GGG/TmIG(2.8)/Pt(7) GGG/TmIG(16.6)/Pt(7)	PLD	GGG/TmIG	Shift htst loop Skyrmion generation	$D = -36 \pm 20$ $D \approx 0$	LEFT -	[27]
GGG/TmIG(2.4-24)/Pt(4) sGGG/TmIG(6)/Pt(4) GGG/TbIG(7.1)/Pt(4) GGG/TbIG(7.1)/Cu(2)/Pt(4) sGGG/BiYIG(6.9)/Pt(4)	PLD	GGG/ReIG	DW depinning	up to $D = -9$ $D = -2.6$ $D = -1.3$ $D = -1.8$ $D \approx 0$	LEFT LEFT LEFT LEFT -	[52]
sGGG/TmIG(10)/Pt(3) sGGG/TmIG(10)/Cu(3)/Pt(3)	PLD	TmIG/HM	Extended droplet model Skyrmion generation	$D = 4$ $D = 1.2$	- -	[58]
GGG(100/110/111)/TmIG(2)/Pt(3) GGG(100/110/111)/YIG(2)/Pt(3) sGGG/YSAG(2)/TmIG(2)/Pt(3) sGGG/YSAG(2)/YIG(2)/Pt(3)	Off-axis sputtering	TmIG/HM (main) YIG/HM (less)	SH-THE Hall measurement	YES YES YES YES	- - - -	[59]
NdGG/TmIG(3.2)/Pt(4) NdGG/TmIG(4)/Pt(4) NdGG/TmIG(6)/Pt(4)	PLD	TmIG/HM	Shift hyst loop SH-THE	$D = 51$ YES $D \approx 0$	- - -	[56]

Continued on next page

[1]When DMI is reported but no precise value is specified in the main text, it is indicated as *YES*.

Material (nm)	**Growth**	**Origin DMI**	**Method**	D (μJ/m^2)	**Chirality**	**Ref**
sGGG/TmIG(6.5)/Pt(4) sGGG/TmIG(6.5)/Cu(3)/Pt(4) sGGG/TmIG(6.5)/YIG(0.9)/Pt(4)	PLD	TmIG/Pt (main) sGGG/TmIG	Extended droplet model	$D \approx 1.01$ $D \approx 0.46$ $D \approx 0.81$	- - -	[54]
sub/TmIG(6.6)/Pt(4) sub: GGG-SGGG-NGG-GYSGG-GSGG	PLD	TmIG/Pt	DW depinning	$D = +7$ no dependent on strain	RIGHT -	[285]
GGG/TmIG(2)/Pt(5) sGGG/TmIG(2)/Pt(5) NGG-YSGG-GSGG/TmIG(2-15)/Pt(4)	PLD	TmIG/Pt	Extended droplet model SH-THE	$D = 2.4$ $D = 28.6$ depend on strain	- - -	[60]
GSGG/YIG(10)/TmIG(20)/Pt(5) GSGG/YIG(10)/TmIG(20)	PLD	TmIG/Pt YIG/TmIG	NV mangetometry	$D > 12$ $D > 12$	RIGHT RIGHT	[64]
sGGG/TmIG(2)/Pt(9) sGGG/TmIG(12)/Pt(9) sGGG/TmIG(4)/PtOx(9)	Sputtering	-	Shift hyst loop	$D = 24$ $D \approx 0$ $D \approx 144$	- - -	[309]
NGG/TmIG(1.9)/BiYIG(4.4) NGG/TmIG(1.9)/BiYIG(4.4)/Pt(2)	PLD	NGG/TmIG	BLS	$D = 14.5 \pm 1.1$ $D = 1 \pm 3$	- -	[310]
GGG/TbIG(2.9)/Pt(4) GGG/TbIG(2.9)/Cu(1.5)/Pt(4) GGG/TbIG(2.9)/W(4) GGG/TbIG(2.9)/Cu(1.5)/W(4)	Sputtering	TbIG/Pt	DW depinning	$D = +1.33 \pm 0.07$ $D = +0.49 \pm 0.06$ $D = +2.00 \pm 0.08$ $D = +2.69 \pm 0.16$	RIGHT RIGHT RIGHT RIGHT	This work

Appendix 7.B: Details of Macrospin Simulation for Anisotropy Extraction

To accurately extract the effective anisotropy field H_K from the IP Hall resistance measurements, we implemented a macrospin simulation in SCILAB [311]. The model describes the equilibrium orientation of a single magnetic domain under the influence of the external field torque and the anisotropy field torque, while also accounting for small experimental misalignments. The corresponding Hall resistance was then calculated from the simulated magnetization orientation and compared to experimental data.

The magnetization is described by its unit vector $\mathbf{m}$, parameterized by the polar and azimuthal angles (θ, ϕ). The total torque acting on $\mathbf{m}$ is written as

$$\mathbf{T}_{\text{tot}} = \mathbf{T}_{\text{ext}} + \mathbf{T}_K, \tag{7.7}$$

where $\mathbf{T}_{\text{ext}}$ is due to the external applied magnetic field $\mathbf{H}_{\text{ext}}$, and $\mathbf{T}_K$ is the torque associated with the perpendicular anisotropy field. Explicitly:

$$\mathbf{T}_{\text{ext}} = -\mu_0 M_s \, \mathbf{m} \times \mathbf{H}_{\text{ext}}, \qquad \mathbf{T}_K = -\mu_0 M_s \, \mathbf{m} \times \mathbf{H}_K, \tag{7.8}$$

with H_K oriented along the $\pm z$ axis. At each field step, the simulation finds the equilibrium magnetization direction by minimizing $|\mathbf{T}_{\text{tot}}|$.

The model requires as inputs:

- Array of applied external fields H_{ext} (swept along the x-axis in the experiment).
- Trial values of the effective anisotropy field H_K.
- Saturation magnetization M_s.
- Spin Hall magnetoresistance (SMR) and SMR-induced anomalous Hall (SMR-AHE) resistances, determined experimentally.
- A small azimuthal misalignment $\phi \neq 0°$, to reproduce the weak asymmetry observed in practice.
- Coercivity H_c, introduced numerically by constraining the system to switch into the opposite hemisphere when H_{ext} changes sign.

Once the equilibrium orientation (θ, ϕ) is obtained for each H_{ext}, the corresponding Hall resistance is computed as

$$R_H = R_H^{\text{SMR}-\text{AHE}} \cos\theta + R_H^{\text{SMR}} \sin(2\phi) \sin^2\theta + R_H^{\text{HE}}, \tag{7.9}$$

where the first term is dominant in the ideal geometry. In the presence of small ϕ misalignments, the SMR contribution introduces measurable asymmetries that improve the fit.

The simulation generates $R_H(H_{\text{ext}})$ curves for a range of trial H_K. The best-fit H_K is determined by minimizing the least-squares deviation between the simulated and experimental curves. This procedure is repeated for all TbIG thicknesses studied. The extracted H_K values are reported in Section 7.2 of the main text.

The code was written in SCILAB using an iterative minimization routine for torque equilibrium. At each field step, the algorithm searches for the orientation θ, ϕ that minimizes $|\mathbf{T}_{\text{tot}}|$. The procedure is computationally inexpensive and yields smooth simulated curves that capture both the main trend and the asymmetries of the measured data.

Appendix 7.C: Automated LabView Program and Measurement Procedure

The measurements of DW depinning are highly time-consuming and represented one of the major experimental limitations of this work. To optimize data acquisition, I developed an automated program in LABVIEW, which allowed continuous measurements over extended periods. The program

significantly reduced operator intervention, although two issues prevented a fully autonomous operation. First, slow sample drift (caused by thermal fluctuations or relaxation of the tape and holders) resulted in a lateral shift of a few microns per hour, sufficient to move the ROI, the pixel set of the camera used for intensity analysis, outside the domain area. This required manual correction approximately every hour. Second, the same drift caused a gradual loss of focus, necessitating manual readjustment roughly every four hours. It is worth noting that, after this project, motorized stages for x–y motion and z focusing were installed to enable fully automated measurements without manual intervention. Using the optimized program, the quantification of the DMI effective field for a single sample typically required about four days of measurements at ~ 10 hours/day.

Fig. 7.20 shows the flowchart of the measurement sequence. The procedure begins with the generation of a reverse domain (blue box). Once the domain is nucleated, a specific IP field H_x is applied together with a dc current I_x. The OOP magnetic field is then ramped within a predefined range that ensures depinning of the DW under the selected H_x and I_x. A typical ramp is 15 Oe with a step size of 0.4 Oe. The average pixel intensity within the ROI is continuously recorded, and the program automatically detects the depinning field H_{dep} from the abrupt intensity change. After obtaining a reliable H_{dep} value for one combination of H_x and I_x, the current is incremented and the procedure repeated.

The measurement is carried out for currents ranging from $-I_{x,\mathrm{max}}$ to $+I_{x,\mathrm{max}}$ (typical parameters: $I_{x,\mathrm{max}} = 1.6$ mA with steps of 0.2 mA, corresponding to 17 different current values), followed by a reversed sweep from $+I_{x,\mathrm{max}}$ to $-I_{x,\mathrm{max}}$ to avoid cumulative thermal effects. For statistical reliability, each depinning event is repeated 20 times under identical H_x and I_x. Once the full set of currents is measured for a given H_x, the IP field is changed, typically covering nine different values between -10 and $+10$ mT with steps of about 2 mT. The same protocol is performed for both UP–DOWN and DOWN–UP DWs by reversing the domain generation procedure (opposite OOP saturation, reversed IP switching field, and identical current pulses). This symmetry check ensures a consistent extraction of the DMI effective field.

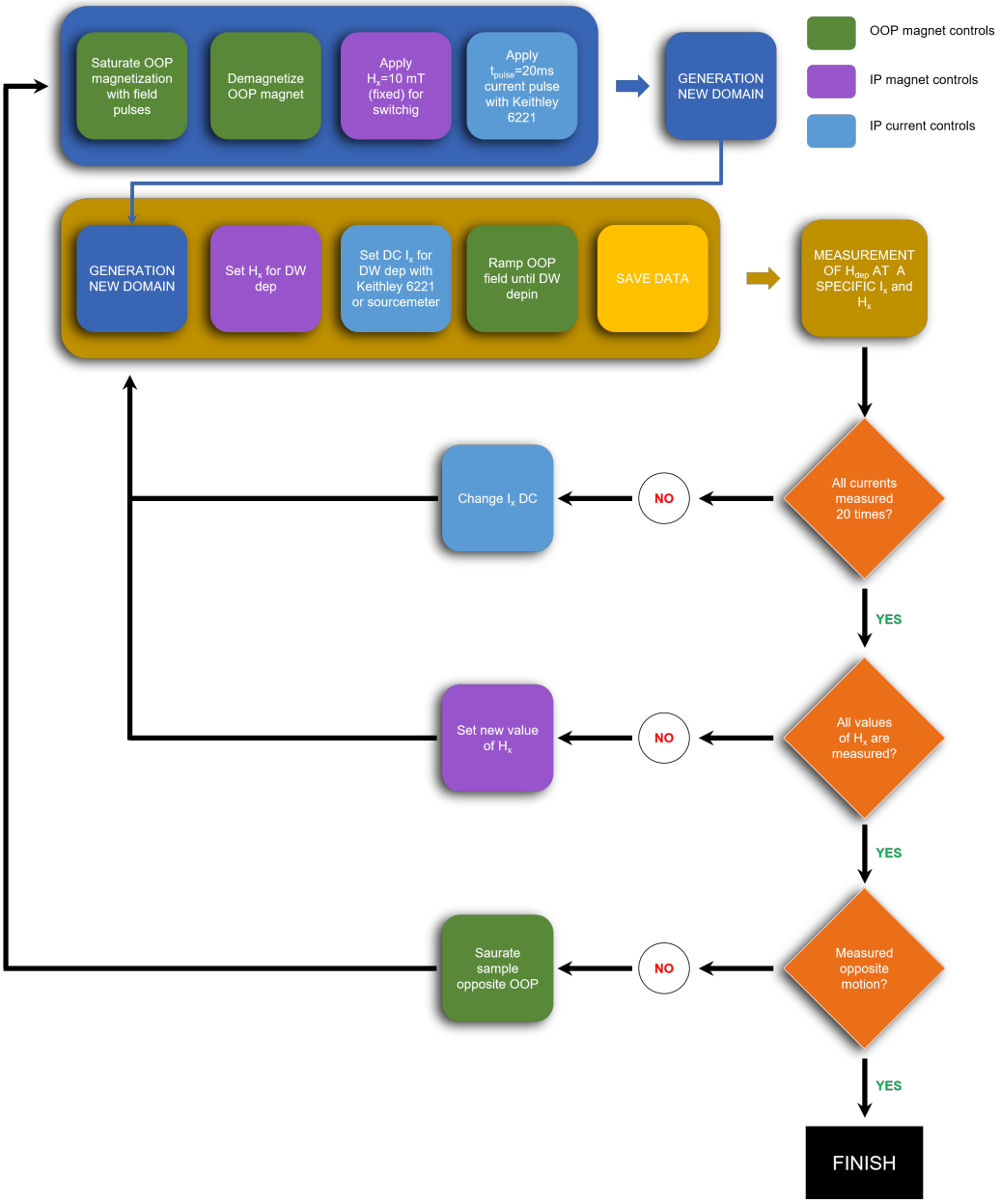

Figure 7.20: Flowchart of the automated measurement sequence implemented in LabVIEW.

Chapter 8

Spin-Orbit Torque Switching in Ultrathin Pt and Light-Metal Overlayers

Contents

In the previous chapter, we focused on the role of TbIG as an active layer for engineering and quantifying the interfacial DMI. In this chapter, we turn our attention to a complementary aspect of spin–orbit physics: the efficiency of current-induced SOT in TbIG-based heterostructures. While TbIG again serves as the magnetic insulator, its role here is more "passive". The emphasis is placed on the metallic overlayers, in particular ultrathin heavy- and light-metal films, which act as the SOT sources. This chapter is based on the manuscript *Efficient Spin-Orbit Torque Switching in a Magnetic Insulator via Ultrathin Pt and Light Metal Overlayers*, currently under revision in *Communications Physics* (Springer Nature).

SOT are a key mechanism for electrically controlling magnetic order in spintronic devices. Pt has become the prototypical material for SOT generation, primarily attributed to its strong bulk SHE and interfacial REE coupling. In this study, we revisit this established framework by investigating ultrathin Pt films interfaced with TbIG. We find that few-atom-thick Pt, which forms a nanogranular morphology, exhibits exceptionally efficient SOT-induced switching. This level of efficiency is particularly notable given the ultrathin and structurally discontinuous nature of the Pt layer, where conventional mechanisms are typically less effective. While the exact origin of the enhanced SOT remains to be fully understood, possible contributing factors include scattering effects related to the granular morphology or non-uniform conduction paths within the Pt film. These findings suggest that structural features at the nanoscale may play a more significant role in SOT generation than previously appreciated, offering a new perspective on ultrathin metal/insulator interfaces.

In addition to Pt alone, we investigate the effect of capping ultrathin Pt with Ti or Mn. Remarkably, both light metals lead to a further increase in the switching efficiency. This observation suggests that such overlayers can actively contribute to SOT generation, most plausibly through orbital current mechanisms rather than conventional spin Hall physics.

Altogether, these findings uncover unconventional pathways for generating SOT in ultrathin, structurally complex heterostructures. They provide new perspectives for optimizing device performance and open alternative strategies toward energy-efficient magnetic switching in spin–orbitronic devices.

The remainder of this chapter is organized as follows. First, we describe the structural and transport characterization of ultrathin Pt films, followed by the experimental methods and results of SOT-induced switching measurements. A detailed analysis of the SOT efficiency trends as a function of Pt morphology is then presented. Finally, we discuss the Ti- and Mn-capped counterparts and examine the influence of these light-metal overlayers on SOT efficiency and energy dissipation.

8.1 Background

The SHE and REE described in Chapter 3 have been central topics in spintronics research for the past two decades, owing to their ability to generate transverse spin accumulation in response to an applied charge current [312, 113]. This spin accumulation can exert SOT on adjacent FM layers [313, 142, 314], enabling electrical control of their magnetization [144, 109, 315]. Although the SHE is a bulk effect and the REE originates at interfaces, both mechanisms produce SOTs with identical symmetry [20]. A considerable research effort has therefore been devoted to disentangling and quantifying their respective contributions, with Pt occupying a central role in these studies [316, 317, 318].

In the past decade, a wide range of additional spin–charge conversion mechanisms have been identified. Examples include topological surface states in topological insulators [319, 320, 321], bulk and interface symmetry breaking in Weyl semimetals [322, 323, 324], van der Waals heterostructures [325], and two-dimensional electron gas systems such as $SrTiO_3$/Ta interfaces [326]. More recently, attention has turned to the OHE, which is the generation of a transverse orbital angular momentum current in response to a longitudinal charge current, even in materials with negligible SOC [40, 41, 42, 139, 327]. This discovery has sparked extensive efforts to explore the range of materials hosting OHE and its implications for spin–orbitronics, particularly with more abundant light metals such as Ti, Mn, and Cu [43, 44, 45, 137, 328, 329, 330, 331]. A key requirement, however, is

the conversion of orbital angular momentum into spin angular momentum in order to exert a torque on magnetization. This conversion is typically achieved within the FM itself or in a secondary HM layer with strong SOC.

REIGs, already introduced extensively in the previous chapters, provide an excellent platform for systematic investigations of SOT. Their chemically sharp interfaces allow integration with a wide variety of materials, enabling quantitative comparisons of SOT efficiencies across different systems. In recent years, REIG-based heterostructures have been used to demonstrate efficient current-induced switching [332, 31, 36]. More recently, these systems have also been employed to probe orbital contributions to SOTs, with notable examples including TmIG/Pt/CuO_x [45], Ta/Pt/TmIG [46], YIG/Pt/CuO_x [47, 48], YIG/Pt/TaO_x [49], and BiYIG/CuO_x [50].

In this context, TbIG is employed in this work as a model system to study unconventional SOT generation mechanisms in ultrathin Pt and in light-metal capped heterostructures. The choice of TbIG is motivated by its well-defined interfaces and tunable perpendicular anisotropy, which make it particularly suitable for disentangling interfacial and orbital contributions to spin–charge conversion.

In this work, TbIG is interfaced with ultrathin Pt layers to investigate the microscopic origins of SOTs at the atomic limit and to assess the role of light-metal overlayers in orbital torque generation. Remarkably, Pt films as thin as 0.6 nm (less than three monolayers) are found to switch the magnetization of TbIG with efficiencies comparable to those of conventional 4 nm-thick Pt layers. This result is unexpected for such ultrathin metallic films. Detailed structural and transport characterization sheds light on this behavior, revealing that the nanogranular morphology of the Pt layer may play a key role. Features such as enhanced scattering or non-uniform conduction paths could contribute to more effective spin current generation or transfer. These findings suggest that nanoscale structural properties can significantly influence SOT efficiency, offering a new perspective on torque generation in ultrathin metal/insulator systems.

Furthermore, we demonstrate that adding light-metal overlayers such as Ti and Mn on ultrathin Pt further enhances the switching efficiency. In particular, Ti reduces the critical switching current density by up to 90% and lowers the power dissipation by approximately 20%. These results point to an active role of light metals in contributing orbital currents, which are subsequently converted into spin currents at the Pt/TbIG interface. Together, these findings highlight unconventional SOT pathways in ultrathin heterostructures and establish new design principles for energy-efficient spin–orbitronic devices.

8.2 Samples Preparation and Characterization

All samples investigated in this study share a common base structure consisting of a GGG(111) substrate with an 8.5 nm-thick layer of TbIG deposited by magnetron sputtering, following the growth recipe described Chapter 5. Since the TbIG thickness was kept constant across all devices, it will not be further mentioned in the text. After deposition, the metallic layers were grown *in situ* in a separate chamber without breaking vacuum.

Two series of samples were fabricated for this work: TbIG/Pt(t_{Pt}) and TbIG/Pt(1.2 nm)/NM(t_{NM}). In the first series, the Pt thickness t_{Pt} was varied between 0.6 and 4 nm in order to study the transport properties and SOT behavior of ultrathin Pt. In the second series, the Pt thickness was fixed at 1.2 nm and capped with either Ti, in the thickness range 3.5 – 18 nm, or Mn (7 nm). None of the samples included an additional protective capping layer, in order to avoid introducing extra

elements and interfaces that could give rise to unintended contributions. While Pt is chemically stable against oxidation, the topmost ∼1.5 nm of Ti and Mn are expected to be partially oxidized. This thickness reduction due to oxidation was not corrected for in the presentation and analysis of the data.

The continuous films were patterned into Hall-bar and racetrack-shaped devices by means of optical lithography, followed by reactive ion etching. All measurements were carried out at room temperature.

8.2.1 Device Geometry and Measurement Protocols

Fig. 8.1a (top) shows an optical micrograph of a standard Hall bar device with electrical contacts and the coordinate system adopted throughout this work. The x-axis corresponds to the direction of current injection. Fig. 8.1b displays the Hall resistance measured in a TbIG/Pt(1.2 nm) sample as a function of the OOP magnetic field. The observed loop corresponds to the AHE (R_{AHE}) component of the SMR, which arises from the interaction between the spin current generated in Pt and the magnetization of TbIG [333, 332]. The hysteresis loop is square, with full remanence at zero field and a coercive field of approximately 50 mT, consistent with TbIG films exhibiting strong PMA [220, 237].

Fig. 8.1c–d illustrate a representative SOT switching measurement, performed using MOKE microscopy on 10 μm-wide racetrack devices optimized for optical contrast (Fig. 8.1a, bottom). The measurement protocol proceeds as follows. First, the magnetization is saturated with an OOP magnetic field. An IP field H_x is then applied along the current injection direction to break the rotational symmetry of the damping-like SOT that drives switching. Subsequently, a series of current pulses (20 ms or 100 ns duration) is applied, sweeping from $-I_{\mathrm{max}}$ to $+I_{\mathrm{max}}$, until a change in MOKE contrast is observed, indicating reversal of the OOP magnetization. To complete the loop, current pulses of opposite polarity are applied, sweeping from $+I_{\mathrm{max}}$ to $-I_{\mathrm{max}}$, thereby restoring the initial configuration.

A typical switching loop is shown in Fig. 8.1d for the TbIG/Pt(0.9 nm) sample. The plotted MOKE signal corresponds to the average pixel intensity within the red-marked region of Fig. 8.1c, clearly revealing the three stages of the switching process. The critical switching current density I_{c} is defined as the minimum current required to switch the magnetization from DOWN (black) to UP (bright). This value is indicated by the red line in Fig. 8.1d.

To enable continuous and efficient execution of this protocol, a new automated LabView program was developed, building on the framework introduced in the previous chapter. This implementation significantly streamlined data acquisition while remaining fully compatible with the experimental requirements of SOT switching. In particular, it allowed each switching event to be repeated at least ten times, ensuring reliable statistics for determining I_{c}.

8.2.2 Atomically-resolved Electron Microscopy and Pt Morphology

To evaluate the structural quality of TbIG, the metallic overlayers, and their interfaces, we performed Z-contrast STEM measurements on two representative samples: GGG/TbIG/Pt(0.6 nm) and GGG/TbIG/Pt(1.2 nm)/Ti(7 nm). The first sample allows direct inspection of the thinnest Pt layer that still exhibits metallic behavior and enables efficient SOT switching, as reported in this

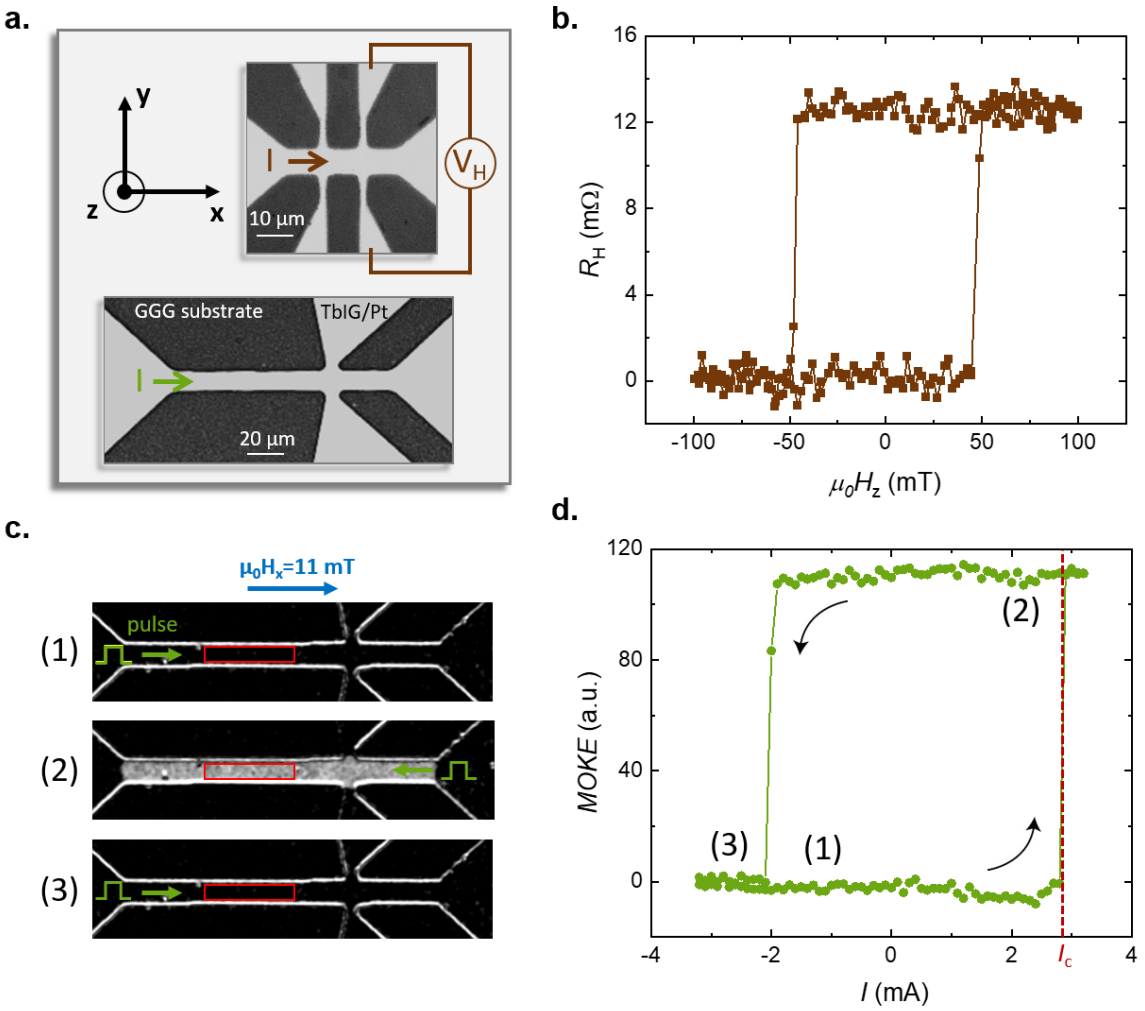

Figure 8.1: (a) Optical images of the Hall bar device used for electrical (top) and MOKE (bottom) measurements. The coordinate system is indicated, with the x-axis corresponding to the direction of current injection in both devices. (b) Representative OOP hysteresis loop measured using the Hall setup for the Pt(1.2 nm) sample, demonstrating PMA with full remanence. (c) SOT switching protocol acquired using the polar MOKE setup. Step (1): the magnetization is saturated in one direction. Step (2): a current pulse reverses the magnetization, as evidenced by the bright optical contrast in the switched region. Step (3): a current pulse of opposite polarity restores the initial state. (d) Corresponding MOKE switching loop obtained by averaging the signal from the pixels in the red-marked region in (c), clearly illustrating the three distinct switching stages.

work. The second sample provides complementary information on the structural quality of the Ti overlayer and its possible interdiffusion into the underlying layers.

Fig. 8.2a and 8.2b show HAADF-STEM cross-sectional images of the two heterostructures. In both cases, the TbIG film appears identical in thickness and crystalline quality, exhibiting a uniform single-phase cubic garnet structure across the full field of view. The interface between the GGG substrate and the TbIG film shows clear structural continuity, confirming coherent epitaxial growth without evidence of relaxation or misfit dislocations. These observations are consistent with the

structural analysis presented in Chapter 7. The consistently high epitaxial quality of TbIG in both samples demonstrates the reproducibility of the growth process and ensures that quantitative comparisons across the different heterostructures studied in this work are reliable.

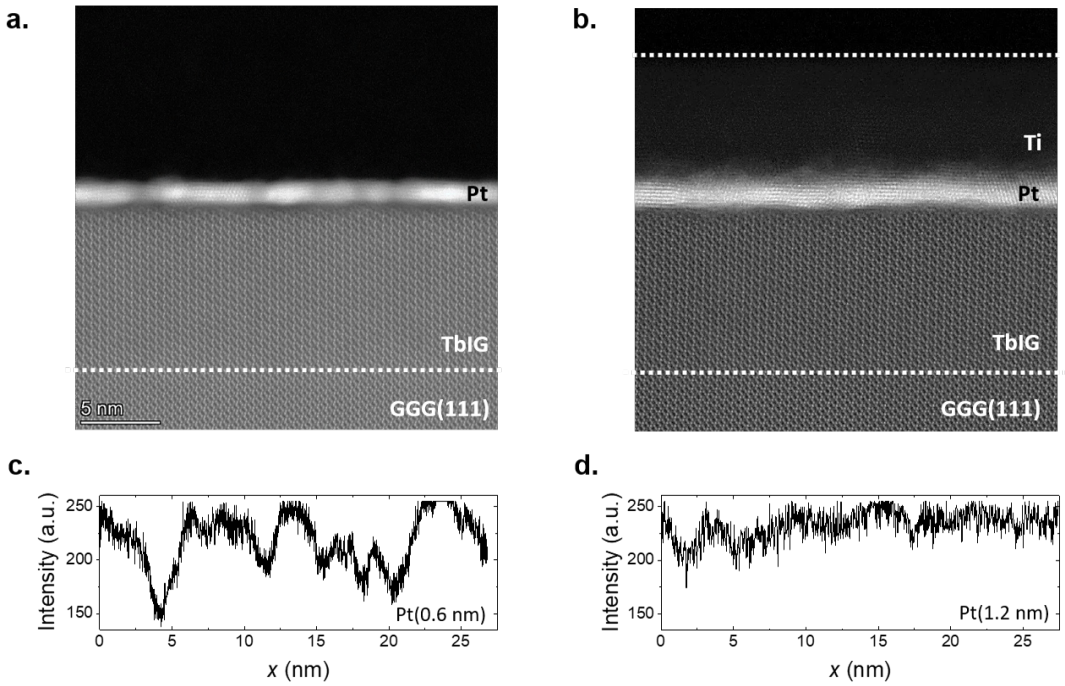

Figure 8.2: (a) HAADF-STEM cross-sectional image of the GGG(111)/TbIG/Pt(0.6 nm) sample. The image confirms the high-quality epitaxial growth of the TbIG layer and reveals the granular morphology of the ultrathin Pt layer. (b) Corresponding HAADF-STEM image for the GGG(111)/TbIG/Pt(1.2 nm)/Ti(7 nm) sample. The TbIG layer is identical to that in (a), while the Pt layer appears continuous and uniform in contrast. A broad intermixed region is observed at the Pt/Ti interface. (c) Intensity profile of the Pt layer in (a). (d) Intensity profile of the Pt layer in (b).

In Fig. 8.2a, the nominally 0.6 nm-thick Pt layer appears significantly thicker in certain regions. To estimate the actual thickness of the largest visible grain, we employed two independent methods: *i*) direct measurement of the brightest region in the TEM image using the scale bar, and *ii*) counting the number of atomic layers and multiplying by the reference interlayer spacing of Pt (0.226 nm) [334]. Both methods yield consistent results, with grain thicknesses of 1.83 nm and 1.81 nm, respectively. This indicates that even in the thinnest Pt sample, individual grains can locally reach up to three times the nominal thickness, likely interconnected by only a few monolayers of Pt, as discussed in the following sections. Such thick grains are expected to play a significant role in determining the local spin-orbit torque generation and current distribution, as elaborated later.

A comparison of the two ultrathin Pt layers in Figs. 8.2a and 8.2b shows that, despite the nominal thickness of the second Pt layer being twice that of the first (1.2 nm vs. 0.6 nm), their average thicknesses (estimated from TEM contrast) are comparable, both close to 1.8 nm. The image corresponding to Pt(0.6 nm) exhibits pronounced regions of high and low contrast, qualitatively reflecting variations in density along the viewing axis and indicating a non-uniform, granular morphology. This suggests that at very low nominal thicknesses, Pt tends to nucleate in isolated

islands, which gradually coalesce into a continuous film upon further deposition. This scenario is further illustrated in Fig. 8.2c, where the intensity profile of the Pt(0.6 nm) layer reveals marked non-uniformity. Such behavior is characteristic of Volmer–Weber (island) growth, commonly observed for metallic films on oxide or garnet substrates [335, 336, 337, 45]. Incomplete wetting leads to the nucleation of Pt clusters rather than layer-by-layer growth. In our case, the threshold for forming a continuous conductive path appears to be around 1 nm. Understanding this transition is crucial, as film continuity strongly affects spin–charge conversion efficiency in spintronic devices.

By contrast, the 1.2 nm Pt layer appears continuous and uniform, supporting the conclusion that beyond a critical thickness of approximately 1 nm the Pt film transitions from a discontinuous granular phase to a fully continuous morphology. The corresponding intensity profile shown in Fig. 8.2d highlights this uniformity. This morphological transition marks a fundamental change in the electronic properties of the film. In the granular regime, the mean free path and local transport properties vary laterally, whereas continuous Pt layers support homogeneous current flow and are expected to yield enhanced SHE efficiency. This morphological evolution is therefore central to understanding spin–charge conversion in ultrathin Pt films, and its implications will be discussed in detail in the following sections.

Motivated by these results, we performed a more rigorous calibration of the Pt deposition rate, which was found to be consistent before and after the deposition of the films shown in Fig. 8.2. Pt layers were calibrated by XRR on SiO_x substrates with deposition times of 65 s, 130 s, and 390 s, corresponding to thicknesses of 5.2, 9.9, and 30.4 nm, respectively (Fig. 8.3a). These yield deposition rates of 0.080, 0.076, and 0.080 nm/s, confirming a consistent average rate of 0.0786 nm/s, slightly above the previous estimate (0.078 nm/s). For a deposition time of 7.8 s (used for 0.6 nm Pt), this results in a thickness of 0.61 nm, within the accuracy of the sputtering system. The linear calibration is shown in Fig. 8.3b. Since the total amount of deposited Pt remains consistent with the pre-calibrated deposition rate, we continue to use the nominal thickness as a labeling method of samples for the remainder of this study, unless stated otherwise. This analysis confirms that the total amount of deposited Pt is consistent with the calibrated deposition rate. For clarity and consistency, we therefore continue to use the nominal thickness as the labeling convention for all Pt films discussed in the remainder of this work.

Interestingly, this inhomogeneous morphology is not detected by AFM. Instead, the film surface appears flat within the measurement resolution, with a RMS roughness of approximately 100 pm, comparable to that of TbIG surfaces capped with thicker Pt layers. AFM scans of TbIG/Pt (0.6 nm) and TbIG/Pt (1.2 nm), shown in Fig. 8.4, reveal nearly identical surface roughness and morphology. This stands in clear contrast to the STEM results of Fig. 8.2, which directly reveal the granular nature of ultrathin Pt. The discrepancy indicates that the characteristic inter-island gaps of Pt at low thicknesses fall below the spatial resolution of AFM. Importantly, despite its inability to capture nanoscale granularity, AFM confirms the absence of large-scale roughness or discontinuities. Moreover, this granular morphology does not hinder electrical conduction, as will be demonstrated by the electrical characterization presented in the following section.

8.2.3 Electron Energy Loss Spectroscopy

To further investigate the chemical sharpness and quality of the interfaces, we acquired EELS elemental maps for the same samples analyzed by STEM. The results are shown in Fig. 8.5a and 8.5b.

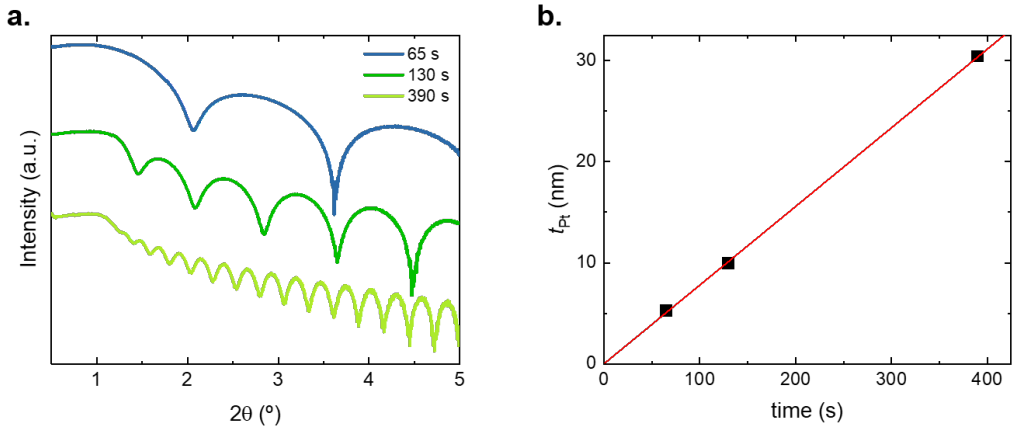

Figure 8.3: (a) XRR data for Pt films deposited on SiO_x with deposition times of 65 s, 130 s, and 390 s. The curves are shifted vertically for clarity. (b) Linear fit of deposition time versus extracted Pt thickness, confirming the consistency of the deposition rate.

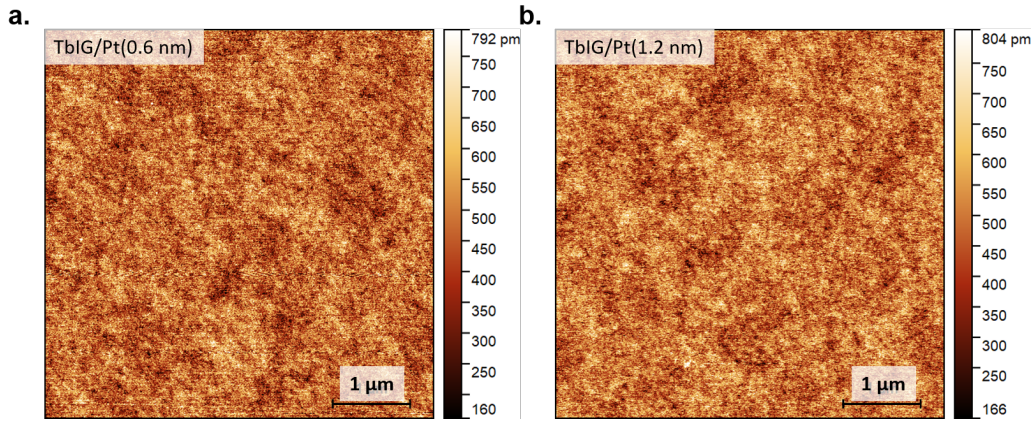

Figure 8.4: AFM scans of (a) TbIG/Pt(0.6 nm) and (b) TbIG/Pt(1.2 nm), both showing flat surfaces with comparable RMS roughness.

These maps reveal the spatial distribution of the constituent elements across the heterostructures.

For the GGG/TbIG/Pt sample, both the GGG/TbIG and TbIG/Pt interfaces (marked by gray vertical lines) appear sharp and well-defined, with negligible interdiffusion. This observation confirms the high crystalline and chemical quality of these interfaces, consistent with the STEM results presented earlier, and suggests favorable conditions for spin current transmission and a large spin-mixing conductance at the Pt/TbIG interface.

In contrast, the GGG/TbIG/Pt/Ti sample exhibits substantially more complex interfacial features. While the GGG/TbIG interface remains intact, the TbIG/Pt interface is significantly modified by interdiffusion between Pt and Ti, which enables Ti to penetrate down to the garnet surface. Within this region, we detect a small but distinct Ti peak that coincides with a dip in the Fe signal, as highlighted in Fig. 8.5c (close-up of the black square in Fig. 8.5b). The relative Ti/Fe peak–dip alignment (indicated by the arrow) strongly suggests that Ti atoms substitute for Fe in the garnet

lattice. This interpretation is further supported by the comparison of the Tb and Fe profiles: while they overlap in the Ti-free sample, they diverge in the Ti-capped case, with Fe showing an earlier onset of depletion. Such substitution effects are consistent with previous reports on intermixing of light metals, such as Al, into garnet lattices [338, 339].

The presence of Ti at the TbIG interface is particularly detrimental to magnetic functionality. Since the magnetic order in TbIG is mediated by Fe sublattices, partial replacement of Fe with non-magnetic Ti locally disrupts the interfacial magnetism. This reduces the efficiency of spin injection across the interface and ultimately degrades the SOT performance. Therefore, while Ti overlayers can strongly influence orbital current contributions (as discussed later), their tendency to diffuse and intermix at ultrathin Pt interfaces must be carefully considered in device optimization.

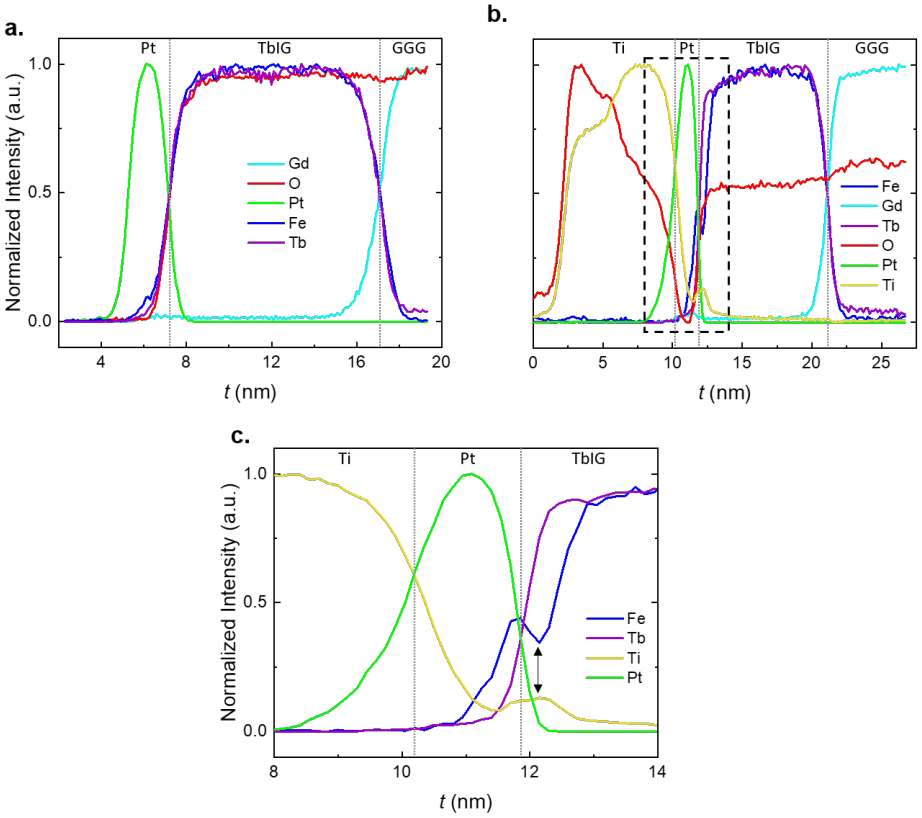

Figure 8.5: (a) EELS elemental map of the GGG/TbIG/Pt(0.6 nm) sample, showing chemically sharp interfaces (gray vertical lines) with negligible interdiffusion between layers. (b) EELS elemental map of the GGG/TbIG/Pt(1.2 nm)/Ti(7 nm) sample, revealing pronounced intermixing between Pt and Ti, and clear Ti diffusion down to the Pt/TbIG interface. (c) Magnified view of the TbIG/Pt interface from the region marked in (b), highlighting the intermixing of Ti into the TbIG layer and the anti-correlated peak in Ti intensity and dip in Fe intensity (black arrow).

8.3 Pt Thickness Dependence of Magnetotransport and SOTs

8.3.1 Resistance and Anomalous Hall Effect

To investigate the magneto-electrical and spin–transport properties of the heterostructures across the Pt thickness series, we performed longitudinal resistance (R_{xx}), anomalous Hall resistance (R_{AHE}), and SOT-induced switching measurements. Fig. 8.6a presents the resistivity ρ as a function of Pt thickness t_{Pt} in blue, and in the inset in red the longitudinal resistance R_{xx}. As expected, ρ increases sharply with decreasing t_{Pt}, with samples below 1 nm exhibiting substantially higher resistivity than their thicker counterparts. Based on this behavior, we distinguish two regimes: *thick* Pt films (1.2–4 nm), which are structurally continuous, and *ultrathin* Pt films ($t_{Pt} < 1.2$ nm), which remain partially discontinuous.

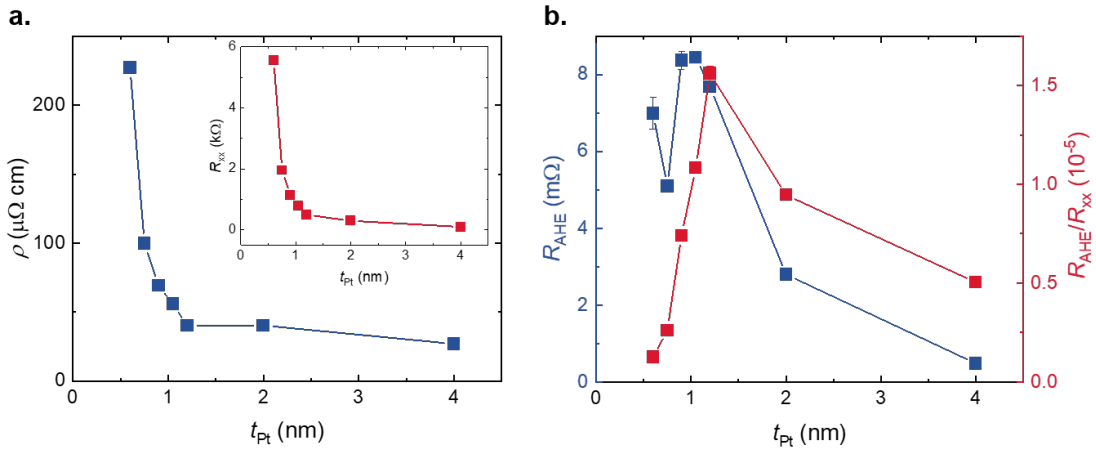

Figure 8.6: (a) Resistivity of the TbIG/Pt(t_{Pt}) bilayer as a function of nominal Pt thickness (longitudinal resistance R_{xx} shown in the inset in red). (b) Left (blue squares): anomalous Hall resistance R_{AHE}, showing an order-of-magnitude increase near $t_{Pt} \approx 1$ nm. Right (red squares): normalized anomalous Hall resistance R_{AHE}/R_{xx}, peaking at $t_{Pt} = 1.2$ nm and decreasing sharply for thinner films.

Fig. 8.6b (left axis) summarizes the anomalous Hall resistance R_{AHE}. For the TbIG/Pt(4 nm) sample, we measure $R_{AHE} \approx 0.5$ mΩ, consistent with previously reported values [237, 61] and literature benchmarks [220]. As the Pt thickness decreases, R_{AHE} rises sharply, reaching a maximum of approximately 8.5 mΩ at $t_{Pt} = 1.05$ nm, over an order of magnitude larger than in the thick-film regime, before slightly decreasing for thinner films. To account for the enhanced scattering at reduced thickness, R_{AHE} is normalized by R_{xx} (Fig. 8.6b, right axis), following the approach commonly applied in SMR analysis via longitudinal transport [333]. The normalized signal exhibits a clear maximum at $t_{Pt} = 1.2$ nm. In conventional spin transport analyses, such a peak typically corresponds to twice the spin diffusion length $\lambda_{SD,Pt}$, which would suggest $\lambda_{SD,Pt} \approx 0.6$ nm. However, this estimate is unreliable in our case, as $\lambda_{SD,Pt}$ is reported to depend on the Pt resistivity [340], which varies significantly with thickness in our samples.

Moreover, in granular Pt, the concept of spin diffusion length cannot be rigorously defined within the standard drift–diffusion framework. The models used to extract $\lambda_{SD,Pt}$ assume continuous films with homogeneous electronic properties, which do not apply in the ultrathin limit. Therefore, we

are cautious when comparing our data to literature values, where resistivity, spin diffusion length, and spin Hall angle are directly correlated such as in Ref. [340]. In our case, the sharp increase in resistivity is not due to a higher density of scattering centers in structurally similar films, but is intrinsically linked to the granular morphology of ultrathin Pt. This makes direct comparisons with conventional systems less straightforward, as the underlying mechanisms governing resistivity and spin transport in our ultrathin, granular Pt films may differ significantly from those in structurally uniform, continuous layers.

In the ultrathin limit, additional effects, such as magnetic proximity or interfacial spin–orbit scattering, may also contribute to the observed AHE behavior. While this unusual trend is intriguing, a detailed investigation of its microscopic origin lies beyond the scope of this work. In the following, we therefore shift our focus to the SOT-induced switching characteristics.

8.3.2 SOT-induced Switching

The SOT switching behavior was investigated using both long (20 ms) and short (100 ns) current pulses in the MOKE setup, following the protocol described above. All measurements were carried out under a nominally identical IP field of $\mu_0 H_{\mathrm{IP}} = 11$ mT. The corresponding critical switching currents are summarized in Fig. 8.7a, where blue and red data points denote the results obtained with millisecond and nanosecond pulses, respectively. The use of nanosecond pulses was aimed at reducing thermal activation, which can artificially facilitate switching in highly resistive devices. However, the experimental data reveal no significant difference in the overall trend: in both pulse regimes, the critical current increases quasi-linearly with increasing Pt thickness. The absolute current required in the nanosecond regime is approximately a factor of 2.4 higher than that for millisecond pulses. This observation confirms that Joule heating plays a less dominant role during nanosecond switching, although it cannot be entirely excluded, as the system remains within a thermally assisted regime [161].

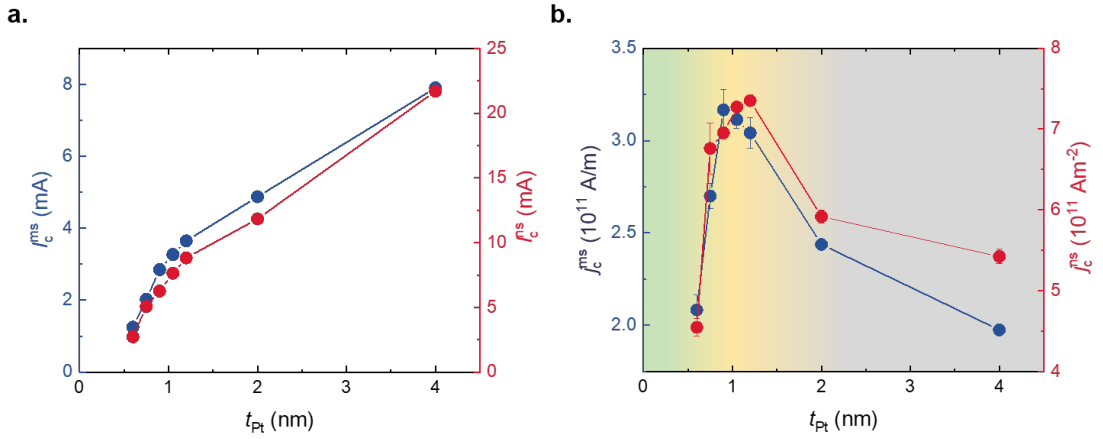

Figure 8.7: (a) Critical switching currents for millisecond pulses I_c^{ms} (left axis, blue circles) and nanosecond pulses I_c^{ns} (right axis, red circles), showing a linear decrease in the "thick" regime and a steeper drop in the "ultrathin" regime. (b) Critical current densities for millisecond j_c^{ms} (left axis, blue circles) and nanosecond j_c^{ns} (right axis, red circles) pulses, showing maximum switching efficiency in both the thickest and thinnest samples.

Fig. 8.7b presents the critical switching current density, estimated using the nominal Pt thickness, for both millisecond (j_c^{ms}, blue circles, left axis) and nanosecond (j_c^{ns}, red circles, right axis) pulses. The two datasets exhibit a consistent trend that can be categorized into three regimes. The two datasets exhibit a consistent trend that can be categorized into three distinct regimes. In the thick, continuous Pt regime (gray shaded region), the switching behavior is consistent with classical SHE expectations. In the intermediate regime (yellow shaded region), the critical current increases markedly, likely due to partial cancellation of spin accumulation from opposite interfaces. Finally, in the ultrathin Pt regime (green shaded region), a surprising enhancement in switching efficiency is observed.

Discussion on SOT Origin in Ultrathin Pt

The exceptionally high switching efficiency observed in the ultrathin regime, particularly for the thinnest Pt layer ($t_{\mathrm{Pt}} = 0.6$ nm), is a striking result. Assuming that the spin mixing conductance at the Pt/TbIG interface remains approximately constant across all samples, the large variations in critical current density (j_c) cannot be directly explained within the framework of conventional bulk SHE or interfacial REE alone.

To highlight this point, Fig. 8.8a compares the experimentally measured j_c with simulated expectations for the two conventional mechanisms. The SHE contribution ($j_{\mathrm{c}}^{\mathrm{SHE}}$, black line) was simulated according to:

$$j_{\mathrm{c}}^{\mathrm{SHE}} \propto \frac{1}{\theta_{\mathrm{SH}}\left(1 - e^{-t_{\mathrm{Pt}}/\lambda_{\mathrm{SD,Pt}}}\right)}, \tag{8.1}$$

where the spin Hall angle θ_{SH} and the spin diffusion length $\lambda_{\mathrm{SD,Pt}}$ were assumed thickness-independent for simplicity. As previously noted, this is a strong simplification that does not reflect experimental findings, which show that both $\lambda_{\mathrm{SD,Pt}}$ and θ_{SH} are highly dependent on Pt resistivity [340]. Nevertheless, while not quantitatively accurate, this model serves as a useful qualitative benchmark within a simplified bulk SHE framework. It allows us to contrast the experimental data with conventional expectations and highlight deviations that may arise from structural effects specific to the ultrathin regime. As expected, this model predicts a steep rise in j_c for $t_{\mathrm{Pt}} < \lambda_{\mathrm{SD,Pt}}$ (with $\lambda_{\mathrm{SD,Pt}} = 1.2$ nm in this example), in stark contrast with the experimental trend in Fig. 8.7b.

A pure REE contribution ($j_{\mathrm{c}}^{\mathrm{REE}}$, light blue line in Fig. 8.8a) would instead yield a thickness-independent response, which is again inconsistent with the observed enhancement at low t_{Pt}. One might expect interfacial torques such as the REE at the Pt/TbIG interface to become more relevant as the bulk SHE contribution weakens in the ultrathin limit. However, REE-induced torques scale directly with the applied current density and therefore should not produce a pronounced thickness dependence in j_c. Moreover, the sign of the switching remains constant across all Pt thicknesses, indicating that any interfacial torque adds constructively to the bulk SHE. In such a scenario, the j_c would be expected to plateau at low thicknesses and gradually decrease for larger t_{Pt}, eventually saturating once $t_{\mathrm{Pt}} \gg \lambda_{\mathrm{SD,Pt}}$. This expected behavior is in clear contradiction with our experimental results, leading us to conclude that canonical interfacial torques alone cannot explain the enhanced switching efficiency observed in the ultrathin Pt regime.

Another possible explanation is thermally assisted switching, arising from the higher resistivity of thinner Pt films. However, as discussed earlier, the comparable trends obtained with millisecond and nanosecond pulses already rule out a dominant thermal contribution. Since device heating scales with power dissipation during current injection, we analyzed the power at the switching threshold,

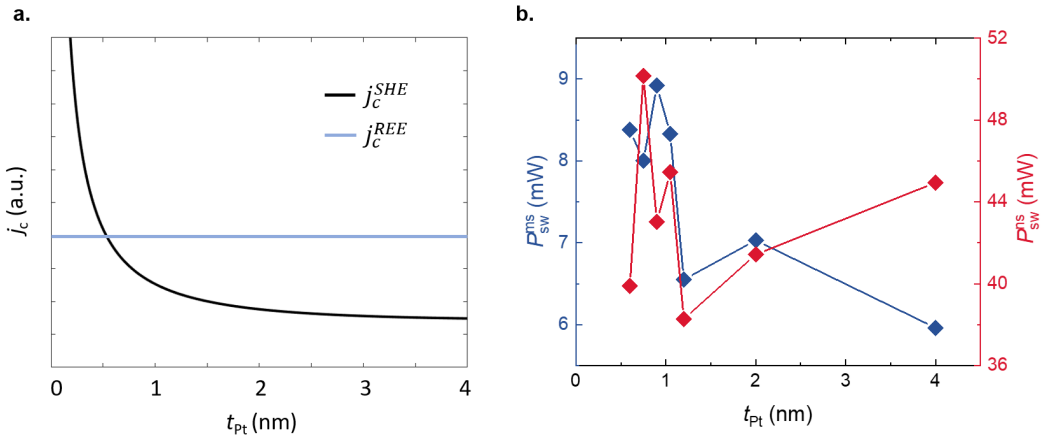

Figure 8.8: (a) Simulated trend of j_c for pure SHE (j_c^{SHE}, black line) and pure REE (j_c^{REE}, light blue line). (b) Total power dissipated during switching, $P_{\mathrm{sw}} = I_c^2 R_{\mathrm{xx}}$, for both millisecond ($P_{\mathrm{sw}}^{\mathrm{ms}}$) and nanosecond ($P_{\mathrm{sw}}^{\mathrm{ns}}$) pulses.

$P_{\mathrm{sw}} = I_c^2 R_{\mathrm{xx}}$, for both pulse durations (Fig. 8.8e). Although P_{sw} varies slightly with Pt thickness, the changes are far too small to account for the pronounced enhancement in switching efficiency. In fact, the thinnest Pt sample exhibits one of the lowest P_{sw} values under nanosecond excitation, effectively ruling out thermal activation as the primary mechanism behind the observed behavior.

Proposed Scenarions of SOT Switching in Ultrathin Pt

We therefore propose two possible scenarios for enhanced SOT efficiency, based on the morphology of our samples. STEM analysis reveals that ultrathin Pt films are laterally inhomogeneous, consisting of thick grains interconnected by thinner regions. Some of these grains locally exceed the Pt spin diffusion length, thereby enabling conventional SHE-driven spin current generation. However, such a scenario alone cannot explain the observed enhancement in SOT switching efficiency. Moreover, it would be expected to produce only partial switching, restricted to the TbIG regions directly beneath the thick Pt grains. This stands in clear contrast to our experimental findings, which consistently show complete magnetization reversal across the entire device. Fig. 8.9 highlights this point by comparing the MOKE signal from an OOP magnetic field scan (8.9a) with that from a single branch of the nanosecond-pulse switching loop (8.9b) in the TbIG/Pt(0.6 nm) sample. Both measurements were carried out under identical conditions, and the intensity difference between up and down magnetization states (approximately 160) is identical in both cases. This unambiguously demonstrates that full magnetization reversal is achieved despite the nanogranular morphology of the ultrathin Pt film.

In the morphological environment characteristic of ultrathin Pt, the first proposed scenario postulates that enhanced scattering at grain boundaries increases the effective spin Hall angle, thereby boosting the charge-to-spin conversion efficiency. An enhancement of scattering, and of resistivity with it, is known in the literature to increase both intrinsic and extrinsic contributions to the SHE. Therefore, while the underlying spin–orbit coupling and spin current generation mechanisms remain fundamentally the same in both thick and ultrathin Pt, the observed enhancement appears to be

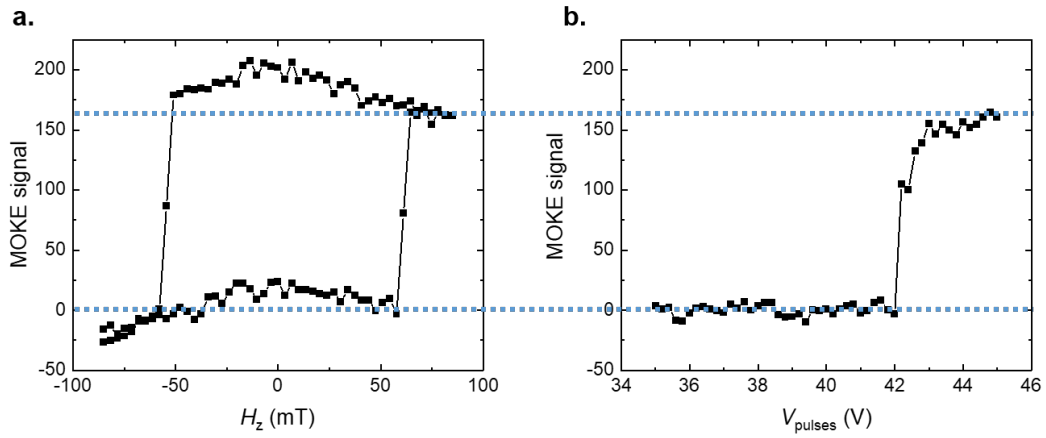

Figure 8.9: (a) Magnetic field hysteresis loop and (b) nanosecond pulse switching branch for TbIG/Pt(0.6 nm). Identical MOKE intensity confirms full switching.

driven by morphology rather than impurity scattering. This distinction is crucial, as it introduces a new regime in which structural disorder, rather than chemical doping, can be harnessed to improve spin–charge conversion efficiency even in sub-nanometer metallic samples.

Given the observed morphology, a second competing scenario can be considered. In ultrathin Pt layers with non-uniform thickness, the granular structure implies a highly non-uniform spatial distribution of current density. The current preferentially flows through the more conductive regions, resulting in locally higher current densities that may be sufficient to induce efficient SOT switching. If most of the current is confined to the grains, the effective current density in these regions would be higher than that estimated using the nominal thickness. From this perspective, the granular morphology plays a key role, not by introducing new scattering mechanisms, but by enabling localized regions with high current density where conventional SHE mechanisms can operate efficiently. Once domain nucleation occurs beneath these grains, full switching can be achieved via domain propagation.

To further support the interpretation that switching in ultrathin Pt occurs preferentially along paths of lower resistance, we analyzed the switching dynamics under nanosecond pulse excitation. These short pulses minimize thermal contributions, offering a more accurate view of the intrinsic switching behavior. The switching delay, denoted as ΔI, was extracted by averaging multiple switching curves, fitting the resulting curve with a Boltzmann sigmoidal function, and computing its derivative. A Gaussian fit was then applied to the derivative, and the full width at half maximum (FWHM) of the Gaussian was used as a quantitative measure of the switching delay. As shown in Fig. 8.10 (left axis, black squares), ΔI generally decreases with increasing Pt thickness, with the exception of an outlier at 1.05 nm. We further estimated the relative current density delay as $\Delta j/j_c$, which was found to be slightly larger for ultrathin Pt compared to thicker Pt (right axis, red squares), increasing from approximately 7% in the thick Pt to almost 20% in the ultrathin case. This trend suggests that the granular morphology leads to more disordered switching, likely involving multiple nucleation sites followed by domain wall expansion.

Another plausible scenario arises if the lateral dimensions of the current/thickness non-uniformity (a few nanometers) are smaller than the domain wall width of TbIG. In such a case, the structure

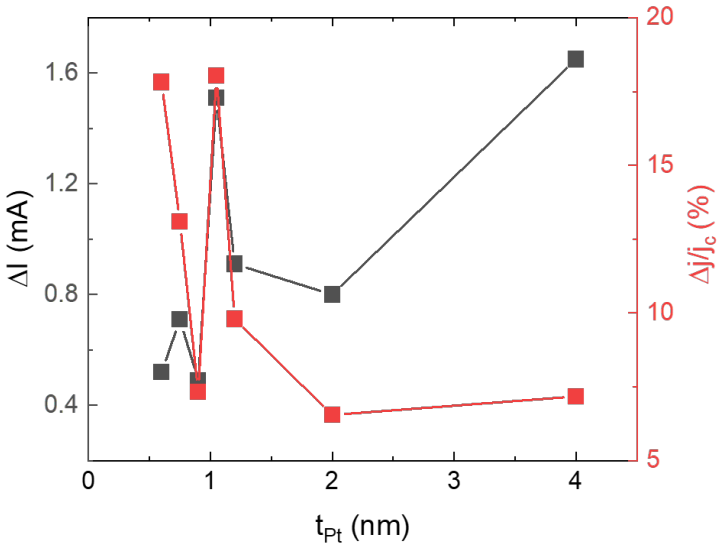

Figure 8.10: The left axis (black squares) shows the extracted switching delay ΔI as a function of Pt thickness. The right axis (red squares) shows the relative current density delay $\Delta j/j_c$, indicating increased switching disorder in ultrathin Pt due to granular morphology.

may be forced to switch fully. In the previous chapter, we estimated the domain wall width for TbIG at this thickness to be approximately 15 nm, which is comparable to the average spacing between Pt grains obtained from our MATLAB simulations (explained in the following sections).

These competing scenarios are, in principle, all possible, and at this stage we cannot exclude one over the other. We hypothesize that they may all contribute simultaneously to the observed enhancement in SOT switching efficiency for ultrathin Pt, and we refer to this collective effect as morphology-induced enhancement of the SHE.

Finally, within this framework, the three experimentally observed regimes of SOT switching efficiency can be rationalized as follows. In thick Pt films, spin–charge conversion is governed by the conventional bulk SHE. In the ultrathin limit, the concerted action of scattering-driven spin Hall processes and local contributions from thick Pt grains leads to enhanced SOT generation, resulting in efficient switching despite the reduced nominal thickness. By contrast, in the intermediate thickness regime, neither mechanism is fully optimized, leading to a reduction in switching efficiency. Unlike interfacial torques or proximity-driven effects, which would yield a thickness-independent response, the morphology-driven enhancement emerges only under specific conditions where the Pt granular structure favors SOT generation.

Taken together, these considerations suggest that while interfacial contributions cannot be fully excluded, morphology-induced enhancement provides the most consistent explanation for the unusually high switching efficiency observed in ultrathin Pt samples. This hypothesis is further substantiated in the following sections, where simulations of nanoscale Pt morphology are compared with experimental resistance data, showing compelling agreement with the proposed mechanism.

8.3.3 Measurements on TbIG/Cu(t)/Pt(1.2 nm) Structures

To further probe the role of the TbIG/Pt interface in SOT generation, we fabricated additional samples in which a Cu spacer layer of variable thickness t was inserted between TbIG and Pt (1.2 nm). Cu is a light metal with intrinsically weak SOC, and therefore inefficient for generating spin currents via the bulk SHE. Although the TbIG/Cu interface possesses broken inversion symmetry and a modest degree of SOC, it could in principle support interfacial SOTs, for example through the REE. However, the weakness of SOC in Cu makes such contributions negligible. In addition, while Cu has been reported to host orbital current generation, particularly in its oxidized form CuOx [331], this effect is irrelevant in the present structures, since no HM layer is present between Cu and TbIG to convert orbital accumulation into spin accumulation.

A crucial property of Cu is its high spin transparency, which allows spin currents generated in the Pt layer to propagate across the spacer with minimal attenuation. This ensures that the torques originating from Pt can still be transmitted to TbIG, enabling efficient magnetization switching despite the absence of direct Pt/TbIG contact. While we cannot exclude that the interfaces TbIG/Pt and TbIG/Cu may differ due to spin memory loss (SML), MPE, or variations in spin mixing conductance or spin transparency, we use these samples to qualitatively assess the possible contributions from the direct TbIG/Pt interface. For simplicity, we do not treat these effects in detail here, but we acknowledge that they may influence the spin transport and torque efficiency. In this way, the TbIG/Cu/Pt heterostructures provide a controlled platform to disentangle the contributions of the direct TbIG/Pt interface from those mediated nonlocally through a Cu spacer. A more quantitative analysis of interfacial effects, including SML, is beyond the scope of this section but remains an important direction for future work.

The Cu spacer layers investigated in this study had thicknesses of 1.5 nm and 3 nm. Fig. 8.11a shows the longitudinal resistance measurements together with a schematic of the multilayer stack, where the reference sample TbIG/Pt(1.2 nm) is indicated by a yellow star at $t_{\mathrm{Cu}} = 0$. Upon insertion of the Cu spacer, the overall resistance increases for $t_{\mathrm{Cu}} = 1.5$ nm. This behavior is attributed to intermixing between Cu and Pt at the interface, an effect that will be further discussed in the context of Ti/Pt intermixing. For the thicker spacer ($t_{\mathrm{Cu}} = 3$ nm), the overall resistance is substantially reduced due to the high conductivity of Cu, which dominates the transport.

The normalized anomalous Hall resistance R_{AHE}/R_{xx}, plotted in Fig. 8.11b, decreases linearly with increasing Cu thickness. This trend is consistent with expectations: since Cu is a light metal with negligible intrinsic SOC, it does not contribute to the AHE. Therefore, no additional AHE signal originates from the Cu spacer, and the measured response simply reflects the dilution of the Pt contribution as the spacer thickness increases.

Fig. 8.11c presents the j_c for the TbIG/Cu(t)/Pt(1.2 nm) structures. Although Cu is generally regarded as spin-transparent and does not contribute directly to SOT generation, we observe a reduction in j_c by approximately a factor of two for both the 1.5 nm and 3 nm Cu spacer layers. This behavior suggests that intermixing at the Cu/Pt interface enhances spin scattering, thereby improving spin current injection from Pt into TbIG via the SHE. The fact that both Cu thicknesses yield similar results indicates that the spacer remains transparent to spin currents as long as it is sufficiently thin. More importantly, the observation of efficient switching even in the presence of the Cu spacer confirms that contributions from the TbIG/Pt interface are negligible. This finding reinforces the conclusion that the dominant source of SOT is the Pt layer itself. It is also important

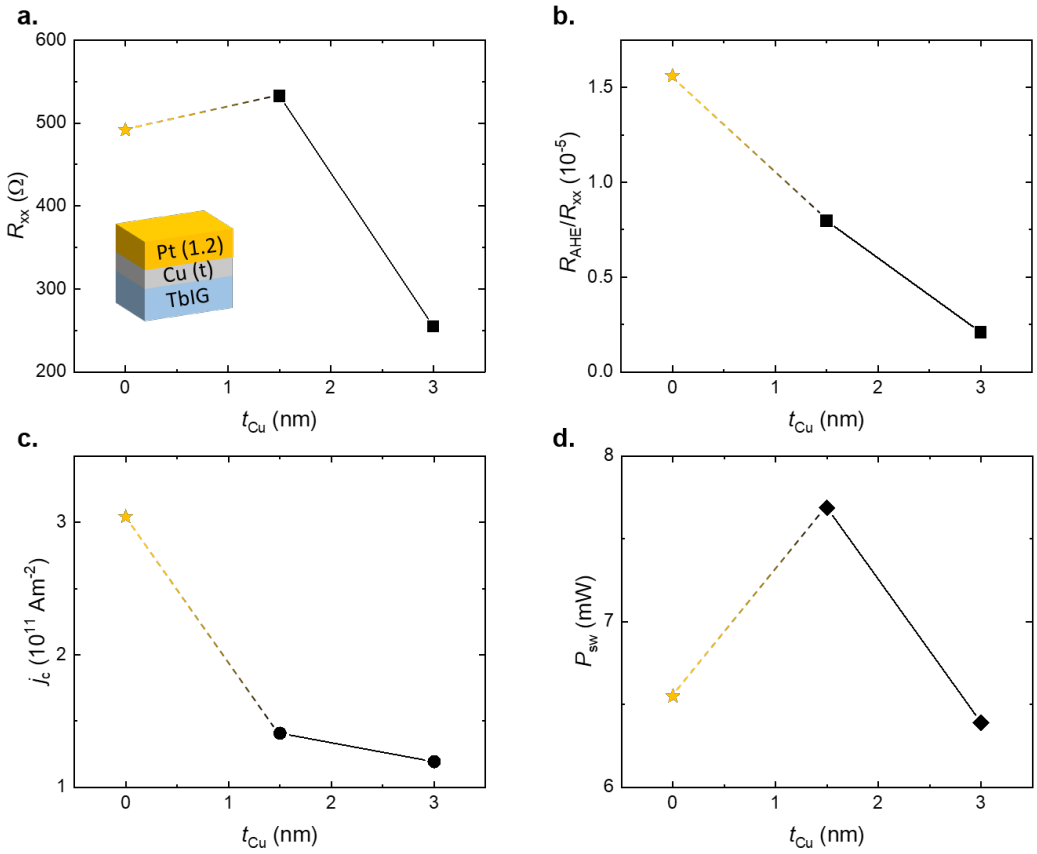

Figure 8.11: (a) Longitudinal resistance of TbIG/Cu(t)/Pt(1.2 nm) trilayers as a function of Cu spacer thickness, along with a schematic of the multilayer stack. The reference sample (TbIG/Pt without Cu) is marked with a yellow star at $t_{\mathrm{Cu}} = 0$. (b) Normalized anomalous Hall resistance R_{AHE}/R_{xx}, showing a linear decrease with increasing Cu thickness, consistent with the dilution of Pt's contribution. (c) Critical switching current density j_c, revealing a reduction by approximately a factor of two for both Cu thicknesses, suggesting enhanced spin injection via the Cu/Pt interface. (d) Power dissipated during switching.

to consider that spin accumulation may not be strictly confined to the Pt layer. Given the high spin transparency of Cu and its thinness in our structures, spin accumulation generated in Pt via the SHE can extend into the Cu layer. This extended spin accumulation may contribute to the overall torque acting on TbIG, potentially enhancing switching efficiency. However, the observed switching behavior remains largely unchanged between the two Cu thicknesses, suggesting that the role of Cu is primarily as a passive conduit rather than an active contributor to spin accumulation.

Fig. 8.11d shows the power dissipated during switching. A slight increase is observed for the 1.5 nm Cu spacer, while the 3 nm spacer restores the power dissipation to baseline levels. This behavior is consistent with the reduced resistance of the thicker Cu layer and its efficient transmission of spin currents.

8.3.4 Granular Structure of Ultrathin Pt

The pronounced enhancement of SOTs in ultrathin Pt films requires further analysis. To this end, we simulated a plausible growth scenario for ultrathin Pt using a custom MATLAB script, guided by the structural and electrical characterization presented above. The simulation models a 100×100 nm^2 matrix, initially populated with a quasi-uniform ultrathin Pt background layer. The presence of this continuous background is supported by two experimental observations. First, the current–voltage (I–V) characteristics of the device with the thinnest Pt layer display strictly Ohmic behavior (Fig. 8.12), confirming the existence of a continuous metallic conduction path between contacts separated by $\sim$300 μm. This rules out transport mechanisms such as hopping or tunneling between isolated Pt islands through the insulating garnet. Second, the MOKE contrast variation induced by current pulses matches that obtained under an external magnetic field (Fig. 8.9), demonstrating that the magnetization reversal occurs uniformly across the probed region. Consequently, the SOTs must be (quasi-)uniformly distributed throughout the device. In the simulation, this background Pt layer is assigned a mean thickness of 0.2 nm (approximately one monolayer), following a Gaussian distribution truncated between 0.1 and 0.3 nm with a standard deviation of 0.04 nm.

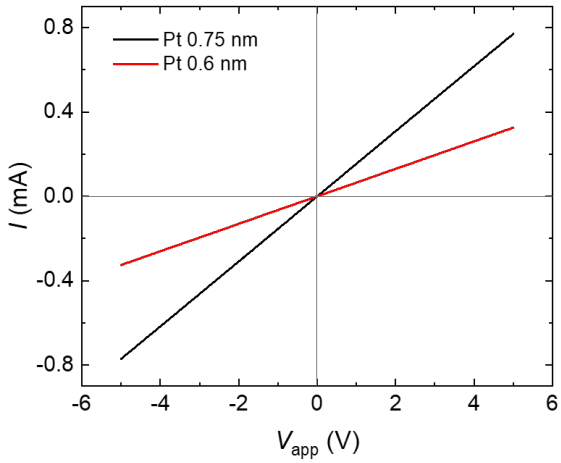

Figure 8.12: I–V curves of TbIG/Pt(0.6 nm, red) and TbIG/Pt(0.75 nm, black). Linear behavior indicates Ohmic conduction.

Subsequently, Pt grains were randomly distributed within the matrix. The grain radii followed a normal distribution with a mean of 3 nm and a standard deviation of 0.8 nm, truncated between 1 and 5 nm. The grain heights were sampled from a Gaussian distribution centered at 1.7 nm with a standard deviation of 0.4 nm, and truncated within the range 0.2–2 nm. To better reproduce realistic sputtering conditions, partial overlap between neighboring grains was permitted, limited to a maximum of 40% of their radius. Grains were iteratively added until the total integrated volume of the simulated film matched the target nominal thickness (e.g., 0.6 nm for the thinnest sample). Using this approach, we generated simulated thickness maps and corresponding histograms for Pt films with nominal thicknesses ranging from 0.6 to 1.2 nm, enabling a direct comparison with experimental observations.

At a nominal thickness of 0.6 nm, the simulated Pt film is predominantly composed of background-

level pixels, with grain-covered regions accounting for less than 50% of the surface (Fig. 8.13a, left). This behavior is consistent with earlier reports of Pt growth on TiO_2(110) [335]. The corresponding local thickness histogram (Fig. 8.13a, right) confirms this observation, displaying a dominant peak associated with background-level regions. Despite the limited grain coverage, the film remains electrically conductive via percolative grain-to-grain pathways. Charge transport in this regime is strongly influenced by enhanced grain boundary scattering, which reduces the effective electronic mean free path. This effect is schematically indicated by the red arrow in Fig. 8.13a, marking one of the few low-resistance trajectories available for electron flow along the x-direction. These localized paths can give rise to elevated current densities, potentially enhancing the effective SOT efficiency.

Importantly, grain boundary scattering not only limits electrical conduction but also enhances spin–orbit interactions, effectively boosting the spin Hall angle in the ultrathin regime. Thus, the same nanogranular morphology that hinders charge transport simultaneously provides a pathway for more efficient spin-to-charge conversion. Taken together, these observations support two complementary mechanisms: (i) localized current density enhancement due to morphological inhomogeneity, and (ii) increased spin–orbit scattering at grain boundaries. Both effects are expected to contribute to the enhanced SOT efficiency observed experimentally in the thinnest Pt layers, and neither can be excluded at this stage.

As the nominal Pt thickness increases to 0.75 nm (Fig. 8.13b, left), the surface coverage by grains rises to approximately 65%. This enhanced connectivity provides more continuous conduction pathways, thereby accounting for the sharp resistance drop reported in Fig. 8.6. At higher thicknesses, namely 0.9 nm and 1.05 nm (Fig. 8.13c and 8.13d, respectively), the connectivity improves further, with grain coverage reaching ∼80% and ∼93%. The corresponding histograms of local Pt thickness (Fig. 8.13b-c, right) capture this transition clearly, showing a progressive shift from a dominant population of background-level pixels (around 0.2 nm) toward an increasing fraction of "thick" pixels (around 1 nm). This morphological evolution signals the transition from a discontinuous, grain-dominated regime to a nearly continuous metallic film.

At a nominal thickness of 1.2 nm, the Pt film exhibits a fully continuous morphology with nearly 100% surface coverage (Fig. 8.13e, left). At this stage, individual grains merge, and the Pt layer assumes an almost uniform structure. Consequently, no further enhancement of scattering is expected from grain boundaries, and the film behaves as a conventional thin metallic layer. This thickness, therefore, marks the onset at which the resistivity of Pt approaches values characteristic of continuous thin films. The corresponding local thickness histogram (Fig. 8.13e, right) displays a Gaussian distribution centered around the nominal thickness, with no pixels remaining at background-level. This confirms the complete coverage and uniformity of the Pt film at this stage of growth.

These simulations support the hypothesis that film morphology enhances the effective SHE in ultrathin Pt. The results reveal three distinct morphological regimes: (i) discontinuous films with grain coverage below 50%, (ii) transitional or percolative films with coverage between 50% and 95%, and (iii) continuous films with coverage exceeding 95%. To quantify this morphological evolution, we calculated the surface area fraction covered by Pt grains as a function of nominal thickness, ranging from 0.2 to 1.2 nm (Fig. 8.14a). Up to 0.6 nm, the grain coverage increases linearly with thickness. Beyond this value, the area fraction progressively saturates toward 100%, deviating from the initial linear trend as the film approaches full continuity.

To correlate the simulated morphological evolution with the experimental transport data, we plotted the resistivity of the complete sample set on a semilogarithmic scale (Fig. 8.14b). Three

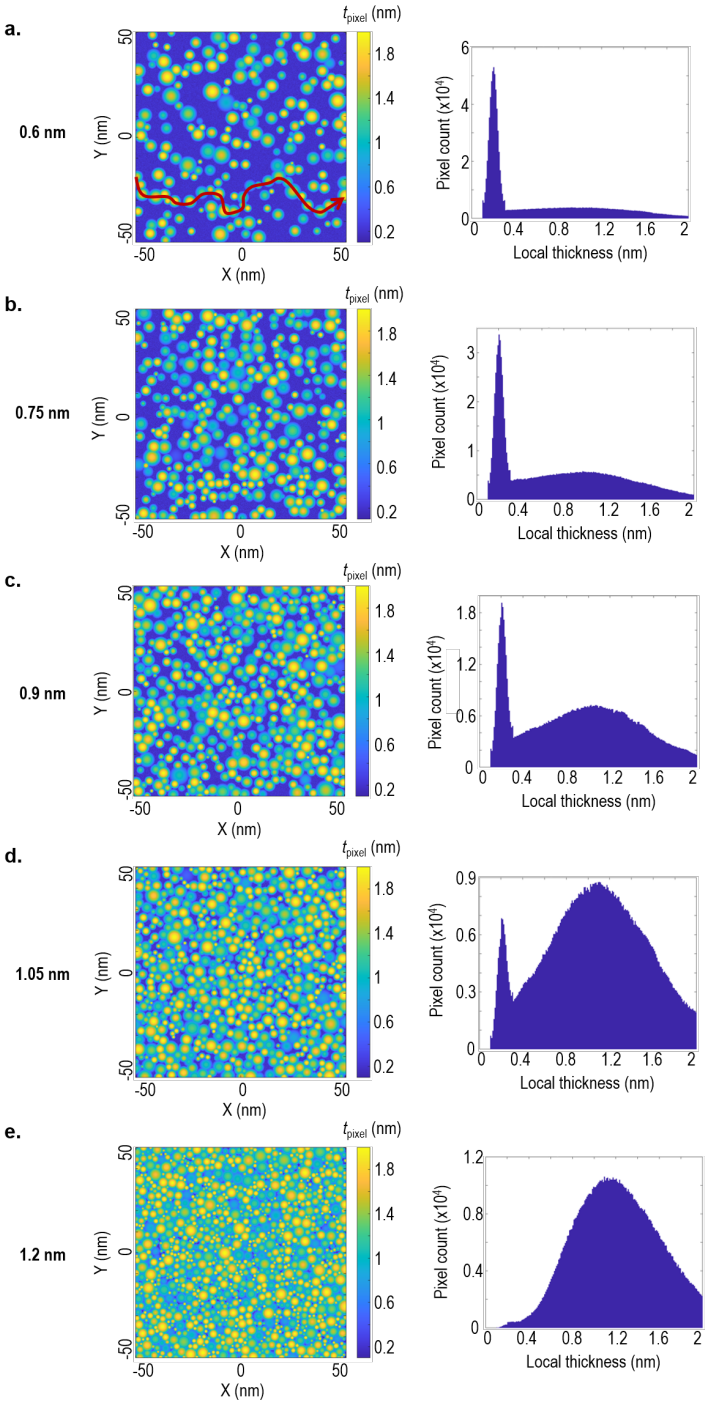

Figure 8.13: Simulated local thickness maps (left) and corresponding histograms of local Pt thickness values (right) for samples with nominal Pt thicknesses of 0.6 nm (a), 0.75 nm (b), 0.9 nm (c), 1.05 nm (d), and 1.2 nm (e). The red arrow in (a) highlights one of the few continuous, low-resistance paths available for electron transport along the x-direction.

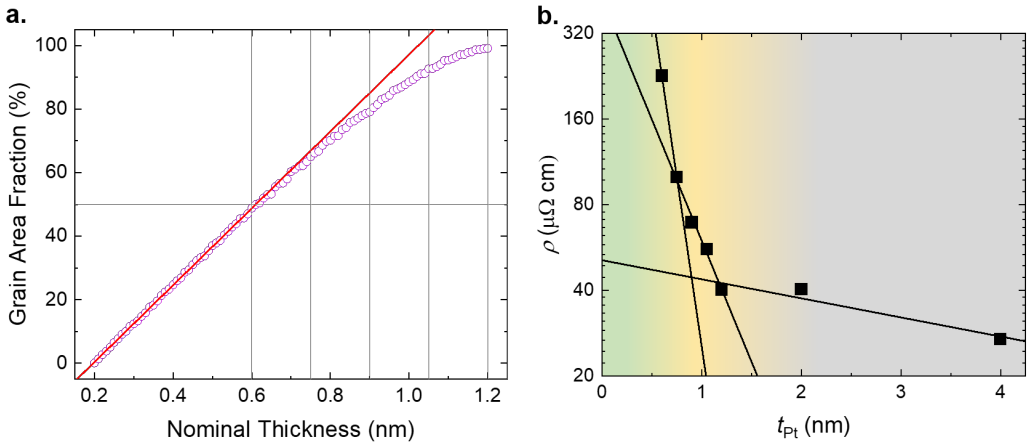

Figure 8.14: (a) Simulated percentage of surface area covered by Pt grains as a function of nominal thickness, ranging from 0.2 to 1.2 nm. Vertical dashed lines indicate the experimentally studied thicknesses. (b) Measured Pt resistivity plotted on a semi-logarithmic scale. Three distinct linear regimes are evident: discontinuous, percolative, and continuous, highlighted using the same background colors as in Fig. 8.7.

distinct linear regimes emerge, in direct correspondence with the morphological transitions described above. Linear fits delineate these regions, which are highlighted using the same background colors as those employed for the j_c in Fig. 8.7, thereby establishing a direct link between film morphology, electrical transport, and SOT switching efficiency.

8.4 Exploring Orbital Torques by Ti and Mn

We next investigated the possibility of generating orbital torques in light-metal–capped heterostructures, using the TbIG/Pt system as the base platform. Specifically, we selected TbIG/Pt(1.2 nm) as the reference structure and deposited Ti overlayers with varying thicknesses, as well as a fixed Mn overlayer. The choice of $t_{\mathrm{Pt}} = 1.2$ nm, despite its relatively low switching efficiency in the bare TbIG/Pt bilayer, was motivated by the fact that thinner Pt layers did not exhibit measurable AHE or SOT-induced switching when capped with Ti. This absence of signal is most likely caused by excessive Ti–TbIG intermixing at the Pt/TbIG interface, which degrades the interfacial spin-mixing conductance. The TbIG/Pt(1.2 nm) base layer proved to be sufficiently robust against such interfacial degradation, while still maintaining a Pt thickness low enough to avoid suppressing orbital-to-spin conversion. This allowed us to demonstrate that strong SOT switching can indeed be recovered and even enhanced when Pt is capped with a light metal.

The Ti capping layers were deposited with nominal thicknesses $t_{\mathrm{Ti}} = 3.5$, 7, 14, and 18 nm. In addition, a sample capped with 7 nm of Mn was fabricated to probe the effect of a different light metal. Fig. 8.15a presents the longitudinal resistance R_{xx} for the full set of stacks. The reference TbIG/Pt(1.2 nm) sample is shown at $t_{\mathrm{Ti}} = 0$ and is marked by a yellow star. Interestingly, the sample with a 3.5 nm Ti overlayer displays a higher resistance than the bare Pt reference, similar to the behavior observed for TbIG/Cu(1.5 nm)/Pt(1.2 nm). This counterintuitive trend can be explained by the formation of a highly resistive intermixed region between Ti and Pt, as directly

evidenced by the TEM and EELS analyses discussed earlier. In this case, the reduced effective thickness of pure Pt available for conduction is only partially compensated by the added Ti, leading to an overall increase in resistance. For thicker Ti capping layers, however, the total resistance decreases in line with expectations, as the additional Ti contributes more effectively to the overall conductivity.

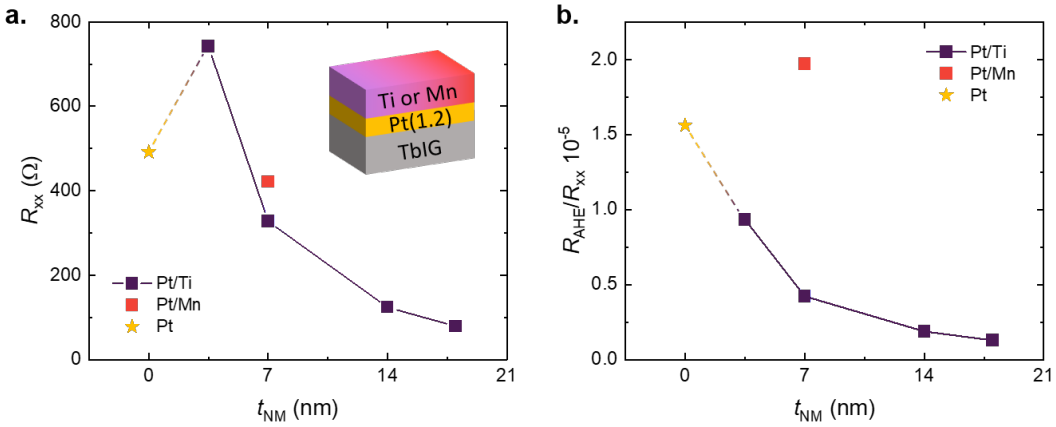

Figure 8.15: (a) Longitudinal resistance R_{xx} for the TbIG/Pt(1.2 nm)/NM(t_{NM}) trilayer as a function of NM thickness (structure shown in the inset). Purple squares correspond to Pt/Ti(t_{Ti}), the red square represents Pt/Mn(7 nm), and the yellow star denotes the Pt(1.2 nm) reference sample. (b) R_{AHE} normalized by R_{xx}. The Ti series (purple squares) shows a clear decrease in normalized R_{AHE} compared to the Pt reference (yellow star), while the Mn sample (red square) displays an enhanced value, suggesting an improvement in interfacial spin transport.

We first examine the normalized anomalous Hall resistance, R_{AHE}/R_{xx}, shown in Fig. 8.15b. For the Ti-capped series, R_{AHE}/R_{xx} decreases monotonically with increasing Ti thickness, consistent with the Pt origin of the signal. In contrast, the Mn-capped sample exhibits a significantly enhanced R_{AHE}/R_{xx} compared to both the Ti-capped structures and the Pt-only reference. This striking difference reflects the fundamentally distinct properties of Ti and Mn. Ti is nonmagnetic and, when intermixed at the TbIG/Pt interface, degrades interfacial quality by reducing spin transparency and spin accumulation. Mn, by contrast, can substitute Fe in the garnet lattice and adopt a magnetic state under suitable valence conditions [341]. It is therefore plausible that Mn at the substituted TbIG interface acquires spin polarization through the magnetic proximity effect, akin to Pt. Such interfacial spin polarization could enhance the AHE response, accounting for the increased R_{AHE} observed in the Mn-capped sample.

We next turn to the switching measurements reported in Fig. 8.16a. Upon insertion of Ti, the total critical switching current density $j_{c,tot}$ decreases dramatically by nearly an order of magnitude. Moreover, increasing Ti thickness further lowers $j_{c,tot}$, suggesting that Ti itself contributes actively to the SOT switching mechanism. A plausible explanation is the OHE: orbital currents generated in Ti may be converted into spin currents in the adjacent Pt layer, where strong SOC enables their transfer as a spin accumulation at the Pt/TbIG interface. Notably, the Mn-capped sample also displays a similarly low switching current, reinforcing the notion that light elements with strong OHE can act as effective contributors to SOT generation.

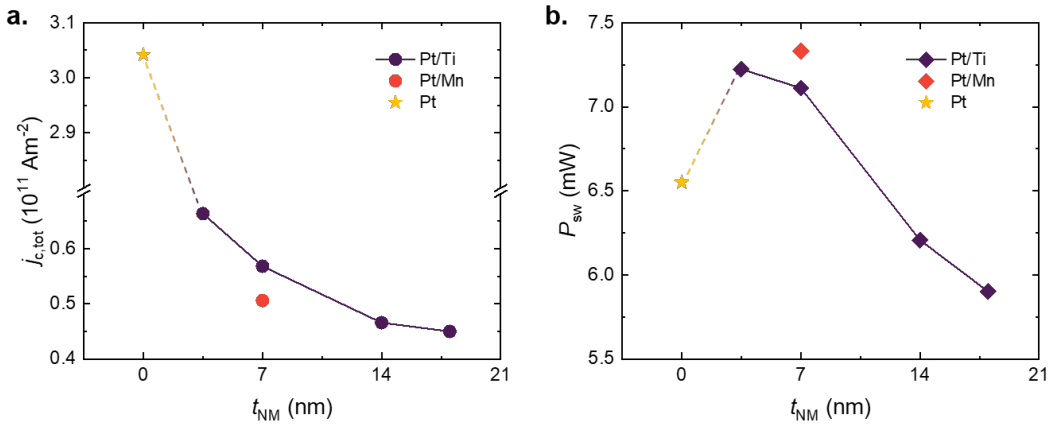

Figure 8.16: (a) Critical switching current density j_c, revealing a reduction of over an order of magnitude for both Ti (purple circles) and Mn (red circles) compared to the reference Pt (yellow star). (b) Total power dissipated during switching, P_{sw}, which initially increases for $t_{NM} < 14$ nm, followed by a decrease for thicker NM layers. This trend suggests that thicker NMs enhance the overall switching efficiency, pointing toward an active role of the normal metal layers in SOT generation.

Furthermore, the power dissipated during switching, P_{sw}, is presented in Fig. 8.16b. For the thinnest Ti sample, P_{sw} increases, which we attribute to a reduced magnetic interface quality at the TbIG/Pt boundary. In this case, the OHE generated in Ti is weak and insufficient to compensate for the loss in spin mixing conductance. By contrast, for thicker Ti layers, P_{sw} decreases, indicating that the OHE contribution becomes substantial and offsets interfacial degradation. Taken together, these results demonstrate that Ti not only reduces the critical current required in Pt but also lowers the total energy cost of switching, thereby confirming its active role in SOT generation.

To further clarify the contribution of the Ti layer to SOT switching, we employed a parallel resistor model to separate the current flowing through Pt (I_{Pt}) and Ti (I_{Ti}). The total resistance of TbIG/Pt(1.2 nm)/Ti(t) samples was first fitted with an exponential decay, yielding an effective resistance for the Pt layer of $R_{Pt} \approx 1737\ \Omega$ (Fig. 8.17a). Assuming the two layers act as parallel resistors, the total resistance can be expressed as:

$$\frac{1}{R_{tot}} = \frac{1}{R_{Pt}} + \frac{1}{R_{Ti}}. \tag{8.2}$$

From this relation, R_{Ti} was extracted for different Ti thicknesses (Fig. 8.17b). The corresponding resistivity values (Fig. 8.17c) are in good agreement with literature reports for sputtered Ti films [241], supporting the validity of the parallel resistor approximation.

The current flowing through each layer was then estimated as:

$$I_{Ti(Pt)} = \frac{I_{tot} R_{tot}}{R_{Ti(Pt)}}. \tag{8.3}$$

As shown in Fig. 8.17d, the current required in Pt to achieve magnetization switching decreases progressively with increasing Ti thickness. This observation reinforces the idea that Ti is not merely a passive overlayer but plays an active role in the SOT process. While interfacial effects at the Pt/Ti boundary could, in principle, generate additional spin accumulation, potentially accounting

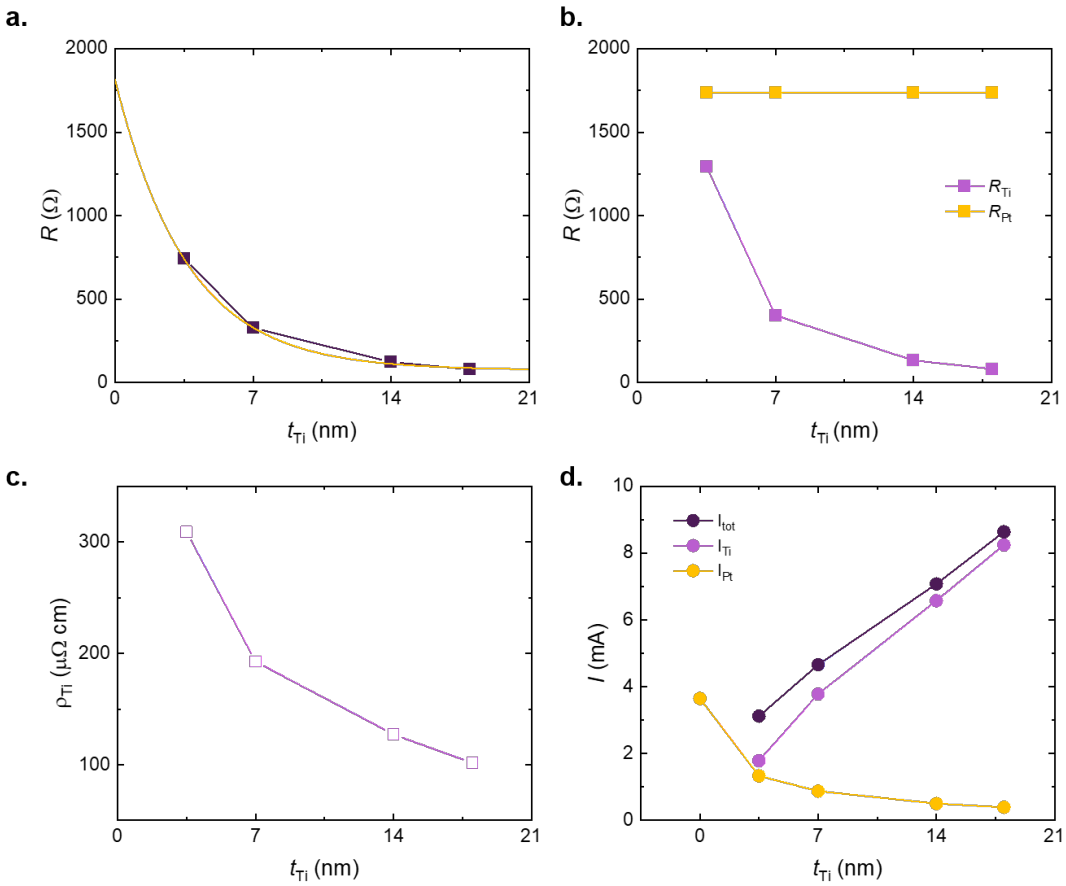

Figure 8.17: (a) Total longitudinal resistance of TbIG/Pt (1.2 nm)/Ti(t) stack. (b) Resistance of Ti layer estimated using a parallel resistor model. (c) Extracted resistivity of Ti as a function of Ti thickness. (d) Total critical switching current (I_{tot}, purple), and calculated current flowing through the Pt (I_{Pt}, yellow) and Ti (I_{Ti}, light purple) layers, respectively, showing a marked decrease in the current required in the Pt to switch the magnetization, indicating that Ti contributes to the SOTs.

for the enhanced efficiency observed in the Pt/Ti(3.5 nm) sample, the monotonic improvement with increasing Ti thickness points toward a bulk-mediated contribution from Ti itself. Such a contribution is consistent with the OHE, whereby orbital currents generated in Ti are converted into spin currents in Pt, and subsequently exert torques on the TbIG layer.

8.5 Conclusions

In this work, we conducted a comprehensive investigation of SOT switching in magnetic insulator heterostructures, focusing on ultrathin Pt layers and the effect of light-metal overlayers.

By combining structural, transport, and magneto-optical measurements, we demonstrated that Pt films with nominal thicknesses below 1 nm, despite their nanogranular morphology, can exhibit remarkably high SOT switching efficiency. This enhancement is attributed to morphology-induced mechanisms, where two complementary effects play a decisive role: (i) grain boundary scattering

enhances spin–orbit interactions, boosting the effective spin Hall angle, and (ii) current redistribution through conductive grains leads to locally elevated current densities, enabling efficient switching even at reduced nominal thickness. These findings highlight how nanoscale structural disorder can be harnessed to improve spin–charge conversion beyond conventional bulk or interfacial mechanisms.

We further established that capping ultrathin Pt with light metals such as Ti and Mn introduces an additional pathway for torque generation through orbital currents. These overlayers not only reduce the critical switching current density but also lower overall power dissipation once a critical thickness is reached, confirming their active role in SOT enhancement. The interplay between OHE in light metals and strong SOC in Pt provides a new conceptual framework for engineering energy-efficient spintronic devices.

Altogether, our findings broaden the fundamental understanding of SOT generation at the atomic scale and emphasize the decisive role of nanoscale morphology and orbital transport phenomena. These insights open promising routes for the design of tailored heterostructures that exploit extrinsic scattering and orbital contributions, offering viable strategies for advancing next-generation spin–orbitronic technologies.

Chapter 9

Observation and Control of Spiral Magnetic Domains in Co/Pt/Co Multilayers

Contents

This project is the only one in this Thesis that focuses exclusively on all-metallic heterostructures. It represents a long-standing and still ongoing effort, with the peculiarity of being the very first project initiated immediately after the construction of the MOKE setup. The choice of the Co/Pt/Co heterostructure was guided by several practical considerations. First, the magnetic contrast provided by a metallic ferromagnet with PMA, in this case Co, is much stronger than that of REIG-based samples, making it an ideal platform for testing and optimizing the performance of the newly built setup. Second, achieving robust PMA in Pt/Co is, in principle, simpler than in garnet films, which allowed for the preparation of suitable samples within a short timeframe. Finally, the

topic of IL-DMI, an emerging and highly active research area at the time, was particularly compelling. Investigating IL-DMI requires magnetic trilayers such as Co/Pt/Co, which could be readily fabricated once the Pt/Co interface was optimized. The central aim of this project is to explore how IL-DMI influences domain formation, a task carried out entirely through MOKE microscopy-based domain imaging.

The study of IL-DMI in metallic multilayers provides a pathway to engineer chiral spin textures and non-collinear magnetic states in synthetic systems. In particular, IL-DMI can promote the stabilization of spiral domains, determine domain-wall chirality, and potentially enable the controlled formation of skyrmions in multilayer stacks. Understanding these effects in a simple metallic trilayer, therefore, constitutes an important step toward exploiting interfacial DMI for spin–orbitronic applications in both metallic and insulating systems.

In this final Chapter, I present the most significant results obtained so far, while noting that further measurements and additional samples will be required to achieve a comprehensive picture, as will be discussed in detail later. As a final remark, many of the MOKE images shown in this Chapter exhibit non-uniform contrast across the field of view, blurred regions, or occasional black spots. These artifacts reflect the ongoing optimization of the MOKE setup, which was carried out in parallel with this project.

9.1 Background

Indirect exchange interactions, whereby two ferromagnetic layers couple through a nonmagnetic spacer, have long been understood in terms of the symmetric RKKY interaction, introduced in Chapter 2. This mechanism, which favors collinear alignment of magnetizations, has been central to the development of GMR and has played a foundational role in the broader field of spintronics [342, 77, 79, 78, 343, 344, 345, 346, 347].

In recent years, a new form of interlayer coupling, the IL-DMI, has been identified. First predicted theoretically in 2019 [172] and soon after confirmed experimentally [173, 174], it can be regarded as the antisymmetric counterpart of conventional interlayer exchange. Unlike conventional DMI, which is confined to interfaces and stabilizes two-dimensional (2D) chiral textures within individual layers, IL-DMI acts across a spacer layer, enabling the stabilization of three-dimensional (3D) chiral spin structures. The interaction arises from SOC in the nonmagnetic spacer, typically a heavy metal such as Ru or Pt, combined with broken inversion symmetry across the trilayer. The ability of IL-DMI to stabilize complex 3D textures, including spiral domains and skyrmions, opens promising opportunities for reconfigurable magnetism and spintronic applications [348, 349]. However, experimentally accessing IL-DMI is highly nontrivial, as it requires heterostructures with orthogonal magnetic anisotropies, carefully controlled interfaces, and optimized spacer thicknesses [350].

In this chapter, we investigate IL-DMI in a fully metallic Co/Pt/Co trilayer, designed such that the bottom Co layer is magnetized IP and the top Co layer OOP. The Pt spacer plays a dual role: it induces PMA at the Co/Pt interface and mediates the chiral interlayer coupling. This minimal but versatile configuration provides an ideal platform to probe IL-DMI using WF- and L-MOKE microscopy.

The chapter is organized as follows. We first describe the design principles and fabrication protocols used to optimize the heterostructure, including plasma cleaning (PC) procedures and systematic variation of layer thicknesses. These steps are essential for achieving sharp interfaces and

robust PMA. We then present MOKE imaging experiments revealing the spontaneous nucleation of spiral magnetic domains around magnetic defects and their field-driven evolution. Finally, we demonstrate deterministic control of domain morphology by lithographically patterning magnetic impurities, highlighting the central role of the IP Co layer and its coupling to the OOP Co layer in stabilizing chiral textures.

Overall, this work establishes the Co/Pt/Co trilayer as a model system for investigating IL-DMI and its role in shaping non-trivial domain structures. The insights gained here provide a foundation for future spin–orbitronic devices that exploit engineered 3D chiral magnetism.

9.2 Heterostructure Description and Optimization

The heterostructure studied in this work is SiO_x/Ti/Co(IP)/Pt/Co(OOP)/Ti (Fig. 9.1), with individual layer thicknesses detailed below. The key design principle is the contrasting magnetic anisotropy of the two cobalt layers: the bottom Co layer is magnetized IP, while the top Co layer is magnetized OOP. This distinction results primarily from their different thicknesses and from the role of the intermediate Pt spacer.

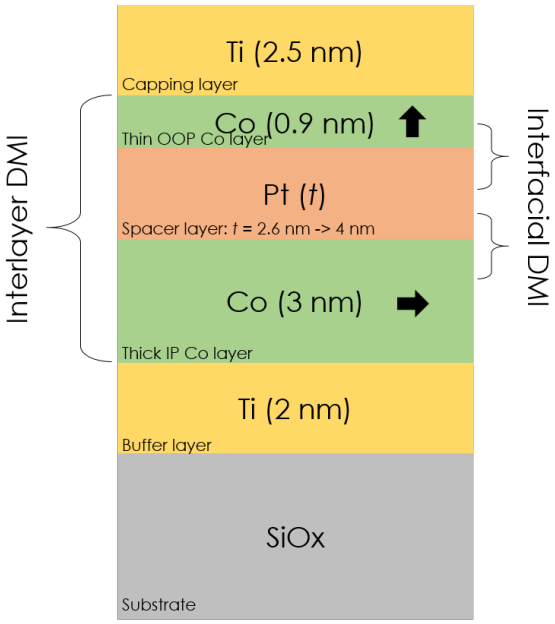

Figure 9.1: Schematic of the SiO_x/Ti/Co/Pt/Co/Ti heterostructure. The bottom Co layer is designed to be IP magnetized, while the top Co layer exhibits OOP magnetization. Pt acts as both a spacer and a source of SOC, while Ti serves as adhesion and capping layer.

9.2.1 Layer Stack Design

The Ti layers serve passive roles in the heterostructure. The bottom Ti layer (2.0 nm) acts as an adhesion layer, and was chosen because of its ability to grow flat and adhere strongly to the Si substrate, thus preventing delamination during the lift-off process. The top Ti layer (2.5 nm)

instead acts as a capping layer, protecting the upper Co film from oxidation while being thin enough to preserve the magnetic contrast in MOKE imaging.

The top Co layer was designed to exhibit OOP magnetization. As established in the literature, sufficiently thin Co layers can develop PMA when interfaced with heavy metals such as Pd or Pt, owing to orbital hybridization at the Co/HM interface. Since this effect is highly thickness-dependent, we chose 0.9 nm as the reference thickness for the top Co layer. Moreover, the Pt/Co interface is known to induce interfacial DMI, which favors Néel-type DWs and other chiral spin textures.

The Pt spacer layer plays a central role. It is required to induce PMA in the top Co layer and, due to its strong SOC, it not only enhances interfacial DMI but also mediates long-range IL-DMI, coupling the two Co layers with orthogonal anisotropies in a chiral fashion. The Pt thickness was varied between 2.2 and 3.2 nm to optimize these effects, as discussed later in this chapter.

Finally, the bottom Co layer was designed to be IP magnetized. To achieve this, it must be thick enough to overcome the PMA contribution induced by its Pt interface. For this reason, a thickness of 3.0 nm was selected as the reference value for the bottom Co layer.

Summary of Layer Roles

- **SiO_x**: Substrate for structural support.
- **Bottom Ti (2.0 nm)**: Adhesion layer ensuring smooth growth and preventing delamination.
- **Bottom Co (3.0 nm)**: IP magnetized ferromagnetic layer.
- **Pt (2.2–3.2 nm)**: Spacer with strong SOC; induces PMA in the top Co, provides interfacial DMI, and mediates IL-DMI between the Co layers.
- **Top Co (0.9 nm)**: OOP magnetized ferromagnetic layer stabilized by PMA at the Co/Pt interface.
- **Top Ti (2.5 nm)**: Protective capping layer preventing oxidation of Co while preserving optical contrast for MOKE.

9.2.2 Optimization of Co/Pt/Co Heterostructure with L-MOKE

Plasma Cleaning and Interface Quality

All layers of the heterostructure were deposited by DC magnetron sputtering. A crucial step for obtaining sharp interfaces and strong interfacial effects is the PC of the SiO_x substrate prior to deposition. The quality of this initial interface strongly determines the subsequent growth of metallic layers, where unwanted imperfections can be particularly detrimental in systems where interfacial SOC and hybridization effects are central to the magnetic properties.

PC is a well-established pre-treatment in thin-film fabrication. In this process, a plasma discharge is generated in the sputtering chamber using Ar gas, and a low RF bias power (here limited to below 50 W) is applied to the substrate holder. Under these conditions, Ar ions are accelerated toward the substrate surface with sufficient kinetic energy to break weakly bound adsorbates, hydrocarbons, and surface oxides, while avoiding significant sputtering damage to the underlying SiO_x. The treatment thus removes surface impurities and yields a chemically clean and physically smooth starting surface.

In addition, PC can promote partial surface activation, increasing the density of dangling bonds, which enhances the adhesion of the subsequently deposited seed layer (Ti in our case).

The influence of PC on the PMA of the top Co layer was systematically investigated. Fig. 9.2 shows representative OOP polar laser MOKE hysteresis loops of the full heterostructure SiO_x/Ti(2)/Co(3)/Pt(2.8)/Co(0.9)/Ti(2.5), prepared under different PC conditions. A small shift observed in the hysteresis loops is likely an artifact arising from either the remanence of the magnetic core or delays in applying/reading the magnetic field during early LabVIEW program executions. Additionally, it is important to note that in the LMOKE setup, the sample holder was manually aligned relative to the magnet for each measurement. This manual alignment may have introduced slight variations in the actual magnetic field applied across different samples.

Stronger or longer PC treatments yield sharper hysteresis loops with higher coercivity, directly reflecting improved interfacial quality and enhanced PMA. The optimal conditions were found to be PC at 50 W for 120 s, which produced the cleanest interfaces and the strongest PMA signal. By contrast, samples fabricated without PC exhibited a dramatic suppression of PMA: the top Co layer becomes IP magnetized, as evidenced by the light green curve in Fig. 9.2, which shows a hard-axis loop with low remanence. This comparison highlights the essential role of interface engineering for stabilizing OOP anisotropy in Co/Pt heterostructures. Finally, for the rest of the samples, a PC of 30 W and 120 s has been consistently used.

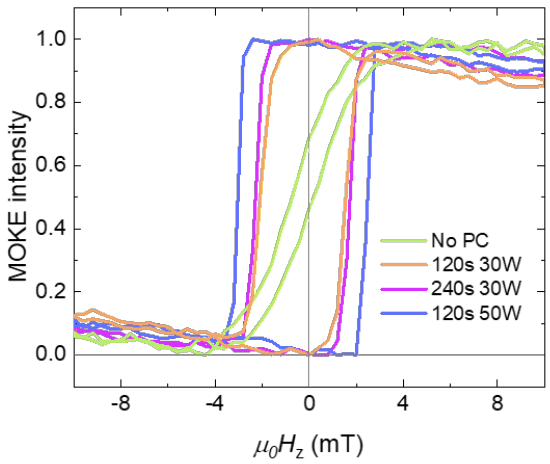

Figure 9.2: Effect of PC on the PMA of the top Co layer in the heterostructure SiO_x/Ti(2)/Co(3)/Pt(2.8)/Co(0.9)/Ti(2.5). Increasing PC power and duration improves interfacial quality, yielding sharper loops and higher coercivity. The strongest PMA was obtained after PC at 50 W for 120 s. In the absence of PC, the top Co layer is IP magnetized, as evidenced by the light green loop with negligible remanence.

Pt Thickness Dependence

We next investigate the effect of varying the Pt spacer thickness on the magnetic anisotropy of the top Co layer. Fig. 9.3 shows representative OOP MOKE hysteresis loops for Pt spacer thicknesses ranging from 2.2 to 3.2 nm. For the thinnest Pt spacer (t_{Pt} = 2.2 nm, yellow curve), the loop exhibits

a predominantly IP character, with reduced remanence and slanted hysteresis. This behavior could be attributed to stronger dipolar coupling from the bottom IP Co layer, whose larger magnetic moment competes with and partially suppresses the perpendicular anisotropy of the ultrathin top Co layer. Other magnetic interactions cannot be excluded in principle. For instance, the Pt spacer may acquire MPE from both Co interfaces (typically extending over ∼1 nm), which could enable direct exchange coupling between the layers. Additionally, interdiffusion at the Pt/Co interfaces may enhance this effect, potentially modifying the magnetic properties of the top Co layer and contributing to the observed suppression of PMA at low Pt thicknesses.

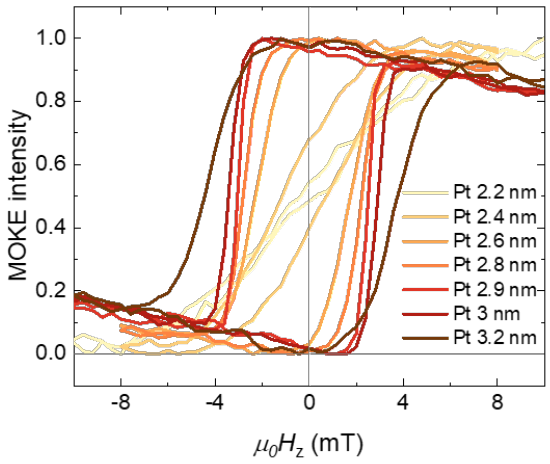

Figure 9.3: OOP MOKE hysteresis loops of the top Co layer in Co/Pt/Co heterostructures for different Pt spacer thicknesses. The perpendicular anisotropy strengthens with increasing Pt thickness, becoming fully developed above 2.6 nm. At 3.2 nm, the loop remains square but exhibits less sharp switching, consistent with a change in domain reversal dynamics.

With increasing Pt thickness, the OOP character of the top Co layer progressively strengthens. For $t_{\mathrm{Pt}} > 2.6$ nm, the hysteresis loops exhibit clear PMA, with full remanence and very low coercivity, consistent with robust interfacial anisotropy at the Pt/Co boundary. Between 2.6 and 3.0 nm, the coercivity gradually increases and the loops become more square, indicating that PMA is fully stabilized in this range.

A subtle change occurs at $t_{\mathrm{Pt}} = 3.2$ nm: while the hysteresis loop still exhibits full remanence and comparable coercivity, the magnetization switching becomes noticeably less sharp. This suggests a less efficient domain expansion process, potentially due to increased pinning or changes in DW dynamics. Although the PMA remains, this observation highlights that the details of domain behavior are sensitive to the precise Pt spacer thickness.

For subsequent characterizations, a Pt thickness of 2.8 nm was chosen. As will be shown in later sections, this thickness provides the most favorable balance of PMA strength and DW behavior, enabling the emergence of chiral magnetic structures in the Co/Pt/Co heterostructures.

OOP and IP Co Thickness Dependence

The thickness of the top Co layer was systematically varied between 0.6 and 0.9 nm to determine the threshold for achieving robust PMA. The corresponding MOKE hysteresis loops are shown in Fig. 9.4a.

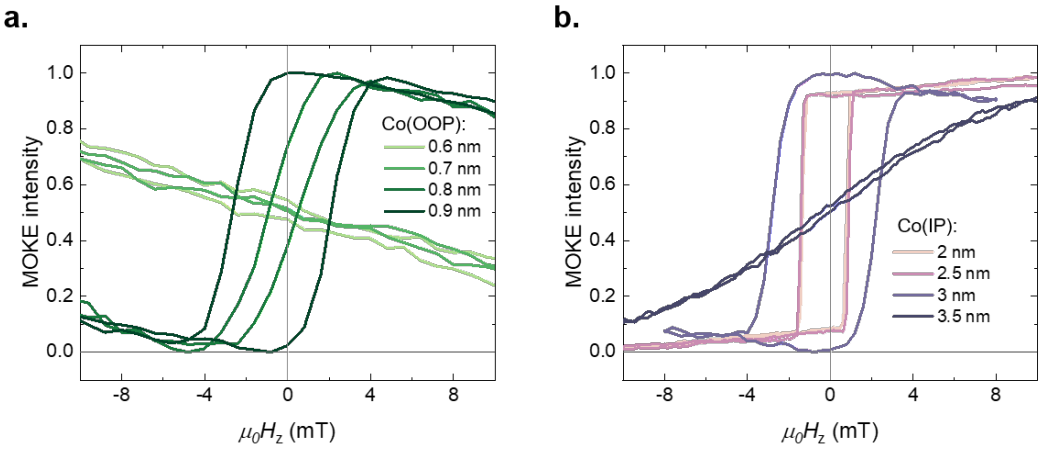

Figure 9.4: (a) OOP MOKE hysteresis loops of the top Co layer for varying thicknesses. No ferromagnetic response is observed for $t_{\mathrm{Co}} \leq 0.7$ nm. At $t_{\mathrm{Co}} = 0.8$ nm, the loop indicates mixed anisotropy with negligible remanence, while at $t_{\mathrm{Co}} = 0.9$ nm, robust PMA is evident from the square loop. (b) OOP MOKE loops for different thicknesses of the bottom IP Co layer, showing strong magnetic coupling between the two Co layers across the Pt spacer.

For the thinnest layers ($t_{\mathrm{Co}} = 0.6$ and 0.7 nm), no magnetic hysteresis is observed. Instead, the MOKE signal displays only a monotonic background with a slight slope, attributable to the Faraday contribution from the applied OOP magnetic field. This indicates that the Co films at these thicknesses are discontinuous or magnetically too weak to sustain stable domains, and thus cannot generate a measurable ferromagnetic signal.

At $t_{\mathrm{Co}} = 0.8$ nm, a hysteresis loop begins to emerge, but with almost zero remanence and a slanted shape that reflects a mixed anisotropy state. The top Co layer in this case lies near the crossover between IP and OOP anisotropy, where interfacial PMA is not yet strong enough to overcome shape anisotropy and dipolar contributions.

Finally, for $t_{\mathrm{Co}} = 0.9$ nm, the hysteresis loop exhibits full remanence and very low coercivity, characteristic of well-developed PMA. This confirms that 0.9 nm is the critical thickness at which the Pt/Co interface stabilizes a robust OOP magnetized state, consistent with previous reports on ultrathin Co/heavy-metal heterostructures. This thickness is therefore adopted as the reference for the top Co layer in all subsequent experiments.

Finally, we investigated the effect of varying the thickness of the bottom IP Co layer while keeping all other layers fixed at their optimized values. Fig. 9.4b shows the OOP MOKE hysteresis loops of the top Co layer for IP Co thicknesses between 2 and 3.5 nm.

These results highlight the strong coupling between the two magnetic layers mediated by the Pt spacer. For relatively thin bottom Co layers (2 and 2.5 nm), the top Co layer retains a well-defined PMA, with square hysteresis loops and full remanence. Increasing the IP Co thickness to 3.0 nm

modifies the loop shape: although the remanence remains 100%, the hysteresis becomes less square and the switching less sharp. This change suggests a modification in the domain nucleation and expansion mechanisms, likely due to altered magnetic configuration, as explained later.

At 3.5 nm, the OOP Co layer no longer shows a square hysteresis but instead exhibits a hard-axis–like loop with no remanence, consistent with the top Co magnetization being pulled entirely IP. In this case, the applied OOP magnetic field during the measurement was not large enough to fully saturate the magnetization, but a clear change in slope around 8 mT suggests that saturation is approached[1]. This result demonstrates that the IP Co thickness is a crucial tuning parameter: beyond a critical value, it completely suppresses the PMA of the top layer.

In summary, the bottom Co layer must be thick enough to remain IP, but not so thick as to suppress the perpendicular anisotropy of the top Co. In the following, we adopt 3.0 nm as the reference thickness, as it ensures robust orthogonal alignment of the two Co layers, which is essential for probing IL-DMI in these heterostructures. The strong dependence of PMA on the bottom Co thickness remains poorly understood and will be further examined in Section 9.3.5.

9.3 Magnetic Spiral Domains

The optimized heterostructure SiO_x/Ti(2)/Co(3)/Pt(2.8)/Co(0.9)/Ti(2.5) was analyzed using WF-MOKE imaging, enabling direct observation of magnetic domains and their field evolution. Due to the polar configuration of the setup, MOKE selectively probes the magnetization of the top Co layer. Even if the bottom Co layer exhibited some perpendicular component, its MOKE signal would be strongly attenuated by the reflective metallic layers above, making its contribution negligible.

Fig. 9.5a and 9.5b present the domain configurations for two nominally identical samples, prepared in different deposition runs. The images were acquired by first saturating the OOP magnetization in one direction, and then slowly sweeping an opposite OOP magnetic field until stable domains appeared (here, around 3.5 mT). A more detailed description of the dynamic evolution of these domains is provided in Section 9.3.1.

In Fig. 9.5a, two main features are observed: (i) small, uniformly distributed point-like domains, likely bubble-like skyrmions, and (ii) a larger circular domain nucleated around a bright defect. In contrast, Fig. 9.5b shows a much higher density of circular domains, each associated with a distinct surface imperfection. The primary difference between the two samples is the number of nucleation centers, which appears to depend on deposition conditions. In this work, we focus on understanding the origin of these circular domains, rather than the more conventional domains that can vary between heterostructures.

Fig. 9.5c provides a zoom of the circular domain highlighted in green in panel (a). Here, the domain reveals a spiral structure that extends in the xy plane with an overall diameter of about 100 μm. The spiral consists of alternating black and white fringes a few microns wide, separated by $\sim$ 2.5 μm, with the spacing gradually decreasing toward the center (shown in Fig. 9.5e and 9.5f). Finally, Fig. 9.5d shows a magnified view of the yellow square in panel (b), where two spiral domains nucleated in close proximity. Their overlap leads to complex intertwined structures rather

[1]It should be noted that, at the time these measurements were taken, the maximum OOP magnetic field was significantly limited due to the use of a smaller coil with a small magnetic core. A larger OOP magnet was implemented later to overcome this limitation.

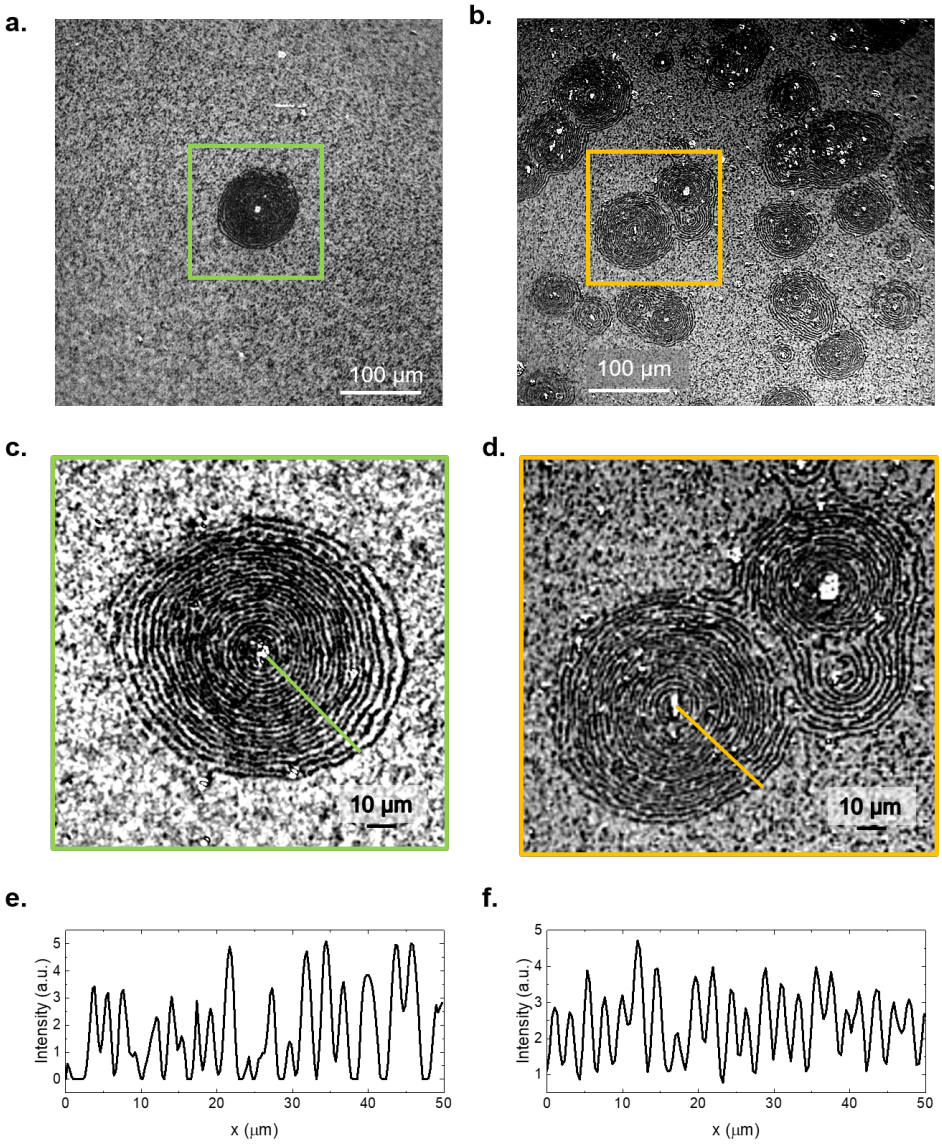

Figure 9.5: MOKE domain images of optimized Co/Pt/Co heterostructures. (a) Spiral-like domain nucleating around a single defect. (b) Multiple spiral domains generated around several surface imperfections. (c) Zoom of the green region in (a), highlighting the fine spiral structure with periodic black and white fringes. (d) Zoom of the yellow region in (b), showing the interaction and overlap of two neighboring spirals. (e) and (f) Intensity profiles of the respective green and yellow lines.

than isolated circular domains, indicating that interactions between neighboring spirals play an important role in the domain morphology.

These observations demonstrate that the optimized Co/Pt/Co heterostructure supports the formation of spiral magnetic domains, nucleated around surface imperfections and stabilized by chiral interactions. The spiral morphology, with its periodic winding DWs and sensitivity to Pt spacer thickness, may be a manifestation of IL-DMI. To better understand the origin of these domains, we first investigate their nucleation and evolution under external OOP fields, then examine the role

of defects using engineered patterned structures, and finally evaluate the effects of an external IP field. While these analyses provide valuable insight into the nature of these structures, definitive conclusions remain elusive at this stage.

9.3.1 Nucleation and Evolution of Magnetic Spirals

To better understand the nucleation and evolution of these peculiar domains, we recorded a video of their generation and annihilation under an applied OOP magnetic field. Selected snapshots from the video are presented in Fig. 9.6a–f, showing the evolution of a representative spiral domain after first saturating the sample in one direction (black contrast), followed by a slow increase of the opposite field from 1 mT (Fig. 9.6a) to 7 mT (Fig. 9.6f), until full saturation is reached at around 8 mT (not shown).

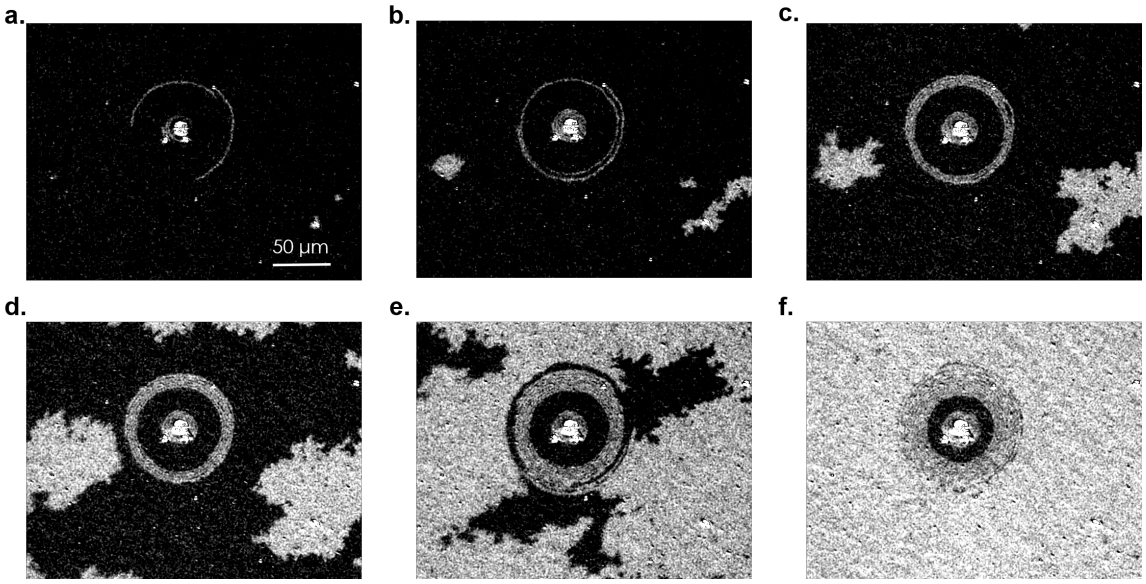

Figure 9.6: Snapshots of the evolution of a spiral domain in the optimized Co/Pt/Co heterostructure, recorded under increasing OOP magnetic field: (a) nucleation at $\mu_0 H_z \approx 1$ mT; (b) expansion and appearance of conventional domains at $\mu_0 H_z \approx 2$ mT; (c–d) further growth at $\mu_0 H_z = 3$ and 4 mT; (e) coexistence with external domains at $\mu_0 H_z \approx 5$ mT; (f) survival of the spiral domain when the background is nearly saturated at $\mu_0 H_z \approx 7$ mT. The spiral collapses only at higher fields (mT).

At low field ($\mu_0 H_z \approx 1$ mT, Fig. 9.6a), the spiral domain is already visible before the nucleation of conventional domains. In some samples, spiral domains appear even at zero field, while here a small finite field was required. Interestingly, the spiral appears to nucleate at two distinct points: one at the outer rim and one close to the central defect, suggesting that defects act as nucleation seeds for both the core and periphery of the spiral.

At $\mu_0 H_z \approx 2$ mT (Fig. 9.6b), external domains nucleate and begin expanding, while the spiral simultaneously grows inward. Further increases of the magnetic field (3–4 mT, Fig. 9.6c–d) lead to the continued expansion of both spiral and conventional domains. At $\mu_0 H_z \approx 5$ mT (Fig. 9.6e), the external domains have grown large enough to approach the spiral, but strikingly, they do not merge with it; instead, they leave a clear outer boundary around the spiral domain. This suggests that

the spiral is energetically stabilized and somewhat "protected" against interactions with neighboring domains.

At $\mu_0 H_z \approx 7$ mT (Fig. 9.6f), the background is nearly saturated, yet the spiral domain persists, acting as a localized region of higher coercivity. Only when the field exceeds ∼8 mT the spiral finally collapses, completing saturation. This spatial variation in coercivity explains why hysteresis loops of samples exhibiting spiral domains appear less sharp than those of ideal PMA films: different regions of the sample switch at different fields, broadening the field window over which magnetization reversal occurs.

9.3.2 Study of Defects

We then investigated the role of defects in the nucleation of the circular (spiral) domains. To this end, we fabricated two samples with the same heterostructure as before, but including patterned regions: one with pre-patterned non-magnetic Ti (thickness 50 nm) dots of different diameters (5, 10, 15, and 20 μm), and one with patterned magnetic Co (thickness 50 nm) dots. The results are summarized in Fig. 9.7.

Fig. 9.7a shows the magnetic image of the sample patterned with Ti dots. In this case, the surface displayed a much higher density of imperfections than usual, likely due to an incorrectly performed cleaning step during processing. These imperfections nucleate numerous spiral domains, which often interact with one another to form complex textures. However, as highlighted by the yellow arrows, the patterned Ti dots do not act as nucleation sites for spirals. This becomes clearer by comparing the zoomed magnetic image (Fig. 9.7b) and the corresponding optical image (Fig. 9.7c). The Ti dots are visible in both images (yellow arrows), but spirals never originate from them. Instead, only structural imperfections (green arrows) coincide with spiral nucleation centers. This demonstrates that non-magnetic defects alone do not influence spiral formation.

In stark contrast, the sample patterned with Co dots (Fig. 9.7d) shows that spiral domains nucleate exactly and exclusively at the position of the four Co dots (green arrows). Moreover, the background is free of additional imperfections, confirming that spiral formation is linked to the presence of magnetic inhomogeneities rather than non-magnetic ones. Thus, magnetic spirals can be deliberately induced and controlled by introducing patterned magnetic defects, enabling control over their number, position, and characteristics.

A first possible explanation for the origin of these spirals, given their nucleation around magnetic impurities, is that the bottom IP Co layer (the first magnetic layer deposited) develops a locally non-uniform magnetization near such defects, potentially forming spiral domains. Upon subsequent deposition of Pt and the OOP Co layer, these local structures may evolve into spiral up–down and down–up domains, stabilized by interfacial DMI at the Pt/Co interfaces. At this stage, it remains unclear whether the spiral pattern originates already in the IP Co layer or emerges only after the full heterostructure is formed. What is certain, however, is that the spirals in the IP layer directly influence the OOP layer through interlayer coupling, as only the top Co layer is probed by MOKE. Moreover, such structures are not observed in simpler Pt/Co(OOP) bilayers. As further evidence, we show that applying a strong IP field to fully saturate the IP Co layer completely suppresses the spirals, strongly indicating that the phenomenon is directly linked to the IP layer and likely mediated by interlayer coupling, such as the IL-DMI discussed earlier.

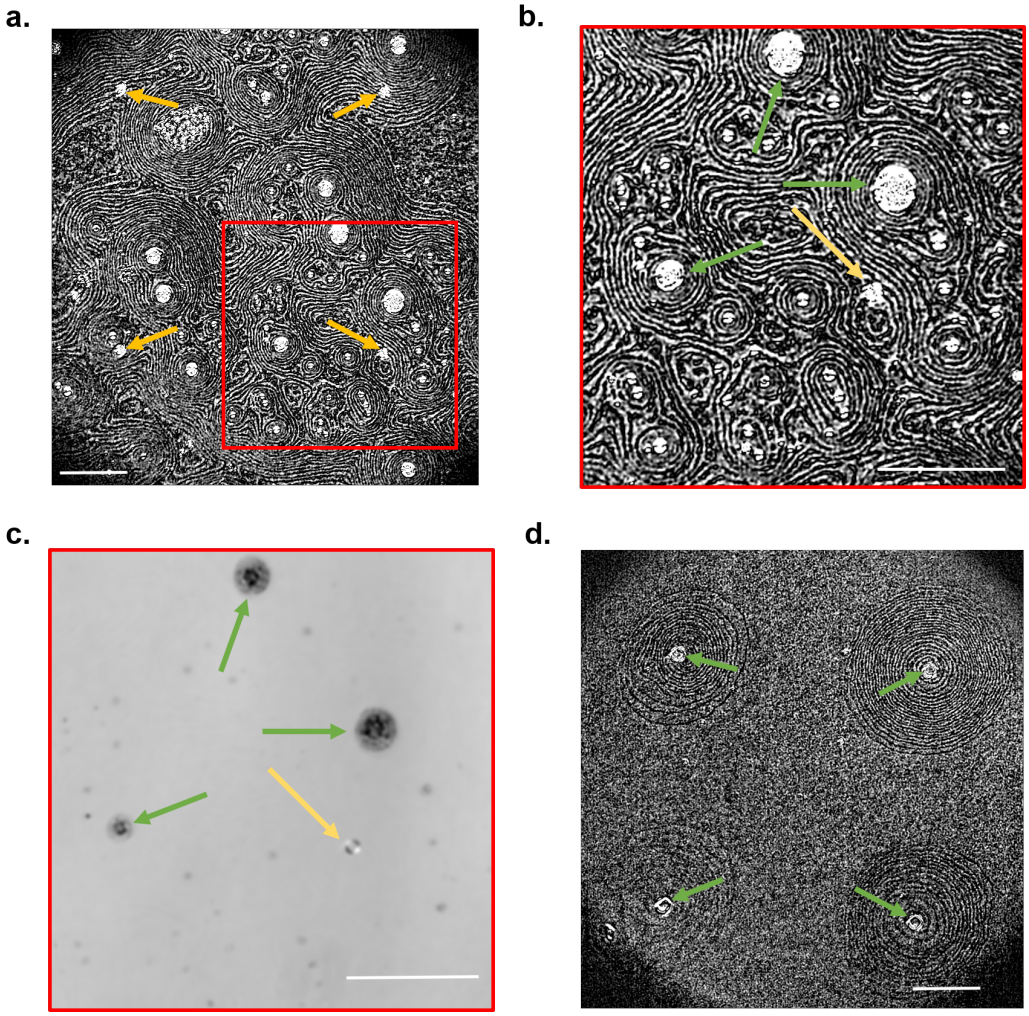

Figure 9.7: Wide-field MOKE images of patterned samples. (a–c) Sample with non-magnetic Ti dots: (a) magnetic image showing a high density of spiral domains, (b) zoom of the red square in (a), and (c) corresponding optical image. Yellow arrows highlight the position of Ti dots, while green arrows identify imperfections producing spirals. (d) Sample with magnetic Co dots, where spirals appear exclusively at the position of the patterned Co regions. Scale bar 50μm in all images.

9.3.3 Patterning of Complex Structures

The distinction between magnetic and non-magnetic impurities can be further appreciated in Fig. 9.8. In panel (a), an "8" pattern was fabricated using Ti, while in panel (b) the same geometry was patterned with Co. The Ti pattern, as in the previous case, has no influence on the magnetic domain distribution: spiral domains nucleate randomly at defects but do not interact with the Ti structure. In contrast, the Co "8" produces a clear magnetic response, with the spiral-like domains adapting to and following the complex geometry of the patterned feature. This demonstrates that magnetic patterning enables deterministic control of the spiral domains, even in non-circular geometries.

Motivated by this observation, we explored the possibility of generating spiral domains with more elaborate shapes by patterning thick magnetic Co structures of different sizes and geometries.

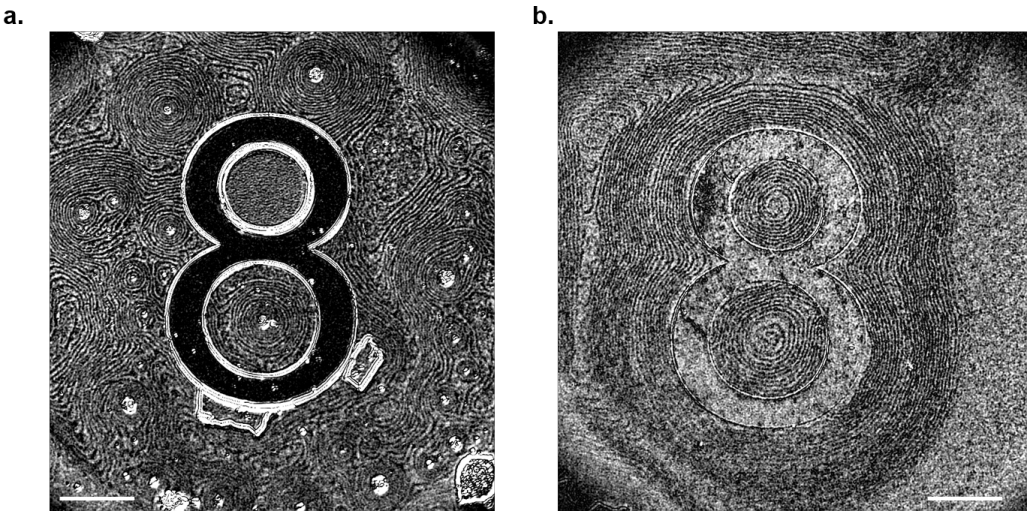

Figure 9.8: Comparison between patterned non-magnetic and magnetic structures. (a) Ti "8" pattern, which does not interact with magnetic spirals. (b) Co "8" pattern, around which spiral domains form, adapting to the complex geometry. Scale bars: 50 μm.

Representative results are shown in Fig. 9.9a–f. The spiral domains faithfully follow the outline of the patterned features, producing intricate domain arrangements that extend both inside and outside the magnetic regions. A particularly striking example is shown in Fig. 9.9c, where a hollow triangular structure was patterned. Spiral domains nucleate along the triangle edges, reproducing its geometry, while the very center of the void remains domain-free. This confirms that the geometry of the patterned magnetic seed directly imprints itself onto the spiral domain configuration, offering a versatile platform for engineering complex domain patterns.

9.3.4 Isolated Magnetic Structures

We next attempted to isolate and further control the size and geometry of the magnetic structures that give rise to spirals and stripes. To this end, we employed a two-step photolithography process. In the first step, magnetic features were patterned by depositing 50 nm of Co (highlighted by green arrows in Fig. 9.10). In the second step, we defined the overall heterostructure geometry (highlighted by orange arrows), while the surrounding regions were left as bare SiO_x substrate. This approach enables direct comparison between different magnetic seeds embedded in heterostructures of controlled shapes and sizes.

Fig. 9.10a shows the case of a circular Co dot surrounded by a circular heterostructure. Here, a well-defined circular spiral domain forms, extending uniformly up to the edge of the patterned region and terminating exactly at the boundary. This demonstrates that both the nucleation center (Co impurity) and the confinement geometry (heterostructure shape) jointly determine the extent of the spiral.

In contrast, rectangular magnetic seeds and heterostructures (Figs. 9.10b and d) do not produce spirals but instead stabilize stripe domains aligned with the rectangular geometry. These stripe domains uniformly fill the patterned magnetic region and extend all the way to its edges. Even in Fig. 9.10e, the stripe domains can be seen reaching the boundary of the heterostructure, suggesting

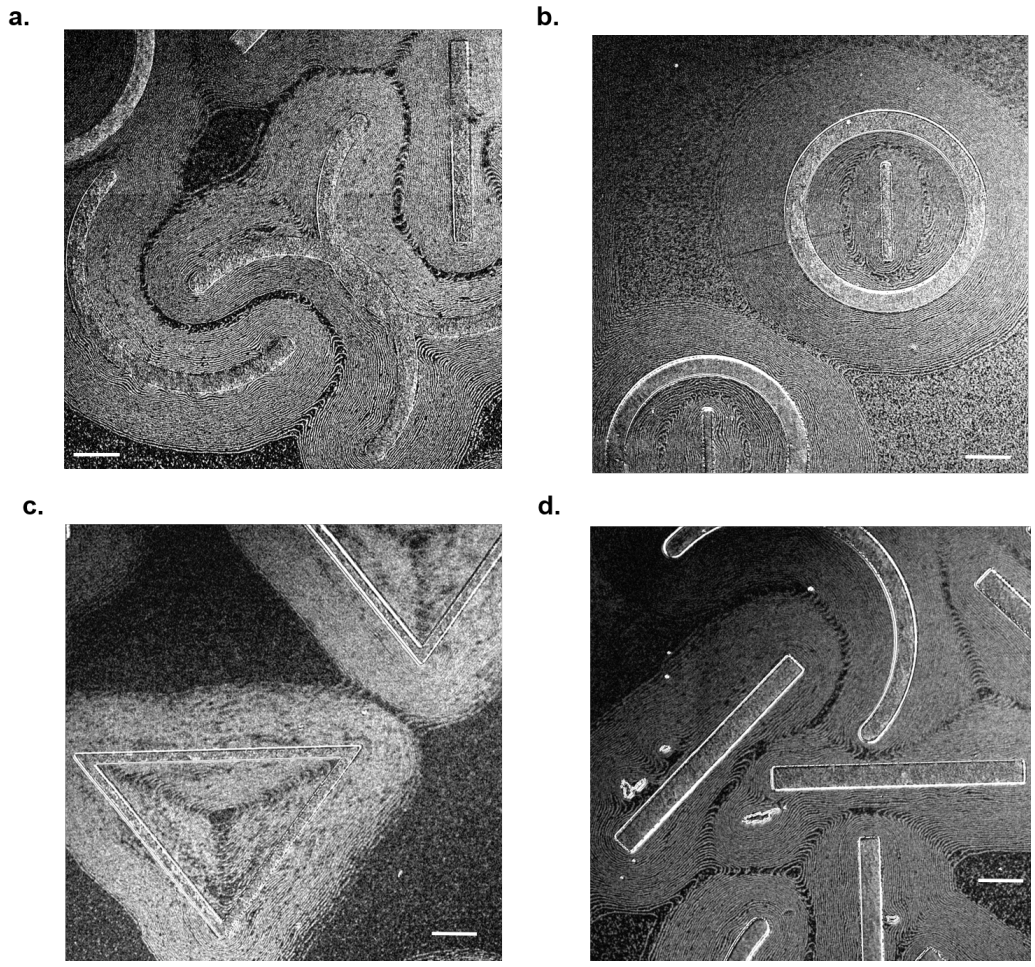

Figure 9.9: Spiral domains generated around patterned Co structures of various geometries and dimensions. The domains follow both the interior and exterior of the magnetic patterns, reproducing their shape. (c) A triangular void structure demonstrates that the domain nucleation conforms to non-circular geometries, leaving the central void domain-free. Scale bars: 50 μm.

that the spatial extent of the domains is set by the total patterned magnetic moment.

A different case is shown in Fig. 9.10c, where a circular Co structure was divided into four disconnected quadrants. Interestingly, only one of the four quadrants hosts magnetic domains, which appear as curved stripes rather than closed spirals. This highlights the sensitivity of the domain morphology to both geometry and continuity of the patterned impurity: disconnected seeds may not provide sufficient magnetic moment or coupling to stabilize full spiral textures.

9.3.5 Role of the IP Co Layer

To assess the role of the bottom IP Co layer in stabilizing the spiral domains, we studied their behavior under the application of an IP magnetic field. Fig. 9.11 shows the evolution of the spiral domains under increasing IP field.

In Fig. 9.11a, spiral domains are first generated by saturating the magnetization OOP and then

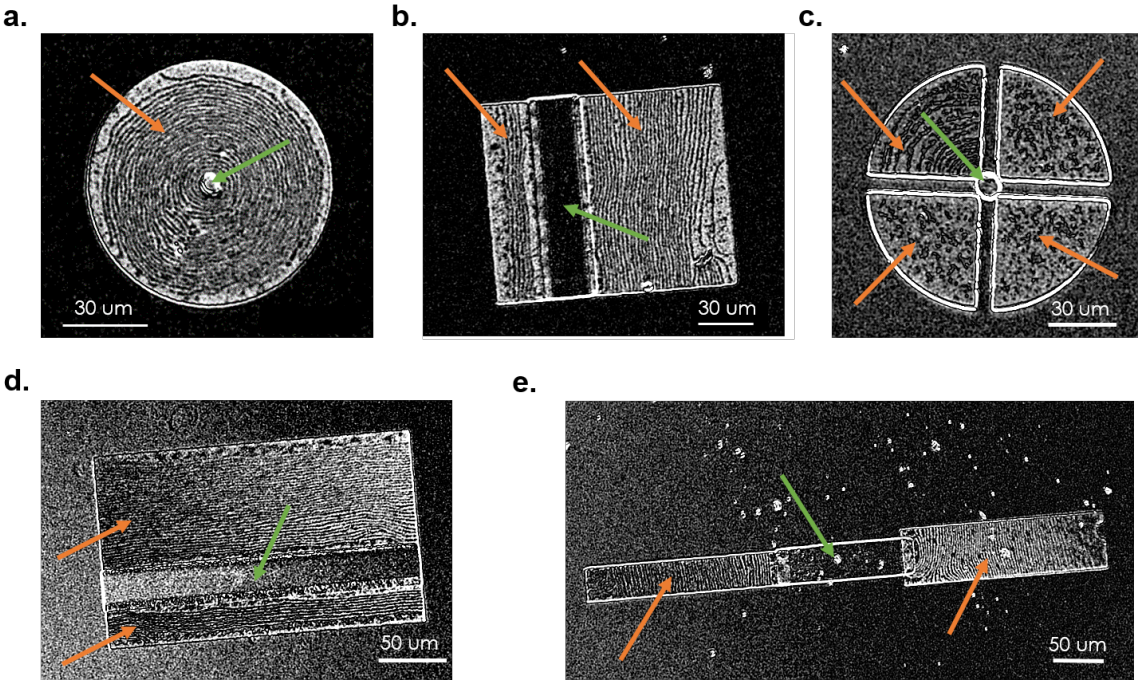

Figure 9.10: Magnetic domain structures in heterostructures patterned by a two-step photolithography process. Green arrows mark the patterned Co impurities (50 nm thick), while orange arrows mark the overall heterostructure geometry. (a) Circular dot and heterostructure produce a spiral extending to the patterned boundary. (b,d) Rectangular geometries stabilize stripe domains covering the full area. (c) A circle divided into quadrants shows domains only in one quarter, in the form of curved stripes. (e) Stripe domains extend to the edges of a rectangular heterostructure.

applying a reversal OOP field of about 3 mT, in the absence of any IP field. As discussed previously, the spirals nucleate around random magnetic impurities and appear with sharp contrast and well-defined fringes. When an IP field of 12 mT is applied (Fig. 9.11b), spiral domains are still observed at the same locations, but their morphology is strongly altered: the fringes appear blurred, their contrast is reduced, and the number of visible lines decreases. This indicates that the IP field partially disrupts the multidomain background of the IP Co layer that is required to sustain the spiral textures. Upon further increasing the IP field to 21.5 mT (Fig. 9.11c), the spiral domains are completely suppressed and cannot be regenerated, even after OOP re-saturation and repeated attempts to nucleate them. At this stage, the wide-field MOKE contrast of ordinary domains also vanishes, and no bright/dark contrast is detected, even though hysteresis loops acquired with laser MOKE still confirm that the top Co layer retains perpendicular anisotropy. Under this IP field, the magnetization of the OOP-oriented Co layer is expected to tilt toward the IP direction but not fully saturate. This is consistent with the expectation that the PMA anisotropy field of the sample is significantly higher than the applied IP field, even though its exact value has not yet been experimentally determined.

Extensive attempts were made to restore the spiral domains after their suppression, including thermal annealing (up to 200 °C) of the heterostructure, demagnetization procedures with alternating OOP or IP fields, and re-saturation under a strong 2 T OOP field. None of these methods

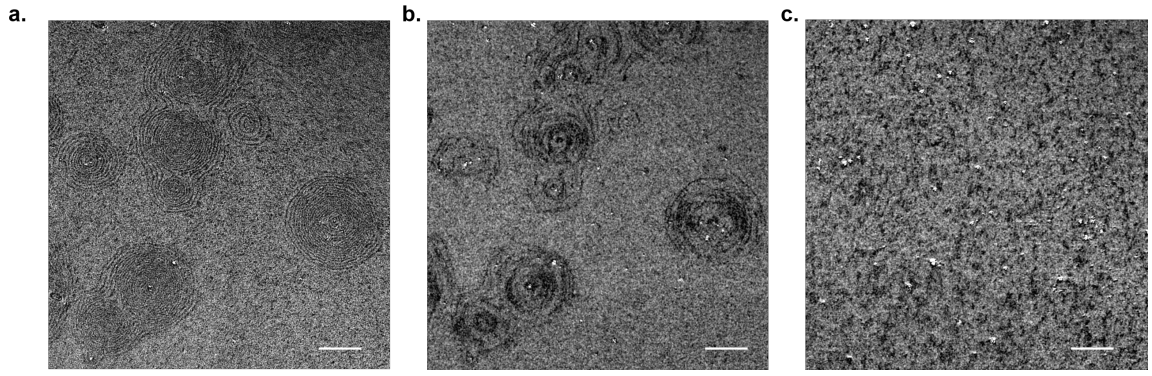

Figure 9.11: Evolution of spiral domains under increasing IP magnetic field. (a) Spiral domains nucleated at 3 mT OOP reversal field in the absence of IP field. (b) Application of a 12 mT IP field blurs the spirals, reducing contrast and fringe definition. (c) At 21.5 mT IP field the spiral domains are completely suppressed and cannot be regenerated, even after OOP re-saturation. Scale bar: 50μm.

succeeded in recovering the spirals. This behavior suggests that once the IP Co magnetization is forced into a uniform single-domain state, it does not relax back into the specific multidomain configuration required to stabilize spiral domains.

To further assess the importance of the IP Co layer, we studied the domain evolution for two additional thicknesses of this layer, 2.0 and 2.5 nm, keeping the rest of the heterostructure unchanged and without any patterned regions. Representative video snippets of domain nucleation and expansion are shown in Fig. 9.12. Panels (a–d) correspond to the sample with a 2.5 nm IP Co layer. In this case, the OOP domains nucleate from defects and exhibit smoother, more regular expansion compared to the optimized structure. The domains grow rapidly under relatively low OOP fields, consistent with the lower coercivity and sharper hysteresis loop reported in Fig. 9.4b, and display sharp and well-defined DWs. As in previous cases, magnetic imperfections interact with the expanding domains. When an expanding domain approaches such an imperfection, it bypasses it, leaving behind a circular unswitched region of opposite contrast. This unswitched region does not transform into a stripe domain but instead forms a circular domain of distinct coercivity, which remains stable against the advancing external domains and only saturates at higher fields. Its reversal process proceeds radially, with the outer shell switching first and the core switching last, reminiscent of the spirals observed earlier, albeit without well-defined fringes.

Fig. 9.12e–h show the evolution for the sample with a 2.0 nm IP Co layer. The nucleation and expansion of the normal OOP domains again occur at even lower fields, in agreement with the further reduced coercivity of this sample. As before, magnetic imperfections give rise to protected domains, but in this case, the resulting structures are distorted and no longer perfectly circular. The imperfection is often displaced toward the edge of the protected region, and after the external domains have saturated, these protected areas collapse in a disordered manner rather than through the well-organized spiral-like motion observed in the 2.5 nm case.

These results demonstrate that the precise thickness of the IP Co layer plays a decisive role in determining the character of the domain structures. For intermediate thicknesses (e.g., 2.5 nm), protected domains exhibit circular symmetry and spiral-like reversal dynamics, whereas thinner IP Co layers (2.0 nm) produce less regular shapes and disordered switching. This highlights the crucial

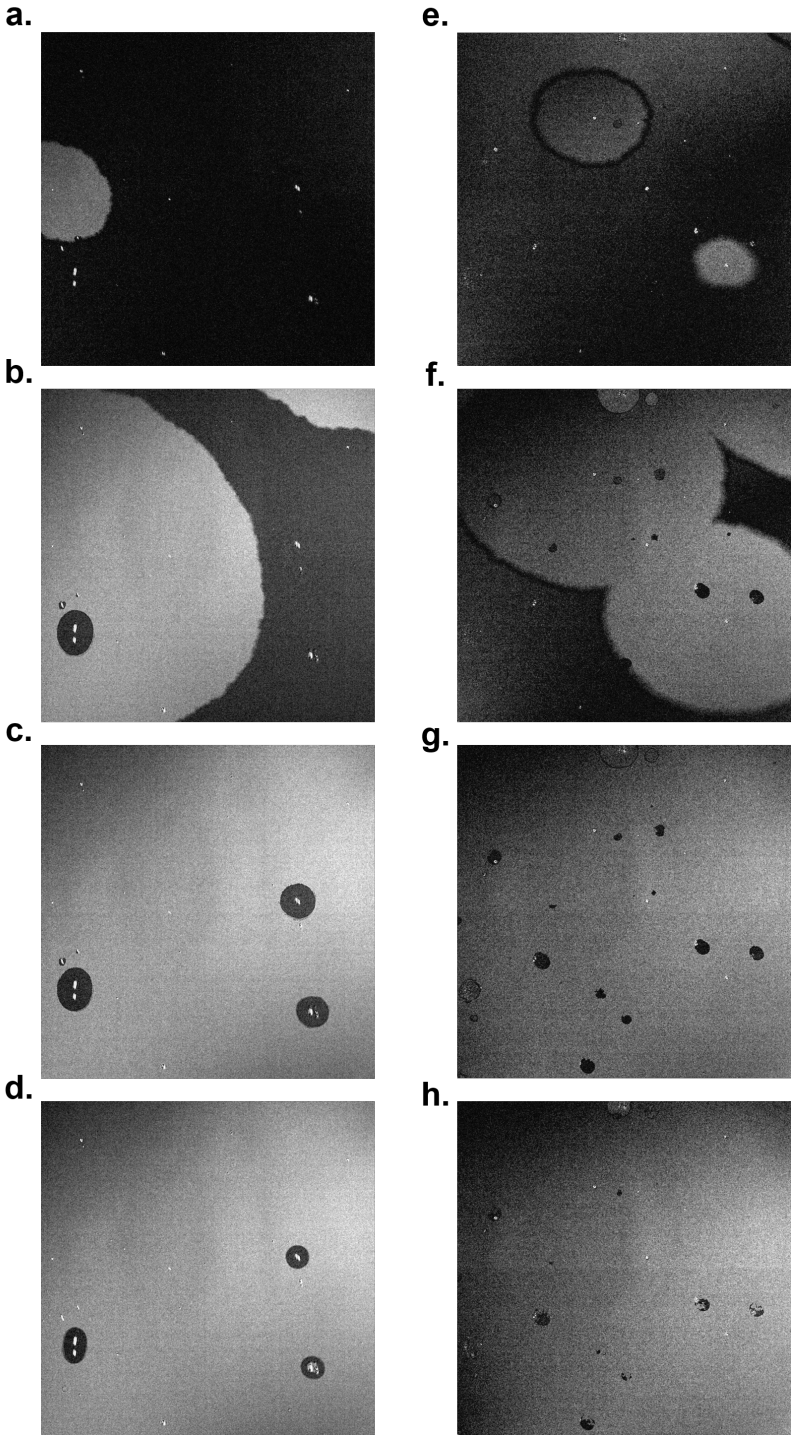

Figure 9.12: Domain nucleation and expansion in Co/Pt/Co heterostructures with different IP Co thicknesses. (a–d) For $t_{\mathrm{Co,IP}} = 2.5$ nm, OOP domains expand smoothly and leave behind stable circular regions at magnetic imperfections, which reverse via a radial process. (e–h) For $t_{\mathrm{Co,IP}} = 2.0$ nm, protected regions are irregular and collapse in a disordered manner, with no spiral-like reversal.

role of the IP Co layer in stabilizing spiral textures and confirms the strong coupling between the IP and OOP Co layers. However, it should be noted that the absence of observable spiral-like domains does not necessarily mean they are completely eliminated; their characteristic size may simply fall below the resolution limit of our MOKE setup, rendering them undetectable.

Since the spirals are observed exclusively in the OOP-sensitive MOKE signal, their origin must lie in the chiral interaction mediated through the Pt spacer. We attribute this to the IL-DMI, which links the multidomain state of the IP Co layer to the formation of chiral domains in the OOP Co layer. When the IP magnetization becomes homogeneous, the chiral coupling channel is suppressed, preventing the nucleation of spiral domains. These results provide further evidence of the central role of IL-DMI in governing the observed non-trivial spin textures.

9.4 Working Hypotheses on Spiral Domains

Although many aspects of the spiral domains remain uncertain, several key observations have emerged from this study. Spiral-like domains consistently nucleate at magnetic defects. Their shape and size can be influenced through photolithography patterning, and they often appear prior to conventional domain structures, occasionally even opposing the direction of the applied external field. This behavior suggests that they may represent a ground-state configuration at $\mu_0 H_{\text{ext}} = 0$ mT. These domains require higher OOP fields to fully collapse, forming a locally stable, "protected" region that resists saturation. The chirality of the spiral winding does not appear to be unequivocally predetermined. However, due to the limited resolution of the imaging setup, a clear determination of chirality is challenging, except in a few rare cases. We hypothesize that chirality may be influenced by local asymmetries or defects that favor the initiation of a spiral in a specific direction, rather than being strictly dictated by a fixed DMI. At this stage, a detailed study of chirality has not yet been conducted. Application of an IP magnetic field leads to the disappearance of these spirals, indicating a transition of the magnetization toward a uniform IP configuration. Over time, both the spiral structures and the OOP magnetic contrast fade, and attempts to restore them have so far been unsuccessful.

Despite these insights, the underlying mechanisms remain unclear. The origin of the spiral domains, the dominant interactions responsible for their formation and stability, and the conditions under which they vanish or could potentially be restored are still not fully understood. Furthermore, similar samples often exhibit different domain behaviors, suggesting a complex dependence on subtle variations in sample properties or fabrication conditions.

We hypothesize that spiral domains originate in the IP layer during sputtering deposition and subsequently couple to the OOP Co layer through interlayer interactions. Magnetic defects present on the substrate surface can distort the magnetization of the IP layer upon deposition, potentially leading to non-uniform configurations such as spirals or circular domains to minimize the total magnetic energy. Patterned or irregular magnetic impurities, with edges that are not perfectly smooth, can further enhance this effect by creating regions where magnetic flux extends beyond the impurity boundaries, influencing the surrounding IP magnetization (see Fig. 9.13a). As the subsequent layers are deposited, the Pt spacer introduces strong spin–orbit coupling, enabling both interfacial DMI and IL-DMI. Assuming IL-DMI is sufficiently strong, the OOP Co layer experiences this non-uniform magnetic environment and adapts by forming spiral domains with alternating up–down magnetization along the radial direction (see Fig. 9.13b). Spiral domains allow for consistent chirality, thereby

minimizing the IL-DMI energy.

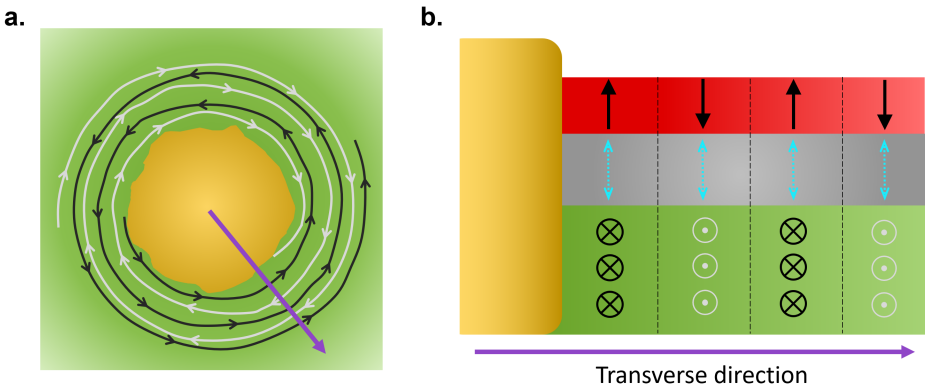

Figure 9.13: (a) Top view sketch of the magnetization configuration in the IP Co layer (green) around a magnetic impurity (yellow). Magnetic spirals with different magnetization directions are shown in black and gray. (b) Cross-sectional view along the purple line in (a), illustrating the chiral coupling between the IP and the OOP Co layer (red), mediated by the IL-DMI (light blue double arrows).

Experimental observations confirm that spiral domains nucleate exclusively around magnetic defects and are suppressed when the IP layer is saturated, reinforcing the idea that their formation is driven by a chiral coupling mechanism rather than conventional dipolar interactions. Thus, spiral domains represent a manifestation of interlayer chirality, stabilized by IL-DMI, and not merely a geometric or stray-field-driven configuration.

This hypothesis is tested across films with different Co and Pt thicknesses, and all evidence points to the active role of IL-DMI. In this framework, the spiral domains represent a manifestation of interlayer chirality, where the magnetization of the top Co layer winds around the defect in response to the underlying IP configuration. The sensitivity of spiral domains to the thickness of the IP Co layer further supports this hypothesis. Thinner IP layers lead to less regular domain shapes and disordered switching, while intermediate thicknesses stabilize circular domains with spiral-like reversal dynamics. The irreversible suppression of spirals upon IP field application suggests that once the IP layer is forced into a uniform state, the chiral coupling channel is disrupted, preventing spiral textures from reforming.

9.5 Conclusion and Future Prospects

In this work, we have investigated Co/Pt/Co heterostructures optimized to host complex magnetic textures. Although we do not yet have direct evidence for the presence of IL-DMI or other chiral coupling mechanisms in our structures, several experimental observations point towards this possibility. In particular, the spontaneous nucleation of spiral-like domains, their sensitivity to the IP Co layer thickness, and their irreversible suppression under applied IP fields all suggest a chiral interlayer mechanism beyond conventional dipolar effects. To fully clarify the origin of these spiral domains, their microscopic properties, and their potential for manipulation, further experimental work will be required, for example, spin-polarized electron microscopy or advanced micromagnetic simulations.

Nevertheless, our results are strongly supported by the growing body of literature reporting IL-DMI in related systems. A number of experimental and theoretical works have established the existence of IL-DMI across a wide variety of multilayers, both with and without additional RKKY-promoting spacers such as Ru. Examples include:

- One of the first demonstrations of IL-DMI was reported in a synthetic antiferromagnet Ta(4)/Pt(4)/Co(0.6)/Pt(0.5)/Ru(t_{Ru})/Pt(0.5)/Co(1)/Pt(4), where the two Co layers are antiferromagnetically coupled [174].
- At the same time, IL-DMI was observed in Ta(4)/Pt(10)/Co(1)/Pt(0.5)/Ru(1)/Pt(0.5)/CoFeB(1.6–2.4)/Pt(2)/Ta(2), where the Co layer is OOP while the CoFeB layer is tilted between OOP and IP [173].
- More recently, IL-DMI has been confirmed in Ta/Pt/Co/Pt/Ru/Pt/Co/Ta multilayers [351].
- Importantly, IL-DMI has also been reported in heterostructures without Ru, e.g., Ta(4)/Pd(3)/[Co(0.5)/Pd(0.8)]$_9$/Pd(3) [352].
- Similar effects were found using Ir as the spacer layer in Pt(60 Å)/Co(10 Å)/Pt(4 Å)/Ir(t)/Pt(4 Å)/Co(9 Å)/Pt(20 Å) [178].
- Simpler metallic trilayers, such as Co(100 nm)/Ag(0.3–3.5 nm)/Co(10 or 15 nm)/SiO_2(10 nm), with both Co layers magnetized IP, have also been shown to host IL-DMI [179].
- Ab initio calculations have predicted IL-DMI in Co/NM/Co trilayers (NM = Cu, Ag, Pt, or Au) [353].
- Experimental confirmation was also obtained in Pt(2)/Co(0.4)/Pt(0.7)/Co(0.4)/Pt(2), although the magnitude of IL-DMI was found to be weaker than in analogous Ir-based stacks [150].
- Finally, theoretical work has demonstrated that orthogonal TbFe (OOP) and Co (IP) layers, separated by Pt, Ir, Pd, or Ru spacers, exhibit IL-DMI with oscillatory dependence on spacer thickness [180].

Altogether, our findings position the Co/Pt/Co trilayer as a promising platform for the study of IL-DMI in minimal metallic systems. By combining careful structural optimization with advanced imaging and complementary characterization techniques, future work will aim to conclusively identify the chiral nature of the coupling and to explore its use in controlling 3D spin textures such as spirals, stripes, and skyrmions. Beyond fundamental interest, such control could pave the way toward reconfigurable spin–orbitronic devices based on engineered interlayer chiral magnetism, or encoding information in domain patterns for high security applications.

Future Work

To fully characterize the spiral domains observed in our Co/Pt/Co heterostructures and disentangle the contributions of each magnetic layer, more advanced imaging techniques are required beyond MOKE microscopy. For this reason, we submitted a proposal to the ALBA synchrotron in Bellaterra (Barcelona) to perform element-specific, high-resolution measurements using Photoemission Electron Microscopy (PEEM) combined with X-ray Magnetic Circular Dichroism (XMCD) and X-ray

Magnetic Linear Dichroism (XMLD). These techniques provide simultaneous spatial and magnetic sensitivity, enabling independent probing of both IP and OOP magnetization components.

The proposal focuses on the BL24-CIRCE beamline at ALBA, which is ideally suited for such studies. Our objectives are to:

1. Resolve the fine structure of the spiral DWs revealed in MOKE imaging.
2. Disentangle the roles of the IP Co layer (3 nm) and the OOP Co layer (0.9 nm) in domain formation.
3. Determine whether IL-DMI is responsible for stabilizing the spiral domain structures.

Two samples were originally selected for the experiments:

- The full heterostructure SiO_x/Ti(2.5 nm)/Co(3 nm)/Pt(2.6 nm)/Co(0.9 nm)/Ti(2.5 nm), to probe OOP magnetic domains in the complete trilayer.
- A "half" heterostructure SiO_x/Ti(2.5 nm)/Co(3 nm)/Pt(2.6 nm), to test whether circular magnetic features already emerge in the IP Co layer, particularly around pre-patterned magnetic impurities (50 nm Co).

The proposal was accepted with one caveat: in order to unambiguously separate the XMCD/XMLD signals of the two magnetic layers, the heterostructure must be redesigned using two different magnetic materials. Specifically, the IP Co layer should be substituted by an IP Fe layer, resulting in a Fe(IP)/Pt/Co(OOP) trilayer. Optimizing this new heterostructure is therefore the next experimental step.

The measurement plan is as follows:

- XMCD-PEEM will be used to directly image the OOP magnetization of the top Co layer.
- XMLD-PEEM will probe the IP magnetization of the bottom Fe (or Co) layer.
- Additionally, cross-sensitivity (XMCD on the IP layer, XMLD on the OOP layer) will be exploited to study the fine structure of the DWs and possible canting effects.

From these experiments, we expect to obtain high-resolution, element-specific images of the spiral domain structures and determine whether they originate from IL-DMI. By imaging the IP and OOP contributions separately, we aim to clarify their interplay in domain stabilization and the role of chiral coupling.

Ultimately, this work will provide fundamental insights into the microscopic origin of spiral domains in Co/Pt multilayers and guide the engineering of heterostructures with tailored IL-DMI. Such control is essential for the development of energy-efficient spintronic and magnonic devices based on reconfigurable chiral textures.

Chapter 10

Conclusion and Outlook

This thesis has investigated magnetic chiral structures in ferrimagnetic insulators and metallic multilayers, with a particular focus on the electrical control of magnetization through SOT. Our work combined experimental design, advanced characterization techniques, and support from theoretical modeling to deepen the understanding of spin–orbit phenomena and their potential for spintronic applications.

- A major contribution of this thesis was the design and implementation of a custom MOKE microscope, enabling high-resolution imaging of magnetic domains and DWs dynamics. This tool was essential for all the experimental projects carried out in this work.

- We characterized the DMI in GGG/TbIG/HM heterostructures as a function of Pt thickness and revealed the essential role of the TbIG/Pt interface in inducing DMI and stabilizing chiral DWs. This addresses an open problem in the literature regarding the origin and quantification of DMI in these systems.

- We found evidence of long-range contributions that extend beyond the immediate interface TbIG/Pt. These non-local interfacial effects significantly influence the stabilization of chiral spin textures in ferrimagnetic insulators, introducing a new degree of freedom for engineering magnetic chirality. This challenges the conventional view that DMI is strictly localized and opens new avenues for controlling chiral textures in insulating systems.

- We demonstrated efficient SOT-driven switching in ultrathin Pt layers, showing that structural disorder and grain boundaries in nanogranular Pt films can enhance spin–orbit efficiency. These results suggest that material morphology, often considered detrimental, can instead be harnessed to improve device performance through two complementary mechanisms: increased spin–orbit scattering at grain boundaries and localized current density enhancement due to morphological inhomogeneity.

- We also explored the role of OHE in light metals within TbIG/Pt-based structures, revealing new opportunities for enhancing switching efficiency and expanding material versatility.

- Finally, our experiments provided evidence for the formation of spiral magnetic domains in Co/Pt/Co multilayers, occurring when the two Co layers are magnetized orthogonally to each

other. This behavior strongly suggests the presence of IL-DMI. Although direct confirmation remains pending, the observed sensitivity of domain structures to IP Co thickness and their irreversible suppression under applied fields support this interpretation.

Collectively, these findings advance the understanding of SOT and chiral magnetic phenomena in both insulating and metallic systems, and point toward novel strategies for optimizing energy efficiency in spintronic devices. By leveraging interfacial engineering, non-local magnetic interactions, and controlled material morphology, future spin–orbitronic platforms may achieve enhanced functionality with reduced power consumption. This work lays the foundation for further exploration of chiral magnetism and SOT phenomena in complex heterostructures, with potential applications in reconfigurable memory, logic, and magnonic technologies.

Building on these results, several promising research directions emerge:

- **Long-Range DMI in Ferrimagnetic Insulators:** Our observation of long-range DMI in TbIG/HM heterostructures opens a new research avenue for understanding chiral interactions in insulating magnets. Future work should focus on elucidating the microscopic origin of this effect, its dependence on interface engineering, and spacer layer thickness. For instance, a systematic study of the Cu spacer thickness in both Pt/TbIG and W/TbIG samples could provide deeper insight into the mechanisms driving the long-range DMI contribution. Expanding the material palette, such as using TmIG or YIG as alternative REIGs, Ti or Al as light metal spacers, and Ta or Au as top HM layers, may further clarify the tunability and universality of this interaction. Importantly, long-range DMI may not be exclusive to REIGs or insulating systems. It could, in principle, extend to fully metallic heterostructures, although its detection may be hindered by the typically stronger DMI present at conventional metallic interfaces such as Pt/Co. In metallic systems, the dominant interfacial DMI may mask subtler contributions from secondary interfaces, making REIG-based heterostructures, with their inherently weaker DMI, an ideal platform for isolating and studying long-range effects. Moreover, probing such interactions in metallic stacks is experimentally challenging, as significantly higher IP magnetic fields (often several hundreds mT) are required to fully compensate the DMI effective field. These field strengths exceed the capabilities of the MOKE setup used in this thesis, which limits the feasibility of such measurements in high-DMI systems.

- **Orbital Currents and Novel Torques:** Further exploration of OHE and their interplay with SOC could unlock new mechanisms for magnetization control, particularly in REIG/light-metal heterostructures. A recent hypothesis suggests that the presence of heavy atoms at the REIG interface may enable orbital-to-spin conversion without the need for an additional HM layer. This opens a promising avenue for designing simplified OHE-based systems. Based on this idea, we investigated TbIG/Ti bilayers. However, no measurable effect was observed, likely due to strong intermixing at the Ti/TbIG interface, which degrades the orbital current transmission. To overcome this limitation, future studies will explore alternative light metals (such as Mn, which in our preliminary results appears to preserve a cleaner TbIG interface) and different REIG compositions to engineer interfaces that support efficient orbital torque generation. In this context, combining a working REIG/light-metal interface with an ultrathin granular Pt layer, demonstrated to enhance scattering and spin-to-charge conversion efficiency, could lead to highly efficient SOT switching with multiple degrees of tunability. Such hybrid

systems may offer a versatile platform for low-power spintronic devices based on orbital currents and interfacial engineering.

- **Interlayer Interactions and IL-DMI:** The study of spiral domains in Co/Pt/Co trilayers raises several open questions regarding the nature and stability of these unique magnetic structures. Understanding the mechanisms that lead to their formation, and the conditions under which they are irreversibly suppressed, would represent a major technological advance. Typically, IL-DMI is investigated in complex multilayer stacks, often involving multiple interfaces and spacer layers. In contrast, the Co/Pt/Co trilayer offers a minimal and straightforward platform to probe interlayer chiral coupling, making it highly attractive for both fundamental studies and device applications. In this context, the proposed experiments at the ALBA synchrotron will be essential. By employing element-specific techniques such as XMCD and XMLD-PEEM, we aim to directly probe the magnetization state of each layer and confirm the role of IL-DMI in stabilizing spiral domains. Furthermore, micromagnetic simulations (e.g., using MuMax3 or OOMMF) could provide deeper insights into the energetics and interplay of micromagnetic interactions. Beyond fundamental interest, the ability to control the shape, size, and fringe spacing of these spirals, along with their generation, suppression, and potential restoration, could enable novel approaches to information encoding. Such domain structures may serve as secure and reconfigurable magnetic states, offering new possibilities for cryptographic data storage and logic architectures based on chiral magnetism.

- **Cryostat Integration and MOKE Optimization:** The optimization of the MOKE setup is an ongoing process. A custom-designed cryostat has already been developed and is awaiting integration into the system. However, the dedicated sample holder and the new OOP magnetic coil required for full functionality are still under construction. Once implemented, this upgrade will enable temperature-dependent studies of compensation points and angular momentum dynamics in REIGs, potentially revealing regimes of ultrafast DW motion and low-power switching. In parallel, new actively damped legs have been acquired for the optical table. These will significantly reduce mechanical vibrations, which currently limit the resolution of magnetic imaging below 1–2 μm. This improvement will allow us to image smaller patterned structures and bubble-like skyrmions (noting that true nanoscale skyrmions remain beyond the resolution limit of our 455 nm blue LED source). For example, we plan to investigate how the size and geometry of REIG/HM etched structures influence SOT switching behavior. Finally, a critical limitation of the current setup is the inability to apply high IP magnetic fields without compromising optical alignment or mechanical stability. Overcoming this constraint is essential for expanding our studies to fully metallic heterostructures, where higher IP fields, often in the range of several hundreds of mT, are required to probe DMI-related phenomena and DW dynamics.

List of Figures

List of Tables

List of Abbreviations

Acronym	Meaning
AD	Aperture Diaphragm
AFM	Atomic Force Microscopy
AHE	Anomalous Hall Effect
AMR	Anisotropic Magnetoresistance
BD	Bit Depth
BFP	Back Focal Plane
BLS	Brillouin Light Scattering
CCD	Charge-Coupled Device
CIDWM	Current-Induced Domain Wall Motion
CMOS	Complementary Metal-Oxide-Semiconductor
DFT	Density Functional Theory
DL	Damping-like (torque)
DMI	Dzyaloshinskii–Moriya Interaction
DW	Domain Wall
EELS	Electron Energy Loss Spectroscopy
FD	Field Diaphragm
FI	Ferrimagnet
FIB	Focused Ion Beam
FL	Field-like (torque)
FL	Focusing Lens
FM	Ferromagnet
FOV	Field of View
FWHM	Full Width at Half Maximum
GdIG	Gadolinium Iron Garnet ($Gd_3Fe_5O_{12}$)
GGG	Gadolinium Gallium Garnet ($Gd_3Ga_5O_{12}$)
GKA	Goodenough–Kanamori–Anderson (rules)
GMR	Giant Magnetoresistance
HAADF	High-Angle Annular Dark-Field
HE	Ordinary Hall Effect
HM	Heavy Metal
HoIG	Holmium Iron Garnet ($Ho_3Fe_5O_{12}$)
IL-DMI	Interlayer Dzyaloshinskii–Moriya Interaction

Acronym	Meaning
IP	In-plane
ISHE	Inverse Spin Hall Effect
LLG	Landau–Lifshitz–Gilbert (equation)
LPF	Low-pass Filter
MOKE	Magneto-Optical Kerr Effect
MPE	Magnetic Proximity Effect
MRAM	Magnetoresistive Random-Access Memory
MTJ	Magnetic Tunnel Junction
NA	Numarical Aperture
NM	Normal Metal
NV	Nitrogen-Vacancy (magnetometry)
OHE	Orbital Hall Effect
OMR	Ordinary (Lorentz) Magnetoresistance
OOP	Out-of-plane
OREE	Orbital Rashba–Edelstein Effect
PHE	Planar Hall Effect
PLD	Pulsed Laser Deposition
PMA	Perpendicular Magnetic Anisotropy
PPMS	Physical Property Measurement System
QE	Quantum Efficiency
REE	Rashba–Edelstein Effect
REIG	Rare-Earth Iron Garnet(s)
RKKY	Ruderman–Kittel–Kasuya–Yosida (interaction)
RMS	Root Mean Square
ROI	Region of Interest
RT	Room Temperature
SHE	Spin Hall Effect
SMR	Spin Hall Magnetoresistance
SNR	Signal–to–Noise Ratio
SOC	Spin–Orbit Coupling
SOT	Spin–Orbit Torque
SPEELS	Spin-Polarized Electron Energy Loss Spectroscopy
SQUID	Superconducting Quantum Interference Device
STEM	Scanning Transmission Electron Microscopy
STT	Spin-Transfer Torque
TMR	Tunnel Magnetoresistance
TbIG	Terbium Iron Garnet ($Tb_3Fe_5O_{12}$)
TmIG	Thulium Iron Garnet ($Tm_3Fe_5O_{12}$)
XRD	X-ray Diffraction
XRR	X-ray Reflectometry
YIG	Yttrium Iron Garnet ($Y_3Fe_5O_{12}$)

List of Symbols

Symbol	Description
e	Elementary charge (C)
$\hbar$	Reduced Planck constant (J·s)
m_e, m^*	Electron mass and effective mass (kg)
g_e	Electron g-factor (dimensionless)
c	Speed of light in vacuum (m/s)
μ_B	Bohr magneton (J/T)
g	Landé g-factor (dimensionless)
L, S, J	Total orbital, spin, and total angular momentum
m_l, m_s, m_j	magnetic, spin and total quantum number
Z	Atominc number
ϵ_0	Vacuum permittivity $(\mathrm{s}^4 \cdot \mathrm{A}^2)(\mathrm{m}^3 \cdot \mathrm{kg})$
μ_0	Vacuum permeability $(\mathrm{kg} \cdot \mathrm{m})/(\mathrm{A}^2 \cdot \mathrm{s}^2) = \mathrm{H/m}$
$\mathbf{M}$	Magnetization vector (A/m)
M_s	Saturation magnetization (A/m)
$\mathbf{m}$	Unit magnetization vector, $\mathbf{m} = \mathbf{M}/M_s$
$\mathbf{H}$	Magnetic field (A/m); H_{eff} effective field
$\mathbf{B}$	Magnetic flux density (T)
$\mathbf{E}$	Electric field (V/m)
V, I	Voltage (V) and current (A)
θ, ϕ	Polar and azimuthal angles of $\mathbf{M}$
ξ	Spin-polarization of interfacial spin accumulation (unit vector)
ρ	resistivity (Ω m)
R	Longitudinal resistance ($R = V/I$, Ω)
R_H	Hall resistance ($R_H = V_H/I$, Ω)
c_{HE}	Ordinary Hall coefficient (Ω/mT)
R_{AHE}	Anomalous Hall resistance amplitude (Ω)
R_{PHE}	Planar Hall resistance amplitude (Ω)
n	Carrier density (m^{-3})
θ_{SH}	Spin Hall angle (dimensionless)
λ_{SD}	Spin diffusion length (nm)
σ	Conductivity (S/m)

Symbol	Description
R_{sq}	Sheet resistance ($\Omega/\square$)
$G_{\uparrow\downarrow}$	Spin-mixing conductance (complex)
μ_s	Spin-dependent chemical potential (J)
D_{diff}	Diffusion constant m^2/s
τ_{sf}	Spin-flip time constant (s)
E_a	Anisotropy energy density (J/m^3)
K_u	Uniaxial anisotropy constant (J/m^3)
K_s, K_v	Surface and Volume (bulk) anisotropy term (J/m^2)
K_{eff}	Effective magnetic anisotropy (J/m^3)
K_{shape}	Shape anisotropy energy density (J/m^3)
K_1	Cubic anisotropy constant (J/m^3)
K_{ME}	Magnetoelastic anisotropy energy density (J/m^3)
A	Exchange stiffness (J/m)
λ_{hkl}	Magnetostriction constant along (hkl) (dimensionless)
$\sigma_{\parallel,\perp}$	IP (OOP) biaxial stress (Pa)
Y	Young's modulus (Pa)
ν	Poisson's ratio (dimensionless)
$\epsilon_{\parallel,\perp}$	IP (OOP) strain (dimensionless)
a	Lattice parameters (nm)
T_{MC}	Magnetic compensation temperature (°C)
T_{A}	Angular momentum compensation temperature (°C)
D	Interfacial DMI constant (mJ/m^2)
H_{DMI}	Effective DMI field (A/m)
Δ_{DW}	Domain wall width (nm)
σ_{BW}	Bloch-wall energy per unit area (J/m^2)
H_K	In-plane wall anisotropy field (A/m)
H_W	Walker breakdown field (A/m)
v_{DW}	Domain wall velocity (m/s)
v_D	Maximum DW velocity at Walker threshold (m/s)
μ	DW mobility
q	DW position (collective coordinate) (m)
φ	DW internal angle (collective coordinate) (rad)
α	Gilbert damping constant (dimensionless)
γ	Gyromagnetic ratio ($\text{rad}\,\text{s}^{-1}\,\text{T}^{-1}$)
α_R	Rashba constant (eV·Å or J·m, per context)
B_R	Rashba effective magnetic field (T)
k_F	Fermi wavevector (m^{-1})
Φ_{K}	Kerr angle (complex)
θ_{K}, ξ_{K}	Kerr rotation (mrad) and ellipticity (dimensionless)
α	Skew angle (mrad)
η	extintion ratio (dimensionless)

List of Publications and Conferences

Journal Articles and Manuscripts

1. Fettizio, M., Fedel, S., Estandia, S., De Sousa, J. A., Avci, C. O., *Sputtered Yttrium Iron Garnet Films with Perpendicular Anisotropy on Silicon*. Submitted.

2. Fedel, S., & Avci, C. O. (2025). *Efficient Spin-Orbit Torque Switching in a Magnetic Insulator via Ultrathin Pt and Light Metal Overlayers*, **preprint**. DOI: https://doi.org/10.21203/rs.3.rs-7418968/v1

3. Fedel, S., Villa, M., Damerio, S., Demiroglu, E., Deger, C., Gazquez, J., & Avci, C. O. (2025). *Evidence of Long-Range Dzyaloshinskii–Moriya Interaction at Ferrimagnetic Insulator/Nonmagnetic Metal Interfaces*, **Advanced Functional Materials**, 2418653. DOI: https://doi.org/10.1002/adfm.202418653

Conferences and Workshops

1. *Efficient Spin-Orbit Torque Switching in a Magnetic Insulator via Ultrathin Pt and Light Metal Overlayers*, **JEMS**, Frankfurt, Germany, 2025. (Oral contribution)

2. *Evidence of Long-Range Dzyaloshinskii-Moriya Interaction at Ferrimagnetic Insulator/ Nonmagnetic Metal Interfaces* , **JEMS**, Frankfurt, Germany, 2025. (Oral contribution)

3. *Evidence of Long-Range Dzyaloshinskii-Moriya Interaction at Ferrimagnetic Insulator/ Nonmagnetic Metal Interfaces* , **820. Wilhelm und Else Heraeus Seminar**, Bad Honnef, Germany, 2024. (Poster)

4. *Evidence of Long-Range Dzyaloshinskii-Moriya Interaction at Ferrimagnetic Insulator/ Nonmagnetic Metal Interfaces* , **JPHD**, Barcelona, Spain, 2024. (Oral contribution)

5. *Evidence of Long-Range Dzyaloshinskii-Moriya Interaction at Ferrimagnetic Insulator/ Nonmagnetic Metal Interfaces* , **Workshop of the Spanish Network on Spintronics**, Madrid, Spain, 2024. (Oral contribution)

6. *Interfacial DMI Characterization in Sputtered Terbium Iron Garnets Thin Films*, **ICM**, Bologna, Italy, 2024. (Poster)

7. *Interfacial DMI Characterization in Sputtered Terbium Iron Garnets Thin Films*, **SPINCOM**, Milano, Italy, 2024. (Poster)

8. *Interfacial DMI Characterization in Sputtered Terbium Iron Garnets Thin Films*, **EMRS**, Strasbourg, France, 2024. (Poster)

9. *Domain Wall Motion in Sputtered Terbium Iron Garnet Thin Films*, **JEMS**, Madrid, Spain, 2023. (Poster)

10. *Domain Wall Motion in Sputtered Terbium Iron Garnet Thin Films*, **SOL-SKYMAG**, San Sebastian, Spain, 2023. (Poster)

11. *Generation and control of vortex magnetic domains in presence of DMI and interlayer coupling*, **PETASPIN**, Messina, Italy, 2022 (Oral contribution - recorded)

12. *Generation and control of vortex magnetic domains in presence of DMI and interlayer coupling*, **ESM**, Saarbrüken, Germany, 2022 (Poster)

Bibliography

[1] N. W. Stauffer, "Energy-efficient computing — MIT Energy Initiative," 2013.

[2] A. Fert and F. N. Van Dau, "Spintronics, from giant magnetoresistance to magnetic skyrmions and topological insulators," *Comptes Rendus. Physique*, vol. 20, no. 7-8, pp. 817–831, 2019.

[3] B. Dieny, I. L. Prejbeanu, K. Garello, P. Gambardella, P. Freitas, R. Lehndorff, W. Raberg, U. Ebels, S. O. Demokritov, J. Akerman, *et al.*, "Opportunities and challenges for spintronics in the microelectronics industry," *Nature Electronics*, vol. 3, no. 8, pp. 446–459, 2020.

[4] S. Valenzuela, P. Gambardella, K. Garello, O. Klein, J. Sierra, and J. Sinova, "Spintronic materials," *Encyclopedia of Condensed Matter Physics*, vol. 2, pp. 159–176, 2024.

[5] U. Gradmann and J. Müller, "Flat ferromagnetic, epitaxial 48Ni/52Fe (111) films of few atomic layers," *physica status solidi (b)*, vol. 27, no. 1, pp. 313–324, 1968.

[6] J. Lodder, "Magnetic recording hard disk thin film media," *Handbook of magnetic materials*, vol. 11, pp. 291–405, 1998.

[7] P. Carcia, A. Meinhaldt, and A. Suna, "Perpendicular magnetic anisotropy in Pd/Co thin film layered structures," *Applied Physics Letters*, vol. 47, no. 2, pp. 178–180, 1985.

[8] P. Carcia, "Perpendicular magnetic anisotropy in Pd/Co and Pt/Co thin-film layered structures," *Journal of applied physics*, vol. 63, no. 10, pp. 5066–5073, 1988.

[9] G. Binasch, P. Grünberg, F. Saurenbach, and W. Zinn, "Enhanced magnetoresistance in layered magnetic structures with antiferromagnetic interlayer exchange," *Physical review B*, vol. 39, no. 7, p. 4828, 1989.

[10] M. N. Baibich, J. M. Broto, A. Fert, F. N. Van Dau, F. Petroff, P. Etienne, G. Creuzet, A. Friederich, and J. Chazelas, "Giant magnetoresistance of (001) Fe/(001) Cr magnetic superlattices," *Physical review letters*, vol. 61, no. 21, p. 2472, 1988.

[11] M. Julliere, "Tunneling between ferromagnetic films," *Physics letters A*, vol. 54, no. 3, pp. 225–226, 1975.

[12] S. Yuasa, T. Nagahama, A. Fukushima, Y. Suzuki, and K. Ando, "Giant room-temperature magnetoresistance in single-crystal Fe/MgO/Fe magnetic tunnel junctions," *Nature materials*, vol. 3, no. 12, pp. 868–871, 2004.

[13] S. Ikeda, J. Hayakawa, Y. Ashizawa, Y. Lee, K. Miura, H. Hasegawa, M. Tsunoda, F. Matsukura, and H. Ohno, "Tunnel magnetoresistance of 604% at 300k by suppression of Ta diffusion in CoFeB/ MgO/ CoFeB pseudo-spin-valves annealed at high temperature," *Applied Physics Letters*, vol. 93, no. 8, 2008.

[14] L.-B. Faber, W. Zhao, J.-O. Klein, T. Devolder, and C. Chappert, "Dynamic compact model of spin-transfer torque based magnetic tunnel junction (mtj)," in *2009 4th International Conference on Design & Technology of Integrated Systems in Nanoscal Era*, pp. 130–135, IEEE, 2009.

[15] G. Prenat, K. Jabeur, P. Vanhauwaert, G. Di Pendina, F. Oboril, R. Bishnoi, M. Ebrahimi, N. Lamard, O. Boulle, K. Garello, *et al.*, "Ultra-fast and high-reliability sot-mram: From cache replacement to normally-off computing," *IEEE Transactions on Multi-Scale Computing Systems*, vol. 2, no. 1, pp. 49–60, 2015.

[16] J. C. Slonczewski, "Current-driven excitation of magnetic multilayers," *Journal of Magnetism and Magnetic Materials*, vol. 159, no. 1-2, pp. L1–L7, 1996.

[17] L. Berger, "Emission of spin waves by a magnetic multilayer traversed by a current," *Physical Review B*, vol. 54, no. 13, p. 9353, 1996.

[18] W. Zhao, Y. Zhang, T. Devolder, J.-O. Klein, D. Ravelosona, C. Chappert, and P. Mazoyer, "Failure and reliability analysis of stt-mram," *Microelectronics Reliability*, vol. 52, no. 9-10, pp. 1848–1852, 2012.

[19] I. Mihai Miron, G. Gaudin, S. Auffret, B. Rodmacq, A. Schuhl, S. Pizzini, J. Vogel, and P. Gambardella, "Current-driven spin torque induced by the rashba effect in a ferromagnetic metal layer," *Nature materials*, vol. 9, no. 3, pp. 230–234, 2010.

[20] A. Manchon, J. Železnỳ, I. M. Miron, T. Jungwirth, J. Sinova, A. Thiaville, K. Garello, and P. Gambardella, "Current-induced spin-orbit torques in ferromagnetic and antiferromagnetic systems," *Reviews of Modern Physics*, vol. 91, no. 3, p. 035004, 2019.

[21] I. M. Miron, T. Moore, H. Szambolics, L. D. Buda-Prejbeanu, S. Auffret, B. Rodmacq, S. Pizzini, J. Vogel, M. Bonfim, A. Schuhl, *et al.*, "Fast current-induced domain-wall motion controlled by the rashba effect," *Nature materials*, vol. 10, no. 6, pp. 419–423, 2011.

[22] K. Garello, F. Yasin, and G. S. Kar, "Spin-orbit torque mram for ultrafast embedded memories: From fundamentals to large scale technology integration," in *2019 IEEE 11th International Memory Workshop (IMW)*, pp. 1–4, IEEE, 2019.

[23] K. Garello, F. Yasin, S. Couet, L. Souriau, J. Swerts, S. Rao, S. Van Beek, W. Kim, E. Liu, S. Kundu, *et al.*, "Sot-mram 300mm integration for low power and ultrafast embedded memories," in *2018 IEEE symposium on VLSI Circuits*, pp. 81–82, IEEE, 2018.

[24] C. O. Avci, "Current-induced magnetization control in insulating ferrimagnetic garnets," *Journal of the Physical Society of Japan*, vol. 90, no. 8, p. 081007, 2021.

[25] C. O. Avci, A. Quindeau, M. Mann, C.-F. Pai, C. A. Ross, and G. S. Beach, "Spin transport in as-grown and annealed thulium iron garnet/platinum bilayers with perpendicular magnetic anisotropy," *Physical Review B*, vol. 95, no. 11, p. 115428, 2017.

[26] J. Ding, C. Liu, Y. Zhang, U. Erugu, Z. Quan, R. Yu, E. McCollum, S. Mo, S. Yang, H. Ding, *et al.*, "Nanometer-thick yttrium iron garnet films with perpendicular anisotropy and low damping," *Physical Review Applied*, vol. 14, no. 1, p. 014017, 2020.

[27] S. Ding, A. Ross, R. Lebrun, S. Becker, K. Lee, I. Boventer, S. Das, Y. Kurokawa, S. Gupta, J. Yang, *et al.*, "Interfacial dzyaloshinskii-moriya interaction and chiral magnetic textures in a ferrimagnetic insulator," *Physical Review B*, vol. 100, no. 10, p. 100406, 2019.

[28] S. Vélez, J. Schaab, M. S. Wörnle, M. Müller, E. Gradauskaite, P. Welter, C. Gutgsell, C. Nistor, C. L. Degen, M. Trassin, *et al.*, "High-speed domain wall racetracks in a magnetic insulator," *Nature communications*, vol. 10, no. 1, p. 4750, 2019.

[29] H. Chen, D. Cheng, H. Yang, D. Wang, S. Zhou, Z. Shi, and X. Qiu, "Magnetization switching induced by magnetic field and electric current in perpendicular TbIG/Pt bilayers," *Applied Physics Letters*, vol. 116, no. 11, 2020.

[30] L. Caretta, S.-H. Oh, T. Fakhrul, D.-K. Lee, B. H. Lee, S. K. Kim, C. A. Ross, K.-J. Lee, and G. S. Beach, "Relativistic kinematics of a magnetic soliton," *Science*, vol. 370, no. 6523, pp. 1438–1442, 2020.

[31] Q. Shao, C. Tang, G. Yu, A. Navabi, H. Wu, C. He, J. Li, P. Upadhyaya, P. Zhang, S. A. Razavi, *et al.*, "Role of dimensional crossover on spin-orbit torque efficiency in magnetic insulator thin films," *Nature communications*, vol. 9, no. 1, p. 3612, 2018.

[32] Y. Li, D. Zheng, C. Liu, C. Zhang, B. Fang, A. Chen, Y. Ma, A. Manchon, and X. Zhang, "Current-induced magnetization switching across a nearly room-temperature compensation point in an insulating compensated ferrimagnet," *ACS nano*, vol. 16, no. 5, pp. 8181–8189, 2022.

[33] H. Bai, Z. Zhu, X. Zhan, M. Yang, G. Li, J. Ke, C. Hu, T. Zhu, and J. Cai, "Polarized neutron reflectometry characterization of perpendicular magnetized $Ho_3Fe_5O_{12}$ films with efficient spin-orbit torque induced switching," *Applied Physics Letters*, vol. 119, no. 21, 2021.

[34] H. Bai, Z. Zhu, J. Ke, G. Li, J. Su, Y. Zhang, T. Zhu, and J. Cai, "Large tunable perpendicular magnetic anisotropy in $Y_{3-x}Tm_xFe_5O_{12}$ (x= 0–3) epitaxial films with minor changes in switching current," *Physical Review Applied*, vol. 17, no. 6, p. 064023, 2022.

[35] L.-Z. Bi, J. Ke, D. Zhang, G. Li, P. Wang, C. Hu, Z. Zhu, Y. Liu, Y. Zhang, and J. Cai, "Field-free switching of $Tm_3Fe_5O_{12}$ on miscut garnet substrates with entangled spin hall magnetoresistance and anomalous hall resistance," *Physical Review B*, vol. 110, no. 13, p. 134415, 2024.

[36] S. Husain, N. F. Prestes, O. Fayet, S. Collin, F. Godel, E. Jacquet, T. Denneulin, R. E. Dunin-Borkowski, A. Thiaville, M. Bibes, *et al.*, "Field-free switching of perpendicular magnetization in an ultrathin epitaxial magnetic insulator," *Nano Letters*, vol. 24, no. 9, pp. 2743–2750, 2024.

[37] M. Yang, L. Sun, Y. Zeng, J. Cheng, K. He, X. Yang, Z. Wang, L. Yu, H. Niu, T. Ji, *et al.*, "Highly efficient field-free switching of perpendicular yttrium iron garnet with collinear spin current," *Nature Communications*, vol. 15, no. 1, p. 3201, 2024.

[38] J. Ke, L. Bi, Z. Zhu, H. Bai, G. Li, C. Hu, P. Wang, Y. Zhang, and J.-W. Cai, "Field-free switching and enhanced electrical detection of ferrimagnetic insulators through an intermediate ultrathin ferromagnetic metal layer," *Advanced Materials Interfaces*, vol. 10, no. 36, p. 2300632, 2023.

[39] L.-Z. Bi, J. Ke, H. Bai, G. Li, Z. Zhu, C. Hu, Y. Cheng, P. Wang, W. Jiang, Y. Zhang, *et al.*, "Field-free and energy-efficient switching of a ferrimagnetic insulator through orbital currents of copper," *Advanced Electronic Materials*, vol. 10, no. 2, p. 2300627, 2024.

[40] T. Tanaka, H. Kontani, M. Naito, T. Naito, D. S. Hirashima, K. Yamada, and J.-i. Inoue, "Intrinsic spin hall effect and orbital hall effect in 4 d and 5 d transition metals," *Physical Review B—Condensed Matter and Materials Physics*, vol. 77, no. 16, p. 165117, 2008.

[41] H. Kontani, T. Tanaka, D. Hirashima, K. Yamada, and J. Inoue, "Giant orbital hall effect in transition metals: Origin of large spin and anomalous hall effects," *Physical review letters*, vol. 102, no. 1, p. 016601, 2009.

[42] D. Go, D. Jo, C. Kim, and H.-W. Lee, "Intrinsic spin and orbital hall effects from orbital texture," *Physical review letters*, vol. 121, no. 8, p. 086602, 2018.

[43] D. Jo, D. Go, and H.-W. Lee, "Gigantic intrinsic orbital hall effects in weakly spin-orbit coupled metals," *Physical Review B*, vol. 98, no. 21, p. 214405, 2018.

[44] D. Go, D. Jo, K.-W. Kim, S. Lee, M.-G. Kang, B.-G. Park, S. Blügel, H.-W. Lee, and Y. Mokrousov, "Long-range orbital torque by momentum-space hotspots," *Physical review letters*, vol. 130, no. 24, p. 246701, 2023.

[45] S. Ding, A. Ross, D. Go, L. Baldrati, Z. Ren, F. Freimuth, S. Becker, F. Kammerbauer, J. Yang, G. Jakob, *et al.*, "Harnessing orbital-to-spin conversion of interfacial orbital currents for efficient spin-orbit torques," *Physical review letters*, vol. 125, no. 17, p. 177201, 2020.

[46] T. Li, L. Liu, X. Li, X. Zhao, H. An, and K. Ando, "Giant orbital-to-spin conversion for efficient current-induced magnetization switching of ferrimagnetic insulator," *Nano Letters*, vol. 23, no. 15, pp. 7174–7179, 2023.

[47] E. Santos, J. Abrão, D. Go, L. De Assis, Y. Mokrousov, J. Mendes, and A. Azevedo, "Inverse orbital torque via spin-orbital intertwined states," *Physical Review Applied*, vol. 19, no. 1, p. 014069, 2023.

[48] J. Mendoza-Rodarte, M. Cosset-Chéneau, B. Van Wees, and M. Guimarães, "Efficient magnon injection and detection via the orbital rashba-edelstein effect," *Physical Review Letters*, vol. 132, no. 22, p. 226704, 2024.

[49] X. Xu, D. Zhang, Z. Liao, P. Yan, Y. Wang, L. Zhang, Z. Zhong, F. Bai, Y. Qu, H. Zhang, *et al.*, "Colossal orbital current induced by gradient oxidation for high-efficiency magnetization switching," *Small*, vol. 20, no. 44, p. 2403881, 2024.

[50] H. Wang, M.-G. Kang, D. Petrosyan, S. Ding, R. Schlitz, L. J. Riddiford, W. Legrand, and P. Gambardella, "Orbital pumping in ferrimagnetic insulators," *Physical Review Letters*, vol. 134, no. 12, p. 126701, 2025.

[51] C. O. Avci, E. Rosenberg, L. Caretta, F. Büttner, M. Mann, C. Marcus, D. Bono, C. A. Ross, and G. S. Beach, "Interface-driven chiral magnetism and current-driven domain walls in insulating magnetic garnets," *Nature nanotechnology*, vol. 14, no. 6, pp. 561–566, 2019.

[52] L. Caretta, E. Rosenberg, F. Büttner, T. Fakhrul, P. Gargiani, M. Valvidares, Z. Chen, P. Reddy, D. A. Muller, C. A. Ross, *et al.*, "Interfacial dzyaloshinskii-moriya interaction arising from rare-earth orbital magnetism in insulating magnetic oxides," *Nature communications*, vol. 11, no. 1, p. 1090, 2020.

[53] S. Ding, L. Baldrati, A. Ross, Z. Ren, R. Wu, S. Becker, J. Yang, G. Jakob, A. Brataas, and M. Kläui, "Identifying the origin of the nonmonotonic thickness dependence of spin-orbit torque and interfacial dzyaloshinskii-moriya interaction in a ferrimagnetic insulator heterostructure," *Physical Review B*, vol. 102, no. 5, p. 054425, 2020.

[54] S. Xia, T. Feng, B. Yang, G. Liu, Y. Tian, P. Wang, X. Wan, B. Wang, and D. Wu, "Source and origin of the interfacial dzyaloshinskii-moriya interaction in a heavy-metal— magnetic-insulator bilayer," *Physical Review B*, vol. 105, no. 18, p. 184417, 2022.

[55] H. Wang, J. Chen, T. Liu, J. Zhang, K. Baumgaertl, C. Guo, Y. Li, C. Liu, P. Che, S. Tu, *et al.*, "Chiral spin-wave velocities induced by all-garnet interfacial dzyaloshinskii-moriya interaction in ultrathin yttrium iron garnet films," *Physical review letters*, vol. 124, no. 2, p. 027203, 2020.

[56] Q. Shao, Y. Liu, G. Yu, S. K. Kim, X. Che, C. Tang, Q. L. He, Y. Tserkovnyak, J. Shi, and K. L. Wang, "Topological hall effect at above room temperature in heterostructures composed of a magnetic insulator and a heavy metal," *Nature Electronics*, vol. 2, no. 5, pp. 182–186, 2019.

[57] A. J. Lee, A. S. Ahmed, J. Flores, S. Guo, B. Wang, N. Bagués, D. W. McComb, and F. Yang, "Probing the source of the interfacial dzyaloshinskii-moriya interaction responsible for the topological hall effect in metal/$Tm_3Fe_5O_{12}$ systems," *Physical review letters*, vol. 124, no. 10, p. 107201, 2020.

[58] S. Xia, S. Zhang, Z. Luan, L. Zhou, J. Liang, G. Liu, B. Yang, H. Yang, R. Liu, and D. Wu, "Interfacial dzyaloshinskii-moriya interaction between ferromagnetic insulator and heavy metal," *Applied Physics Letters*, vol. 116, no. 5, 2020.

[59] A. J. Lee, S. Guo, J. Flores, B. Wang, N. Bagués, D. W. McComb, and F. Yang, "Investigation of the role of rare-earth elements in spin-hall topological hall effect in Pt/ferrimagnetic-garnet bilayers," *Nano Letters*, vol. 20, no. 6, pp. 4667–4672, 2020.

[60] Z. Xu, Q. Liu, Y. Ji, X. Li, J. Li, J. Wang, and L. Chen, "Strain-tunable interfacial dzyaloshinskii–moriya interaction and spin-hall topological hall effect in $Pt/Tm_3Fe_5O_{12}$ heterostructures," *ACS Applied Materials & Interfaces*, vol. 14, no. 14, pp. 16791–16799, 2022.

[61] S. Fedel, M. Villa, S. Damerio, E. Demiroglu, C. Deger, J. Gazquez, and C. O. Avci, "Evidence of long-range dzyaloshinskii–moriya interaction at ferrimagnetic insulator/nonmagnetic metal interfaces," *Advanced Functional Materials*, p. 2418653, 2025.

[62] L. Caretta, M. Mann, F. Büttner, K. Ueda, B. Pfau, C. M. Günther, P. Hessing, A. Churikova, C. Klose, M. Schneider, *et al.*, "Fast current-driven domain walls and small skyrmions in a compensated ferrimagnet," *Nature nanotechnology*, vol. 13, no. 12, pp. 1154–1160, 2018.

[63] A. S. Ahmed, A. J. Lee, N. Bagués, B. A. McCullian, A. M. Thabt, A. Perrine, P.-K. Wu, J. R. Rowland, M. Randeria, P. C. Hammel, *et al.*, "Spin-hall topological hall effect in highly tunable Pt/ferrimagnetic-insulator bilayers," *Nano letters*, vol. 19, no. 8, pp. 5683–5688, 2019.

[64] S. Vélez, S. Ruiz-Gómez, J. Schaab, E. Gradauskaite, M. S. Wörnle, P. Welter, B. J. Jacot, C. L. Degen, M. Trassin, M. Fiebig, *et al.*, "Current-driven dynamics and ratchet effect of skyrmion bubbles in a ferrimagnetic insulator," *Nature Nanotechnology*, vol. 17, no. 8, pp. 834–841, 2022.

[65] S. S. Parkin, M. Hayashi, and L. Thomas, "Magnetic domain-wall racetrack memory," *science*, vol. 320, no. 5873, pp. 190–194, 2008.

[66] R. Bläsing, A. A. Khan, P. C. Filippou, C. Garg, F. Hameed, J. Castrillon, and S. S. Parkin, "Magnetic racetrack memory: From physics to the cusp of applications within a decade," *Proceedings of the IEEE*, vol. 108, no. 8, pp. 1303–1321, 2020.

[67] L. Sheng, J. Chen, H. Wang, and H. Yu, "Magnonics based on thin-film iron garnets," *Journal of the Physical Society of Japan*, vol. 90, no. 8, p. 081005, 2021.

[68] J. M. Coey, *Magnetism and magnetic materials*. Cambridge university press, 2010.

[69] S. Blundell, *Magnetism in condensed matter*. OUP Oxford, 2001.

[70] K. Shanavas, Z. S. Popović, and S. Satpathy, "Theoretical model for rashba spin-orbit interaction in d electrons," *Physical Review B*, vol. 90, no. 16, p. 165108, 2014.

[71] L. Néel, "Propriétés magnétiques des ferrites; ferrimagnétisme et antiferromagnétisme," in *Annales de physique*, vol. 12, pp. 137–198, 1948.

[72] L. Néel, "Preuves expérimentales du ferromagnétisme et de l'antiferromagnétisme," in *Annales de l'institut Fourier*, vol. 1, pp. 163–183, 1949.

[73] L. Šmejkal, J. Sinova, and T. Jungwirth, "Emerging research landscape of altermagnetism," *Physical Review X*, vol. 12, no. 4, p. 040501, 2022.

[74] S. F. Edwards and P. W. Anderson, "Theory of spin glasses," *Journal of Physics F: Metal Physics*, vol. 5, no. 5, p. 965, 1975.

[75] P. W. Anderson, "New approach to the theory of superexchange interactions," *Physical Review*, vol. 115, no. 1, p. 2, 1959.

[76] J. Kanamori, "Superexchange interaction and symmetry properties of electron orbitals," *Journal of Physics and Chemistry of Solids*, vol. 10, no. 2-3, pp. 87–98, 1959.

[77] M. A. Ruderman and C. Kittel, "Indirect exchange coupling of nuclear magnetic moments by conduction electrons," *Physical Review*, vol. 96, no. 1, p. 99, 1954.

[78] T. Kasuya, "A theory of metallic ferro-and antiferromagnetism on zener's model," *Progress of theoretical physics*, vol. 16, no. 1, pp. 45–57, 1956.

[79] K. Yosida, "Magnetic properties of Cu-Mn alloys," *Physical Review*, vol. 106, no. 5, p. 893, 1957.

[80] D. Aristov, "Indirect rkky interaction in any dimensionality," *Physical Review B*, vol. 55, no. 13, p. 8064, 1997.

[81] P. Simon, R. López, and Y. Oreg, "Ruderman-kittel-kasuya-yosida and magnetic-field interactions in coupled kondo quantum dots," *Physical review letters*, vol. 94, no. 8, p. 086602, 2005.

[82] A. Hindmarch and B. Hickey, "Direct experimental evidence for the ruderman-kittel-kasuya-yosida interaction in rare-earth metals," *Physical review letters*, vol. 91, no. 11, p. 116601, 2003.

[83] P. Bruno and C. Chappert, "Oscillatory coupling between ferromagnetic layers separated by a nonmagnetic metal spacer," *Physical review letters*, vol. 67, no. 12, p. 1602, 1991.

[84] S. Parkin, R. Bhadra, and K. Roche, "Oscillatory magnetic exchange coupling through thin copper layers," *Physical review letters*, vol. 66, no. 16, p. 2152, 1991.

[85] D. Sander, "The correlation between mechanical stress and magnetic anisotropy inultrathin films," *Reports on Progress in Physics*, vol. 62, no. 5, p. 809, 1999.

[86] L. Néel, "Anisotropie magnétique superficielle et surstructures d'orientation," *Journal de Physique et le Radium*, vol. 15, no. 4, pp. 225–239, 1954.

[87] M. Johnson, P. Bloemen, F. Den Broeder, and J. De Vries, "Magnetic anisotropy in metallic multilayers," *Reports on Progress in Physics*, vol. 59, no. 11, p. 1409, 1996.

[88] I. Campbell and A. Fert, "Transport properties of ferromagnets," *Ferromagnetic Materials*, vol. 3, pp. 751–795, 1982.

[89] T. R. Mcguire and R. I. Potter, "Anisotropic Magnetoresistance in Ferromagnetic 3D Alloys," *IEEE Transactions on Magnetics*, vol. 11, no. 4, pp. 1018–1038, 1975.

[90] J. Smit, "Magnetoresistance of ferromagnetic metals and alloys at low temperatures," *Physica*, vol. 17, pp. 612–627, jun 1951.

[91] C. O. Avci, *Current-induced effects in ferromagnetic heterostructures due to spin-orbit coupling*. PhD thesis, ETH Zurich, 2015.

[92] H. Nakayama, M. Althammer, Y.-T. Chen, K.-i. Uchida, Y. Kajiwara, D. Kikuchi, T. Ohtani, S. Geprägs, M. Opel, S. Takahashi, *et al.*, "Spin hall magnetoresistance induced by a nonequilibrium proximity effect," *Physical review letters*, vol. 110, no. 20, p. 206601, 2013.

[93] M. Althammer, S. Meyer, H. Nakayama, M. Schreier, S. Altmannshofer, M. Weiler, H. Huebl, S. Geprägs, M. Opel, R. Gross, *et al.*, "Quantitative study of the spin hall magnetoresistance in ferromagnetic insulator/normal metal hybrids," *Physical Review B—Condensed Matter and Materials Physics*, vol. 87, no. 22, p. 224401, 2013.

[94] Y.-T. Chen, S. Takahashi, H. Nakayama, M. Althammer, S. T. Goennenwein, E. Saitoh, and G. E. Bauer, "Theory of spin hall magnetoresistance," *Physical Review B—Condensed Matter and Materials Physics*, vol. 87, no. 14, p. 144411, 2013.

[95] S. Vélez, A. Bedoya-Pinto, W. Yan, L. E. Hueso, and F. Casanova, "Competing effects at Pt/YIG interfaces: Spin hall magnetoresistance, magnon excitations, and magnetic frustration," *Physical Review B*, vol. 94, no. 17, p. 174405, 2016.

[96] E. H. Hall, "On a New Action of the Magnet on Electric Currents," *Am. J. Math.*, vol. 2, no. 3, pp. 287–292, 1879.

[97] N. Nagaosa, J. Sinova, S. Onoda, A. H. MacDonald, and N. P. Ong, "Anomalous hall effect," *Reviews of modern physics*, vol. 82, no. 2, pp. 1539–1592, 2010.

[98] R. Karplus and J. Luttinger, "Hall effect in ferromagnetics," *Physical Review*, vol. 95, no. 5, p. 1154, 1954.

[99] J. Smit, "The spontaneous hall effect in ferromagnetics i," *Physica*, vol. 21, no. 6-10, pp. 877–887, 1955.

[100] J. Smit, "The spontaneous hall effect in ferromagnetics ii," *Physica*, vol. 24, no. 1-5, pp. 39–51, 1958.

[101] C. Goldberg and R. Davis, "New galvanomagnetic effect," *Physical Review*, vol. 94, no. 5, p. 1121, 1954.

[102] B. Miao, S. Huang, D. Qu, and C. Chien, "Physical origins of the new magnetoresistance in Pt/YIG," *Physical review letters*, vol. 112, no. 23, p. 236601, 2014.

[103] X. Liang, G. Shi, L. Deng, F. Huang, J. Qin, T. Tang, C. Wang, B. Peng, C. Song, and L. Bi, "Magnetic proximity effect and anomalous hall effect in $Pt/Y_3Fe_{5-x}Al_xO_{12}$ heterostructures," *Physical Review Applied*, vol. 10, no. 2, p. 024051, 2018.

[104] S. R. Park and C. Kim, "Microscopic mechanism for the rashba spin-band splitting: Perspective from formation of local orbital angular momentum," *Journal of Electron Spectroscopy and Related Phenomena*, vol. 201, pp. 6–17, 2015.

[105] Y. A. Bychkov and E. I. Rashba, "Oscillatory effects and the magnetic susceptibility of carriers in inversion layers," *Journal of physics C: Solid state physics*, vol. 17, no. 33, p. 6039, 1984.

[106] V. M. Edelstein, "Spin polarization of conduction electrons induced by electric current in two-dimensional asymmetric electron systems," *Solid State Communications*, vol. 73, no. 3, pp. 233–235, 1990.

[107] P. Noel, *Dynamical spin injection and spin to charge current conversion in oxide-based Rashba interfaces and topological insulators*. PhD thesis, Université Grenoble Alpes, 2019.

[108] P. Gambardella and I. M. Miron, "Current-induced spin–orbit torques," *Philosophical Transactions of the Royal Society A: Mathematical, Physical and Engineering Sciences*, vol. 369, no. 1948, pp. 3175–3197, 2011.

[109] L. Liu, C.-F. Pai, Y. Li, H. Tseng, D. Ralph, and R. Buhrman, "Spin-torque switching with the giant spin hall effect of tantalum," *Science*, vol. 336, no. 6081, pp. 555–558, 2012.

[110] J. Hirsch, "Spin hall effect," *Physical review letters*, vol. 83, no. 9, p. 1834, 1999.

[111] A. Hoffmann, "Spin hall effects in metals," *IEEE transactions on magnetics*, vol. 49, no. 10, pp. 5172–5193, 2013.

[112] S. O. Valenzuela and M. Tinkham, "Direct electronic measurement of the spin hall effect," *Nature*, vol. 442, no. 7099, pp. 176–179, 2006.

[113] J. Sinova, S. O. Valenzuela, J. Wunderlich, C. H. Back, and T. Jungwirth, "Spin hall effects," *Reviews of modern physics*, vol. 87, no. 4, pp. 1213–1260, 2015.

[114] S. Murakami, "Spin hall effect and inverse spin hall effect," *Spintronics for Next Generation Innovative Devices*, pp. 77–98, 2015.

[115] R. Ramaswamy, J. M. Lee, K. Cai, and H. Yang, "Recent advances in spin-orbit torques: Moving towards device applications," *Applied Physics Reviews*, vol. 5, no. 3, 2018.

[116] J. Bass and W. P. Pratt, "Spin-diffusion lengths in metals and alloys, and spin-flipping at metal/metal interfaces: anexperimentalist's critical review," *Journal of Physics: Condensed Matter*, vol. 19, no. 18, p. 183201, 2007.

[117] M. Gradhand, D. V. Fedorov, P. Zahn, and I. Mertig, "Spin hall angle versus spin diffusion length: Tailored by impurities," *Physical Review B—Condensed Matter and Materials Physics*, vol. 81, no. 24, p. 245109, 2010.

[118] R. S. Nair, E. Barati, K. Gupta, Z. Yuan, and P. J. Kelly, "Spin-flip diffusion length in 5 d transition metal elements: A first-principles benchmark," *Physical review letters*, vol. 126, no. 19, p. 196601, 2021.

[119] E. Saitoh, M. Ueda, H. Miyajima, and G. Tatara, "Conversion of spin current into charge current at room temperature: Inverse spin-hall effect," *Applied physics letters*, vol. 88, no. 18, 2006.

[120] B. Miao, S. Huang, D. Qu, and C. Chien, "Inverse spin hall effect in a ferromagnetic metal," *Physical review letters*, vol. 111, no. 6, p. 066602, 2013.

[121] K. Ando, S. Takahashi, J. Ieda, Y. Kajiwara, H. Nakayama, T. Yoshino, K. Harii, Y. Fujikawa, M. Matsuo, S. Maekawa, *et al.*, "Inverse spin-hall effect induced by spin pumping in metallic system," *Journal of applied physics*, vol. 109, no. 10, 2011.

[122] M. Isasa, E. Villamor, L. E. Hueso, M. Gradhand, and F. Casanova, "Temperature dependence of spin diffusion length and spin hall angle in au and Pt," *Physical Review B*, vol. 91, no. 2, p. 024402, 2015.

[123] M. S. El Hadri, J. Gibbons, Y. Xiao, H. Ren, H. Arava, Y. Liu, Z. Liu, A. Petford-Long, A. Hoffmann, and E. E. Fullerton, "Large spin-to-charge conversion in ultrathin gold-silicon multilayers," *Physical Review Materials*, vol. 5, no. 6, p. 064410, 2021.

[124] Y. Niimi, H. Suzuki, Y. Kawanishi, Y. Omori, T. Valet, A. Fert, and Y. Otani, "Extrinsic spin hall effects measured with lateral spin valve structures," *Physical Review B*, vol. 89, no. 5, p. 054401, 2014.

[125] K. Ando and E. Saitoh, "Inverse spin-hall effect in palladium at room temperature," *Journal of Applied Physics*, vol. 108, no. 11, 2010.

[126] X. Tao, Q. Liu, B. Miao, R. Yu, Z. Feng, L. Sun, B. You, J. Du, K. Chen, S. Zhang, *et al.*, "Self-consistent determination of spin hall angle and spin diffusion length in Pt and Pd: The role of the interface spin loss," *Science advances*, vol. 4, no. 6, p. eaat1670, 2018.

[127] S.-I. Kim, D.-J. Kim, M.-S. Seo, B.-G. Park, and S.-Y. Park, "Dependence of inverse-spin hall effect and spin-rectified voltage on tantalum thickness in Ta/CoFeB bilayer structure," *Applied Physics Letters*, vol. 106, no. 3, 2015.

[128] R. Yu, B. Miao, L. Sun, Q. Liu, J. Du, P. Omelchenko, B. Heinrich, M. Wu, and H. Ding, "Determination of spin hall angle and spin diffusion length in β-phase-dominated tantalum," *Physical Review Materials*, vol. 2, no. 7, p. 074406, 2018.

[129] K. Sriram, R. Mondal, J. Pradhan, A. Haldar, and C. Murapaka, "Structural phase engineering of (α+ β)-W for a large spin hall angle and spin diffusion length," *The Journal of Physical Chemistry C*, vol. 127, no. 46, pp. 22704–22712, 2023.

[130] W. Chen, G. Xiao, Q. Zhang, and X. Zhang, "Temperature study of the giant spin hall effect in the bulk limit of β-W," *Physical Review B*, vol. 98, no. 13, p. 134411, 2018.

[131] G. Sala, *Magnetization dynamics induced by spin and orbital currents in ferro-and ferrimagnets*. PhD thesis, ETH Zurich, 2022.

[132] T. Chuang, C. Pai, and S. Huang, "Cr-induced perpendicular magnetic anisotropy and field-free spin-orbit-torque switching," *Physical Review Applied*, vol. 11, no. 6, p. 061005, 2019.

[133] Z. Zheng, Q. Guo, D. Jo, D. Go, L. Wang, H. Chen, W. Yin, X. Wang, G. Yu, W. He, *et al.*, "Magnetization switching driven by current-induced torque from weakly spin-orbit coupled Zr," *Physical Review Research*, vol. 2, no. 1, p. 013127, 2020.

[134] H.-W. Ko, H.-J. Park, G. Go, J. H. Oh, K.-W. Kim, and K.-J. Lee, "Role of orbital hybridization in anisotropic magnetoresistance," *Physical Review B*, vol. 101, no. 18, p. 184413, 2020.

[135] J. Kim, D. Go, H. Tsai, D. Jo, K. Kondou, H.-W. Lee, and Y. Otani, "Nontrivial torque generation by orbital angular momentum injection in ferromagnetic-metal/Cu/Al_2O_3 trilayers," *Physical Review B*, vol. 103, no. 2, p. L020407, 2021.

[136] S. Lee, M.-G. Kang, D. Go, D. Kim, J.-H. Kang, T. Lee, G.-H. Lee, J. Kang, N. J. Lee, Y. Mokrousov, *et al.*, "Efficient conversion of orbital hall current to spin current for spin-orbit torque switching," *Communications Physics*, vol. 4, no. 1, p. 234, 2021.

[137] D. Lee, D. Go, H.-J. Park, W. Jeong, H.-W. Ko, D. Yun, D. Jo, S. Lee, G. Go, J. H. Oh, *et al.*, "Orbital torque in magnetic bilayers," *Nature communications*, vol. 12, no. 1, p. 6710, 2021.

[138] S. Ding, Z. Liang, D. Go, C. Yun, M. Xue, Z. Liu, S. Becker, W. Yang, H. Du, C. Wang, *et al.*, "Observation of the orbital rashba-edelstein magnetoresistance," *Physical review letters*, vol. 128, no. 6, p. 067201, 2022.

[139] Y.-G. Choi, D. Jo, K.-H. Ko, D. Go, K.-H. Kim, H. G. Park, C. Kim, B.-C. Min, G.-M. Choi, and H.-W. Lee, "Observation of the orbital hall effect in a light metal Ti," *Nature*, vol. 619, no. 7968, pp. 52–56, 2023.

[140] A. Aharoni, *Introduction to the Theory of Ferromagnetism*, vol. 109. Clarendon Press, 2000.

[141] S. Zhang, P. Levy, and A. Fert, "Mechanisms of spin-polarized current-driven magnetization switching," *Physical review letters*, vol. 88, no. 23, p. 236601, 2002.

[142] K. Garello, I. M. Miron, C. O. Avci, F. Freimuth, Y. Mokrousov, S. Blügel, S. Auffret, O. Boulle, G. Gaudin, and P. Gambardella, "Symmetry and magnitude of spin–orbit torques in ferromagnetic heterostructures," *Nature nanotechnology*, vol. 8, no. 8, pp. 587–593, 2013.

[143] K. Chen and S. Zhang, "Roles of nonlocal conductivity on spin hall angle measurement," *Physical Review B*, vol. 96, no. 13, p. 134401, 2017.

[144] I. M. Miron, K. Garello, G. Gaudin, P.-J. Zermatten, M. V. Costache, S. Auffret, S. Bandiera, B. Rodmacq, A. Schuhl, and P. Gambardella, "Perpendicular switching of a single ferromagnetic layer induced by in-plane current injection," *Nature*, vol. 476, no. 7359, pp. 189–193, 2011.

[145] Q. Shao, P. Li, L. Liu, H. Yang, S. Fukami, A. Razavi, H. Wu, K. Wang, F. Freimuth, Y. Mokrousov, *et al.*, "Roadmap of spin–orbit torques," *IEEE transactions on magnetics*, vol. 57, no. 7, pp. 1–39, 2021.

[146] Z. Zheng, Y. Zhang, V. Lopez-Dominguez, L. Sánchez-Tejerina, J. Shi, X. Feng, L. Chen, Z. Wang, Z. Zhang, K. Zhang, *et al.*, "Field-free spin-orbit torque-induced switching of perpendicular magnetization in a ferrimagnetic layer with a vertical composition gradient," *Nature communications*, vol. 12, no. 1, p. 4555, 2021.

[147] X. Zhao, S. Zhang, R. Han, Y. Li, J. Li, B. Zhang, F. Luo, Y. Ai, Z. Xie, H. Wang, *et al.*, "Field-free spin–orbit torque switching in a perpendicularly magnetized bilayer with a large interfacial saturation magnetization gradient," *Applied Surface Science*, vol. 688, p. 162388, 2025.

[148] R. Liu, J. Chen, Z. Li, X. Lu, Y. Lu, T. Liu, Y. Zhang, Y. Yuan, L. Wei, D. Wu, *et al.*, "Field-free spin–orbit torque-induced magnetization switching in the Ir Mn/CoTb bilayers with a spontaneous in-plane exchange bias," *ACS Applied Materials & Interfaces*, vol. 15, no. 44, pp. 51971–51978, 2023.

[149] T. M. J. Cham, R. J. Dorrian, X. S. Zhang, A. H. Dismukes, D. G. Chica, A. F. May, X. Roy, D. A. Muller, D. C. Ralph, and Y. K. Luo, "Exchange bias between van der waals materials: Tilted magnetic states and field-free spin–orbit-torque switching," *Advanced Materials*, vol. 36, no. 13, p. 2305739, 2024.

[150] W. He, C. Wan, C. Zheng, Y. Wang, X. Wang, T. Ma, Y. Wang, C. Guo, X. Luo, M. E. Stebliy, *et al.*, "Field-free spin–orbit torque switching enabled by the interlayer dzyaloshinskii–moriya interaction," *Nano Letters*, vol. 22, no. 17, pp. 6857–6865, 2022.

[151] Y.-C. Li, Y.-H. Huang, C.-C. Huang, Y.-T. Liu, and C.-F. Pai, "Field-free switching in symmetry-breaking multilayers: the critical role of interlayer chiral exchange," *Physical Review Applied*, vol. 20, no. 2, p. 024032, 2023.

[152] X. Deng, Y. Zhao, T. Zhu, J. Zhang, H. Huang, P. Dou, Y. Wang, J. Li, H. Bai, X. Zhan, *et al.*, "Controllable generation of interlayer dzyaloshinskii-moriya interactions in the l 10-FePt/Pt/Fe multilayers for field-free magnetization switching," *NPG Asia Materials*, vol. 17, no. 1, p. 21, 2025.

[153] M.-G. Kang, S. Lee, and B.-G. Park, "Field-free spin-orbit torques switching and its applications," *npj Spintronics*, vol. 3, no. 1, p. 8, 2025.

[154] V. Kateel, V. Krizakova, S. Rao, K. Cai, M. Gupta, M. G. Monteiro, F. Yasin, B. Sorée, J. De Boeck, S. Couet, *et al.*, "Field-free spin–orbit torque driven switching of perpendicular magnetic tunnel junction through bending current," *Nano Letters*, vol. 23, no. 12, pp. 5482–5489, 2023.

[155] F. Xue, S.-J. Lin, M. Song, W. Hwang, C. Klewe, C.-M. Lee, E. Turgut, P. Shafer, A. Vailionis, Y.-L. Huang, *et al.*, "Field-free spin-orbit torque switching assisted by in-plane unconventional spin torque in ultrathin [Pt/Co] n," *Nature communications*, vol. 14, no. 1, p. 3932, 2023.

[156] Z. Zhang, Z. Li, Y. Chen, F. Zhu, Y. Yan, Y. Li, L. He, J. Du, R. Zhang, J. Wu, *et al.*, "Field-free spin-orbit torque switching in perpendicularly magnetized Ta/CoFeB/MgO/NiO/Ta with a canted antiferromagnetic insulator NiO interlayer," *Advanced Functional Materials*, vol. 35, no. 5, p. 2414643, 2025.

[157] G. D. Chaves-O'Flynn, G. Wolf, J. Z. Sun, and A. D. Kent, "Thermal stability of magnetic states in circular thin-film nanomagnets with large perpendicular magnetic anisotropy," *Physical Review Applied*, vol. 4, no. 2, p. 024010, 2015.

[158] C. Bi, L. Huang, S. Long, Q. Liu, Z. Yao, L. Li, Z. Huo, L. Pan, and M. Liu, "Thermally assisted magnetic switching of a single perpendicularly magnetized layer induced by an in-plane current," *Applied Physics Letters*, vol. 105, no. 2, 2014.

[159] D. Li, S. Chen, Y. Zuo, J. Yun, B. Cui, K. Wu, X. Guo, D. Yang, J. Wang, and L. Xi, "Roles of joule heating and spin-orbit torques in the direct current induced magnetization reversal," *Scientific Reports*, vol. 8, no. 1, p. 12959, 2018.

[160] V. Krizakova, E. Grimaldi, K. Garello, G. Sala, S. Couet, G. S. Kar, and P. Gambardella, "Interplay of voltage control of magnetic anisotropy, spin-transfer torque, and heat in the spin-orbit-torque switching of three-terminal magnetic tunnel junctions," *Physical Review Applied*, vol. 15, no. 5, p. 054055, 2021.

[161] K. Garello, C. O. Avci, I. M. Miron, M. Baumgartner, A. Ghosh, S. Auffret, O. Boulle, G. Gaudin, and P. Gambardella, "Ultrafast magnetization switching by spin-orbit torques," *Applied Physics Letters*, vol. 105, no. 21, 2014.

[162] I. Dzyaloshinsky, "A thermodynamic theory of "weak" ferromagnetism of antiferromagnetics," *Journal of Physics and Chemistry of Solids*, vol. 4, pp. 241–255, 1 1958.

[163] T. Moriya, "Anisotropic superexchange interaction and weak ferromagnetism," *Physical Review*, vol. 120, pp. 91–98, 1960.

[164] T. Moriya, "New mechanism of anisotropic superexchange interaction," *Physical Review Letters*, vol. 4, pp. 228–230, 1960.

[165] R. E. Camley and K. L. Livesey, "Consequences of the dzyaloshinskii-moriya interaction," *Surface Science Reports*, vol. 78, p. 100605, 2023.

[166] D. A. Smith, "New mechanisms for magnetic anisotropy in localised s-state moment materials," *Journal of Magnetism and Magnetic Materials*, vol. 1, pp. 214–225, 1976.

[167] A. Fert and P. M. Levy, "Role of anisotropic exchange interactions in determining the propertiesof spin-glasses," *Physical Review letters*, vol. 44, pp. 1538–1541, 1980.

[168] A. Fert, "Magnetic and transport properties of metallic multilayers," *Materials Science Forum*, vol. 59-60, pp. 439–480, 1991.

[169] R. E. Camley and K. L. Livesey, "Consequences of the dzyaloshinskii-moriya interaction," *Surface Science Reports*, vol. 78, p. 100605, 8 2023.

[170] A. Thiaville, S. Rohart, É. Jué, V. Cros, and A. Fert, "Dynamics of dzyaloshinskii domain walls in ultrathin magnetic films," *Europhysics Letters*, vol. 100, no. 5, p. 57002, 2012.

[171] Y.-C. Lau, D. Betto, K. Rode, J. Coey, and P. Stamenov, "Spin–orbit torque switching without an external field using interlayer exchange coupling," *Nature nanotechnology*, vol. 11, no. 9, pp. 758–762, 2016.

[172] E. Y. Vedmedenko, P. Riego, J. A. Arregi, and A. Berger, "Interlayer dzyaloshinskii-moriya interactions," *Physical review letters*, vol. 122, no. 25, p. 257202, 2019.

[173] A. Fernández-Pacheco, E. Vedmedenko, F. Ummelen, R. Mansell, D. Petit, and R. P. Cowburn, "Symmetry-breaking interlayer dzyaloshinskii–moriya interactions in synthetic antiferromagnets," *Nature materials*, vol. 18, no. 7, pp. 679–684, 2019.

[174] D.-S. Han, K. Lee, J.-P. Hanke, Y. Mokrousov, K.-W. Kim, W. Yoo, Y. L. Van Hees, T.-W. Kim, R. Lavrijsen, C.-Y. You, *et al.*, "Long-range chiral exchange interaction in synthetic antiferromagnets," *Nature materials*, vol. 18, no. 7, pp. 703–708, 2019.

[175] Y.-H. Huang, C.-C. Huang, W.-B. Liao, T.-Y. Chen, and C.-F. Pai, "Growth-dependent interlayer chiral exchange and field-free switching," *Physical Review Applied*, vol. 18, no. 3, p. 034046, 2022.

[176] C. O. Avci, C.-H. Lambert, G. Sala, and P. Gambardella, "Chiral coupling between magnetic layers with orthogonal magnetization," *Physical review letters*, vol. 127, no. 16, p. 167202, 2021.

[177] S. D. Pollard, J. A. Garlow, K.-W. Kim, S. Cheng, K. Cai, Y. Zhu, and H. Yang, "Bloch chirality induced by an interlayer dzyaloshinskii-moriya interaction in ferromagnetic multilayers," *Physical review letters*, vol. 125, no. 22, p. 227203, 2020.

[178] S. Liang, R. Chen, Q. Cui, Y. Zhou, F. Pan, H. Yang, and C. Song, "Ruderman–kittel–kasuya–yosida-type interlayer dzyaloshinskii–moriya interaction in synthetic magnets," *Nano Letters*, vol. 23, no. 18, pp. 8690–8696, 2023.

[179] J. A. Arregi, P. Riego, A. Berger, and E. Y. Vedmedenko, "Large interlayer dzyaloshinskii-moriya interactions across Ag -layers," *Nature Communications*, vol. 14, no. 1, p. 6927, 2023.

[180] E. Demiroglu, K. Hancioglu, I. Yavuz, C. O. Avci, and C. Deger, "Oscillatory behavior of interlayer dzyaloshinskii-moriya interaction by spacer thickness variation," *Physical Review B*, vol. 109, no. 14, p. 144422, 2024.

[181] A. Fert, V. Cros, and J. Sampaio, "Skyrmions on the track," *Nature Nanotechnology*, vol. 8, pp. 152–156, 3 2013.

[182] U. K. Roessler, A. Bogdanov, and C. Pfleiderer, "Spontaneous skyrmion ground states in magnetic metals," *Nature*, vol. 442, no. 7104, pp. 797–801, 2006.

[183] S. Mühlbauer, B. Binz, F. Jonietz, C. Pfleiderer, A. Rosch, A. Neubauer, R. Georgii, and P. Böni, "Skyrmion lattice in a chiral magnet," *Science*, vol. 323, no. 5916, pp. 915–919, 2009.

[184] O. Boulle, J. Vogel, H. Yang, S. Pizzini, D. de Souza Chaves, A. Locatelli, T. O. Menteş, A. Sala, L. D. Buda-Prejbeanu, O. Klein, *et al.*, "Room-temperature chiral magnetic skyrmions in ultrathin magnetic nanostructures," *Nature nanotechnology*, vol. 11, no. 5, pp. 449–454, 2016.

[185] V. T. Pham, N. Sisodia, I. Di Manici, J. Urrestarazu-Larrañaga, K. Bairagi, J. Pelloux-Prayer, R. Guedas, L. D. Buda-Prejbeanu, S. Auffret, A. Locatelli, *et al.*, "Fast current-induced skyrmion motion in synthetic antiferromagnets," *Science*, vol. 384, no. 6693, pp. 307–312, 2024.

[186] W. Kang, Y. Huang, X. Zhang, Y. Zhou, and W. Zhao, "Skyrmion-electronics: An overview and outlook," *Proceedings of the IEEE*, vol. 104, no. 10, pp. 2040–2061, 2016.

[187] E. Martinez, "The stochastic nature of the domain wall motion along high perpendicular anisotropy strips with surface roughness," *Journal of Physics: Condensed Matter*, vol. 24, no. 2, p. 024206, 2011.

[188] S.-W. Jung, W. Kim, T.-D. Lee, K.-J. Lee, and H.-W. Lee, "Current-induced domain wall motion in a nanowire with perpendicular magnetic anisotropy," *Applied Physics Letters*, vol. 92, no. 20, 2008.

[189] N. L. Schryer and L. R. Walker, "The motion of 180 domain walls in uniform dc magnetic fields," *Journal of Applied Physics*, vol. 45, no. 12, pp. 5406–5421, 1974.

[190] P. J. Metaxas, J. P. Jamet, A. Mougin, M. Cormier, J. Ferré, V. Baltz, B. Rodmacq, B. Dieny, and R. Stamps, "Creep and flow regimes of magnetic domain-wall motion in ultrathin Pt/Co/Pt films with perpendicular anisotropy," *Physical review letters*, vol. 99, no. 21, p. 217208, 2007.

[191] G. S. Beach, C. Nistor, C. Knutson, M. Tsoi, and J. L. Erskine, "Dynamics of field-driven domain-wall propagation in ferromagnetic nanowires," *Nature materials*, vol. 4, no. 10, pp. 741–744, 2005.

[192] P. J. Metaxas, "Creep and flow dynamics of magnetic domain walls: weak disorder, wall binding, and periodic pinning," in *Solid State Physics*, vol. 62, pp. 75–162, Elsevier, 2010.

[193] T. H. Pham, J. Vogel, J. Sampaio, M. Vaňatka, J.-C. Rojas-Sánchez, M. Bonfim, D. Chaves, F. Choueikani, P. Ohresser, E. Otero, *et al.*, "Very large domain wall velocities in Pt/Co/Gd Ox and Pt/Co/Gd trilayers with dzyaloshinskii-moriya interaction," *Europhysics Letters*, vol. 113, no. 6, p. 67001, 2016.

[194] V. Krizakova, J. P. Garcia, J. Vogel, N. Rougemaille, D. d. S. Chaves, S. Pizzini, and A. Thiaville, "Study of the velocity plateau of dzyaloshinskii domain walls," *Physical Review B*, vol. 100, no. 21, p. 214404, 2019.

[195] X. Waintal and M. Viret, "Current-induced distortion of a magnetic domain wall," *Europhysics Letters*, vol. 65, no. 3, p. 427, 2004.

[196] G. Tatara and H. Kohno, "Theory of current-driven domain wall motion: Spin transfer versus momentum transfer," *Physical review letters*, vol. 92, no. 8, p. 086601, 2004.

[197] S. Zhang and Z. Li, "Roles of nonequilibrium conduction electrons on the magnetization dynamics of ferromagnets," *Physical review letters*, vol. 93, no. 12, p. 127204, 2004.

[198] K. Ueda, T. Koyama, R. Hiramatsu, D. Chiba, S. Fukami, H. Tanigawa, T. Suzuki, N. Ohshima, N. Ishiwata, Y. Nakatani, *et al.*, "Temperature dependence of carrier spin polarization determined from current-induced domain wall motion in a Co/Ni nanowire," *Applied Physics Letters*, vol. 100, no. 20, 2012.

[199] A. Thiaville, Y. Nakatani, J. Miltat, and Y. Suzuki, "Micromagnetic understanding of current-driven domain wall motion in patterned nanowires," *Europhysics Letters*, vol. 69, no. 6, p. 990, 2005.

[200] K.-S. Ryu, L. Thomas, S.-H. Yang, and S. Parkin, "Chiral spin torque at magnetic domain walls," *Nature nanotechnology*, vol. 8, no. 7, pp. 527–533, 2013.

[201] K.-S. Ryu, S.-H. Yang, L. Thomas, and S. S. Parkin, "Chiral spin torque arising from proximity-induced magnetization," *Nature communications*, vol. 5, no. 1, p. 3910, 2014.

[202] T. Koyama, D. Chiba, K. Ueda, K. Kondou, H. Tanigawa, S. Fukami, T. Suzuki, N. Ohshima, N. Ishiwata, Y. Nakatani, *et al.*, "Observation of the intrinsic pinning of a magnetic domain wall in a ferromagnetic nanowire," *Nature materials*, vol. 10, no. 3, pp. 194–197, 2011.

[203] T. Koyama, K. Ueda, K.-J. Kim, Y. Yoshimura, D. Chiba, K. Yamada, J.-P. Jamet, A. Mougin, A. Thiaville, S. Mizukami, *et al.*, "Current-induced magnetic domain wall motion below intrinsic threshold triggered by walker breakdown," *Nature nanotechnology*, vol. 7, no. 10, pp. 635–639, 2012.

[204] S. Ghosh, T. Komori, A. Hallal, J. Peña Garcia, T. Gushi, T. Hirose, H. Mitarai, H. Okuno, J. Vogel, M. Chshiev, *et al.*, "Current-driven domain wall dynamics in ferrimagnetic nickel-doped mn4n films: very large domain wall velocities and reversal of motion direction across the magnetic compensation point," *Nano Letters*, vol. 21, no. 6, pp. 2580–2587, 2021.

[205] T. Gushi, M. Jovičević Klug, J. Peña Garcia, S. Ghosh, J.-P. Attané, H. Okuno, O. Fruchart, J. Vogel, T. Suemasu, S. Pizzini, *et al.*, "Large current driven domain wall mobility and gate tuning of coercivity in ferrimagnetic mn4n thin films," *Nano Letters*, vol. 19, no. 12, pp. 8716–8723, 2019.

[206] S. Emori, U. Bauer, S.-M. Ahn, E. Martinez, and G. S. Beach, "Current-driven dynamics of chiral ferromagnetic domain walls," *Nature materials*, vol. 12, no. 7, pp. 611–616, 2013.

[207] A. Khvalkovskiy, V. Cros, D. Apalkov, V. Nikitin, M. Krounbi, K. Zvezdin, A. Anane, J. Grollier, and A. Fert, "Matching domain-wall configuration and spin-orbit torques for efficient domain-wall motion," *Physical Review B—Condensed Matter and Materials Physics*, vol. 87, no. 2, p. 020402, 2013.

[208] M. Kuepferling, A. Casiraghi, G. Soares, G. Durin, F. Garcia-Sanchez, L. Chen, C. H. Back, C. H. Marrows, S. Tacchi, and G. Carlotti, "Measuring interfacial dzyaloshinskii-moriya interaction in ultrathin magnetic films," *Reviews of Modern Physics*, vol. 95, no. 1, p. 015003, 2023.

[209] R. Soucaille, M. Belmeguenai, J. Torrejon, J.-V. Kim, T. Devolder, Y. Roussigné, S.-M. Chérif, A. Stashkevich, M. Hayashi, and J.-P. Adam, "Probing the dzyaloshinskii-moriya interaction in CoFeB ultrathin films using domain wall creep and brillouin light spectroscopy," *Physical Review B*, vol. 94, no. 10, p. 104431, 2016.

[210] D.-Y. Kim, N.-H. Kim, Y.-K. Park, M.-H. Park, J.-S. Kim, Y.-S. Nam, J. Jung, J. Cho, D.-H. Kim, J.-S. Kim, *et al.*, "Quantitative accordance of dzyaloshinskii-moriya interaction between domain-wall and spin-wave dynamics," *Physical Review B*, vol. 100, no. 22, p. 224419, 2019.

[211] H. Forestier and G. Guiot-Guillain, "A new series of ferromagnetic bodies: the ferrites of rare earths," *Compt. rend.*, vol. Vol: 230, 05 1950.

[212] S. Geller and M. Gilleo, "Structure and ferrimagnetism of yttrium and rare-earth–iron garnets," *Acta Crystallographica*, vol. 10, no. 3, pp. 239–239, 1957.

[213] A. H. Eschenfelder, *Magnetic bubble technology*, vol. 14. Springer Science & Business Media, 1980.

[214] A. Serga, A. Chumak, and B. Hillebrands, "YIG magnonics," *Journal of Physics D: Applied Physics*, vol. 43, no. 26, p. 264002, 2010.

[215] A. V. Chumak, V. I. Vasyuchka, A. A. Serga, and B. Hillebrands, "Magnon spintronics," *Nature physics*, vol. 11, no. 6, pp. 453–461, 2015.

[216] L. Cornelissen, J. Liu, R. Duine, J. B. Youssef, and B. Van Wees, "Long-distance transport of magnon spin information in a magnetic insulator at room temperature," *Nature Physics*, vol. 11, no. 12, pp. 1022–1026, 2015.

[217] Ü. Özgür, Y. Alivov, and H. Morkoç, "Microwave ferrites, part 1: fundamental properties," *Journal of materials science: Materials in electronics*, vol. 20, no. 9, pp. 789–834, 2009.

[218] J. Bauer, E. Rosenberg, and C. Ross, "Perpendicular magnetic anisotropy and spin mixing conductance in polycrystalline europium iron garnet thin films," *Applied Physics Letters*, vol. 114, no. 5, 2019.

[219] M. Kubota, A. Tsukazaki, F. Kagawa, K. Shibuya, Y. Tokunaga, M. Kawasaki, and Y. Tokura, "Stress-induced perpendicular magnetization in epitaxial iron garnet thin films," *Applied Physics Express*, vol. 5, no. 10, p. 103002, 2012.

[220] E. R. Rosenberg, L. Beran, C. O. Avci, C. Zeledon, B. Song, C. Gonzalez-Fuentes, J. Mendil, P. Gambardella, M. Veis, C. Garcia, *et al.*, "Magnetism and spin transport in rare-earth-rich epitaxial terbium and europium iron garnet films," *Physical Review Materials*, vol. 2, no. 9, p. 094405, 2018.

[221] G. F. Dionne, *Magnetic oxides*, vol. 14. Springer, 2009.

[222] L. Néel, "Antiferromagnetism and ferrimagnetism," *Proceedings of the Physical Society. Section A*, vol. 65, p. 869, nov 1952.

[223] E. E. Anderson, "Molecular field model and the magnetization of YIG," *Phys. Rev.*, vol. 134, pp. A1581–A1585, Jun 1964.

[224] J. Finley and L. Liu, "Spintronics with compensated ferrimagnets," *Applied Physics Letters*, vol. 116, no. 11, 2020.

[225] C. Stanciu, A. Kimel, F. Hansteen, A. Tsukamoto, A. Itoh, A. Kirilyuk, and T. Rasing, "Ultrafast spin dynamics across compensation points in ferrimagnetic GdFeCo: The role of angular momentum compensation," *Physical Review B—Condensed Matter and Materials Physics*, vol. 73, no. 22, p. 220402, 2006.

[226] K.-J. Kim, S. K. Kim, Y. Hirata, S.-H. Oh, T. Tono, D.-H. Kim, T. Okuno, W. S. Ham, S. Kim, G. Go, *et al.*, "Fast domain wall motion in the vicinity of the angular momentum compensation temperature of ferrimagnets," *Nature materials*, vol. 16, no. 12, pp. 1187–1192, 2017.

[227] J. Fu, M. Hua, X. Wen, M. Xue, S. Ding, M. Wang, P. Yu, S. Liu, J. Han, C. Wang, *et al.*, "Epitaxial growth of $Y_3Fe_5O_{12}$ thin films with perpendicular magnetic anisotropy," *Applied Physics Letters*, vol. 110, no. 20, 2017.

[228] S. M. Zanjani and M. C. Onbaşlı, "Predicting new iron garnet thin films with perpendicular magnetic anisotropy," *Journal of Magnetism and Magnetic Materials*, vol. 499, p. 166108, 2020.

[229] Y. Sun, Y.-Y. Song, H. Chang, M. Kabatek, M. Jantz, W. Schneider, M. Wu, H. Schultheiss, and A. Hoffmann, "Growth and ferromagnetic resonance properties of nanometer-thick yttrium iron garnet films," *Applied Physics Letters*, vol. 101, no. 15, 2012.

[230] M. Onbasli, A. Kehlberger, D. H. Kim, G. Jakob, M. Kläui, A. V. Chumak, B. Hillebrands, and C. A. Ross, "Pulsed laser deposition of epitaxial yttrium iron garnet films with low gilbert damping and bulk-like magnetization," *Apl Materials*, vol. 2, no. 10, 2014.

[231] T. Liu, H. Chang, V. Vlaminck, Y. Sun, M. Kabatek, A. Hoffmann, L. Deng, and M. Wu, "Ferromagnetic resonance of sputtered yttrium iron garnet nanometer films," *Journal of Applied Physics*, vol. 115, no. 17, 2014.

[232] C. Wu, C. Tseng, K. Lin, C. Cheng, S. Yeh, Y. Fanchiang, M. Hong, and J. Kwo, "High-quality single-crystal thulium iron garnet films with perpendicular magnetic anisotropy by off-axis sputtering," *AIP Advances*, vol. 8, no. 5, 2018.

[233] N. Kumar, N. Kim, Y. Park, N. Hur, J. Jung, K. Han, and K. Yee, "Epitaxial growth of terbium iron garnet thin films with out-of-plane axis of magnetization," *Thin Solid Films*, vol. 516, no. 21, pp. 7753–7757, 2008.

[234] V. H. Ortiz, M. Aldosary, J. Li, Y. Xu, M. I. Lohmann, P. Sellappan, Y. Kodera, J. E. Garay, and J. Shi, "Systematic control of strain-induced perpendicular magnetic anisotropy in epitaxial europium and terbium iron garnet thin films," *APL Materials*, vol. 6, no. 12, 2018.

[235] Y. Liu, H. Wong, K. Lam, K. Chan, C. Mak, and C. Leung, "Anomalous hall effect in $Pt/Tb_3Fe_5O_{12}$ heterostructure: Effect of compensation point," *Journal of Magnetism and Magnetic Materials*, vol. 468, pp. 235–240, 2018.

[236] Y. Li, X. Yang, H. Bai, M. Wang, D. Cheng, C. Song, Z. Yuan, Y. Liu, and Z. Shi, "Strain-tunable magnetic compensation temperature of epitaxial $Tb_3Fe_5O_{12}$ thin films," *Physical Review B*, vol. 108, no. 18, p. 184403, 2023.

[237] S. Damerio and C. O. Avci, "Sputtered terbium iron garnet films with perpendicular magnetic anisotropy for spintronic applications," *Journal of Applied Physics*, vol. 133, no. 7, 2023.

[238] S. Iida, "Magnetostriction constants of rare earth iron garnets," *Journal of the Physical Society of Japan*, vol. 22, no. 5, pp. 1201–1209, 1967.

[239] C.-F. Pai, L. Liu, Y. Li, H. Tseng, D. Ralph, and R. Buhrman, "Spin transfer torque devices utilizing the giant spin hall effect of tungsten," *Applied Physics Letters*, vol. 101, no. 12, 2012.

[240] D. Choi, "Phase transformation in thin tungsten films during sputter deposition," *Microelectronic Engineering*, vol. 183, pp. 19–22, 2017.

[241] K. Korotkova, D. Bainov, S. Smirnov, I. Yunusov, and Y. Zhidik, "Electrical conductivity and optical properties of nanoscale titanium films on sapphire for localized plasmon resonance-based sensors," *Coatings*, vol. 10, no. 12, p. 1165, 2020.

[242] M. Faraday, "I. experimental researches in electricity.—nineteenth series," *Philosophical Transactions of the Royal Society of London*, vol. 136, pp. 1–20, 12 1846.

[243] J. Kerr, "Xliii. on rotation of the plane of polarization by reflection from the pole of a magnet," *The London, Edinburgh, and Dublin Philosophical Magazine and Journal of Science*, vol. 3, pp. 321–343, 5 1877.

[244] J. Kerr, "Xxiv. on reflection of polarized light from the equatorial surface of a magnet," *The London, Edinburgh, and Dublin Philosophical Magazine and Journal of Science*, vol. 5, pp. 161–177, 3 1878.

[245] Z. Q. Qiu and S. D. Bader, "Surface magneto-optic kerr effect," 3 2000.

[246] T. Haider, "A review of magneto-optic effects and its application," *International Journal of Electromagnetics and Applications*, vol. 7, pp. 17–24, 2017.

[247] A. Kimel, A. Zvezdin, S. Sharma, S. Shallcross, N. De Sousa, A. García-Martín, G. Salvan, J. Hamrle, O. Stejskal, J. McCord, *et al.*, "The 2022 magneto-optics roadmap," *Journal of Physics D: Applied Physics*, vol. 55, no. 46, p. 463003, 2022.

[248] C. Rizal, H. Shimizu, and J. R. Mejía-Salazar, "Magneto-optics effects: new trends and future prospects for technological developments," *magnetochemistry*, vol. 8, no. 9, p. 94, 2022.

[249] Z. Q. Qiu and S. D. Bader, "Surface magneto-optic kerr effect (smoke)," *Journal of Magnetism and Magnetic Materials*, vol. 200, pp. 664–678, 10 1999.

[250] P. N. Argyres, "Theory of the faraday and kerr effects in ferromagnetics," *Physical Review*, vol. 97, pp. 334–345, 1 1955.

[251] P. S. Pershan, "Magneto-optical effects," *Journal of Applied Physics*, vol. 38, pp. 1482–1490, 1967.

[252] J. Zak, E. Moog, C. Liu, and S. Bader, "Universal approach to magneto-optics," *Journal of Magnetism and Magnetic Materials*, vol. 89, pp. 107–123, 9 1990.

[253] U. Tiwari, R. Ghosh, and P. Sen, "Theory of magneto-optic kerr effects," *Physical Review B*, vol. 49, pp. 2159–2162, 1 1994.

[254] W. Kuch, R. Schäfer, P. Fischer, and F. U. Hillebrecht, *Magnetic Microscopy of Layered Structures*, vol. 57. Springer Berlin Heidelberg, 2015.

[255] E. Collett, "Jones calculus," in *Field guide to polarization*, Spie Bellingham, 2005.

[256] W. Voigt, *Magneto-und elektrooptik*. No. 3, BG Teubner, 1908.

[257] W. Wettling, "Magneto-optics of ferrites," *Journal of Magnetism and Magnetic Materials*, vol. 3, pp. 147–160, 3 1976.

[258] H. R. Hulme, "The faraday effect in ferromagnetics," *Proceedings of the Royal Society of London. Series A, Containing Papers of a Mathematical and Physical Character*, vol. 135, pp. 237–257, 2 1932.

[259] J. Hamrle, "Magneto-optical kerr effect (moke)," 2014.

[260] H. Kronmuller and S. S. P. Parkin, *Handbook of magnetism and advanced magnetic materials. Vol. 2, Micromagnetism*. John Wiley & Sons, 2007.

[261] R. Schäfer, "Investigation of domains and dynamics of domain walls by the magneto-optical kerr-effect," *Handbook of magnetism and advanced magnetic materials*, 2007.

[262] D. Neff, A. Hoemke, A. R. Attig, and H. C. Mireles, "Developing a kerr microscope for upper-division solid-state physics laboratories," *American Journal of Physics*, vol. 82, pp. 574–582, 6 2014.

[263] C. Ballentine, R. Fink, J. Araya-Pochet, and J. Erskine, "Exploring magnetic properties of ultrathin epitaxial magnetic structures using magneto-optical techniques," *Applied Physics A*, vol. 49, no. 5, pp. 459–466, 1989.

[264] E. D. Salmon and J. C. Canman, "Proper alignment and adjustment of the light microscope," *Current Protocols in Cell Biology*, vol. 00, 10 1998.

[265] M. W. Davidson and T. J. Fellers, "Understanding conjugate planes and köhler illumination,"

[266] J. Waters, "Microscope alignment for optimal image quality: Köhler illumination," 2019.

[267] G. Holst, "scmos — die eierlegende wollmilchsau der bildsensorik?," *Optik & Photonik*, vol. 4, pp. 37–39, 10 2009.

[268] R. Grunsby, "Scientific cmos (scmos) technology: An overview," 2012.

[269] F. Huang, T. M. P. Hartwich, F. E. Rivera-Molina, Y. Lin, W. C. Duim, J. J. Long, P. D. Uchil, J. R. Myers, M. A. Baird, W. Mothes, M. W. Davidson, D. Toomre, and J. Bewersdorf, "Video-rate nanoscopy using scmos camera–specific single-molecule localization algorithms," *Nature Methods*, vol. 10, pp. 653–658, 7 2013.

[270] "Orca-flash4.0 v3 digital cmos camera c13440-20cu technical note," 2018.

[271] "Scientific cmos (scmos) image sensor."

[272] K. W. Busch and M. A. Busch, *Light Polarization and Signal Processing in Chiroptical Instrumentation*, pp. 73–151. Elsevier, 5 2018.

[273] K. Fukushima, D. E. Kharzeev, and H. J. Warringa, "Chiral magnetic effect," *Physical Review D*, vol. 78, p. 074033, Oct 2008.

[274] R. Naaman and D. H. Waldeck, "Chiral-induced spin selectivity effect," *The Journal of Physical Chemistry Letters*, vol. 3, no. 16, pp. 2178–2187, 2012. PMID: 26295768.

[275] E. Jué, C. Safeer, M. Drouard, A. Lopez, P. Balint, L. Buda-Prejbeanu, O. Boulle, S. Auffret, A. Schuhl, A. Manchon, *et al.*, "Chiral damping of magnetic domain walls," *Nature materials*, vol. 15, no. 3, pp. 272–277, 2016.

[276] S.-H. Yang, R. Naaman, Y. Paltiel, and S. S. P. Parkin, "Chiral spintronics," *Nature Reviews Physics*, vol. 3, pp. 328–343, 4 2021.

[277] S.-W. Cheong and X. Xu, "Magnetic chirality," *npj Quantum Materials*, vol. 7, no. 1, p. 40, 2022.

[278] J. P. Tetienne, T. Hingant, L. J. Martínez, S. Rohart, A. Thiaville, L. H. Diez, K. Garcia, J. P. Adam, J. V. Kim, J. F. Roch, I. M. Miron, G. Gaudin, L. Vila, B. Ocker, D. Ravelosona, and V. Jacques, "The nature of domain walls in ultrathin ferromagnets revealed by scanning nanomagnetometry," *Nature Communications*, vol. 6, p. 6733, 4 2015.

[279] P. Sutcliffe, "Hopfions in chiral magnets," *Journal of Physics A: Mathematical and Theoretical*, vol. 51, p. 375401, aug 2018.

[280] N. Kent, N. Reynolds, D. Raftrey, I. T. Campbell, S. Virasawmy, S. Dhuey, R. V. Chopdekar, A. Hierro-Rodriguez, A. Sorrentino, E. Pereiro, *et al.*, "Creation and observation of hopfions in magnetic multilayer systems," *Nature communications*, vol. 12, no. 1, p. 1562, 2021.

[281] M. Baumgartner, K. Garello, J. Mendil, C. O. Avci, E. Grimaldi, C. Murer, J. Feng, M. Gabureac, C. Stamm, Y. Acremann, *et al.*, "Spatially and time-resolved magnetization dynamics driven by spin–orbit torques," *Nature nanotechnology*, vol. 12, no. 10, pp. 980–986, 2017.

[282] J. Ryu, C. O. Avci, M. Song, M. Huang, R. Thompson, J. Yang, S. Ko, S. Karube, N. Tezuka, M. Kohda, K.-J. Kim, G. S. D. Beach, and J. Nitta, "Deterministic current-induced perpendicular switching in epitaxial Co/Pt layers without an external field," *Advanced Functional Materials*, vol. 33, no. 35, p. 2209693, 2023.

[283] S. Woo, K. Litzius, B. Krüger, M.-Y. Im, L. Caretta, K. Richter, M. Mann, A. Krone, R. M. Reeve, M. Weigand, *et al.*, "Observation of room-temperature magnetic skyrmions and their current-driven dynamics in ultrathin metallic ferromagnets," *Nature materials*, vol. 15, no. 5, pp. 501–506, 2016.

[284] Y. Yang, T. Liu, L. Bi, and L. Deng, "Recent advances in development of magnetic garnet thin films for applications in spintronics and photonics," *Journal of Alloys and Compounds*, vol. 860, p. 158235, 4 2021.

[285] T. Fakhrul, S. Huang, Y. Song, B. Khurana, G. S. Beach, and C. A. Ross, "Influence of substrate on interfacial dzyaloshinskii-moriya interaction in epitaxial $Tm_3Fe_5O_{12}$ films," *Physical Review B*, vol. 107, p. 054421, 2 2023.

[286] Z. Ren, K. Qian, M. Aldosary, Y. Liu, S. K. Cheung, I. Ng, J. Shi, and Q. Shao, "Strongly heat-assisted spin-orbit torque switching of a ferrimagnetic insulator," *APL Materials*, vol. 9, p. 051117, 5 2021.

[287] J. M. Liang, X. W. Zhao, Y. K. Liu, P. G. Li, S. M. Ng, H. F. Wong, W. F. Cheng, Y. Zhou, J. Y. Dai, C. L. Mak, and C. W. Leung, "The thickness effect on the compensation temperature of rare-earth garnet thin films," *Applied Physics Letters*, vol. 122, p. 242401, 6 2023.

[288] T. Li, W. Luo, J. Wu, X. Li, H. Yang, X. Zhao, and H. An, "Field-free magnetization switching with full scale in $Pt/Tm_3Fe_5O_{12}$ bilayer on vicinal substrate," *Applied Physics Express*, vol. 17, p. 033003, 3 2024.

[289] K.-S. Lee, S.-W. Lee, B.-C. Min, and K.-J. Lee, "Threshold current for switching of a perpendicular magnetic layer induced by spin hall effect," *Applied Physics Letters*, vol. 102, no. 11, 2013.

[290] J. Slonczewski, A. Malozemoff, and E. Giess, "Temperature dependence of exchange stiffness in garnet bubble films," *Applied Physics Letters*, vol. 24, no. 8, pp. 396–397, 1974.

[291] R. Wolfe, A. P. Malozemoff, and J. C. Slonczewski, *Magnetic Domain Walls in Bubble Materials*. Elsevier, 1979.

[292] A. W. J. Wells, P. M. Shepley, C. H. Marrows, and T. A. Moore, "Effect of interfacial intermixing on the dzyaloshinskii-moriya interaction in Pt/Co/Pt," *Physical Review B*, vol. 95, p. 054428, Feb 2017.

[293] A. Hrabec, N. A. Porter, A. Wells, M. J. Benitez, G. Burnell, S. McVitie, D. McGrouther, T. A. Moore, and C. H. Marrows, "Measuring and tailoring the dzyaloshinskii-moriya interaction in perpendicularly magnetized thin films," *Physical Review B - Condensed Matter and Materials Physics*, vol. 90, p. 020402, 7 2014.

[294] S. Emori, E. Martinez, K.-J. Lee, H.-W. Lee, U. Bauer, S.-M. Ahn, P. Agrawal, D. C. Bono, and G. S. Beach, "Spin hall torque magnetometry of dzyaloshinskii domain walls," *Physical Review B*, vol. 90, no. 18, p. 184427, 2014.

[295] Y.-K. Park, D.-Y. Kim, J.-S. Kim, Y.-S. Nam, M.-H. Park, H.-C. Choi, B.-C. Min, and S.-B. Choe, "Experimental observation of the correlation between the interfacial dzyaloshinskii–moriya interaction and work function in metallic magnetic trilayers," *NPG Asia Materials*, vol. 10, no. 10, pp. 995–1001, 2018.

[296] F. Ajejas, Y. Sassi, W. Legrand, S. Collin, J. Peña Garcia, A. Thiaville, S. Pizzini, N. Reyren, V. Cros, and A. Fert, "Interfacial potential gradient modulates dzyaloshinskii-moriya interaction in Pt/Co/metal multilayers," *Physical Review Materials*, vol. 6, no. 7, p. L071401, 2022.

[297] X. Ma, G. Yu, S. A. Razavi, L. Chang, L. Deng, Z. Chu, C. He, K. L. Wang, and X. Li, "Correlation between the dzyaloshinskii-moriya interaction and spin-mixing conductance at an antiferromagnet/ferromagnet interface," *Physical Review B*, vol. 98, p. 104428, 9 2018.

[298] X. Ma, G. Yu, C. Tang, X. Li, C. He, J. Shi, K. L. Wang, and X. Li, "Interfacial dzyaloshinskii-moriya interaction: Effect of 5d band filling and correlation with spin mixing conductance," *Physical Review Letters*, vol. 120, p. 157204, 4 2018.

[299] Q. Shao, A. Grutter, Y. Liu, G. Yu, C.-Y. Yang, D. A. Gilbert, E. Arenholz, P. Shafer, X. Che, C. Tang, *et al.*, "Exploring interfacial exchange coupling and sublattice effect in heavy metal/ferrimagnetic insulator heterostructures using hall measurements, x-ray magnetic circular dichroism, and neutron reflectometry," *Physical Review B*, vol. 99, no. 10, p. 104401, 2019.

[300] G. Kresse and J. Hafner, "Ab initio molecular dynamics for liquid metals," *Physical Review B*, vol. 47, pp. 558–561, 1 1993.

[301] G. Kresse and J. Furthmüller, "Efficient iterative schemes for ab initio total-energy calculations using a plane-wave basis set," *Physical Review B*, vol. 54, pp. 11169–11186, 10 1996.

[302] H. J. Xiang, E. J. Kan, S.-H. Wei, M.-H. Whangbo, and X. G. Gong, "Predicting the spin-lattice order of frustrated systems from first principles," *Physical Review B*, vol. 84, p. 224429, 12 2011.

[303] C. Deger, "Strain-enhanced dzyaloshinskii–moriya interaction at Co/Pt interfaces," *Scientific Reports*, vol. 10, p. 12314, 7 2020.

[304] J. P. Perdew, K. Burke, and M. Ernzerhof, "Generalized gradient approximation made simple," *Physical Review Letters*, vol. 77, pp. 3865–3868, 10 1996.

[305] G. Kresse and D. Joubert, "From ultrasoft pseudopotentials to the projector augmented-wave method," *Physical Review B*, vol. 59, pp. 1758–1775, 1 1999.

[306] V. Wang, N. Xu, J.-C. Liu, G. Tang, and W.-T. Geng, "Vaspkit: A user-friendly interface facilitating high-throughput computing and analysis using vasp code," *Computer Physics Communications*, vol. 267, p. 108033, 10 2021.

[307] H. Yang, A. Thiaville, S. Rohart, A. Fert, and M. Chshiev, "Anatomy of dzyaloshinskii-moriya interaction at Co/Pt interfaces," *Physical review letters*, vol. 115, no. 26, p. 267210, 2015.

[308] P. Jadaun, L. F. Register, and S. K. Banerjee, "The microscopic origin of dmi in magnetic bilayers and prediction of giant dmi in new bilayers," *npj Computational Materials*, vol. 6, p. 88, 7 2020.

[309] Z. Ye, Z. Chen, Z. Chen, W. Jia, T. Gao, L. Liu, H. Zheng, Q. Zeng, Q. Wang, N. Wang, B. Xiang, T. Lin, M. Qiu, S. Li, J. Shi, Z. Hou, K. Ando, and H. An, "Spin-orbit torque and interfacial dzyaloshinskii–moriya interaction in heavy metal/ferrimagnetic insulator deposited by magnetron sputtering," *Advanced Electronic Materials*, vol. 8, p. 2100590, 1 2022.

[310] T. Fakhrul, B. Khurana, B. H. Lee, S. Huang, H. T. Nembach, G. S. Beach, and C. A. Ross, "Damping and interfacial dzyaloshinskii–moriya interaction in thulium iron garnet/bismuth-substituted yttrium iron garnet bilayers," *ACS Applied Materials & Interfaces*, vol. 16, no. 2, pp. 2489–2496, 2024.

[311] S. Enterprises *et al.*, "Scilab: Free and open source software for numerical computation," *Scilab Enterprises, Orsay, France*, vol. 3, 2012.

[312] A. Manchon, H. C. Koo, J. Nitta, S. M. Frolov, and R. A. Duine, "New perspectives for rashba spin–orbit coupling," *Nature materials*, vol. 14, no. 9, pp. 871–882, 2015.

[313] J. Kim, J. Sinha, M. Hayashi, M. Yamanouchi, S. Fukami, T. Suzuki, S. Mitani, and H. Ohno, "Layer thickness dependence of the current-induced effective field vector in Ta— CoFeB— MgO," *Nature materials*, vol. 12, no. 3, pp. 240–245, 2013.

[314] C. O. Avci, K. Garello, C. Nistor, S. Godey, B. Ballesteros, A. Mugarza, A. Barla, M. Valvidares, E. Pellegrin, A. Ghosh, *et al.*, "Fieldlike and antidamping spin-orbit torques in as-grown and annealed Ta/CoFeB/MgO layers," *Physical Review B*, vol. 89, no. 21, p. 214419, 2014.

[315] C. O. Avci, K. Garello, I. Mihai Miron, G. Gaudin, S. Auffret, O. Boulle, and P. Gambardella, "Magnetization switching of an MgO/Co/Pt layer by in-plane current injection," *Applied physics letters*, vol. 100, no. 21, 2012.

[316] A. Manchon, "Spin hall effect versus rashba torque: a diffusive approach," *arXiv preprint arXiv:1204.4869*, 2012.

[317] X. Fan, H. Celik, J. Wu, C. Ni, K.-J. Lee, V. O. Lorenz, and J. Q. Xiao, "Quantifying interface and bulk contributions to spin–orbit torque in magnetic bilayers," *Nature communications*, vol. 5, no. 1, p. 3042, 2014.

[318] Y. Du, H. Gamou, S. Takahashi, S. Karube, M. Kohda, and J. Nitta, "Disentanglement of spin-orbit torques in Pt/Co bilayers with the presence of spin hall effect and rashba-edelstein effect," *Physical Review Applied*, vol. 13, no. 5, p. 054014, 2020.

[319] A. R. Mellnik, J. Lee, A. Richardella, J. L. Grab, P. J. Mintun, M. H. Fischer, A. Vaezi, A. Manchon, E.-A. Kim, N. Samarth, *et al.*, "Spin-transfer torque generated by a topological insulator," *Nature*, vol. 511, no. 7510, pp. 449–451, 2014.

[320] F. Bonell, M. Goto, G. Sauthier, J. F. Sierra, A. I. Figueroa, M. V. Costache, S. Miwa, Y. Suzuki, and S. O. Valenzuela, "Control of spin–orbit torques by interface engineering in topological insulator heterostructures," *Nano Letters*, vol. 20, no. 8, pp. 5893–5899, 2020.

[321] F. Binda, S. Fedel, S. F. Alvarado, P. Noël, and P. Gambardella, "Spin–orbit torques and spin hall magnetoresistance generated by twin-free and amorphous $Bi_{0.9}Sb_{0.1}$ topological insulator films," *Advanced Materials*, vol. 35, no. 45, p. 2304905, 2023.

[322] P. Li, W. Wu, Y. Wen, C. Zhang, J. Zhang, S. Zhang, Z. Yu, S. A. Yang, A. Manchon, and X.-x. Zhang, "Spin-momentum locking and spin-orbit torques in magnetic nano-heterojunctions composed of weyl semimetal WTe_2," *Nature communications*, vol. 9, no. 1, p. 3990, 2018.

[323] S. Shi, S. Liang, Z. Zhu, K. Cai, S. D. Pollard, Y. Wang, J. Wang, Q. Wang, P. He, J. Yu, *et al.*, "All-electric magnetization switching and dzyaloshinskii–moriya interaction in WTe_2/ferromagnet heterostructures," *Nature nanotechnology*, vol. 14, no. 10, pp. 945–949, 2019.

[324] Y. Zhang, H. Xu, K. Jia, G. Lan, Z. Huang, B. He, C. He, Q. Shao, Y. Wang, M. Zhao, *et al.*, "Room temperature field-free switching of perpendicular magnetization through spin-orbit torque originating from low-symmetry type ii weyl semimetal," *Science Advances*, vol. 9, no. 44, p. eadg9819, 2023.

[325] W. Tang, H. Liu, Z. Li, A. Pan, and Y.-J. Zeng, "Spin-orbit torque in van der waals-layered materials and heterostructures," *Advanced Science*, vol. 8, no. 18, p. 2100847, 2021.

[326] C. Grezes, A. Kandazoglou, M. Cosset-Cheneau, L. M. V. Arche, P. Noël, P. Sgarro, S. Auffret, K. Garello, M. Bibes, L. Vila, *et al.*, "Non-volatile electric control of spin-orbit torques in an oxide two-dimensional electron gas," *Nature Communications*, vol. 14, no. 1, p. 2590, 2023.

[327] I. Lyalin, S. Alikhah, M. Berritta, P. M. Oppeneer, and R. K. Kawakami, "Magneto-optical detection of the orbital hall effect in chromium," *Physical review letters*, vol. 131, no. 15, p. 156702, 2023.

[328] G. Sala and P. Gambardella, "Giant orbital hall effect and orbital-to-spin conversion in 3d, 5d, and 4f metallic heterostructures," *Physical Review Research*, vol. 4, no. 3, p. 033037, 2022.

[329] H. Hayashi, D. Jo, D. Go, T. Gao, S. Haku, Y. Mokrousov, H.-W. Lee, and K. Ando, "Observation of long-range orbital transport and giant orbital torque," *Communications Physics*, vol. 6, no. 1, p. 32, 2023.

[330] A. Bose, F. Kammerbauer, R. Gupta, D. Go, Y. Mokrousov, G. Jakob, and M. Kläui, "Detection of long-range orbital-hall torques," *Physical Review B*, vol. 107, no. 13, p. 134423, 2023.

[331] S. Damerio and C. O. Avci, "Tunable spin and orbital torques in Cu-based magnetic heterostructures," *Nano letters*, vol. 25, no. 6, pp. 2181–2187, 2025.

[332] C. O. Avci, A. Quindeau, C.-F. Pai, M. Mann, L. Caretta, A. S. Tang, M. C. Onbasli, C. A. Ross, and G. S. Beach, "Current-induced switching in a magnetic insulator," *Nature materials*, vol. 16, no. 3, pp. 309–314, 2017.

[333] H. Nakayama, M. Althammer, Y.-T. Chen, K. Uchida, Y. Kajiwara, D. Kikuchi, T. Ohtani, S. Geprägs, M. Opel, S. Takahashi, R. Gross, G. E. W. Bauer, S. T. B. Goennenwein, and E. Saitoh, "Spin hall magnetoresistance induced by a nonequilibrium proximity effect," *Phys. Rev. Lett.*, vol. 110, p. 206601, May 2013.

[334] W. B. Pearson, *A handbook of lattice spacings and structures of metals and alloys*. Elsevier, 1967.

[335] H.-P. Steinrück, F. Pesty, L. Zhang, and T. E. Madey, "Ultrathin films of Pt on TiO_2 (110): Growth and chemisorption-induced surfactant effects," *Physical Review B*, vol. 51, no. 4, p. 2427, 1995.

[336] J. S. Agustsson, U. B. Arnalds, A. S. Ingason, K. B. Gylfason, K. Johnsen, S. Olafsson, and J. T. Gudmundsson, "Growth, coalescence, and electrical resistivity of thin Pt films grown by dc magnetron sputtering on SiO_2," *Applied Surface Science*, vol. 254, no. 22, pp. 7356–7360, 2008.

[337] P. Andreazza, C. Andreazza-Vignolle, J. Rozenbaum, A.-L. Thomann, and P. Brault, "Nucleation and initial growth of platinum islands by plasma sputter deposition," *Surface and Coatings Technology*, vol. 151, pp. 122–127, 2002.

[338] S. Geller, H. Williams, G. Espinosa, and R. Sherwood, "Importance of intrasublattice magnetic interactions and of substitutional ion type in the behavior of substituted yttrium iron garnets," *Bell System Technical Journal*, vol. 43, no. 2, pp. 565–623, 1964.

[339] M. Gilleo and S. Geller, "Substitution for iron in ferrimagnetic yttrium-iron garnet," *Journal of Applied Physics*, vol. 29, no. 3, pp. 380–381, 1958.

[340] E. Sagasta, Y. Omori, M. Isasa, M. Gradhand, L. E. Hueso, Y. Niimi, Y. Otani, and F. Casanova, "Tuning the spin hall effect of pt from the moderately dirty to the superclean regime," *Physical Review B*, vol. 94, no. 6, p. 060412, 2016.

[341] J. WANG, J. YANG, Y. JIN, and T. QIU, "Effect of manganese addition on the microstructure and electromagnetic properties of YIG," *Journal of Rare Earths*, vol. 29, no. 6, pp. 562–566, 2011.

[342] S. S. Parkin, "Systematic variation of the strength and oscillation period of indirect magnetic exchange coupling through the 3d, 4d, and 5d transition metals," *Physical Review Letters*, vol. 67, no. 25, p. 3598, 1991.

[343] M. D. Stiles, "Interlayer exchange coupling," *Journal of Magnetism and Magnetic Materials*, vol. 200, no. 1-3, pp. 322–337, 1999.

[344] J. J. de Vries, J. Kohlhepp, F. Den Broeder, R. Coehoorn, R. Jungblut, A. Reinders, and W. De Jonge, "Exponential dependence of the interlayer exchange coupling on the spacer thickness in mbe-grown Fe/SiFe/Fe sandwiches," *Physical review letters*, vol. 78, no. 15, p. 3023, 1997.

[345] M. Y. Zhuravlev, E. Y. Tsymbal, and A. Vedyayev, "Impurity-assisted interlayer exchange coupling across a tunnel barrier," *Physical review letters*, vol. 94, no. 2, p. 026806, 2005.

[346] Q. Yang, L. Wang, Z. Zhou, L. Wang, Y. Zhang, S. Zhao, G. Dong, Y. Cheng, T. Min, Z. Hu, *et al.*, "Ionic liquid gating control of rkky interaction in FeCoB/Ru/FeCoB and $(Pt/Co)_2/Ru/(Pt/Co)_2$ multilayers," *Nature communications*, vol. 9, no. 1, p. 991, 2018.

[347] X. Wang, Q. Yang, L. Wang, Z. Zhou, T. Min, M. Liu, and N. X. Sun, "E-field control of the rkky interaction in FeCoB/Ru/FeCoB/pmn-Pt (011) multiferroic heterostructures," *Advanced Materials*, vol. 30, no. 39, p. 1803612, 2018.

[348] R. Lavrijsen, J.-H. Lee, A. Fernández-Pacheco, D. C. Petit, R. Mansell, and R. P. Cowburn, "Magnetic ratchet for three-dimensional spintronic memory and logic," *Nature*, vol. 493, no. 7434, pp. 647–650, 2013.

[349] A. Fernández-Pacheco, R. Streubel, O. Fruchart, R. Hertel, P. Fischer, and R. P. Cowburn, "Three-dimensional nanomagnetism," *Nature communications*, vol. 8, no. 1, p. 15756, 2017.

[350] X. Zhao and J. Zhao, "Interlayer dzyaloshinskii-moriya interaction in spintronics," *npj Spintronics*, vol. 3, no. 1, p. 25, 2025.

[351] J. Yun, B. Cui, Q. Cui, X. He, Y. Chang, Y. Zhu, Z. Yan, X. Guo, H. Xie, J. Zhang, *et al.*, "Anisotropic interlayer dzyaloshinskii–moriya interaction in synthetic ferromagnetic/antiferromagnetic sandwiches," *Advanced Functional Materials*, vol. 33, no. 33, p. 2301731, 2023.

[352] R. Chen, F. Xu, Q. Cui, J. Liang, Y. Zhou, N. Wang, F. Pan, F. Xue, H. Yang, and C. Song, "Anisotropic interlayer dzyaloshinskii-moriya interactions in synthetic ferromagnetic multilayers," *Science bulletin*, vol. 68, no. 9, pp. 878–882, 2023.

[353] T. Matthies, L. Rózsa, L. Szunyogh, R. Wiesendanger, and E. Y. Vedmedenko, "Interlayer and interfacial dzyaloshinskii-moriya interaction in magnetic trilayers: first-principles calculations," *Physical Review Research*, vol. 6, no. 4, p. 043158, 2024.